To the Graduate Council:

I am submitting herewith a thesis written by Chuck Brandon Thomas entitled "Processing, Mechanical Behavior, and Microstructural Characterization of Liquid Phase Sintered Intermetallic-Bonded Ceramic Composites." I have examined the final copy of this thesis for form and content and recommend that it be accepted in partial fulfillment of the requirements for the degree of Master of Science, with a major in Metallurgical Engineering.

Peter K. Liaw, Major Professor

We have read this thesis
and recommend its acceptance:

C R Brooks

J. T. Meek

Terry Tiegs

Accepted for the Council:

Associate Vice Chancellor and
Dean of The Graduate School

PROCESSING, MECHANICAL BEHAVIOR, AND MICROSTRUCTURAL CHARACTERIZATION OF LIQUID PHASE SINTERED INTERMETALLIC-BONDED CERAMIC COMPOSITES

A Thesis
Presented for the
Master of Science
Degree
The University of Tennessee, Knoxville

Chuck Brandon Thomas
August 1996

ACKNOWLEDGEMENTS

I am grateful to my Thesis Committee of Dr. Peter Liaw, Dr. Charlie Brooks, and Dr. Thomas Meek for their invaluable advice and assistance in performing this research. I would like to thank Terry Tiegs of the Ceramics Processing Group at Oak Ridge National Laboratory for sharing his wealth of ceramics knowledge with me and for his guidance and suggestions. I am very appreciative of Cliff Davisson, Jim Kiggans, Paul Menchhofer, and Claudia Walls of the Ceramics Processing Group at Oak Ridge National Laboratory for assisting me in equipment operation.

I should also recognize the assistance given to me by the faculty, staff, and students of the Materials Science and Engineering Department. The advice I received from Dr. Ray Buchanan on corrosion testing of my material was extremely beneficial. I appreciate the patience that Doug Fielden of the Machine Shop had in the machining of numerous samples and fixtures required for my research. I am grateful to Ted Long and Greg Jones of the Electronics Shop for their time and advice and for keeping the testing facilities in working order. I also appreciate Naren Miriyala for his time and patience in operating the bend test fixture for me. The advice I received from Robert Perrin on corrosion testing and many other issues was very much appreciated.

I will always be indebted to my parents, Charles and Peggy Thomas, for their love and for the support they have given me through the years in reaching this point in my life.

My wife, Deborah, is due the greatest amount of gratitude. Her love, patience, reassurance, and humor provided me with the motivation and perseverance necessary to reach this goal.

This research was conducted in cooperation with the University of Tennessee, Knoxville under contract 11X-SS400V with Martin Marietta Energy Systems, Inc. and was sponsored by the U. S. Department of Energy, Assistant Secretary for Energy Efficiency and Renewable Energy, Office of Industrial Technologies, Advanced Industrial Materials (AIM) Program, under contract DE-AC05-84OR21400 with Martin Marietta Energy Systems, Inc.

ABSTRACT

Intermetallic-bonded ceramic (IBC) composites with various amounts of a WC or TiC carbide phase mixed with a Ni_3Al or FeAl binder phase were successfully fabricated by liquid phase sintering and hot isostatic compaction methods. The influence of carbide type, binder type, and binder content on the flexural strength, hardness, fracture toughness, and corrosion resistance of IBC composites was investigated. Experimental techniques used to characterize the mechanical behavior included Vickers hardness, four-point flexure at 25 and 800°C, indentation fracture, indentation strength, and mass loss corrosion testing. In addition, the microstructure was characterized using optical and scanning electron microscopy to examine the polished and etched microstructures, the cracks located at the corners of the hardness indents, and the fracture surfaces produced by the flexure testing. Correlations were made between the mechanical properties of flexural strength and hardness and the microstructural parameter of contiguity. Experimental results indicate that the strength at 800°C of IBC composites with Ni_3Al compares favorably to the room-temperature strength. At 25°C, plastic deformation of the Ni_3Al and FeAl binders occurs, but the strength of the composite with FeAl is higher due to strong bonding along the carbide-binder interfaces. WC-based composites yielded higher flexural strength and fracture toughness

values, while TiC-based composites produced higher hardness values. Increased binder amounts produced higher values of flexural strength and fracture toughness due to a reduction in the number of carbide-carbide interfaces and an increase in plastic deformation in the crack-tip region, respectively. The Ni_3Al composites corroded in 10% nitric acid but resisted corrosion in 10% hydrochloric and 10% sulfuric acids. The FeAl composite exhibited opposite behavior in the three acids. The contiguity was observed to be proportional to the hardness but inversely proportional to the flexural strength.

TABLE OF CONTENTS

CHAPTER		PAGE
I.	INTRODUCTION	1
II.	LITERATURE REVIEW	3
	Historical Development	3
	Materials Studied	9
	Tungsten Monocarbide (WC)	10
	Titanium Carbide (TiC)	11
	Nickel Aluminide (Ni_3Al)	12
	Iron Aluminide (FeAl)	15
	Liquid Phase Sintering	17
	Wetting	18
	Variations of Liquid Phase Processes	20
	Classic Three-Stage Theory of Liquid Phase Sintering	21
	Rearrangement	22
	Solution-Reprecipitation	23
	Solid State	24
	Mechanical Property Measurement	25
	Hardness	25
	Flexural Strength	27
	Indentation Fracture Toughness	30
	Indentation Fracture Method	32
	Indentation Strength Method	35
	Relations Between Properties and Microstructure	37
	Microstructural Parameters	37
	Hardness/Microstructure Relationships	39
	Strength/Microstructure Relationships	41
	Fracture Toughness/Microstructure Relationships	43
III.	PRELIMINARY EXPERIMENTAL PROCEDURES	46
	Processing of IBC Composites	46
	Wet-Blending	47
	Axial Compaction	48
	Cold Isostatic Compaction	48
	Liquid Phase Sintering	49
	Hot Isostatic Compaction	50
	Characterization of IBC Composites	50
	Green Density	51
	Archimedes Density	51
	Hardness	53
	Optical Microscopy	53

CHAPTER		PAGE
IV.	**PRELIMINARY RESULTS AND DISCUSSION**	54
	Green Density	54
	Archimedes Density	54
	Hardness	58
	Optical Microscopy	61
V.	**EXPERIMENTAL PROCEDURES**	62
	Processing of Selected IBC Composites	62
	Wet-Blending	62
	Cold Isostatic Compaction	63
	Liquid Phase Sintering	64
	Hot Isostatic Compaction	64
	Characterization of Selected IBC Composites	65
	Mechanical Property Characterization	65
	Archimedes Density	65
	Hardness	65
	Flexural Strength	66
	Fracture Toughness	66
	Indentation Fracture Method	66
	Indentation Strength Method	67
	Mass Loss Corrosion Resistance	67
	Microstructural Characterization	68
	Microstructure Examination	68
	Fractography	69
	Property/Microstructure Correlations	69
VI.	**RESULTS AND DISCUSSION**	70
	Mechanical Property Characterization	70
	Archimedes Density	70
	Hardness	71
	Flexural Strength	72
	Indentation Fracture Toughness	77
	Mass Loss Corrosion Resistance	81
	Microstructural Characterization	83
	Microstructure Examination	83
	Porosity Measurements	83
	Indent Tip Areas	86
	Etched Microstructures	90
	Microstructural Parameter Measurement	91
	Fractography	93
VII.	**CONCLUSIONS**	99

CHAPTER	PAGE
VIII. RECOMMENDATIONS FOR FUTURE WORK	102
REFERENCES	103
APPENDIX	112
VITA	219

LIST OF TABLES

TABLE		PAGE
2.1.	Historical development of cemented carbides used as cutting tools (23, 24).	113
2.2.	Selected properties of tungsten carbide (WC) (5, 23, 26-28, 79).	114
2.3.	Selected properties of titanium carbide (TiC) (5, 23, 26, 28, 79).	115
2.4.	Selected properties of nickel aluminide (Ni_3Al) (31).	116
2.5.	Selected properties of iron aluminide (FeAl) (31).	117
2.6.	Summary of fracture toughness equations used for radial crack systems (49-52, 80, 81).	118
3.1.	Nominal compositions of Ni_3Al alloys.	119
3.2.	Average particle size and chemical analysis of tested WC powders.	120
3.3.	Summary of compositions tested.	121
4.1.	Green density and percent theoretical density for green specimens.	122
4.2.	Archimedes density and percent theoretical density for IBC composites.	123
4.3.	Vickers hardness results for IBC composites.	124
6.1.	Average percent theoretical density of flexure bars machined from disks.	125
6.2.	Vickers hardness results for selected IBC composites.	126
6.3.	Average room-temperature and high-temperature flexural strength for selected IBC composites.	127
6.4.	Fracture toughness results calculated from indentation fracture methods.	128

TABLE		PAGE
6.5.	Fracture toughness results calculated from indentation strength method.	129
6.6.	Average corrosion penetration rates for continuous immersion tests.	130
6.7.	Average corrosion penetration rates for discontinuous immersion tests.	131
6.8.	Results of microstructural parameter measurements.	132

LIST OF FIGURES

FIGURE		PAGE
1.1.	Strength of advanced aluminides as a function of temperature (71).	133
2.1.	Wetting of various carbides by Ni_3Al in a vacuum of 1.33×10^{-2} Pa at 1400°C (4).	134
2.2.	Fracture toughness as a function of binder content for WC-Ni_3Al and TiC-Ni_3Al compared to previous work on WC-Co (19).	135
2.3.	W-C phase diagram (72).	136
2.4.	Unit cell of WC (24).	137
2.5.	Effect of temperature on the hardness of some transition metal carbides (24).	138
2.6.	Scanning electron micrographs of 0.8 μm and 2.3 μm WC powders.	139
2.7.	Ti-C phase diagram (73).	140
2.8.	Unit cell of TiC (33).	141
2.9.	Scanning electron micrograph of 1-3 μm TiC powder.	142
2.10.	Ni-Al phase diagram (74).	143
2.11.	Unit cell of Ni_3Al (31).	144
2.12.	Oxidation of Ni_3Al (IC-50) compared to other alloys (75).	145
2.13.	Effect of boron additions on tensile elongation and yield strength in Ni_3Al containing 24 at.% Al (71).	146
2.14.	Scanning electron micrographs of IC-15, IC-50, and IC-218 Ni_3Al alloy powders.	147
2.15.	Fe-Al phase diagram (76).	148

FIGURE		PAGE
2.16.	Unit cell of FeAl (31).	149
2.17.	Scanning electron micrograph of FeAl powder.	150
2.18.	Schematic diagram illustrating surface energy equilibrium in wetting (c) and contact angles which produce good wetting (a) and poor wetting (b) (35).	151
2.19.	Bridging of particulate solids associated with a wetting liquid during the initial stage of liquid phase sintering (35).	152
2.20.	Schematic diagram illustrating the three overlapping stages of liquid phase sintering (35).	153
2.21.	Mechanism of grain growth during liquid phase sintering (35).	154
2.22.	Hardness as a function of cobalt content and carbide grain size in WC-Co (1).	155
2.23.	Schematic diagram illustrating the difference between 3- and 4-point loading (77).	156
2.24.	Tensile stress distribution in 3- and 4-point bending bars (41).	157
2.25.	Transverse rupture strength as a function of WC grain size in WC-Co (24).	158
2.26.	Strength as a function of cobalt content in WC-Co (69).	159
2.27.	Transverse rupture strength as a function of temperature in a WC-Co alloy (44).	160
2.28.	Fracture toughness as a function of cobalt content and carbide grain size in WC-Co (13).	161
2.29.	Fracture toughness as a function of temperature for several WC-Co alloys (1).	162
2.30.	Schematic diagram illustrating types of crack systems formed around an indent (46).	163

FIGURE		PAGE
2.31.	Hardness as a function of cobalt mean free path, cobalt content, and carbide grain size in WC-Co (24).	164
2.32.	Transverse rupture strength as a function of cobalt mean free path and cobalt content in WC-Co (24).	165
2.33.	Transverse rupture strength as a function of contiguity in WC-Co (44).	166
2.34.	Transverse rupture strength as a function of degree of separation in WC-Co (64).	167
2.35.	Transverse rupture strength as a function of structure parameter in WC-Co (64).	168
2.36.	Fracture toughness as a function of cobalt mean free path and carbide grain size in WC-Co (65).	169
2.37.	Fracture toughness as a function of contiguity and carbide grain size in WC-Co (65).	170
3.1.	Oblique blenders used during wet-blending.	171
3.2.	Die, punch, and base used during axial compaction of powders.	172
3.3.	Hydraulic press used during axial compaction of powders.	173
3.4.	Pressure vessel used during cold isostatic compaction of powders.	174
3.5.	Schematic diagram illustrating steps involved in wetbag isostatic compaction of powders (78).	175
3.6.	Batch-type vacuum furnace used for sintering of IBC composites.	176
3.7.	Vacuum furnace used for hot isostatic compaction of IBC composites.	177
3.8.	Apparatus used for measuring Archimedes density of IBC composites.	178

FIGURE		PAGE
4.1.	Effect of binder content on percent theoretical density.	179
4.2.	Effect of carbide size on percent theoretical density.	179
4.3.	Effect of binder type on percent theoretical density.	180
4.4.	Effect of carbide size on Vickers hardness.	180
4.5.	Effect of carbide type on Vickers hardness.	181
4.6.	Effect of binder type on Vickers hardness.	181
4.7.	Effect of binder content on Vickers hardness.	182
4.8.	Polished surface of CS 5-3.	182
4.9.	Polished surface of CS 3-1.	183
4.10.	Polished surface of CS 9-1.	183
5.1.	Schematic diagram illustrating the tests performed on each disk portion.	184
5.2.	Schematic diagram illustrating the polystyrene foam container and metal filler insert used in the cold isostatic compaction of selected IBC composites.	185
5.3.	MTS electro-hydraulic testing frame and Centorr vacuum furnace used in the room- and high-temperature flexure testing.	186
6.1.	Final average percent theoretical densities as a function of composition.	187
6.2.	Effect of binder content on final average percent theoretical densities for selected IBC composites.	187
6.3.	Vickers hardness as a function of composition and indent load.	188
6.4.	Effect of carbide type and indent load on Vickers hardness for selected IBC composites.	188

FIGURE PAGE

6.5. Effect of binder type and indent load on Vickers hardness for selected IBC composites. 189

6.6. Effect of binder content and indent load on the Vickers hardness for selected IBC composites. 189

6.7. Flexural strength as a function of composition and temperature. 190

6.8. Typical stress versus crosshead displacement curves obtained at room temperature. 191

6.9. Typical stress versus midspan deflection curves obtained at room temperature. 191

6.10. Typical stress versus crosshead displacement curves obtained at 800°C. 192

6.11. Typical stress versus midspan deflection curves obtained at 800°C. 192

6.12. Plastic deformation of flexure bars at 800°C. 193

6.13. Effect of carbide type and temperature on flexural strength for selected IBC composites. 194

6.14. Effect of binder type and temperature on flexural strength for selected IBC composites. 194

6.15. Effect of binder content and temperature on flexural strength for selected IBC composites. 195

6.16. Fracture toughness as a function of composition and method. 195

6.17. Effect of carbide type and method on fracture toughness for selected IBC composites. 196

6.18. Effect of binder type and method on fracture toughness for selected IBC composites. 196

6.19. Effect of binder content and method on fracture toughness for selected IBC composites. 197

FIGURE		PAGE
6.20.	Average corrosion penetration rate as a function of composition and immersion acid for continuous tests.	198
6.21.	Average corrosion penetration rate as a function of composition and immersion acid for discontinuous tests.	198
6.22.	CS-1 composite showing Type A06 porosity and region of interconnected porosity.	199
6.23.	CS-1 composite showing Type A04 porosity.	199
6.24.	CS-3 composite showing Type A04 porosity.	200
6.25.	CS-7 composite showing Type A04 porosity and large regions of interconnected porosity.	200
6.26.	CS-7 composite showing large regions of interconnected porosity.	201
6.27.	CS-9 composite showing Type A08 porosity.	201
6.28.	First indent area of CS-1 showing only two cracks.	202
6.29.	Second indent area of CS-1 showing only five cracks.	202
6.30.	Third indent area of CS-1 showing only a few cracks and a region of interconnected porosity.	203
6.31.	Fourth indent area of CS-1 showing no cracks.	203
6.32.	First indent area of CS-3 showing a short crack.	204
6.33.	Second indent area of CS-3 showing only two cracks.	204
6.34.	Third indent area of CS-3 showing one crack and a region of interconnected porosity.	205
6.35.	Fourth indent area of CS-3 showing all four types of cracking.	205
6.36.	First indent area of CS-7 showing long crack extension.	206

FIGURE		PAGE
6.37.	Second indent area of CS-7 showing interconnected porosity, unbonded TiC, and Ni_3Al pools.	206
6.38.	Third indent area of CS-7 showing several regions of porosity.	207
6.39.	Fourth indent area of CS-7 showing the path of a crack.	207
6.40.	First indent area of CS-9 showing only two cracks through carbide grains.	208
6.41.	Second indent area of CS-9 showing only one crack.	208
6.42.	Etched microstructure of CS-1.	209
6.43.	Etched microstructure of CS-3.	209
6.44.	Etched microstructure of CS-7.	210
6.45.	Etched microstructure of CS-9.	210
6.46.	Fracture surface of CS-1 showing three different fracture types.	211
6.47.	Fracture surface of CS-1 showing carbide-binder debonding and transgranular fracture of the binder.	211
6.48.	Secondary image of fracture surface of CS-1.	212
6.49.	Backscattered image of fracture surface of CS-1.	212
6.50.	Fracture surface of CS-3 showing two types of fracture.	213
6.51.	Fracture surface of CS-3 showing transgranular fracture of the binder and carbide-binder interfacial debonding.	213
6.52.	Second fracture surface of CS-3 showing binder transgranular fracture and carbide-binder interfacial debonding.	214
6.53.	Third fracture surface of CS-3 showing binder transgranular fracture and carbide-binder interfacial debonding.	214

FIGURE		PAGE
6.54.	Fracture surface of CS-7 showing large pit and porosity.	215
6.55.	Fracture surface of CS-7 showing mate of pit and porosity.	215
6.56.	Fracture surface of CS-7 showing large areas of unbonded TiC.	216
6.57.	Fracture surface of CS-7 showing large pores, unbonded TiC, and binder transgranular fracture.	216
6.58.	Fracture surface of CS-7 showing both types of transgranular fracture and carbide-binder debonding.	217
6.59.	Second fracture surface of CS-7 showing both types of transgranular fracture and carbide-binder debonding.	217
6.60.	Backscattered (L) and secondary (R) images of fracture surface of CS-9 showing transgranular fracture.	218
6.61.	Fracture surface of CS-9 showing transgranular fracture.	218

CHAPTER I

INTRODUCTION

Cemented carbides, which are carbides held together by a binder, or 'cementing', phase, belong to a class of materials known as hard metals that exhibit high hardness and wear resistance. The earliest and still the most popular form of cemented carbides are the tungsten carbide - cobalt (WC-Co) materials in which hard WC particles are bound by a soft, ductile Co binder. Cemented carbides are used in a wide range of applications, including metal cutting, mining, construction, rock drilling, metal forming, structural components, and wear parts. Roughly half of all cemented carbide production is used for metal cutting applications (1).

Over the past 70 years, the basic WC-Co cemented carbide, which is used for machining cast iron, nonferrous metals, nonmetallic materials and in nonmachining operations, has been modified to meet specific applications. Materials such as titanium carbide (TiC) and tantalum carbide (TaC) were added to WC-Co to impart crater resistance and reduce high-temperature wear, respectively, which allowed the machining of steels. Binders such as nickel (Ni) and iron (Fe) were used to replace Co, but the hardness and strength of WC-Ni and WC-Fe were inferior to WC-Co (2).

The life of WC-Co cemented carbides is limited by the elevated-temperature strength and corrosion resistance of the Co binder.

Furthermore, about 65% of the world supply of Co is in Zambia and Zaire, and the U. S. imports over 90% of its Co (3). Thus, it would be desirable to replace the Co binder with one having better high-temperature strength, corrosion resistance, and cost.

The intermetallic alloy nickel aluminide (Ni_3Al) wets WC, which is critical to the success of the liquid phase sintering process, almost completely after one minute at 1400°C (4). As shown in Figure 1.1, advanced aluminides based on Ni_3Al have superior high-temperature strength when compared to Hastelloy-X and 316 stainless steel.[1] Nickel-based binders have also shown better corrosion resistance than Co (5, 6). Cemented carbides containing Ni_3Al will be less expensive than those containing Co (7). Therefore, Ni_3Al is a candidate for replacing the Co binder in WC-Co cemented carbides. Little information exists on the replacement of Co in cemented carbides with intermetallics such as Ni_3Al.

The purpose of this research was to utilize the optimum processing parameters in the fabrication of intermetallic-bonded ceramic (IBC) composites by liquid phase sintering to yield samples for mechanical property testing and microstructural characterization. Moreover, the relationships between mechanical properties and microstructural parameters were studied.

[1] All figures and tables are located in the Appendix.

CHAPTER II

LITERATURE REVIEW

HISTORICAL DEVELOPMENT

The development of modern cemented carbides dates back to 1923 when Karl Schröter mixed tungsten monocarbide (WC) with up to 10% (by weight) of a metal from the iron group, compacted the powders, and liquid phase sintered them at temperatures near the melting point of the binder (8). In Schröter's second patent, he calls for up to 20% of the binder which he limits to Co (9). Sintered cemented carbides were commercially introduced in 1927 by Krupp under the name of "Widia" from the German *wie Diamant* which means *like diamond* (10). In the United States, a division of the General Electric Company, Carboloy, began cemented carbide production in 1928 and held the American patent rights (11).

Another development of this time period was in TiC-based hardmetals which were patented by Schwarzkopf in 1931 (12). The disadvantages of using TiC were that it was brittle, had poor high-temperature hardness, and was not readily wetted by the Ni binder. The addition of molybdenum (Mo) powder to TiC in the 1950's, however, produced a TiC core enclosed by a (Ti, Mo) layer that promoted wetting by Ni. Due to the high hardness, good wear resistance, brittleness, and low

hot hardness of TiC, TiC-based hardmetals are primarily employed in high-speed finishing with slow feed rates and low cutting depths (2).

Further advances in cemented carbides came about as a result of the need to tailor the composition of the hard metals in order to optimize them for specific applications. The WC-Co alloys gave superior performance when they were used to machine cast iron and nonferrous metals. When used to cut steel, however, they were susceptible to diffusion wear and chemical attack. The WC diffuses relatively quickly into the chip surface of ferrous alloys which leads to chemical breakdown and cratering of the WC-Co alloy (13). In 1929, Schwarzkopf modified the WC-Co alloy by replacing some or all of the WC with carbides such as TiC and TaC to form solid solutions which are resistant to the chemical attacks (14). This development permitted the use of cemented carbides in the high-speed machining of steels.

More detailed historical information can be found in Schwarzkopf's and Kieffer's *Cemented Carbides* (11) and in Brookes' *Hardmetals and Other Hard Materials* (15). Additionally, Table 2.1 illustrates critical developments which have occurred from the 1920's to the early 1980's in WC-based and WC-free cemented carbides used as cutting tools.

Some of the more recent developments (i.e., from the last 10-15 years) in cemented carbide research have focused on the replacement of the Co binder with mixtures of Ni and Al. Viswanadham et al. (16) attempted

to strengthen the binder in WC-Ni by alloying it with Al to produce controlled dispersions of γ' (Ni_3Al) in the binder. They fabricated WC-(Ni, Al) with 4 to 12 wt.% Al by liquid phase sintering and hot isostatic pressing operations. The WC-(Ni, Al) samples were subjected to a variety of heat treatments that took place in the solid state. Thus, the only microstructural parameters that were varied were the amount, size, and distribution of γ' in the binder phase. Viswanadham et al. (16) concluded that γ' provided little or no strengthening to the binder regardless of its size or distribution. Furthermore, they showed that the presence of γ' had a disadvantageous effect on fracture toughness.

Fortunately, other work has been more promising. Tumanov et al. (4) investigated the wettability of TiC, WC, and (Ti, W)C solid solutions by molten Ni_3Al. They showed that the wetting angle between WC and Ni_3Al approached zero after one minute at 1400°C. TiC was not wetted as well as WC by the Ni_3Al, but the wetting angle approached 40° after 5 minutes as shown in Figure 2.1. The significance of the wetting angle is discussed later, but, in general, as the wetting angle decreases, the probability of a powder composite becoming highly dense during liquid phase sintering increases. Tumanov et al. (4) also established that a two-phase diffusion area was formed in TiC-Ni_3Al as a result of the solubility of TiC in molten

Ni_3Al. Virtually no two-phase diffusion area, however, was formed in WC-Ni_3Al at temperatures up to 1400°C. This result led them to conclude that the solubility of WC in molten Ni_3Al is not significant in comparison to the solubility of WC in Co. Finally, Tumanov et al. (4) examined the microstructure of WC-Ni_3Al and observed that the WC grains are not faceted as they are in WC-Co, which is probably a result of the lower solubility of WC in Ni_3Al than in Co.

Almond and Roebuck (17) examined the use of Co-Ni, Ni-Al, Ni-Cr(Chromium)-Mo, and Ni-Cr-Mo-Al as binder phases for WC hard metals. They found that WC-Ni alloys had lower toughness and strength than WC-Co, and the addition of Al to form γ' raised the strength but lowered the fracture toughness. On the other hand, solid solution strengthening by adding Cr and Mo increased the hardness without decreasing the toughness and gave properties which compared favorably to WC-Co. When both γ' and solid solution strengthening were employed, the hardness and toughness values obtained were better than those of WC-Co. The results they obtained on WC with Ni alloy binder phases showed that certain compositions should be capable of giving mechanical properties which are better than or equal to those of WC-Co.

Tiegs and McDonald (7, 18) examined the use of Ni_3Al with alloying additions of boron (B), hafnium (Hf), zirconium (Zr), cesium (Ce) and Cr as

a binder for WC and TiC. They blended the powders, which ranged in composition from 5-20 wt.% Ni_3Al, to give a homogeneous mixture and then hot-pressed them at 1150-1350°C at 27.6 MPa (4 ksi) for one hour. Highly dense composites were obtained for a variety of compositions. Tiegs and McDonald (7, 18) showed that the hardness of the alloys increased with increasing Zr content or decreasing Al content. They also found that for composites reaching at least 99% theoretical density, the hardness decreased, and the toughness increased with increasing Ni_3Al content. Tiegs and McDonald (7, 18) illustrated that WC-Ni_3Al has higher hardness than WC-Co for the same binder content, and the high-temperature strength of Ni_3Al allows the properties of WC-Ni_3Al to be retained at higher temperatures when compared to WC-Co.

Since 1992, the Metals and Ceramics Division at Oak Ridge National Laboratory has been researching the relationships among processing, mechanical properties, and microstructure of IBC composites. Alexander et al. (19) fabricated WC- and TiC-based composites with a Ni_3Al binder via the hot-pressing technique. Indentation fracture toughness testing was performed on the composites, and the results indicated that the fracture toughness of the IBC composites was consistent with that of WC-Co as shown in Figure 2.2. Moreover, R-curve behavior in WC-Ni_3Al was exhibited since the fracture toughness values increased as a function of the

indent load. This behavior would be consistent with crack-wake toughening mechanisms that would be anticipated from crack-bridging and plastic deformation processes (19).

Becher et al. (20) studied the use of an iron aluminide (FeAl) binder as an alternative to Ni_3Al due to FeAl's excellent oxidation and corrosion resistance and its low density. Additionally, they noted that Fe is not as hazardous as Ni. Becher et al. (20) mixed prealloyed Fe-40 at.% Al and TiC, heated the powder to 1450°C in vacuum, and maintained the temperature for 15 minutes. The measured densities of the TiC-FeAl composites typically exceeded 95% theoretical density.

In 1993, Alexander et al. (21) fabricated specimens of WC-Ni_3Al and TiC-Ni_3Al by pressureless sintering of compacted samples at 1550 and 1600°C. This form of processing is attractive because complex-shaped parts can be made more easily than in hot-pressing.

In 1994, Plucknett et al. (6) fabricated specimens of WC-Ni_3Al and TiC-Ni_3Al by pressureless sintering of compacted samples. At temperatures of 1475°C and above, densities of greater than 97% theoretical were achieved for TiC-Ni_3Al with slightly lower densities for WC-Ni_3Al. The specimens were indented with 50 kg loads and exhibited minimal radial cracking which indicates high toughness. They performed elevated-temperature flexure strength tests on the hot-pressed versions of these

composites and found, as expected, that the IBC composites had significantly better high-temperature strength retention than WC-Co. Plucknett et al. (6) also performed mass loss corrosion resistance testing on the IBC composites and WC-Co. They found that the IBC composites had much better corrosion resistance than WC-Co in 10% nitric and 10% sulfuric acids, but both materials had approximately the same amount of corrosion resistance in 10% hydrochloric acid.

Thus, IBC composites have previously been fabricated by the techniques of hot-pressing and liquid phase sintering. Work has been performed on characterizing the mechanical properties and microstructure of hot-pressed IBC composites. However, the mechanical properties and microstructure of liquid phase sintered IBC composites have not been characterized. Furthermore, the relationships between the mechanical properties and microstructural parameters of liquid phase sintered IBC composites have not been studied.

MATERIALS STUDIED

The IBC composites employed in this study typically consist of two out of the four following materials: WC, TiC, Ni_3Al, and FeAl. Each composite incorporates one of the carbides, WC or TiC, with one of the aluminides, Ni_3Al or FeAl. In this section, various properties of the four constituents will be discussed.

Tungsten Monocarbide (WC)

Tungsten forms two hexagonal carbides, the monocarbide (WC) with 6.13 wt.% C and ditungsten carbide (W_2C) with 3.16 wt.% C. The W-C phase diagram, with W_2C and WC denoted by β and δ, respectively, is shown in Figure 2.3. By observing Figure 2.3, it is obvious that WC has very little tolerance for changes in its carbon content. A deficiency in carbon can lead to the formation of W_2C whose brittleness may not be desired in the final product. On the other hand, excess carbon in the form of graphite can lead to lower values of transverse rupture strength (22).

As shown in Figure 2.4, WC has a hexagonal crystal structure with two atoms per unit cell and has lattice constants of a = 0.2906 nm and c = 0.2837 nm giving a c/a ratio of 0.976 (23). The carbon atoms are located in either all of the 1/2, 2/3, 1/2 positions or all of the 2/3, 1/3, 1/2 positions in a hexagonal lattice of tungsten atoms (24). The operative slip system for WC is $\langle 11\bar{2}3\rangle \{1\bar{1}00\}$ (25).

When compared to other refractory carbides, the thermodynamic stability of WC is relatively low with a standard free energy of formation of -40 ± 2 kJ/mol at 25°C (26). The room-temperature hardness of WC is also relatively low with reported values ranging from 1800-2200 kg/mm^2 (5, 23, 26-28). The hardness values have such a large scatter due to the fact that WC crystals are anisotropic. The elevated-temperature hardness of WC,

however, is higher than that of all the other refractory carbides as shown in Figure 2.5. Some of the physical and mechanical properties of WC are presented in Table 2.2.

The preferred method for WC production is the direct carburization of tungsten powder with carbon black. The powders are blended to obtain a uniform distribution of carbon, and the mixture is heated in a hydrogen atmosphere between 1400 and 1500°C to produce tungsten carbide particles ranging in size from 0.5 to 30 μm. The higher carburizing temperature is used when coarse powders are desired (1). Scanning electron micrographs of the 0.8 and 2.3 μm (average particle size) WC powder used are presented in Figure 2.6.

Titanium Carbide (TiC)

Titanium forms two cubic carbides, the monocarbide (TiC) with 10 to 19.3 wt.% C and dititanium carbide (Ti_2C) with 10 to 12.4 wt.% C. The Ti-C phase diagram is shown in Figure 2.7. By examining Figure 2.7, it is clear that TiC has a wide range of homogeneity, and its maximum carbon content is somewhat less than the stoichiometric composition. Thus, if there is a slight carbon deficiency in TiC, an extra phase will not be produced (23).

Titanium carbide has a face-centered cubic (FCC) structure with four atoms per unit cell and has a lattice parameter of 0.4330 nm (23). In this

structure, every titanium and carbon atom is surrounded by six nearest-neighbors of the other species in an octahedral configuration as shown in Figure 2.8. The active slip system for TiC is $\langle 1\bar{1}0\rangle$ {110} (29).

The thermodynamic stability of TiC is relatively high with a standard free energy of formation of -183 ± 2 kJ/mol at room temperature (26). The room-temperature hardness of TiC is the highest of all the refractory carbides with a Vickers hardness value of 3000 kg/mm^2 (5, 23, 26, 28). A drawback to the use of TiC, however, is that its hardness decreases more than the hardness of most other carbides with increasing temperature as shown in Figure 2.5. Physical and mechanical properties of TiC are presented in Table 2.3.

Titanium carbide powder is produced by the reduction and carburization of pure titanium dioxide (TiO_2) with carbon black. The powders are blended by wet or dry milling for an extended period of time, and the mixture is carburized by the gas phase of carbon monoxide (CO) between 1600 and 1700°C (30). A scanning electron micrograph of the 1-3 μm TiC powder used is presented in Figure 2.9.

Nickel Aluminide (Ni_3Al)

The nickel aluminide, Ni_3Al, is an intermetallic compound that forms at the Ni-rich end of the Ni-Al system as shown in Figure 2.10.

Ni_3Al has a $L1_2$ crystal structure, an ordered derivative of the face-centered cubic (FCC) structure, below its peritectic temperature of 1390°C. As presented in Figure 2.11, the unit cell of Ni_3Al has a total of 4 atoms with 3 Ni atoms at the face-centered positions and Al at the corners (31).

Ni_3Al has a low density, relatively high melting temperature, and excellent strength and oxidation resistance at elevated temperatures. The strength of Ni_3Al-based advanced aluminides increases with temperature up to approximately 900°C as displayed in Figure 1.1. Furthermore, the oxidation resistance of Ni_3Al (IC-50) is superior to that of 316 stainless steel and Hastelloy-X as illustrated in Figure 2.12. Several physical and mechanical properties of Ni_3Al are presented in Table 2.4.

The use of polycrystalline Ni_3Al was restricted, however, for some time because of its poor ductility and brittle intergranular fracture. Even highly pure Ni_3Al, in which no grain boundary segregation of impurities occurs, displayed intergranular fracture indicating inherent brittleness (31). Further research was required to determine an approach for strengthening the grain boundaries of polycrystalline Ni_3Al.

Aoki and Izumi (32) were the first to microalloy Ni_3Al with B, and they observed a drastic improvement in the room-temperature ductility. The addition of approximately 0.1 wt.% B resulted in an increase in the

cohesion or intrinsic strength of the grain boundaries. Boron additions also intensify dislocation generation and promote slip transmission across grain boundaries (31). The effect of boron additions on the room-temperature ductility and yield strength of Ni_3Al is illustrated in Figure 2.13. It can be easily observed in Figure 2.13 that the addition of just 0.02 wt.% B increases the ductility of Ni_3Al from less than 10% to greater than 40%.

Efforts to further improve the strength of Ni_3Al have centered on macroalloying additions. Ni_3Al can be strengthened by solid solution strengthening mechanisms because it can preserve long-range order while dissolving a sizable amount of alloying additions. The extent of solid solution in Ni_3Al is determined by the atomic size misfit and the difference in the heats of formation between Ni_3Al and Ni_3X, where X represents the alloying addition. Zirconium and hafnium are most effective in improving the high-temperature strength. Chromium is added to reduce dynamic embrittlement in oxidizing environments at elevated temperatures (31).

Zirconium is a dopant that reacts with damaging impurities and binds them in a harmless form such as precipitates located within the grains. Zirconium substitutes almost exclusively for Al sublattice sites. Studies on the mechanical properties of Ni_3Al alloys indicate that elements

which substitute on Al sites harden the alloys more effectively than elements which substitute on Ni or both Ni and Al sites. Ni_3Al alloys contain up to 5 at.% Zr to increase the high-temperature strength (31).

The addition of chromium promotes the rapid formation of protective chromium oxide (Cr_2O_3) films which prevent oxygen from penetrating the grain boundaries and base metals. Chromium substitutes for both Ni and Al sublattice sites. Ni_3Al alloys contain up to 10 at.% Cr to enhance the ductility at temperatures ranging from 400 to 900°C and to increase the fatigue resistance at temperatures above 500°C (31).

Powders of Ni_3Al alloys are typically produced by inert gas atomization. A melt of the Ni_3Al alloy flows out of a tundish in a single stream, which is disintegrated into droplets by inert gas exiting a nozzle at high pressure. The average particle size of gas-atomized powders ranges from 20 to 300 μm (33). Scanning electron micrographs of the three different Ni_3Al alloy powders used (IC-15, IC-50, and IC-218) are presented in Figure 2.14. Each of the Ni_3Al alloy powders has a particle size of less than 44 μm (0.0017 inches).

Iron Aluminide (FeAl)

The iron aluminide, FeAl, is an intermetallic compound that forms at the Fe end of the Fe-Al system as shown in Figure 2.15. FeAl has a B2

crystal structure, an ordered derivative of the body-centered cubic (BCC) structure, below its critical ordering temperature of 1250°C. FeAl has wide solubility limits ranging from 36 to 50 at.% Al. The particular FeAl used in this work contains 40 at.% Al. As shown in Figure 2.16, the unit cell of FeAl has a total of 2 atoms with an Al atom at the body-centered position and Fe at the corners (31).

FeAl has a low density along with excellent corrosion and oxidation resistance at elevated temperatures. This excellent resistance originates from the ability of iron aluminides to form protective Al_2O_3 scales in oxidizing and sulfidizing environments. The iron aluminides, however, have a couple of disadvantages in that they have low ductility and fracture toughness at room temperature along with poor strength at temperatures above 600°C (31).

The fracture mode of FeAl depends on the Al concentration. FeAl containing less than 40 at.% Al fails mainly by transgranular cleavage fracture, but FeAl containing 40 at.% or more Al fails at room temperature by brittle intergranular fracture and exhibits little ductility. The room-temperature ductility of FeAl with less than 40 at.% Al ranges from 2 to 4% for materials with grain sizes of 150 to 200 μm. If the grain size is refined, the ductility can be increased to about 6 to 8% (31). Research by Liu, Lee, and McKamey (34) showed that environmental embrittlement, rather than intrinsic brittleness, was a major cause of low ductility in FeAl with 36.5

at.% Al. They concluded that water vapor was the main source of embrittlement.

Unlike the yield strength of Ni_3Al, the yield strength of FeAl is independent of temperature below 600°C, but the strength falls rapidly with higher temperatures. The only exception is found in coarse-grained FeAl material which contains less than 40 at.% Al. Its strength shows a slight increase with temperature up to 600°C (31). Several physical and mechanical properties of FeAl are presented in Table 2.5.

Powders of FeAl alloys are typically manufactured by the process of inert gas atomization as discussed in the previous section. A scanning electron micrograph of the FeAl powder used is presented in Figure 2.17. The FeAl powder has a particle size of less than 44 μm (0.0017 inches).

LIQUID PHASE SINTERING*

The term *sintering* refers to the phenomenon that occurs when packed powders "bond together when heated to temperatures in excess of approximately half of the absolute melting temperature." More specifically, sintering in the presence of a liquid phase refers to the coexistence of a liquid phase with a particulate solid at a temperature higher than the melting point of the phase which becomes liquid.

* Much of this discussion is paraphrased from R. M. German (Ref. 35) unless otherwise noted.

Three requirements must be met to achieve successful liquid phase sintering:

- a certain amount of liquid phase available,
- a certain amount of solid solubility in the liquid, and
- liquid wetting of the particulate solid.

First, enough liquid must be present, and it must wet the solid in order to develop sufficient capillary pressure which allows particle necks to form and small pores to be filled. Second, there must be some amount of solid solubility in the liquid in order for the changes in particle size and shape to take place during the solution-reprecipitation stage of densification.

Liquid phase sintering is typically performed without the application of an external pressure; therefore, liquid phase sintering is a type of pressureless sintering. External pressure is not necessary since the driving force for densification is the capillary pressure exerted by the liquid on the particulate solid. To develop the required capillary pressure, the liquid needs to wet the solid particles. Hence, the wetting characteristics of the materials involved are critical to the success of the liquid phase sintering technique.

Wetting

The term *wetting* refers to the equilibrium that occurs between the surface energies of solid, liquid, and vapor phases when a liquid drop rests

on a solid substrate. The relationship between the surface energies is given by the equation:

$$\gamma_{LV} \cdot \cos\theta = \gamma_{SV} - \gamma_{SL} \qquad [1]$$

where γ_{LV}, γ_{SV}, and γ_{SL} are the surface energies of the liquid-vapor interface, solid-vapor interface, and solid-liquid interface, respectively. The contact angle is represented by θ, and its value (which ranges from 0° to 180°) characterizes the degree of wetting. A schematic diagram of the surface energy equilibrium is shown in Figure 2.18c.

When the surface energy of the solid-vapor interface, γ_{SV}, is high, the liquid wants to spread out along the solid substrate to reduce γ_{SV}. Thus, wetting of the solid by the liquid, as shown in Figure 2.18a, occurs as the contact angle varies from 90° to 0°. Complete wetting, i.e. spreading, occurs when $\theta = 0°$. If the surface energy of the solid-liquid interface, γ_{SL}, is high, the liquid desires to minimize the interfacial area of the solid and liquid to reduce γ_{SL}. Hence, the liquid remains in a drop-like shape as shown in Figure 2.18b and does not wet the solid as θ ranges from 90° to 180°. Figure 2.19 illustrates the bridging of particulate solids associated with a wetting liquid during the initial stage of liquid phase sintering.

The wetting of metallic carbides such as WC and TiC has been previously studied by Ramqvist (36). He found that WC was completely

wetted ($\theta = 0°$) by Co, Ni, and Fe. TiC was wetted better by Ni ($\theta = 23°$) than by Co ($\theta = 25°$) or Fe ($\theta = 28°$).

More recently, research by Alexander et al. (21) on Ni_3Al-bonded ceramic composites has shown good wetting of TiC and WC particulates by various types of Ni_3Al alloys. Furthermore, highly dense composites of TiC-Ni_3Al and WC-Ni_3Al were recently fabricated by the liquid phase sintering technique as previously discussed. Thus, the production of dense IBC composites by liquid phase sintering is quite feasible due in part to the wetting characteristics of the systems examined.

Variations of Liquid Phase Processes

The liquid in liquid phase sintering is acquired by one of two methods:

- using mixed powders in transient or permanent liquid phase sintering
- using a prealloyed powder in supersolidus sintering.

When a powder mixture is employed, a liquid develops as the mixture is heated during the sintering cycle. The solubility of the liquid in the solid determines whether the liquid is transient or permanent during sintering. If the liquid has a high solubility in the solid, it will react with the solid and disappear as sintering time increases. Hence, the liquid will only be present temporarily, i.e., transient liquid phase sintering. Conversely, if the liquid has a low solubility in the solid, it will be in

equilibrium with the solid phase and be present permanently, i.e., permanent liquid phase sintering.

When a prealloyed powder is used, liquid forms when the powder is heated to a temperature between the solidus and liquidus temperatures. Since a prealloyed powder is used, liquid phase forms within each particle which creates a homogeneous distribution of liquid leading to rapid densification. The supersolidus sintering process is highly temperature-dependent. Depending on composition, the accuracy of the sintering temperature must be kept at ± 2 to 10 K (33). If prealloyed powder is available, and temperature and compositional variations can be carefully controlled, supersolidus sintering is usually a successful sintering method.

In the current research, mixed powders of WC-Ni_3Al, TiC-Ni_3Al, WC-FeAl, and Al_2O_3-TiC-Ni_3Al were used. The binder phase of Ni_3Al or FeAl formed the liquid upon heating, and the liquid was permanent due to the fact that Ni_3Al or FeAl do not have a high solubility in WC or TiC.

Classic Three-Stage Theory of Liquid Phase Sintering

Price et al. (37) are credited with developing the classic three-stage theory of liquid phase sintering in their research on tungsten heavy alloys. The theory assumes that densification begins after liquid formation and occurs in three overlapping stages:

- rearrangement,
- solution-reprecipitation, and
- solid state.

A schematic diagram of the three stages is shown in Figure 2.20.

Rearrangement

In the first part of rearrangement, the liquid phase develops as the mixed powders are heated to a sufficiently high temperature. If an adequate amount of liquid forms and it wets the solid, the resulting capillary forces cause the liquid to permeate the particle necks and small pores. Particle sliding occurs as the solid particles rearrange to yield a more efficient packing, and porosity is greatly reduced as the system strives to minimize its interfacial energy, thereby leading to rapid densification. The rate of densification decreases, however, as porosity is reduced because the viscosity in the system increases.

The degree of densification achieved during the rearrangement stage is strongly dependent both on the amount of liquid present and liquid wetting of the solid, and on the particle size and shape and the green density of the compact. Small particles typically produce better rearrangement since they can be packed more efficiently, but if the particles have an irregular shape, rearrangement is hindered. Rearrangement can also be limited by a high green density. Prior to sintering, the powders are compacted, and connections are made between the powders. During

heating, the connections between the particulate solids produce solid state bonds which prevent complete rearrangement of the solid particles.

Solution-Reprecipitation

As the solution-reprecipitation stage begins, the densification rate attained during rearrangement decreases. The main steps in solution-reprecipitation are:

- dissolution of particulate solid in the surrounding liquid,
- diffusive transport through the liquid, and
- reprecipitation of dissolved material on particles at other locations.

Obviously, the solubility and diffusivity characteristics of the system are of great significance to the successful completion of this stage. The compact generally contains particulate solids of various sizes, producing differences in solubility. Smaller particles will dissolve first because their higher solubility in the surrounding liquid leads to the formation of a concentration gradient in the liquid.

Diffusion then ensues as material moves from the small grains and reprecipitates on the large grains. Hence, the diffusion process leads to the formation of larger grains resulting in a decrease in the number of grains. Moreover, as the material is transported and reprecipitated, the shape of the larger grains gradually changes in a process called grain shape accommodation. This process yields a more efficient packing of the larger

grains and leads to the elimination of pores which remained after rearrangement.

Solid State

During the third and final stage, solid state sintering occurs. By the time this stage is reached, a rigid solid skeleton of material has formed via the solution-reprecipitation process. Because of the fixed structure, rearrangement processes are hampered, and the densification rate slows further than in the previous stage. Moreover, many of the few remaining pores become trapped, and the elimination of these pores becomes very difficult due to the rigid solid skeleton. If the closed pores contain gas, they will grow with sintering time in order to allow the gas pressure in the pores to decrease.

Grain coarsening also takes place during the final stage as illustrated in Figure 2.21. The necks between the grains in the rigid skeleton grow by reprecipitation of dissolved material or by solid state diffusion processes. For the most part, the entire microstructure including grains and pores continues to grow with increasing amounts of sintering time. Large grains and pores are not desirable in many sintered products because of a resulting decline in mechanical properties. Thus, the sintering time must be optimized to allow the desired amount of densification without acquiring too much microstructural coarsening.

MECHANICAL PROPERTY MEASUREMENT

Hardness

The hardness of cemented carbides is usually measured by the Vickers diamond pyramid indentation test (HV) or the Rockwell A-scale diamond cone indentation test (HRA). A wide range of loads (1 gram to 50 kg) can be used for the Vickers test, but the Rockwell A test requires a load of 60 kg. For either test, the flat surface of the test sample should be finely ground, polished, and placed at a right angle to the indenter axis (1). After the indent is made, the diagonals of the indent are measured and are used in the following equation to calculate the Vickers hardness (HV):

$$H_V = \frac{1.8544 \times L}{d^2} \qquad [2]$$

where L = load (kg) and d = average diagonal (mm). Measurements should not be performed on asymmetrical or chipped indents or if cracks emanate from points other than the corners of the indent.

When the hardness of cemented carbides is discussed, the difference between real or true hardness and apparent hardness must be discerned. In the case of true hardness, measurements are taken on individual grains of material to eliminate porosity effects. Thus, the true or real hardness of cemented carbides is actually an indication of microhardness. The apparent hardness of cemented carbides, however, represents the macrohardness of the sintered material and takes into account the effects of

porosity (38). Hence, the apparent hardness is typically lower than the real or true hardness, yet it gives a more accurate representation of the hardness to be expected in application.

The scatter and degree of uncertainty in reported hardness values for cemented carbides have been known for some time. In the 1950's, Schwarzkopf and Kieffer (11) noted that Vickers hardness values were not comparable to those of metals and alloys due to the residual porosity and structure of cemented carbides. Farooq and Davies (39) reported a scatter of 50 HV in their testing of WC-Fe-Co-NiMoB and WC-stainless steel alloys which had reached 99.5% theoretical density. A study sponsored by the Versailles project on Advanced Materials and Standards (40) indicated that hardness tests may be used for engineering ceramics if it is acknowledged that errors as high as 15% and biases lead to high levels of uncertainty. Data in the text by Thümmler and Oberacker (33) indicate a scatter of 100 HV at a load of 10 kg and a scatter of 250 HV at a load of 1 gram for a hardened sintered steel. An increase in the amount of scatter is evident with decreasing load. When the load decreases, the volume of material indented decreases as well. As a result, the amount of scatter increases due to the presence of pores in the indent area (38).

The hardness of cemented carbides is strongly dependent upon composition, microstructure, and temperature. For alloys which have a similar carbide grain size but differing amounts of binder phase (e.g. Co,

Ni_3Al, or FeAl), the hardness decreases with increasing amounts of the ductile binder as shown in Figure 2.22. This trend is due to the hardness values of the constituent materials present in the composite; therefore, less carbide phase will yield a lower hardness. If the alloys have the same binder content but varying carbide grain sizes, the hardness increases with decreasing size of the carbide grains. This behavior is also present in Figure 2.22. The hardness of cemented carbides decreases with increasing temperature. This is a result of the decrease in hardness of the carbides with increasing temperature as illustrated in Figure 2.5.

The dependence of hardness on microstructural parameters, such as contiguity of the carbide phase and mean free path, i.e. thickness, of the binder phase, has been researched and will be discussed later.

Flexural Strength

The fracture strength of cemented carbides is measured by the flexure test. In this test, an increasing load is applied by one or two carbide cylinders at the center of a bar with rectangular cross section as it rests on two other carbide cylinders. If only one cylinder is used to apply the load, the test is referred to as a 3-point bending test, but if two cylinders are employed, 4-point bending occurs as shown in Figure 2.23. Before the test is performed, the dimensions of the test bar and the distance between the carbide cylinders are measured. The measured values are then used in the

following equation from simple beam theory to calculate the flexural strength in 4-point bending:

$$\sigma_f = \frac{3PL}{4bd^2} \qquad [3]$$

where σ_f = flexural strength (MPa), P = breakload (N), L = support span (mm) of the two outer carbide cylinders, b = specimen width (mm), and d = specimen thickness (mm).

Flexural strength determination using a 4-point bending test is favored over the use of a 3-point bending test. Figure 2.24 shows the difference in tensile stress distribution for 3- and 4-point bend specimens. In 3-point bending, the maximum tensile stress occurs at only one line on the surface of the test bar. Furthermore, the odds of finding a large flaw on the surface at the line of maximum stress are extremely low. In 4-point bending, the maximum stress occurs along the tensile surface between the load points. The area and volume subjected to maximum or high tensile stress in 4-point bending is much larger than in 3-point bending. Hence, the probability is greater that a large flaw will be exposed to a high stress in 4-point bending (41). Thus, the use of 4-point bending tests is preferred since they yield more realistic strength results.

The flexural strength of a material strongly depends on the surface finish and the presence, size, and geometry of internal defects such as pores, impurities, or precipitates. Fracture in a material will initiate at the

particular defect which has the most detrimental combination of local stress, defect size, and defect geometry (42). Usually, defects found in a material are arranged randomly with regard to size, geometry, and relative position. The flexural strength of a material will then have a large degree of scatter based upon the random nature of the defects. Because of the wide variation in strength results, at least 10 specimens are tested in bending to provide a mean flexural strength (13). Due to the high amount of scatter, the standard deviation about the mean is often in excess of 10% (43).

As in the case of hardness, the flexural strength of cemented carbides is strongly dependent upon composition, microstructure, and temperature. For alloys having the same binder content but different carbide grain sizes, the flexural strength reaches a maximum at some intermediate carbide grain size as shown in Figure 2.25. Exner and Gurland (44) explained this behavior in terms of crack propagation. They suggested that in alloys with small carbide grains, fracture occurred in the binder phase. Large carbide grains yielded fracture by the carbide phase. When an intermediate carbide size was used, fracture proceeded through both phases giving maximum strength.

Likewise, in alloys having the same carbide grain size but varying amounts of binder, the optimum flexural and tensile strength occurs at some intermediate binder content as illustrated in Figure 2.26. Gurland and Norton (45) suggested that low strength at low binder content could be

attributed to the presence of a large number of carbide-carbide interfaces. They also proposed that low flexural strength at high binder content could be caused by the low yield strength of the resulting thick binder layer.

The flexural strength of cemented carbides with a Co binder phase decreases rapidly with increasing temperature after a maximum at approximately 200°C. Exner and Gurland (44) suggest that the slight increase around 200°C is due to an increased ductility of the Co binder or to a reduction in thermal stresses. This behavior is presented in Figure 2.27.

The dependence of flexural strength on microstructural parameters such as carbide contiguity and binder mean free path has been studied and will be discussed later.

Indentation Fracture Toughness

The fracture toughness of cemented carbides is strongly dependent upon composition, microstructure, and temperature. For alloys which have a similar carbide grain size but differing amounts of binder phase, the fracture toughness increases with increasing amounts of the ductile binder as shown in Figure 2.28. With more binder phase present, the occurrence of plastic deformation in the crack-tip region increases, thereby resulting in a dissipation of strain energy and an increase in fracture toughness.

If the alloys have the same binder content but varying carbide grain sizes, the fracture toughness increases with increasing size of the carbide

grains. This behavior is also present in Figure 2.28 and occurs because more energy will be required for the crack to propagate through or around the larger carbides, which results in an increased fracture toughness.

The fracture toughness of cemented carbides with a Co binder increases rapidly beginning at a temperature of approximately 600°C as shown in Figure 2.29. Thus, cemented carbides with a Co binder seem to have a transition temperature around 600°C at which plasticity and creep processes become significant. The transition temperature strongly depends on the composition and microstructure of the cemented carbide (13).

The dependence of fracture toughness on carbide contiguity and binder mean free path has also been researched and will be discussed later.

Standard tests for measuring the fracture toughness of engineering ceramics are non-existent; however, many techniques are available. Indentation methods for determining the fracture toughness of ceramics and cemented carbides have received much attention since the late 1970's because of the methods' relative simplicity and their demand for a small amount of material (49-56, 80, 81). The two indentation techniques receiving attention are the indentation fracture method and the indentation strength method.

Indentation Fracture Method

In this method, a Vickers indentation is placed on the flat, polished surface of the sample. Cracks formed at the corners of the indentation are then measured to determine the fracture toughness of the material. The cracks measured may be of the half-penny radial type or the shallow Palmqvist type as depicted in Figure 2.30b and Figure 2.30c, respectively. Radial cracks form in brittle solids while Palmqvist cracks form in materials such as cemented carbides which display more plasticity (46). The difference between the two types of cracks is difficult to visually ascertain in opaque materials such as cemented carbides without sectioning the test specimen (47).

A crack initiates below the contact point of the indenter when it reaches a critical load due to the formation of a tensile stress component. This subsurface crack is commonly described as being penny-shaped and referred to as the median crack. The median crack takes the form of two mutually perpendicular penny-shaped cracks lying in directions parallel to the indentation diagonals. As the indenter and subsequent load are withdrawn, the subsurface median cracks become unstable and expand toward the surface. The cracks which reach the surface are then called radial cracks and have a half-penny shape as shown in Figure 2.30 (46, 48).

In some brittle systems, shallow radial cracks termed Palmqvist cracks can form on the surface before the subsurface median crack.

Palmqvist crack formation is associated with low indentation loads, i.e., less than 15 N (1.5 kgf), or with specimens having a rough surface finish or relatively high toughness, i.e., WC-Co (46, 48). Palmqvist cracks have been observed in WC at loads of 1 to 10 N (0.1 to 1.0 kgf) in work performed by Anstis et al. (49).

Evans and Charles (50) were the first to develop a practical equation which allowed the fracture toughness in the form of the stress intensity factor, K_{IC}, to be calculated from measurements of radial cracks. They derived an approximate analysis of the elastic/plastic indentation stress field and obtained the following equation:

$$K_{IC} = 0.0752 \frac{P}{c^{3/2}} \qquad [4]$$

where K_{IC} = fracture toughness ($MPa\sqrt{m}$), P = load (N), and c = average crack length (m) of the 4 radial cracks from the center of the indent to the crack tip. Equation [4] is especially important because many equations subsequently developed follow the same format. The general format for these equations is:

$$K_{IC} = A \left(\frac{E}{H}\right)^{n} \frac{P}{c^{3/2}} \qquad [5]$$

where E = Young's modulus (GPa) and H = Vickers hardness (GPa). A and n are constants determined empirically by averaging data acquired from

different materials specified as reference ceramics or numerically by finite element analysis (46).

Lawn et al. (51) separated the stress field around the indent into two distinct mathematical entities: an elastic component at full load and a residual component at complete unload. They concluded that the radial crack system developed due to the residual stress component during unloading. Their conclusion led to the following equation:

$$K_{IC} = 0.0175 \left(\frac{E}{H}\right)^{1/2} \frac{P}{c^{3/2}} \qquad [6]$$

where $A = 0.0175$ and $n = 0.5$.

Several other equations considering the radial crack system and following the same format as Equation [5] were developed by using different curve-fitting methods and are summarized in Table 2.6.

Niihara et al. (52) measured the length of Palmqvist cracks in WC-Co and used the experimental data to yield the following equation:

$$\frac{K_{IC}\phi}{H a^{1/2}} \left(\frac{H}{E\phi}\right)^{2/5} = 0.035 \left(\frac{\ell}{a}\right)^{-1/2} \qquad [7]$$

where ϕ = constraint factor (≈ 3), a = indent half-diagonal (m), and ℓ = total length (m) of all 4 Palmqvist surface cracks.

Several equations have been proposed which are applicable to both radial and Palmqvist crack systems. Blendell (53) applied a curve-fitting method to experimental data for Palmqvist and radial cracks to obtain:

$$\frac{K_{IC}\phi}{H a^{1/2}}\left(\frac{H}{E\phi}\right)^{2/5} = 0.055 \log\left(\frac{8.4\,a}{c}\right) \qquad [8]$$

Evans (54) also developed an equation applicable to both crack systems. He derived a polynomial form giving:

$$\frac{K_{IC}}{H a^{1/2}}\left(\frac{H}{E}\right)^{2/5} = 10^{\,y} \qquad [9]$$

where

$$y = 15.32\,x^5 - 24.97\,x^4 + 11.23\,x^3 - 2.02\,x^2 - 0.34\,x - 1.59$$

and

$$x = \log\left(\frac{c}{a}\right)$$

Finally, Lankford (55) used experimental data from radial and Palmqvist cracks and a curve-fitting method to yield:

$$\frac{K_{IC}\phi}{H a^{1/2}}\left(\frac{H}{E\phi}\right)^{2/5} = 0.142\left(\frac{c}{a}\right)^{-1.56} \qquad [10]$$

Indentation Strength Method

In the indentation strength method, a Vickers indentation is introduced on the smoothly polished tensile surface of a 4-point bend bar used for flexure strength testing. The indentation is made in the center of the tensile side, and it is oriented such that the pyramidal edges are aligned with respect to the longitudinal axis of the bar (56). The bar is then tested

in 4-point bending to determine the flexural strength as previously discussed.

Chantikul et al. (56) conducted a fracture mechanics analysis to derive an equation for calculating the fracture toughness by the indentation strength method. The equation they derived is:

$$K_{IC} = \eta_V^R \left(\frac{E}{H}\right)^{1/8} \left(\sigma_f P^{1/3}\right)^{3/4} \qquad [11]$$

where K_{IC} = fracture toughness ($MPa\sqrt{m}$), P = indentation load (N), σ_f = flexural strength (MPa), E = Young's modulus (GPa), and H = Vickers hardness (GPa). The geometrical constant, η_V^R, was determined empirically to be 0.59 ± 0.12 by averaging data acquired from different materials specified as reference ceramics.

The indentation strength method has not been used or studied as extensively as the indentation fracture method, but it offers several advantages. One advantage of this method is the elimination of crack length measurements (56). Additionally, the accuracy of this method seems to be comparable to the indentation fracture technique, and more consistent values of fracture toughness are obtained than in the notched-beam technique (48). The main disadvantage of using the indentation strength method is that only one value of fracture toughness can be obtained for each specimen.

RELATIONS BETWEEN PROPERTIES AND MICROSTRUCTURE

Microstructural Parameters

The microstructure of cemented carbides is typically characterized by four parameters:

- volume fraction of the carbide or binder phase (V_C or V_B, respectively),
- carbide particle size (d, mean linear intercept),
- contiguity of the carbide phase (C), and
- mean free path of the binder phase (λ).

The volume fraction of the carbide or binder phase may be determined by a lineal analysis or point counting method as described by Vander Voort (57). In lineal analysis, lines are placed on the micrograph to form a grid. The total length of lines intercepting the phase of interest, L_α, is measured and divided by the total length of all lines, L_T, to give:

$$V_\alpha = \frac{\Sigma L_\alpha}{L_T} \qquad [12]$$

where V_α = the volume fraction of the phase of interest. A grid of lines is also used in the point counting method. Each intersection of the gridlines constitutes a single point. The number of points lying within the phase of interest, P_α, are counted and divided by the total number of points, P_T, to give:

$$V_\alpha = \frac{\Sigma P_\alpha}{P_T} \qquad [13]$$

Points which lie on the phase boundary are counted as one-half. Typically, the number of total points ranges from 16 to 100 (57).

The carbide particle size may be determined by measuring the mean linear intercept. A lineal method is used in measuring the number of carbide grains intersected by the lines from an overlay. The equation used to measure the mean linear intercept is:

$$d = \frac{V_C L_T}{N_C} \qquad [14]$$

where d = carbide particle size, V_C = volume fraction of the carbide phase, N_C = number of carbides intersected by lines, and L_T = total length of the lines at a magnification of 1X (57).

Gurland (58) defines contiguity as "the average fraction of surface area shared by one grain of a phase with all neighboring grains of the same phase." Contiguity is also determined by lineal analysis. Lines are placed on the micrograph, and the number of intersections with the carbide-carbide and carbide-binder interfaces is counted. The equation for determining the contiguity of the carbide phase is:

$$C_C = \frac{2 N_{CC}}{2 N_{CC} + N_{CB}} \qquad [15]$$

where C_C = contiguity of the carbide phase, N_{CC} = number of carbide-carbide interfaces intersected, and N_{CB} = number of carbide-binder interfaces intersected. The measurement of contiguity requires no

assumptions concerning volume fraction, particle size, and particle shape (58).

The mean free path, i.e. thickness, of the binder phase is difficult to measure directly because of image resolution problems and the tedious amount of work required. Fortunately, a relation exists between the three parameters measured thus far and the binder mean free path. The binder mean free path is calculated from:

$$\lambda = d \frac{V_B}{(1 - V_B)(1 - C_c)} \qquad [16]$$

where V_B = volume fraction of the binder phase (1-V_C), and λ = mean free path of the binder phase (59).

The hardness, flexural strength, and fracture toughness of cemented carbides are all functions of carbide contiguity and binder mean free path.

Hardness/Microstructure Relationships

The hardness of cemented carbides decreases with increasing mean free path of the binder as shown in Figure 2.31. Clearly, from Figure 2.31, the hardness cannot be determined precisely unless the carbide particle size or binder content is known along with the binder mean free path. Thus, the binder mean free path, alone, cannot be used to quantify the hardness of cemented carbides (44). As previously shown in Figure 2.22, the hardness of cemented carbides decreases with increasing binder content. Since the carbide contiguity also decreases with an increasing binder

content, it is apparent that the hardness decreases as the contiguity decreases.

Several models have been presented which relate hardness to the microstructure of cemented carbides (59-63). Of these, the model which has received the most attention is the one proposed by Lee and Gurland (59). They used the concept of plastic limit analysis to determine the effect of carbide contiguity on the hardness of WC-Co cemented carbides. The equation developed was:

$$H_c = C V_{WC} H_{WC} + (1 - C V_{WC}) H_m \qquad [17]$$

where H_c = hardness of the composite, C = carbide contiguity, V_{WC} = volume fraction of WC, H_{WC} = *in situ* hardness of WC, and H_m = *in situ* hardness of the binder phase.

Lee and Gurland (59) then developed two equations to determine the *in situ* hardness values of the carbide and binder for Equation [17]. First, in determining H_m, they obtained experimental data on the *in situ* hardness of Co at various Co contents of the alloys. Then, they calculated the binder mean free path using Equation [16]. The carbide particle size was taken as 2 μm, and the contiguity was estimated from a plot of contiguity versus carbide volume fraction. Next, Lee and Gurland (59) plotted H_m versus the reciprocal of the binder mean free path and obtained a linear equation:

$$H_m = 304 + 12.7\lambda^{-1/2} \qquad [18]$$

where H_m is in kgf/mm^2.

In determining the *in situ* hardness of the WC, H_{WC}, Lee and Gurland (59) performed hardness tests on hot-pressed compacts of WC which had particle sizes of 2 to 4 μm. Then, they plotted the hardness of the compacts versus the reciprocal of the WC particle size and obtained another linear equation:

$$H_{WC} = 1382 + 23.1\, d^{-1/2} \qquad [19]$$

They assumed that the *in situ* hardness of the carbide phase followed the same Hall-Petch relation as the bulk hardness of the hot-pressed WC.

Finally, Lee and Gurland (59) compared their model to experimental data by plotting measured hardness values of WC-Co against hardness values calculated from Equations [17-19]. They obtained a linear fit as the agreement between measured and calculated hardness values was excellent.

Strength/Microstructure Relationships

The flexural strength also depends upon binder mean free path and carbide contiguity. The flexural strength reaches a maximum at some optimum binder mean free path as shown in Figure 2.32. This type of behavior was explained previously for flexural strength as a function of binder content and carbide particle size. By inspecting Figures 2.25, 2.26,

and 2.32, it is clear that the flexural strength, as in the case of hardness, cannot be described by the binder mean free path alone. The binder content or carbide particle size must also be specified (44). The flexural strength decreases with increasing contiguity as displayed in Figure 2.33. This behavior may be due to an increase in the weak carbide-carbide interfaces and to a decrease in the ability of the binder phase to plastically deform in the crack-tip region.

Gurland (64) studied the variation of fracture strength in cemented carbides as a function of binder mean free path. He divided this variation into two ranges which correspond to the ascending and descending portions of the curves shown in Figure 2.32.

In the ascending portion of the curve, the binder mean free path remains below the critical value required to yield the maximum strength. In this case, the variation of strength with binder mean free path was based upon the Griffith failure criterion. The composites located in this region fail catastrophically as the fracture is continuous and remains almost entirely within the carbide phase. By examining the ascending portion of the curve carefully, it is apparent that the strength is linearly proportional to the binder mean free path before maximum strength is reached. Gurland (64) showed in Figure 2.34 that linear behavior could easily be seen by plotting the strength of compositions in the ascending portion of the curve against the degree of separation (1 - C, where C = contiguity).

The binder mean free path remains above the critical value required to yield the maximum strength in the descending portion of the curve. In this case, the strength variation is based upon a dispersion-hardening relation as the strength depends on the spacing and fracture resistance of the carbide particles. Composites in this region fail by a discontinuous mechanism characterized by localized plastic deformation of the binder and discontinuous cracking of carbide particles. Gurland (64) derived a linear relation from theory on the strain-hardening increment due to dispersions:

$$\sigma_f = K\left(\frac{V_{WC}^{2/3}}{d}\right) \qquad [20]$$

where σ_f = flexural strength and the quantity $(V_{WC})^{2/3}/d$ = the structure parameter which consists of the volume fraction of the carbide phase, V_{WC}, and the carbide particle size, d. He plotted the strengths of the materials on the descending portions of the curves versus the square root of the structure parameter as shown in Figure 2.35.

Fracture Toughness/Microstructure Relationships

Finally, the fracture toughness of cemented carbides also depends on binder mean free path and carbide contiguity. Chermant and Osterstock (65) have shown in Figure 2.36 that for samples having the same carbide particle size, the fracture toughness increases linearly with increasing binder mean free path. As with hardness and flexural strength, the fracture

toughness cannot be determined from the binder mean free path alone. When the thickness of the binder phase increases, there will be a greater occurrence of plastic deformation in the crack-tip region. As the amount of plastic deformation increases, more strain energy will be dissipated, leading to an increase in fracture toughness. Chermant and Osterstock (65) have also shown in Figure 2.37 that fracture toughness decreases exponentially with increasing carbide contiguity. The increasing amount of contact between carbides allows crack propagation to occur much more easily, thereby reducing the fracture toughness.

Numerous models have been proposed to relate fracture toughness to microstructural parameters in cemented carbides (65-68). The models proposed thus far have followed widely different theoretical approaches, and many weaknesses exist among them. A great deal of assumptions have been made, such as characterization of the fracture path, which do not agree with experimental observations (69).

Chermant and Osterstock (65) developed a model in which cleavage of the carbide particles at the crack-tip was considered to be the critical event in crack extension. Crack extension would occur when energy stored in the dislocation pile-up having a length of the binder mean free path was converted into the surface energy of a cleaved carbide particle. The relation developed was:

$$2\gamma_{WC} = A\left(\frac{\lambda^2}{d}\right) \qquad [21]$$

where γ_{WC} = surface energy of WC, A = a constant, d = carbide particle size, and λ = binder mean free path. They showed that G_{IC}, the critical strain energy release rate, was linearly dependent on λ^2/d.

Pickens and Gurland (67) developed a model in which ductile fracture of the binder phase was critical to crack extension. Crack extension would occur when the crack opening displacement reached a critical value equal to the binder mean free path. The relation developed was:

$$G_{IC} = \alpha \sigma \lambda \qquad [22]$$

where α = a constant and σ = the *in situ* yield stress of the binder. They showed that G_{IC} was linearly dependent on the binder mean free path, λ.

CHAPTER III

PRELIMINARY EXPERIMENTAL PROCEDURES

PROCESSING OF IBC COMPOSITES

Four different types of composites were examined: WC-Ni_3Al, TiC-Ni_3Al, WC-FeAl, and Al_2O_3-TiC-Ni_3Al. The WC and TiC were produced by Kennemetal, Inc., and the three types of Ni_3Al as well as the FeAl were argon gas-atomized by Homogeneous Metals, Inc. The types of Ni_3Al employed were IC-15, IC-50, and IC-218 where IC stands for intermetallic compound. The IC-15 contains Ni_3Al with B; IC-50 consists of Ni_3Al with B and Zr; and IC-218 contains Ni_3Al with B, Cr, and Zr. The amounts of each element present in the three Ni_3Al alloys are shown in Table 3.1. The average particle size and the carbon and oxygen content obtained by chemical analysis of the WC powders are presented in Table 3.2. Table 3.3 displays a summary of the compositions tested and includes the variations in carbide type, carbide size, binder type, and binder content.

The stages of processing for the powders were wet-blending, axial compaction, cold isostatic compaction, liquid phase sintering, and hot isostatic compaction. All processing of the IBC composites was performed at the Ceramic Processing Group of the Metals and Ceramics Division at Oak Ridge National Laboratory.

Wet-Blending

Various compositions of powders, as shown in Table 3.3, were blended. Each constituent powder was removed from its container, weighed, and added in the specified amounts to 500 ml bottles made of high-density polyethylene (HDPE). Then, 2 wt.% polyvinylpyridine (PVP) was added to the powders to give the samples strength after compaction and to reduce the amount of powder oxidation. The addition of PVP is beneficial because it allows for greater ease in handling the disks after compaction, and it leaves essentially no ash to hinder particle bonding during sintering.

Next, clean WC blending media ranging in size from 1.0 to 1.5 cm (approximately 0.4 to 0.6 inches) in diameter were added to each bottle in a 4:1 media mass/powder mass ratio. The mass of the WC media was measured and recorded before and after blending. In order to prevent powder oxidation and to minimize heating during blending, isopropanol was added to the bottles until each was full. The bottles were then tightly closed with tape to prevent leaking, and the powders were blended for 24 hours in oblique blenders as pictured in Figure 3.1.

Only four bottles could be placed in the blenders at one time, and due to the build up of heat, the 24-hour blending time had to be split into 4 six-hour intervals. The excess heat was due to the use of the relatively large WC media which produce a greater impact energy than smaller

media. The use of smaller blending media, however, would have led to undesirable particle size reduction. After blending, the bottles were opened, and the WC media were separated from the powder/isopropanol slurry. The slurry was then poured back into the bottles, and the mixture was placed under a hood for several days in order to evaporate the isopropanol. As a final drying treatment, the powder was placed in an oven at 60°C for 30 minutes. Finally, the dried powder was sifted through a -325 mesh (Tyler equivalent size) sieve to yield powder with a particle size of less than 44 μm (0.0017 inches).

Axial Compaction

In axial, i.e. unidirectional, compaction, 25 grams of loose powder was poured into a die with a diameter of 2.9 cm (approximately 1.1 inches). The die, punch, and base, as pictured in Figure 3.2, were lubricated with a mixture of stearic acid and acetone to reduce friction, thereby facilitating easy punch and sample removal. The hydraulic press is pictured in Figure 3.3. The powders were pressed at 69 MPa (10 ksi) for 30 seconds into specimens approximately 2.54 cm (1 inch) in diameter. Typically, 4 disks were axially pressed for each composition.

Cold Isostatic Compaction

Using the pressure vessel shown in Figure 3.4, the axially pressed disks were isostatically pressed to further densify them before sintering. A

schematic of the process is shown in Figure 3.5. Each disk was double-bagged in latex rubber bags and vacuum-sealed. The disks were placed into a plastic cup with holes in its bottom. The pressing chamber, containing a mixture of water and hydraulic fluid, was opened; the cup was lowered into it; and the chamber was closed. Then, the disks were isostatically pressed at 276 MPa (40 ksi). The chamber was depressurized slowly and carefully, and the bags were removed and cut open to retrieve the isostatically compacted samples. Twelve disks were isostatically pressed during each cycle.

Liquid Phase Sintering

The compacted IBC disks were placed in covered, circular alumina crucibles approximately 7.5 cm (3 inches) in diameter. Typically, three disks were arranged in each round crucible. Three round crucibles were then placed in covered, rectangular alumina crucibles which measured 20 by 15 cm (8 by 6 inches). The rectangular crucibles were loaded into a 901 Brew vacuum furnace as pictured in Figure 3.6. The following sintering cycle was used.

1. Under low vacuum (10 - 200 mTorr), heat from room temperature to 300°C at 5°C/minute, and hold for 1 hour.
2. Heat from 300°C to 1200°C at 10°C/minute, and hold for 1 hour.
3. Heat from 1200°C to desired sintering temperature (1500°C, 1550°C, or 1600°C) in 35 minutes, and hold for 1 hour.

4. Add argon to pressurize to 1 atmosphere at the desired sintering temperature, and hold for 1 hour.
5. Cool to 1000°C in 25 minutes in argon.
6. Cool to room temperature at 10°C/minute in argon.

Usually, one disk of each composition was sintered at each temperature.

Hot Isostatic Compaction

The sintered IBC disks were arranged in round and rectangular crucibles as described in the previous section. The specimens were then loaded into a vacuum furnace as pictured in Figure 3.7. The disks were heated under vacuum to a temperature of approximately 1350°C. Next, nitrogen was added so that the furnace was pressurized to a maximum of 1.9 MPa (275 psi) as the temperature was increased from 1350 to 1495°C. This procedure, the final processing operation, was performed to close some of the porosity which remained after sintering.

CHARACTERIZATION OF IBC COMPOSITES

The steps involved in the preliminary characterization of the IBC composites included the measurement of green density, Archimedes (immersion) density, and hardness. The composites were also examined by an optical microscope. The density and hardness measurements were conducted at ORNL, while the microscopy work was performed in the metallography laboratory at the University of Tennessee.

Green Density

Green density measurements were performed on the green (unsintered) disks after they were pressed by the cold isostatic procedure. These calculations were carried out to acquire some notion of how dense the composites were after compacting but before sintering. Using calipers, the diameter and thickness of each disk was measured to the nearest 0.001 inch (0.0254 mm). Then, the mass of each disk was determined to the nearest 0.01 gram on a balance.

The green density for each disk was calculated by dividing the mass of the disk by its volume. Next, the theoretical density of each composition was calculated using the densities and volume fractions of the composite constituents. Finally, the percent theoretical density of the green disks was determined by dividing the green density by the theoretical density and multiplying by 100 to obtain a percentage.

Archimedes Density

Archimedes or immersion density measurements were performed on the sintered disks after they had undergone sintering and hot isostatic compaction. These measurements were conducted in order to determine the percentage of theoretical density which had been attained via the sintering and hot isostatic compacting processes. A picture of the

Archimedes density apparatus is shown in Figure 3.8. The procedure used to calculate the Archimedes density for each disk is as follows:

1. Each disk was carefully weighed to the nearest 0.0001 gram.
2. Several (7-9) disks were placed in a HDPE container and immersed in 2.5 to 5 cm (1-2 inches) of 200 proof ethanol. The container with the samples was placed in a dessicator, which was then placed under vacuum until bubbles stopped emerging from the ethanol. Typically, this step took 10-15 minutes. The dessicator remained evacuated for another hour.
3. A bridge was arranged over the stage area of the balance. The container with the samples was placed on the bridge, and the balance was zeroed. Then, the suspension wire was placed on the bridge, and the wire was adjusted to hang freely in the ethanol. Next, the suspended wire weight was recorded.
4. A disk was placed on the wire, and the suspended sample weight was recorded for each disk in the container.
5. The container was removed from the bridge. The bridge was then removed from the balance, the regular stage was returned, and the balance was zeroed. Each disk was removed from the ethanol, dried quickly with a soft, lint-free paper towel, and weighed. The saturated weight of each disk was recorded.
6. The temperature of the ethanol was recorded to determine its density.
7. Finally, the following formula was used to determine the density of each disk.

$$\text{Density} = \frac{(\text{Dry weight})(\text{Density of ethanol})}{\text{Saturated wt.} + \text{Suspended wire wt.} - \text{Suspended sample wt.}} \quad [23]$$

Hardness

The IBC disks were cut in half along the diameter by a diamond saw and mounted in epoxy at the University of Tennessee. The specimens were then automatically polished through 0.25 μm in the Metallography Laboratory at ORNL.

Hardness testing was performed by a Buehler hardness machine with a Vickers indenter at loads of 5, 10, 20, 30, and 50 kg using a loading speed of 100 μm/sec and a contact time of 15 seconds. At least three indents at each load were formed in various sections of the flat, polished specimens. The dimensions of the indents were measured and recorded, and Equation [2] was used to calculate the Vickers hardness for each IBC composite at each indent load.

Optical Microscopy

Each specimen's polished surface was examined by an optical microscope. Photomicrographs of the hardness indent areas were taken at magnifications of 100X and 400X.

CHAPTER IV

PRELIMINARY RESULTS AND DISCUSSION

GREEN DENSITY

Results of the green density calculations are presented in Table 4.1. The percent theoretical density values for the green specimens range from approximately 51 to 74% with a standard deviation no greater than 2% for each composition. Each composition appears to have a green density which is sufficient for sintering and hot isostatic compaction. The two compositions having green densities on the order of 70+% theoretical density are the IBC-45 and CS-8 series as labeled in Tables 3.3 and 4.1. When green densities are this high, the particles become immobile, and the rearrangement process in sintering is inhibited (35). Thus, low densities can be expected for these two compositions after they undergo sintering and hot isostatic compaction.

ARCHIMEDES DENSITY

Results of the Archimedes density calculations are presented in Table 4.2 according to sintering temperature. The percent theoretical density values for the sintered specimens range from approximately 60 to 105%. Both the aforementioned IBC-45 and CS-8 series yielded theoretical

densities of only 88% possibly because of their high green densities, which prohibited rearrangement during sintering.

The two series of samples which yielded greater than 100% theoretical density were IBC-56 and IBC-57. These samples contain 68 and 81 vol.% Ni_3Al, respectively, and were slightly deformed. The reason for acquiring theoretical densities of more than 100% can probably be attributed to the evaporation of a portion of the liquid Ni_3Al in the vacuum sintering furnace. The presence of a relatively large amount of liquid Ni_3Al led to deformation of the samples.

The IBC-58 specimen achieved 99.3% theoretical density after sintering at 1500°C; however, it slumped, i.e. deformed, since it contains 95 vol.% of the Ni_3Al liquid phase. The CS-2 series, which contains only 19 vol.% Ni_3Al, never attained a theoretical density greater than 82.4%, regardless of the sintering temperature, due to an insufficient amount of liquid phase present during sintering. Thus, it appears that for high densification to occur, at least 19 vol.% but no greater than 68 vol.% Ni_3Al can be used without the sample deforming.

The effect of binder content on the percent theoretical density at a sintering temperature of 1550°C is shown in Figure 4.1. Each composite in Figure 4.1 contains WC having an average particle size of 2.3 μm. The IBC composites followed the expected behavior as increasing binder content

yielded higher densification. As binder content increases, more liquid phase becomes available which aids densification during the rearrangement process (35). The CS-3 composite containing 47 vol.% Ni_3Al reached 99.4% theoretical density, while CS-1, which contains 34 vol.% Ni_3Al attained 95.6% theoretical density. The CS-2 composite, which contains the lowest amount of Ni_3Al at 19 vol.%, achieved only 82.4% theoretical density. Also, as observed in Figure 4.1, a smaller amount of FeAl (39 vol.%) can be used to achieve approximately the same density than if Ni_3Al (47 vol.%) is used.

The effect of carbide particle size on the percent theoretical density is displayed in Figure 4.2. Each composite in Figure 4.2 contains WC and 34 vol.% of the IC-50 Ni_3Al binder phase. Generally, higher densities are obtained as the particle size decreases due to better packing of the smaller particles during the rearrangement stage (35). The IBC-45 and CS-1 series followed this expected behavior. The CS-4 series, however, which utilized WC powder with an average particle size of 0.8 μm, never achieved greater than 81% theoretical density. This behavior may be explained by the presence of 0.25 wt.% oxygen on the fine WC powders as shown in Table 3.2. Since oxides are generally not wetted well, the liquid Ni_3Al would not spread over the fine WC powders as effectively, thereby leading to lower density values during sintering.

The effect of binder type on percent theoretical density at a sintering temperature of 1550°C is shown in Figure 4.3. Each composite in Figure 4.3 contains WC with a carbide particle size of 2.3 μm. The binder content for the Ni_3Al-containing composites is 34 vol.%, while the content of FeAl in CS-9 is 39 vol.%. The CS-9 with FeAl yielded the highest density which is probably due to the increased amount of binder present. Among the composites with Ni_3Al binders, CS-1 with IC-50 containing B and Zr yielded the highest densities. The CS-6 composite with IC-218 containing B, Cr, and Zr, gave the next highest density value, and CS-5 with IC-15 containing B yielded the lowest density. Thus, the presence of Zr in the IC-50 and IC-218 binders apparently gives better densification. This behavior could be explained by the ability of Zr to react with impurities and bind them as harmless precipitates within the Ni_3Al grains. On the other hand, the presence of Cr in IC-218 appears to produce composites of lower density when compared to IC-50. The chromium addition may promote the formation of stable Cr_2O_3 on the carbide surfaces if any oxygen was available during the processing stages. As previously described, the oxides would not be wetted well by the Ni_3Al, leading to poor densification.

The IBC-43, CS-2, CS-4, CS-5, CS-6, and CS-8 series were all characterized by large amounts of porosity which may be due to a combination of factors. Insufficient blending of the powders leads to the

formation of carbide agglomerates which may not be penetrated by the liquid phase. Large voids typically lie within carbide agglomerates between the carbide particles (70). Some of the closed porosity in these samples may be due to gas entrapped in the pores during sintering. Another portion of the total porosity may be present because of an uneven density distribution which occurred during axial or cold isostatic compaction. Finally, some of the porosity could be due to the presence of impurities picked up during the blending, drying, and compaction of the powders before sintering (23).

The densities of the sintered specimens increased after hot isostatic compaction to values ranging from about 68 to 100% as shown in Table 4.2. The IBC-56, -57, and -58 series, which had deformed during sintering, were not subjected to this treatment.

By inspecting the densities achieved during sintering and hot isostatic compaction in Table 4.2 and the trends observed in Figures 4.1 - 4.3, it is apparent that the CS-1, -3, -7, and -9 series of composites are the most desirable for obtaining theoretical densities of greater than 94% when sintered at one of the temperatures listed.

HARDNESS

Results of the Vickers hardness measurements are presented in Table 4.3 according to sintering temperature. The hardness values ranged from 3.5 to 14.0 GPa (359 to 1423 kg/mm^2) for all compositions tested.

The effect of carbide particle size on Vickers hardness at a sintering temperature of 1500°C is shown in Figure 4.4. Each composite in Figure 4.4 contains WC and 34 vol.% of the IC-50 Ni_3Al binder phase. The CS-4 composite, with an average carbide particle size of 0.8 μm, gave a Vickers hardness of 12.8 ± 0.6 GPa, while CS-1, with a carbide size of 2.3 μm, yielded a Vickers hardness of 9.1 ± 0.6 GPa. For IBC-45, which has a carbide size of 5-8 μm, the Vickers hardness dropped to 7.3 ± 0.6 GPa. Thus, the hardness of IBC composites decreases with increasing carbide particle size, indicating a Hall-Petch relationship in IBC composites.

The effect of carbide type on Vickers hardness at a sintering temperature of 1500°C is shown in Figure 4.5. Both composites in Figure 4.5 contain 34 vol.% of the IC-50 Ni_3Al and have similar carbide particle sizes. The CS-1 composite, which contains WC, gave a Vickers hardness of 9.1 ± 0.6 GPa. The CS-7 composite, which contains TiC instead of WC, yielded a Vickers hardness of 11.5 ± 0.7 GPa. This behavior can be attributed to the bulk hardness of TiC being greater than that of WC.

The effect of binder type on Vickers hardness at a sintering temperature of 1500°C is shown in Figure 4.6. Each composite in Figure 4.6 contains WC with a carbide particle size of 2.3 μm. The binder content for the Ni_3Al-containing composites is 34 vol.%, while the content of FeAl in

CS-9 is 39 vol.%. The CS-6 composite, which contains IC-218 (Ni_3Al with additions of B, Cr, and Zr), illustrates the effect of solid solution hardening. When compared to the other Ni_3Al-containing composites (CS-1 with IC-50 and CS-5 with IC-15), the CS-6 had the highest Vickers hardness at 10.1 ± 0.8 GPa. In addition, the CS-1 composite had a greater hardness (9.1 ± 0.6 GPa) than the CS-5 composite (6.6 ± 0.4 GPa) due to the Zr present in the IC-50 binder used with CS-1. The CS-9 composite, which contains FeAl, had a Vickers hardness (9.1 ± 0.1 GPa) similar to that of the CS-1 composite.

The effect of binder content on the Vickers hardness at a sintering temperature of 1550°C is shown in Figure 4.7. Each composite in Figure 4.7 contains WC having an average particle size of 2.3 μm. The CS-1, -2, and -3 composites contain the same IC-50 Ni_3Al binder but in varying amounts. The CS-2 composite yielded a Vickers hardness of only 7.3 ± 0.3 GPa, but it was expected to have the highest hardness value because it contains the lowest amount of the ductile IC-50 at 19 vol.%. Both the CS-1 and CS-3 composites, however, yielded higher hardness values of 9.1 ± 0.6 GPa and 8.5 ± 0.3 GPa, respectively. This behavior could be attributed to the low density achieved for the CS-2 composite during sintering. Higher amounts of porosity in CS-2 would lead to lower hardness values. The CS-2 series

never reached greater than 82% theoretical density, while the CS-1 and CS-3 series reached at least 95% after hot isostatic compaction.

OPTICAL MICROSCOPY

Photomicrographs of the areas around the hardness indents on each specimen were taken. The pictures were taken to examine the polished surface for porosity and to ensure that the hardness indents were not chipped and were symmetrical. Large variations in porosity were observed on the polished surfaces of the specimens.

Figure 4.8 illustrates the polished surface of CS 5-3 which contains a large amount of porosity. According to Table 4.2, CS 5-3 only reached 73% theoretical density, and it contains 21.6% open porosity. Figure 4.8 supports these density calculations.

Conversely, Figures 4.9 and 4.10 illustrate the polished surfaces of CS 3-1 and CS 9-1, respectively, which contain very little porosity. Sample CS 3-1 attained 99.9% theoretical density after hot isostatic compaction, and CS 9-1 reached 98.5% as shown in Table 4.2.

Based upon the degree of densification, the Vickers hardness values, the observed microstructures, and the trends presented in Figures 4.1 - 4.7, the CS-1, -3, -7, and -9 series were selected for further study. The selection of these four compositions represented the end of the first phase of work performed.

CHAPTER V

EXPERIMENTAL PROCEDURES

PROCESSING OF SELECTED IBC COMPOSITES

Three composite disks measuring approximately 70 mm in diameter and 7 mm in thickness were processed for each of the four selected compositions: CS-1, CS-3, CS-7, and CS-9. For each composition, the disks were designated with A, B, or C. For example, the disks for the CS-1 series were referred to as CS-1A, CS-1B, and CS-1C. The dimensions of the disks were required in order to allow several (7-9) flexure bars of sufficient dimensions to be electrodischarge-machined. The remaining portions of the disks were used as specimens for hardness testing, corrosion testing, and microstructural characterization. A schematic diagram illustrating the use for each portion of a single disk is shown in Figure 5.1. The processing of these large disks was similar in nature to the processing of the disks fabricated in the preliminary work.

Wet-Blending

The CS-1, -3, -7, and -9 series of IBC composite powders were wet-blended as previously described in Chapter III.

Cold Isostatic Compaction

Due to the desired large diameter and small thickness of the composite disks, sufficient strength could not be achieved using axial compaction methods. Disks of this size fabricated using axial compaction would easily crumble after being removed from the hydraulic press. Thus, a method had to be developed for compacting the powders using cold isostatic compaction. Preliminary work in cold isostatic compaction utilized disks measuring 25.4 mm (1 inch) in diameter which had previously been axially compacted.

A solid metal filler insert was placed in the bottom of a polystyrene foam cup as shown in Figure 5.2. The diameter of the insert was sufficiently large so that when powder was poured on its surface and compacted, disks of 70 mm in diameter could be fabricated. Approximately 200 grams of CS-1, -3, -7, or -9 powder was poured on the surface of the insert and enclosed by the sides of the cup. Then, another piece of polystyrene foam was cut to fit over the surface of the powder. The additional piece was placed in the cup, and it leveled the top surface of the powder. The cup was then placed in a dessicator and held under vacuum for approximately 15 minutes to remove air enclosed within the powder mass. The top piece of polystyrene foam was taped tightly inside the cup to fully enclose the powder, and the top edges of the cup were trimmed.

Each polystyrene container was double-bagged in latex rubber bags and vacuum-sealed. The container was placed into a plastic cup with holes in its bottom. The pressing chamber, containing a mixture of water and hydraulic fluid, was opened; the cup was lowered into it; and the chamber was closed. Then, the container was isostatically pressed at 276 MPa (40 ksi). The chamber was depressurized slowly and carefully, and the container was removed and cut open to retrieve the isostatically compacted disk. Only one polystyrene container and, therefore, one disk could be cold isostatic compacted during each cycle.

Liquid Phase Sintering

The CS-1, -3, -7, and -9 series of cold isostatic compacted disks were liquid phase sintered as previously described in Chapter III. The CS-3 and CS-9 series of disks were sintered at 1550°C, while 1600°C was used to sinter the CS-1 and CS-7 series of disks. These temperatures yielded the highest densities for each composition in the work previously discussed.

Hot Isostatic Compaction

The CS-1, -3, -7, and -9 series of sintered disks were hot isostatic compacted as previously described in Chapter III.

CHARACTERIZATION OF SELECTED IBC COMPOSITES

Mechanical Property Characterization

After the selected disks were fabricated, they were sent to Chand Kare, Inc. in order for flexure bars to be electrodischarge-machined. Due to budgetary and time constraints, only 2 of the 3 disks fabricated for each composition could be machined. A total of 52 flexure bars were machined: 18 bars for CS-7, 14 each for CS-3 and CS-9, and 6 for CS-1.

Archimedes Density

Before the flexure specimens were tested to determine the flexural strength, they were used in the Archimedes density test as previously described in Chapter III. This test was performed in order to measure the percent theoretical density attained during processing for each of the four compositions.

Hardness

For each composition, a surface on one of the remaining disk sections was automatically polished as shown in Figure 5.1. Vickers indents were placed on the polished surfaces using loads of 30 and 50 kg, a loading speed of 100 μm/sec, and a load time of 15 seconds. The diagonals of the indents were measured and used in Equation [2] to determine the

hardness. Five indents were made at each load to obtain an average value of hardness.

Flexural Strength

An MTS electro-hydraulic testing frame located at the University of Tennessee, as shown in Figure 5.3, was used to determine the flexural strength for each of the four compositions in 4-point bending of the rectangular bar specimens. The dimensions of the specimens were 4 mm wide by 3 mm thick by 50 mm long, and the outer support span was 40 mm. The specimens were monotonically loaded using displacement control at a crosshead displacement rate of 0.5 mm/min. Data on the load, crosshead displacement, and midspan deflection was obtained by a computer for each specimen. The specimens were tested at room temperature and at 800 ± 10°C to examine the composites' high-temperature strength. Tests conducted at 800 ± 10°C were performed in argon at a pressure of one atmosphere using the Centorr vacuum furnace shown in Figure 5.3. The furnace was heated at a rate of 30°C/minute.

Fracture Toughness

Indentation Fracture Method

When the indent diagonals were measured, the cracks emanating from the corners of the indents were also measured. Equations [5] through

[10] were used along with the equations in Table 2.6 to determine the fracture toughness of each composition by the indentation fracture method.

Indentation Strength Method

Several flexure bars tested at room temperature contained an indent on the center of their tensile face in order to determine fracture toughness by the indentation strength method. Equation [11] was used to calculate the fracture toughness from the measurements made in flexure and hardness testing. A comparison between the fracture toughness values obtained by this technique and the indentation fracture method was made.

Mass Loss Corrosion Resistance

For each composition, six of the remaining disk sections were masked with a paint/epoxy mixture in order to obtain exposed corrosion areas of similar size. The masked specimens were immersed in aerated solutions of 10% hydrochloric acid, 10% nitric acid, and 10% sulfuric acid for 96 hours at room temperature. Two disk sections from each of the four compositions were immersed in each of the three acids; thus, a total of 24 disk sections were tested. Twelve of the samples were immersed in the different acids for 96 continuous hours. The other twelve specimens were immersed for 48 hours, removed from the acids, scrubbed, rinsed in distilled water, and dried in an oven at 80°C for one hour. These samples

were then placed back in the acids for an additional 48 hours. The first series of tests will be referred to as continuous tests, while the other series will be called the discontinuous tests. The mass of the samples was measured before and after immersion to determine the amount of material lost due to corrosion. From the mass of material lost, the area exposed, and the time of exposure, the average corrosion penetration rate (CPR) was calculated for each composite immersed in the different acid environments.

Microstructural Characterization

Microstructure Examination

The polished sections used for hardness testing were also utilized to determine the porosity present in each of the compositions by optical microscopy. After the hardness tests were conducted, scanning electron microscopy was used to examine the cracks emanating from the corners of the indents. The remaining disk sections were polished, etched with Murakami's reagent, and viewed with a scanning electron microscope as shown in Figure 5.1. Numerous photomicrographs were taken in order to conduct measurements of carbide particle size, carbide contiguity, and binder mean free path using point intersection and lineal analysis.

Fractography

After the bar specimens were fractured in 4-point bending, their surfaces were examined using a scanning electron microscope to investigate the fracture mechanisms of each composition. Fracture surfaces of both the room-temperature and 800°C flexure specimens were examined.

PROPERTY/MICROSTRUCTURE CORRELATIONS

Attempts were made to relate the hardness, flexural strength, and fracture toughness to the microstructural parameters of binder mean free path and carbide contiguity. Because a limited amount of mechanical property data was obtained due to the nature and expense of the material, and due to the fact that a small number of samples and compositions were studied, the relations observed between properties and microstructure were limited in scope.

CHAPTER VI

RESULTS AND DISCUSSION

MECHANICAL PROPERTY CHARACTERIZATION

Archimedes Density

Results of the Archimedes density calculations of the flexure bars are shown in Table 6.1. The average percent theoretical density was calculated by taking the mean of the percent theoretical density determined for each flexure bar machined from a particular disk. Then, the two average percent theoretical densities obtained for each particular composition were averaged to yield a final average percent theoretical density. The final average percent theoretical densities ranged from approximately 93 to 99%, and they are plotted as a function of composition in Figure 6.1.

The only disk not reaching a high density was CS 1-A, which had an average percent theoretical density of only 89.9%. Both CS-1 disks (A and B) were sintered at the same sintering temperature and were cold isostatically compacted from the same batch of wet-blended powder. Thus, the difference in density of the two CS-1 disks could be attributed to some parameter of the cold isostatic compaction procedure. One possible problem could be the failure to sufficiently degas the powder after pouring it into the polystyrene foam container. Another possible reason for the

lower density could be the use of a depressurization rate which was too rapid.

The effect of binder content on average percent theoretical density is shown in Figure 6.2. Each composite in Figure 6.2 contained WC having an average particle size of 2.3 μm. A comparison of CS-1 and CS-3 reveals that density increases with increasing binder content. The same behavior has previously been reported and explained in Chapter IV.

Hardness

Results of the Vickers hardness measurements on the selected IBC composites are presented in Table 6.2 and Figure 6.3 according to composition. The average hardness values ranged from 7.4 to 10.1 GPa (755 to 1035 kg/mm^2) for the four compositions tested.

The effect of carbide type on Vickers hardness is shown in Figure 6.4. Both composites in Figure 6.4 contain 34 vol.% of the IC-50 Ni_3Al and have similar carbide particle sizes. A comparison of CS-1 and CS-7 shows that the hardness of TiC-based composites is higher than that of WC-based composites if the composites have a similar carbide particle size and the same binder type and content. This trend is consistent with the hardness of monolithic TiC being higher than that of WC as shown in Tables 2.2 and 2.3.

The effect of binder type on Vickers hardness is shown in Figure 6.5. Both composites in Figure 6.5 contain WC with a carbide particle size of 2.3 μm. The binder content for the Ni_3Al-containing CS-1 composite is 34 vol.%, while the content of FeAl in CS-9 is 39 vol.%. A comparison of CS-1 and CS-9 indicates that the hardness of composites containing FeAl is similar to the hardness of composites containing Ni_3Al if the composites have the same carbides of identical particle size.

The effect of binder content on Vickers hardness is shown in Figure 6.6. Both composites in Figure 6.6 contain WC having an average particle size of 2.3 μm and the same IC-50 Ni_3Al binder but in varying amounts. A comparison of CS-1 and CS-3 indicates that the hardness of IBC composites decreases with increasing binder content if the composites contain the same carbide of a specific particle size and the same binder type.

The effects of carbide type, binder type, and binder content on Vickers hardness were previously reported and explained in Chapter IV. In addition, the trends reported in this chapter support those reported in Chapter IV.

Flexural Strength

Results of the room-temperature (25°C) and 800°C flexural strength tests are presented in Table 6.3 and Figure 6.7 according to composition. The average room-temperature flexural strength values ranged from 688 to

1791 MPa, and the average 800°C flexural strength values ranged from 541 to 1133 MPa.

Typical stress versus crosshead displacement and stress versus midspan deflection curves for the room-temperature tests are presented in Figures 6.8 and 6.9. Figures 6.10 and 6.11 show the typical stress versus crosshead displacement and stress versus midspan deflection curves for the 800°C tests.

Several assumptions are made when the flexural strength is calculated from simple beam theory. First, the material is assumed to be isotropic and homogeneous. Second, the elastic modulus in tension and compression is assumed to be identical. Third, the material is assumed to be linearly elastic to failure, and failure occurs in a brittle, catastrophic manner.

Inspection of the room-temperature curves in Figures 6.8 and 6.9 indicates that nearly linear behavior is obtained for all four IBC composites. Examination of the curves produced by the 800°C tests in Figures 6.10 and 6.11 shows that they do not remain linear until failure occurs. The exception to the non-linear behavior was the CS-7 composite, which remained linear to failure in all high-temperature tests. In the case of CS-9, the flexure bars tested at 800°C did not fracture but underwent a large amount of plastic deformation. The tests for CS-9 were terminated before fracture because the bars were bending to such a degree that they were

touching the bottom test fixture. One of the CS-3 bars behaved in the same manner at 800°C. The strength values obtained from the bars which did not fracture were invalid and not used in calculating the average flexural strength. The behavior observed for the FeAl-containing CS-9 bars was expected as the strength of FeAl decreases rapidly with increasing temperature above 600°C (82). Figure 6.12 illustrates the degree of deformation each of the four compositions underwent at 800°C.

A maximum of four bars were tested for each condition of room temperature, 800°C, and room temperature with an indent for performing indentation strength testing. According to Military Standard 1942 (MR), the recommended number of specimens for obtaining a reasonable mean strength value is ten (77). Furthermore, only one bar of the CS-1 composite was tested at 800°C.

The effect of composition on flexural strength is presented in Figure 6.7. The flexural strengths at both room temperature and 800°C are similar to each other in the CS-3 and CS-7 composites. The comparable strengths illustrate the influence of the high-temperature strength of the Ni_3Al binders present in CS-3 and CS-7 on the high-temperature strength of IBC composites. Unlike the CS-3 and CS-7 composites, the 800°C strength of the CS-1 composite did not compare favorably to the room-temperature strength, but only one bar was tested at high temperature. As previously discussed, the high-temperature strength values obtained for CS-9 are

invalid, and are probably inflated. Nevertheless, the high-temperature strength of the FeAl-containing CS-9 does not compare favorably to the 800° strength of the Ni_3Al-containing CS-1 and CS-3 composites.

The effect of carbide type on flexural strength is shown in Figure 6.13. Both composites in Figure 6.13 contain 34 vol.% of the IC-50 Ni_3Al and have similar carbide particle sizes. The CS-1 composite, which contains WC, gave a room-temperature flexural strength of 1142 ± 187 MPa. The CS-7 composite, which contains TiC instead of WC, yielded a room-temperature flexural strength of 688 ± 34 MPa. Thus, the flexural strength of the WC-based composite is greater than that of the TiC-based composite. This behavior may be due to a combination of two factors. First, the flexural strength of monolithic WC is greater than that of TiC as observed in Tables 2.2 and 2.3. Second, examination of the microstructure and fracture surface of the TiC-based composite led to the discovery of areas of interconnected porosity and unbonded TiC, i.e., TiC not surrounded by the Ni_3Al binder. Microstructures and fractography will be presented later in this chapter.

The effect of binder type on flexural strength is shown in Figure 6.14. Both composites in Figure 6.14 contain WC with a carbide particle size of 2.3 μm. The binder content for the Ni_3Al-containing CS-1 composite is 34 vol.%, while the content of FeAl in CS-9 is 39 vol.%. The CS-1 composite

yielded a room-temperature flexural strength of 1142 ± 187 MPa, while the CS-9 composite gave a strength of 1791 ± 69 MPa. This behavior could be due to a combination of factors. First, the CS-9 composite attained a higher density than CS-1 which would make it more likely to have a higher strength. Second, the CS-9 composite contains 5 vol.% more binder phase which may have led to the lower carbide contiguity measured, corresponding to higher strength. Third, examination of the microstructures and fracture surfaces of CS-1 and CS-9 indicates that the carbide-binder interfaces in CS-9 are not as prone to debonding as the interfaces are in CS-1.

The effect of binder content on flexural strength is shown in Figure 6.15. Both composites in Figure 6.15 contain WC having an average particle size of 2.3 μm and the same IC-50 Ni_3Al binder but in varying amounts. The CS-1 composite, which contains 34 vol.% Ni_3Al, gave a room-temperature flexural strength of 1142 ± 187 MPa. The CS-3 composite, which contains 47 vol.% Ni_3Al, yielded a room-temperature flexural strength of 1199 ± 144 MPa. As stated earlier, the optimum flexural strength occurs at some intermediate binder content as shown in Figure 2.26. Lower strength at lower binder content appears to be due to an increased number of carbide-carbide interfaces in CS-1. The contiguity measured for CS-1 was 0.39, but CS-3 had a contiguity of only 0.31.

Indentation Fracture Toughness

Results of the fracture toughness tests are presented in Tables 6.4 and 6.5 and in Figure 6.16 according to composition. The K_{IC} values in Table 6.4 calculated from the 10 different equations differ in quantity by at least a factor of 2 for each of the IBC composites. An average K_{IC} value was determined for each composition in Table 6.4, and the relationship between fracture toughness and composition was plotted in Figure 6.16. The average fracture toughness values ranged from 13.2 to 24.9 MPa$\sqrt{m}$ for the four compositions tested, but a relatively large standard deviation exists in all compositions.

The K_{IC} values obtained by the indentation strength method are shown in Table 6.5. The average fracture toughness values obtained by this method ranged from 15.2 to 33.0 MPa$\sqrt{m}$. Fracture toughness results were not obtained by this method for the CS-3 composite because all CS-3 bars fractured at points other than the indent. The indentation strength method requires fracture to occur at the indent for meaningful K_{IC} results. One bar for each of the other three compositions fractured at points other than the indent, and the results obtained were invalid and not presented. The standard deviation between values calculated from the indentation strength method was much lower than the deviation reported for the indentation fracture method.

Rigney and Lewandowski (83) reported a room-temperature fracture toughness of boron-doped polycrystalline Ni_3Al with 24 at.% Al to be greater than 29 MPa$\sqrt{m}$. Schneibel and Jenkins (84) reported 16-40 MPa$\sqrt{m}$ as the fracture toughness of polycrystalline FeAl with 40 at.% Al. The tests performed by Schneibel and Jenkins (84) were conducted in air at various crack growth rates. The higher K_{IC} values were obtained at the highest crack growth rate as the environmental effects were reduced (84). Thus, the K_{IC} values determined by both methods in the range of 20 to 35 MPa$\sqrt{m}$ are not unreasonable results for the IBC composites.

Inspection of Tables 6.4 and 6.5 reveals that the different equations and methods utilized to calculate the fracture toughness exhibit a discernible quantitative difference. One cause for uncertainty in the determination of the K_{IC} values is the use of an averaged Young's modulus value in the calculation (49). The average Young's modulus was determined by taking the average of the upper-bound isostrain condition,

$$E_C = V_M E_M + V_P E_P \qquad [24]$$

and the lower-bound isostress condition,

$$\frac{1}{E_C} = \frac{V_M}{E_M} + \frac{V_P}{E_P} \qquad [25]$$

where E_C = the composite modulus, V_M and E_M = the volume fraction and modulus of the matrix, and V_P and E_P = the volume fraction and modulus

of the particles. Frommeyer (85) reports that negative deviation from Equation [24] and positive deviation from Equation [25] has been observed in systems such as Ni-TiC and WC-Co. Thus, the average of Equations [24] and [25] was appropriate for developing the fracture toughness results and conducting qualitative comparisons of the IBC composites.

Binner and Stevens (48) report that the use of the indentation fracture technique should provide a K_{IC} value accurate to within approximately 30% of the true K_{IC} measured by conventional notched specimens. If the K_{IC} results determined by both indentation fracture and strength methods are compared, and it is assumed for the purpose of comparison that the true K_{IC} is the indentation strength value, the indentation fracture K_{IC} value for CS-1 is within 25% of the indentation strength K_{IC} result. Likewise, the accuracy is 13% for CS-7 and 24% for CS-9.

Because of the significant quantitative differences between indentation fracture methods, an average K_{IC} value was determined from all indentation fracture equations for each composite. The average K_{IC} value from the indentation fracture technique and the K_{IC} value determined by the indentation strength method were then used to make qualitative comparisons between the different composites.

The effect of carbide type on fracture toughness is shown in Figure 6.17. Both composites in Figure 6.17 contain 34 vol.% of the IC-50 Ni_3Al and have similar carbide particle sizes. The CS-1 composite, which contains WC, produced a fracture toughness greater than that of the TiC-containing CS-7. The factors underlying the effect of carbide type on fracture toughness are similar to the factors which contribute to the effect of carbide type on flexural strength. Like flexural strength, the fracture toughness of monolithic WC is greater than that of TiC as shown in Tables 2.2 and 2.3. Moreover, examination of the microstructure and fracture surface of the CS-7 composite led to the discovery of areas of interconnected porosity and unbonded TiC which would lower the fracture toughness of CS-7.

The effect of binder type on fracture toughness is shown in Figure 6.18. Both composites in Figure 6.18 contain WC with a carbide particle size of 2.3 μm. The binder content for the Ni_3Al-containing CS-1 composite is 34 vol.%, while the content of FeAl in CS-9 is 39 vol.%. The CS-1 composite yielded a fracture toughness less than the K_{IC} of the CS-9 composite. As in the case of the effect of binder type on flexural strength, the CS-9 composite attained a higher density than CS-1 which would make it more likely to have a higher fracture toughness. In addition, the fracture toughness of the FeAl in the CS-9 composite may be greater than the K_{IC} of

Ni_3Al in the CS-1 composite according to the measurements of Rigney and Lewandowski (83) and Schneibel and Jenkins (84).

The effect of binder content on fracture toughness is shown in Figure 6.19. Both composites in Figure 6.19 contain WC having an average particle size of 2.3 μm and the same IC-50 Ni_3Al binder but in varying amounts. The CS-1 composite, which contains 34 vol.% Ni_3Al, yielded a K_{IC} which was slightly less than the fracture toughness of the CS-3 composite, which contains 47 vol.% Ni_3Al. As previously mentioned, the fracture toughness increases with increasing amounts of binder. Plastic deformation in the crack-tip region increases with the presence of more binder phase and leads to a higher fracture toughness. The difference in K_{IC} values for these two IBC composites, however, was not significant considering that CS-3 contains 13 vol.% more ductile Ni_3Al.

Mass Loss Corrosion Resistance

Results of the continuous mass loss immersion tests are presented in Table 6.6 and Figure 6.20, and results of the discontinuous mass loss immersion tests are given in Table 6.7 and Figure 6.21. The average corrosion penetration rates (CPR) are reported in units of μm/day and the more traditional mils/yr. Figures 6.20 and 6.21 show the average CPR as a function of the composite and the acid in which it was immersed. The

binder phase in cemented carbides is typically the phase to corrode, while the carbide phase remains unaffected.

As seen in Figure 6.20, the Ni_3Al-containing composites (CS-1, -3, and -7) actively corrode in 10% nitric acid, but CS-9 with FeAl appears to undergo passivation, i.e., form an adherent protective oxide layer, in the strongly oxidizing acid. Conversely, CS-9 actively corrodes in the 10% hydrochloric and 10% sulfuric acids, but the Ni_3Al-containing composites undergo passivation in the same acids.

Inspection of Tables 6.6 and 6.7 and Figures 6.20 and 6.21 reveals that no significant differences exist between the CPRs obtained during the continuous and discontinuous tests. This behavior indicates that the composites which do not actively corrode in specific acids quickly form a protective oxide layer and undergo passivation.

Finally, it is possible that the IBC composites underwent localized corrosion at the phase boundaries. In WC-Co alloys, the phase boundaries corrode at a higher rate than the center of the binder regions (86). During the reprecipitation stage of sintering, a thin Co-rich layer, which would tend to have a high corrosion rate, forms around the WC particles. If localized corrosion did occur in the IBC composites, the average CPRs reported here are higher than the average CPRs which would have been calculated had only uniform corrosion occurred. A higher average CPR is

obtained in localized corrosion because the CPR at the phase boundaries is much higher than the CPR over the rest of the specimen's surface.

MICROSTRUCTURAL CHARACTERIZATION

Microstructure Examination

Porosity Measurements

Before they were used for hardness testing, the polished, unetched sections were utilized to determine the porosity present in each of the compositions by optical microscopy. Numerous photomicrographs were taken in order to characterize the porosity using a chart method for cemented carbides as described in ASTM B276-91 (87). Using this method, pores ranging in size up to 10 μm are classified as Type A and those between 10 and 25 μm are designated as Type B. A number 02, 04, 06, or 08 follows the Type A or B designation and signifies the vol.% of pores present in the sample. The number 02 indicates 0.02 vol.% porosity, 04 corresponds to 0.06 vol.%, 06 indicates 0.20 vol.%, and 08 signifies 0.60 vol.% porosity.

Figures 6.22 - 6.27 show the porosity present in each of the four selected IBC composites. In Figure 6.22, the porosity of CS-1 was determined to be Type A06 corresponding to 0.20 vol.% porosity with pores of 10 μm or less. One particular region in Figure 6.22 appeared to consist of

interconnected porosity (indicated by the left arrow). The porosity in Figure 6.23, which is another photomicrograph of the CS-1 composite, was estimated as Type A04, signifying 0.06 vol.% porosity with pores of 10 μm or less. Other regions of CS-1 were also examined and consistently yielded Type A04 or A06 porosity.

In Figure 6.24, the porosity of CS-3 was determined to be Type A04, indicating that only 0.06 vol.% porosity was observed with pores of 10 μm or less. Scratches which remained after polishing were not counted in determining the porosity. The scratches were present in other regions of CS-3, and the measurement of porosity in the other regions consistently produced Type A04.

Figure 6.25 shows the polished microstructure of the TiC-containing composite CS-7. The porosity rating of CS-7 was more difficult to determine than for CS-1 and CS-3. The pores which were 10 μm or less occurred as Type A04 porosity indicating only 0.06 vol.% porosity. Pores of approximately 60 μm, however, were observed in Figure 6.25 and designated as interconnected porosity. Figure 6.26 shows the interconnected porosity located in Figure 6.25 but at a higher magnification. Close inspection of the interconnected porosity in Figures 6.25 and 6.26 revealed that the binder phase was absent from these regions. The interconnected porosity was actually agglomerates of TiC which were not penetrated by the liquid Ni_3Al during sintering. Also present in Figures

6.25 and 6.26 are "pools" of Ni_3Al ranging in size from 10 to 50 μm. Based on these microstructural observations, it appears that a good dispersion of Ni_3Al in TiC may not have occurred during the wet-blending process. Another possibility is that a sufficient amount of Ni_3Al was available for wetting of the TiC particles, and the pools of Ni_3Al were the "left-overs" which were not required for successful sintering. The regions of interconnected porosity containing the unbonded TiC certainly contributed to the low values of flexural strength and fracture toughness measured for the CS-7 composite.

Figure 6.27 shows the polished microstructure of the CS-9 composite which contained WC and FeAl. The porosity rating for CS-9 was estimated as Type A08 which corresponds to 0.60 vol.% porosity with pore sizes of 10 μm or less. The measurement of porosity in other areas of the specimen's polished surface consistently yielded Type A08 porosity. The nature of this porosity, i.e., whether it was inherent or a result of the polishing procedure, is questionable for several reasons. First, the microstructure remains the same over the entire polished surface. Second, each of the composites was polished using the same procedure, but the CS-9 composite contains FeAl instead of Ni_3Al and produced a different polished microstructure. Third, the CS-9 composite attained the highest density of all four composite types. Fourth, it is the author's opinion that if the CS-9

composite contains this much inherent porosity, it would not produce the highest values of room-temperature flexural strength and fracture toughness when qualitatively compared to the other three IBC composites.

Indent Tip Areas

After the hardness testing was completed, the polished, unetched sections were examined in a scanning electron microscope to observe the behavior of the cracks generated in the indent tip area for each of the composites. Numerous photomicrographs were taken in order to characterize the cracking mechanisms of the IBC composites.

Note that most of the subsequent SEM photomicrographs will contain a notation indicating the type of fracture observed. Transgranular fracture of the binder phase will be termed **B TF**, and transgranular fracture of the carbide phase will be denoted by **C TF**. The notation **C-C IF** will designate intergranular fracture between carbide phases, and **C-B IF** will be used to indicate intergranular fracture between the carbide and binder phases. The notations for transgranular and intergranular fracture of the carbide and binder phases were developed in order to allow the reader to view as much of the microstructure and fractography as possible.

Figures 6.28 - 6.41 display the indent tip areas for each of the four selected IBC composites. Figures 6.28 - 6.31 show the cracking observed around the indents in the CS-1 composite. Figures 6.28 and 6.29 do not

contain extensive cracking, but only a few cracks in select areas. Both types of intergranular fracture are noticed along with carbide transgranular fracture.

Carbide transgranular fracture and carbide-carbide intergranular fracture are also observed in Figure 6.30 along with a region of interconnected porosity. This type of porosity was located earlier in CS-1 using an optical microscope. At this magnification, it appears that this region is like the ones already observed at low magnification in CS-7. The binder phase of Ni_3Al is absent from the porous region, and all that remains is an agglomerate of WC particles bonded to each other. Regions such as these will definitely lead to lower values of flexural strength and fracture toughness. Areas of interconnected porosity in CS-1, however, do not appear to be as numerous or as large as the areas occurring in CS-7.

Figure 6.31 shows the indent tip area of CS-1 without any cracking on the surface. This observation, along with the sporadic cracking seen in Figures 6.28 - 6.30, indicates that the CS-1 composite probably has a high fracture toughness and is capable of producing the K_{IC} measured by the indentation strength method as shown in Table 6.5.

Figures 6.32 - 6.35 show the cracking observed around the indents in the CS-3 composite. Figure 6.32 contains a very short crack extending from the indent tip area through a large carbide and then along a carbide-binder interface. Figure 6.33 does not contain extensive cracking, but only a few

cracks in select areas. Figures 6.32 and 6.33 both contain carbide transgranular fracture along with carbide-binder intergranular fracture.

Figure 6.34 is free of cracking except for one carbide-binder interface. Figure 6.34 also indicates that interconnected porosity is present in the CS-3 composites. This type of porosity was not previously observed when the porosity ratings were performed with an optical microscope.

Figure 6.35 indicates all four types of cracking which can occur in IBC composites. It is important to notice that the majority of cracking in Figure 6.35 is along the carbide-binder interface. Figures 6.32 - 6.34 also contain carbide-binder intergranular fracture. This behavior implies that the carbide-binder interfaces in CS-3 are not strong due to weak bonding of the WC and Ni_3Al phases. The weak interfaces could be due to the formation of an intermediate compound or impurity segregation during the solution-reprecipitation stage of sintering. Another possible cause of the weak interfaces could be the differences in the thermal expansion coefficients of the two phases. Upon cooling, residual thermal stresses could have developed at the carbide-binder interfaces, lowering the strength of the bond between the two phases. Kingery et al. (88) report that if the various phases present in a composite have different thermal expansion coefficients, microstresses develop along the grain boundaries.

Figures 6.36 - 6.39 show the cracking observed around the indents in the TiC-containing CS-7 composite. The cracks observed in the CS-7

composite were much longer than the cracks measured in the other composites. Figure 6.36 is a photomicrograph taken at low magnification to illustrate the extent of the crack growth typically seen in the CS-7 composite. A region of interconnected porosity and unbonded TiC is also observed in Figure 6.36.

Figure 6.37 indicates carbide transgranular fracture in CS-7. The other types of fracture probably exist along the crack length, but it cannot be stated with any certainty the types which actually occur. Again, a region of interconnected porosity and unbonded TiC is observed in Figure 6.37 along with the Ni_3Al pools.

Figures 6.38 and 6.39 show the presence of binder transgranular fracture and carbide-binder intergranular fracture in CS-7. Porosity is also observed in Figure 6.38, but it is unclear if the porosity is interconnected. Again, the abundance of interconnected porosity and unbonded TiC contributed to low values of strength and fracture toughness for the CS-7 composite.

Figures 6.40 and 6.41 show the cracking observed around the indents in the CS-9 composite, which contained FeAl as the binder phase. Numerous indents were examined, but extensive cracking around the indents in CS-9 was not evident. Figure 6.40 indicates only carbide transgranular fracture, but Figure 6.41 shows carbide and binder transgranular and carbide-carbide intergranular fracture.

Interestingly, carbide-binder intergranular fracture was not observed around *any* indents in CS-9, which implies that the carbide-binder interface in CS-9 is stronger than those interfaces in the other IBC composites. The CS-9 composite, however, contained the same WC that was used in the CS-3 composite which exhibited weak carbide-binder interfaces. The difference in thermal expansion coefficients between WC and FeAl is greater than the one occurring between WC and Ni_3Al. Thus, one would expect the thermal residual stresses in CS-9 to be greater than the ones in CS-3. Yet, the CS-9 composite appeared to have a higher bonding strength between the WC and FeAl. However, investigation into the formation of thermal residual stresses between the carbide and binder phases was not conducted in this research. There is no clear reason why this type of behavior occurred.

Etched Microstructures

Figures 6.42 - 6.45 display the etched microstructures for each of the four selected IBC composites. Figure 6.42 shows the microstructure of CS-1, and the binder phase of Ni_3Al appears to be well dispersed among the WC grains.

Figure 6.43 displays the etched microstructure of the CS-3 composite. The Ni_3Al pools which had previously been noticed in CS-7 also appeared in the etched microstructure of CS-3. The Ni_3Al pools were not clearly

visible in Figure 6.24 and Figures 6.32 - 6.35. The difference in grain size between the WC grains in CS-1 and CS-3 was also noticed. The presence of larger grains in CS-1 is a result of having a greater amount of solid carbide phase. The grain growth rate is accelerated with increasing amounts of solid phase because the diffusion distance between solid particles decreases (35).

Figure 6.44 shows the etched microstructure of CS-7 which had already been shown to contain Ni_3Al pools. Figure 6.45 displays the etched microstructure of CS-9. The FeAl binder appears to be well dispersed among the WC grains in the CS-9 composite, and the carbide grain size appears to be very fine.

Microstructural Parameter Measurement

Results of measurements conducted to determine the microstructural parameters are presented in Table 6.8. The parameters were measured using point intersection and lineal analysis methods previously described in Chapter II. Photomicrographs of the etched microstructures similar to the ones shown in Figures 6.42 - 6.45 were used to conduct the measurements. Measurements were conducted on areas of higher magnification for the IBC composites in order to accurately count the number of points lying within a particular phase or the number of boundary intersections.

Meaningful correlations between the mechanical properties and the binder mean free path were not able to be performed in this research. The main problem encountered can be located in Table 6.8. The binder mean free path of CS-1 is 5.1 μm and that of CS-3 is 3.3 μm. Thus, in this study the binder mean free path has decreased with increasing binder content, since CS-1 contains 34 vol.% Ni_3Al and CS-3 has 47 vol.% Ni_3Al. Generally, the binder mean free path increases with increasing binder content for a particular carbide particle size as discussed in Chapter II. The binder mean free path in the CS-3 composite, however, is low because of the presence of the Ni_3Al pools.

The other problem discovered in using the data presented is the fact that the data is very limited in scope. As seen in Figures 2.31, 2.32, and 2.36, variations in carbide particle size *and* binder content are needed to fully understand the effect of binder mean free path on the mechanical properties. For materials containing the same carbide and binder types in this research, there was no difference in carbide particle size.

Correlations were able to be made, however, between contiguity and a couple of the mechanical properties. As previously shown in Figure 6.6, the hardness of IBC composites decreases with increasing binder content since the CS-1 composite with 34 vol.% Ni_3Al has a higher hardness than the CS-3 composite which contains 47 vol.% Ni_3Al. Inspection of Table 6.8

indicates that the carbide contiguity of the CS-1 and CS-3 composites decreases with increasing binder content. The CS-1 composite yielded a contiguity of 0.39, and CS-3 produced a contiguity of 0.31. Since hardness and contiguity both decrease with increasing binder content, hardness decreases as contiguity decreases for IBC composites.

A correlation can also be made between contiguity and flexural strength. As shown in Figure 6.15, flexural strength increases as binder content increases since the strength of the CS-3 composite is greater than the strength of the CS-1 composite. As in the previous paragraph, the contiguity of CS-1 and CS-3 decreases with increasing binder content. Therefore, since flexural strength increases and contiguity decreases with increasing binder content, flexural strength will increase as contiguity decreases for IBC composites. This is reasonable because flexural strength is lower in cases when there is a large amount of weak carbide-carbide interfaces.

A correlation could not be made between contiguity and fracture toughness since the correlation, as shown in Figure 2.37, is exponential and depends on different values of carbide particle size.

Fractography

Figures 6.46 - 6.61 display the fracture surfaces of the flexure bars broken at room temperature for each of the four selected IBC composites.

Figures 6.46 - 6.49 show the fracture surface of the CS-1 composite. Figure 6.46 illustrates three types of fracture paths. Several carbides fractured in a transgranular manner, and carbide-binder intergranular fracture (debonding) can be located throughout Figure 6.46.

The most intriguing feature in Figure 6.46, however, is the appearance of the transgranular fracture of the ductile Ni_3Al binder. The author expected to observe a classical dimple pattern in the binder indicating ductile behavior, but was instead surprised by a cleavage pattern which is associated with brittle fracture. After further research, the author discovered that transgranular fracture in boron-doped Ni_3Al is identified by stepped features whose facets appear to be defined by {111} planes. Thus, it appears that on a local scale boron does not provide completely ductile behavior, even though it contributes to high ductility on a macroscopic scale. The reasons for this behavior are not understood, but they may be related to the relatively high work-hardening rate of boron-doped Ni_3Al (89).

Figure 6.47 provides an example of the carbide-binder intergranular fracture observed in CS-1. The point indicated by **C-B IF** is a hole in which a WC particle rested before being pulled out upon fracture. A similar debonding region is located to the left of the labeled hole. Transgranular fracture of the binder was also observed.

Figures 6.48 and 6.49 display images of the fracture surface of CS-1 obtained by secondary and backscattered electrons, respectively. The secondary image is typically better in allowing the viewer to perceive depth on the fracture surface, while the backscattered image illustrates compositional differences. Figure 6.48 shows regions of carbide-binder debonding and binder transgranular fracture. Figure 6.49 displays the same fracture types, but it reveals a large region of binder transgranular fracture that could not be seen in Figure 6.48. The carbides are also revealed more distinctly in Figure 6.49.

Carbide-binder intergranular fracture and binder transgranular fracture appear in Figures 6.46 - 6.49, indicating that the carbide-binder interfaces in CS-1 are not strong, and plastic deformation is occurring in the ductile Ni_3Al binder.

Fracture surfaces of the CS-3 composite are shown in Figures 6.50 - 6.53. Figure 6.50 illustrates the extent of carbide-binder intergranular fracture present in CS-3, and it also shows an example of a carbide transgranular fracture.

Figures 6.51 - 6.53 illustrate nicely the stepped features associated with transgranular fracture of the boron-doped Ni_3Al binder in CS-3. These figures also indicate that a large amount of carbide-binder intergranular fracture is present in CS-3. Several regions of debonding can be located in each of the figures. Figure 6.52 displays two areas in which the

carbide and binder were still in place after fracture but were beginning to break away from each other.

The fracture surfaces of CS-3, as in the case of CS-1, indicate that the carbide-binder interfaces are not strong, and plastic deformation is occurring in the Ni_3Al binder.

Fracture surfaces of the CS-7 composite are displayed in Figures 6.54 - 6.59. Figures 6.54 and 6.55 are photomicrographs of the tensile side of two mating fracture surfaces. Figure 6.54 shows the tensile surface at its top edge and a large pit measuring approximately 500 μm in length lying just beneath the surface. Appearing with the large pit are a substantial number of pores which seem to follow the border of the pit. In comparison, Figure 6.55 displays the mate of the pit, i.e., the "block" of material pulled out of the pit during fracture. A large amount of porosity is present in Figure 6.55 as well. Thus, it appears that the porosity, which is likely interconnected in the CS-7 composite, led to the large amount of material being removed during fracture.

Figures 6.56 and 6.57 illustrate the proportions of interconnected porosity and unbonded TiC present in the CS-7 composite. The unbonded TiC particles are clearly visible in Figure 6.56 along with a substantial amount of carbide-binder intergranular fracture. Transgranular fracture of the binder is observed in Figure 6.57 in combination with unbonded TiC and a deep porous region.

Figures 6.58 and 6.59 display transgranular fracture of the carbide and binder regions and carbide-binder intergranular fracture. The stepped features associated with the fracture of the boron-doped Ni_3Al are clearly present in these photomicrographs. Figure 6.58 shows a region in which the carbide and binder were pulling apart during fracture, but the carbide particle did not break loose.

The fracture surface of the TiC-based CS-7 composite indicates, as in the case of CS-1 and CS-3, that the carbide-binder interfaces are not strong and that plastic deformation is occurring in the Ni_3Al binder phase. In addition to the behavior observed in CS-1 and CS-3, the carbides in CS-7 appear to undergo more transgranular fracture. This behavior is expected as the strength and fracture toughness values of WC are greater than those of TiC. Finally, the appearance and quantity of interconnected porosity and unbonded TiC regions lead to lower strength and fracture toughness values than might be expected in the CS-7 composite.

Figures 6.60 and 6.61 illustrate the typical fracture surfaces observed in the FeAl-containing CS-9 composite. Figure 6.60 is a split image of the fracture surface. The backscattered image appears on the left, and the secondary image is on the right side. Inspection of Figure 6.60 shows that the FeAl binder is dispersed well among the WC grains, and fracture only occurs in the carbide and binder in a transgranular manner. Figure 6.61 also indicates the transgranular fracture of carbide and binder. Several

areas of the fracture surface of CS-9 were examined, but no clearly discernible areas of carbide-binder intergranular fracture were located. In addition, intergranular fracture of the carbide-binder areas was not found when the indent tip areas of CS-9 were examined (Figures 6.40 and 6.41).

The fracture surface of the FeAl-containing CS-9 composite indicates that fracture occurs differently in CS-9 than in the Ni_3Al-containing composites. The absence of carbide-binder intergranular fracture in CS-9 indicates that the carbide-binder interfaces have a high bonding strength. Plastic deformation of the binder also occurs in CS-9 as well as in the other IBC composites. The appearance of the fractured binder is different, however, as tearing appears in FeAl. The CS-9 composite attained the highest values of room-temperature strength and fracture toughness. The absence of carbide-binder intergranular fracture certainly was a factor in contributing to the excellent mechanical properties at room-temperature.

Examination of the fracture surfaces of the CS-1, CS-3, and CS-7 flexure specimens tested at 800°C revealed that no obvious differences exist between the fracture mechanisms of these composites at room temperature and 800°C. This observation is consistent with the similarity between the room-temperature and 800°C flexural strength values for these Ni_3Al-containing composites.

CHAPTER VII

CONCLUSIONS

- Liquid phase sintering and hot isostatic compaction techniques can be effectively used to fabricate highly dense intermetallic-bonded ceramic (IBC) composites.
- IBC composites which contain the IC-50 Ni_3Al binder have high-temperature strengths at 800°C that compare favorably to the room-temperature strength values. The high-temperature strength of Ni_3Al is responsible for the behavior. IBC composites containing a Fe - 40 at.% Al binder do not retain high strength values at 800°C since the strength of the FeAl falls rapidly above 600°C.
- The room-temperature strength of the FeAl-containing composite, however, is greater than the strength values obtained at 25°C for the Ni_3Al-containing composites. Based on examination of the cracks around indents and fractography, the bond between WC and FeAl appears to be stronger than that between WC and Ni_3Al, which leads to higher strength values. Nevertheless, the Ni_3Al plastically deforms and also provides high room-temperature strength.
- For IBC composites having the same type and amount of binder and the same carbide particle size, the WC-based composites have greater

flexural strength and fracture toughness values, while the TiC-based composites have greater hardness values. This behavior is due to the properties of monolithic WC and TiC.

- For IBC composites having the same types of carbide and binder and the same carbide particle size, the composites containing a larger amount of binder have higher flexural strength and fracture toughness values but lower hardness values than the composites having less binder. With greater amounts of binder, the number of carbide-carbide interfaces decreases, yielding a higher flexural strength, and plastic deformation in the crack-tip region increases, giving a higher fracture toughness. Hardness decreases with increasing binder because a lower amount of the hard carbide phase is present in the composite.
- Fracture toughness values calculated by the indentation fracture method were accurate to within 25% of the fracture toughness values calculated by the indentation strength method.
- When continuously or discontinuouly immersed for 96 hours at room temperature, the Ni_3Al-containing composites actively corrode in 10% nitric acid, but they appear to passivate in 10% hydrochloric acid and 10% sulfuric acid. Conversely, the FeAl-containing composite appears to passivate in the 10% nitric acid, but it actively corrodes in the other two acids.

- Contiguity is proportional to hardness but inversely proportional to flexural strength. As binder content increases, hardness and contiguity decrease. Thus, hardness decreases with contiguity. As binder content increases, contiguity decreases, but flexural strength increases since the number of carbide-carbide interfaces is reduced.

CHAPTER VIII

RECOMMENDATIONS FOR FUTURE WORK

- Utilize transmission electron microscopy (TEM) and other analytical methods to examine the carbide-binder interfaces.
- Determine fracture toughness by more conventional methods such as single-edge notched specimens.
- Conduct additional flexure testing to acquire strength values with lower deviations. Twenty to thirty specimens for each temperature and composition should be sufficient.
- Conduct cyclic-anodic polarization tests to examine the composites' active/passive behavior and their susceptibility to localized corrosion.

REFERENCES

REFERENCES

1. A. T. Santhanam, P. Tierney, and J. L. Hunt, "Cemented Carbides," ***ASM Handbook*** , Vol. 2, ASM International, 1992, p. 950.

2. V. A. Tracey, "Nickel in Hardmetals," ***Refractory Metals & Hard Materials***, Vol. 11, 1992, p. 137.

3. R. Komanduri, "Substitution of Ceramics for Conventional Tools," ***Ceramic Engineering and Science Proceedings***, July/August 1984, p. 450.

4. A. V. Tumanov, Yu. V. Gostev, V. S. Panov, and Yu. F. Kots, "Wetting of TiC-WC System Carbides with Molten Ni_3Al," ***Soviet Powder Metallurgy and Metal Ceramics***, Consultants Bureau, New York, October 1986, p. 428.

5. H. J. Scussel, "Friction and Wear of Cemented Carbides," ***ASM Handbook***, Vol. 18, ASM International, 1992, p. 795.

6. K. P. Plucknett, T. N. Tiegs, P. F. Becher, S. B. Waters, and P. A. Menchhofer, "Crack Resistant Composites: Metallic and Intermetallic-Bonded Ceramic Composites," ***ORNL/TM-13225***, Oak Ridge National Laboratory, Metals and Ceramics Division, Oak Ridge, TN, April, 1996.

7. T. N. Tiegs and R. R. McDonald, "Ductile Ni_3Al Alloys as Bonding Agents for Ceramic Materials," United States Patent 4,919,718, 1990.

8. K. Schröter, United States Patent 1,549,615, 1925.

9. K. Schröter, United States Patent 1,721,416, 1929.

10. Friedrich Krupp A. G., United States Patent 1,757,846, 1930.

11. P. Schwarzkopf and R. Kieffer, ***Cemented Carbides***, The Macmillan Company, New York, 1960.

12. P. Schwarzkopf, Austrian Patent 160,171, 1931.

13. B. Johannesson, "The Fracture Behaviour of Hardmetals - With Particular Reference to the Effects of Temperature," Ph.D. Dissertation, Chalmers University of Technology, Göteborg, Sweden, 1987.

14. Deutsche Edelstahlwerke A. G., German Patent 720,502, (patented May 17, 1929; issued 1942).

15. K. J. A. Brookes, ***Hardmetals and Other Hard Materials***, International Carbide Data, Hertfordshire, United Kingdom, 1992.

16. R. K. Viswanadham, P. G. Lindquist, and J. A. Peck, "Preparation and Properties of WC-(Ni, Al) Cemented Carbides," ***Science of Hard Materials***, Plenum Press, New York, 1983, p. 873.

17. E. A. Almond and B. Roebuck, "Identification of Optimum Binder Phase Compositions for Improved WC Hard Metals," ***Materials Science and Engineering***, Vol. A105/106, 1988, p. 237.

18. T. N. Tiegs and R. R. McDonald, "Ductile Ni_3Al Alloys as Bonding Agents for Ceramic Materials in Cutting Tools," United States Patent 5,015,290, 1991.

19. K. B. Alexander, J. H. Schneibel, T. N. Tiegs, H. T. Lin, and P. F. Becher, "Metallic and Intermetallic-Bonded Ceramic Composites," ***Annual Progress Report FY1992***, Oak Ridge National Laboratory, Metals and Ceramics Division, Oak Ridge, TN, June, 1993.

20. P. F. Becher, J. H. Schneibel, T. N. Tiegs, K. B. Alexander, K. P. Plucknett, and S. B. Waters, "Crack Resistant Composites: Metallic and Intermetallic-Bonded Ceramic Composites," Oak Ridge National Laboratory, Metals and Ceramics Division, Oak Ridge, TN, 1993.

21. K. B. Alexander, J. H. Schneibel, T. N. Tiegs, H. T. Lin, and P. F. Becher, "Metallic and Intermetallic-Bonded Ceramic Composites," ***ORNL/TM-12763***, Oak Ridge National Laboratory, Metals and Ceramics Division, Oak Ridge, TN, June, 1994.

22. W. D. Jones, ***Fundamental Principles of Powder Metallurgy***, Edward Arnold, London, 1960.

23. H. E. Exner, "Physical and Chemical Nature of Cemented Carbides," ***International Metals Reviews***, Vol. 4, American Society for Metals, 1979, p. 149.

24. V. K. Sarin, "Cemented Carbide Cutting Tools," ***Advances in Powder Technology***, American Society for Metals, 1982, p. 253.

25. R. E. Smallman, "Microstructure and Deformation Aspects of Some Specialty Steels and Hard Metals," ***Specialty Steels and Hard Materials***, Pergamon Press, Oxford, 1983, p. 141.

26. D. H. Jack, "Refractory Carbides," ***Concise Encyclopedia of Advanced Ceramic Materials***, R. J. Brook, Ed., Pergamon Press, 1991, p. 391.

27. J. H. Westbrook and E. R. Stover, "Carbides for High-Temperature Applications," ***High-Temperature Materials and Technology***, John Wiley & Sons, Inc., 1967, p. 312.

28. P. T. B. Shaffer, "Engineering Properties of Carbides," ***Engineered Materials Handbook***, Vol. 4, ASM International, 1991, p. 804.

29. D. J. Rowcliffe and G. E. Hollox, ***Journal of Materials Science***, Vol. 6, 1971, p. 1270.

30. J. L. Ellis and C. G. Goetzel, "Cermets," ***ASM Handbook*** , Vol. 2, ASM International, 1992, p. 978.

31. C. T. Liu, J. O. Stiegler, and F. H. Froes, "Ordered Intermetallics," ***ASM Handbook***, Vol. 2, ASM International, 1992, p. 913.

32. K. Aoki and O. Izumi, ***Nippon Kinzoku Gakkaishi***, Vol. 43, 1979, p. 1190.

33. F. Thümmler and R. Oberacker, ***An Introduction to Powder Metallurgy***, The Institute of Materials, London, 1993.

34. C. T. Liu, E. H. Lee, and C. G. McKamey, "An Environmental Effect as the Major Cause for Room-Temperature Embrittlement in FeAl," ***Scripta Metallurgica***, Vol. 23, 1989, p. 875.

35. R. M. German, ***Liquid Phase Sintering***, Plenum Press, New York, 1985.

36. L. Ramqvist, "Wetting of Metallic Carbides by Liquid Copper, Nickel, Cobalt, and Iron," ***International Journal of Powder Metallurgy***, Vol. 1, No. 4, 1965.

37. G. H. S. Price, C. J. Smithells, and S. V. Williams, "Sintered Alloys. Part I - Copper-Nickel-Tungsten Alloys Sintered with a Liquid Phase Present," ***Journal of the Institute of Metals***, Vol. 62, 1938, p. 239.

38. G. F. Bocchini, "The Influence of Porosity on the Characteristics of Sintered Materials," ***International Journal of Powder Metallurgy***, Vol. 22, No. 3, 1986, p. 185.

39. T. Farooq and T. J. Davies, "Tungsten Carbide Hard Metals Cemented with Ferroalloys," ***International Journal of Powder Metallurgy***, Vol. 27, No. 4, 1991, p. 347.

40. C. C. Wu, D. Lewis, and K. R. McKinney, "Strength and Toughness Measurements of Ceramic Fiber Composites," ***Fracture Mechanics of Ceramics***, Vol. 7, R. C. Bradt, A. G. Evans, D. P. H. Hasselman, and F. F. Lange, Ed., Plenum Press, 1986.

41. D. W. Richerson, ***Modern Ceramic Engineering: Properties, Processing, and Use in Design***, Marcel Dekker, Inc., New York, 1982.

42. H. F. Fischmeister, "Toughness in High Speed Steels and Hard Metals," ***Specialty Steels and Hard Materials***, Pergamon Press, Oxford, 1983, p. 127.

43. G. D. Quinn and R. Morrell, "Design Data for Engineering Ceramics: A Review of the Flexure Test," ***Journal of the American Ceramic Society***, Vol. 74, No. 9, 1991, p. 2037.

44. H. E. Exner and J. Gurland, "A Review of Parameters Influencing Some Mechanical Properties of Tungsten Carbide-Cobalt Alloys," ***Powder Metallurgy***, Vol. 13, No. 25, 1970, p. 13.

45. J. Gurland and J. T. Norton, in "Plansee Proceeding 1955," F. Benesovsky, Ed., Pergamon Press, Oxford, 1956, p. 99.

46. M. Sakai and R. C. Bradt, "Fracture Toughness Testing of Brittle Materials," ***International Materials Reviews***, Vol. 38, No. 2, 1993, p. 53.

47. R. Warren and H. Matzke, "Indentation Testing of a Broad Range of Cemented Carbides," ***Science of Hard Materials***, Plenum Press, New York, 1983, p. 563.

48. J. G. P. Binner and R. Stevens, "The Measurement of Toughness by Indentation," ***Transactions of the British Ceramic Society***, Vol. 83, No. 6, 1984, p. 168.

49. G. R. Anstis, P. Chantikul, B. R. Lawn, and D. B. Marshall, "A Critical Evaluation of Indentation Techniques for Measuring Fracture Toughness: I, Direct Crack Measurements," ***Journal of the American Ceramic Society***, Vol. 64, No. 9, 1981, p. 533.

50. A. G. Evans and E. A. Charles, "Fracture Toughness Determinations by Indentation," ***Journal of the American Ceramic Society***, Vol. 59, No. 7-8, 1976, p. 371.

51. B. R. Lawn, A. G. Evans, and D. B. Marshall, "Elastic/Plastic Indentation Damage in Ceramics: The Median Radial Crack System," ***Journal of the American Ceramic Society***, Vol. 63, No. 9-10, 1980, p. 574.

52. K. Niihara, R. Morena, and D. P. H. Hasselman, "Evaluation of K_{IC} of Brittle Solids by the Indentation Method with Low Crack-to-Indent Ratios," ***Journal of Materials Science Letters***, Vol. 1, 1982, p. 13.

53. J. E. Blendell, "The Origins of Internal Stresses in Polycrystalline Alumina and Their Effects on Mechanical Properties," Ph.D. Dissertation, Massachusetts Institute of Technology, Cambridge, Massachusetts, 1979.

54. A. G. Evans, "Fracture Toughness: The Role of Indentation Techniques," ***Fracture Mechanics Applied to Brittle Materials***, ASTM STP 678, S. W. Freiman, Ed., American Society for Testing and Materials, Philadelphia, Pennsylvania, 1979.

55. J. Lankford, "Indentation Microfracture in the Palmqvist Crack Regime: Implications for Fracture Toughness Evaluation by the Indentation Method," ***Journal of Materials Science Letters***, Vol. 1, 1982, p. 493.

56. P. Chantikul, G. R. Anstis, B. R. Lawn, and D. B. Marshall, "A Critical Evaluation of Indentation Techniques for Measuring Fracture Toughness: II, Strength Method," ***Journal of the American Ceramic Society***, Vol. 64, No. 9, 1981, p. 539.

57. G. F. Vander Voort, ***Metallography: Principles and Practice,*** McGraw-Hill, Inc., New York, 1984.

58. J. Gurland, "Observations on the Structure and Sintering Mechanism of Cemented Carbides," ***Transactions of the Metallurgical Society of AIME,*** Vol. 215, 1959, p. 601.

59. H. C. Lee and J. Gurland, "Hardness and Deformation of Cemented Tungsten Carbide," ***Materials Science and Engineering,*** Vol. 33, 1978, p. 125.

60. J. L. Chermant, A. Deschanvres, G. Hautier, A. Iost, and G. Manier, ***Phys. Status Solidi,*** Vol. 15, 1973, p. K149 (in French).

61. G. Grathwohl and R. Warren, "The Effect of Cobalt Content on the Microstructure of Liquid-Phase Sintered TaC-Co Alloys," ***Materials Science and Engineering,*** Vol. 14, 1974, p. 55.

62. R. Warren and M. B. Waldron, ***Powder Metallurgy Int.,*** Vol. 7, 1975, p. 18.

63. M. T. Langier, "A Microstructural Model for Hardness in WC-Co Composites," ***Acta Metallurgica,*** Vol. 33, 1985, p. 2093.

64. J. Gurland, "The Fracture Strength of Sintered Tungsten Carbide-Cobalt Alloys in Relation to Composition and Particle Spacing," ***Transactions of the Metallurgical Society of AIME,*** Vol. 227, 1963, p. 1146.

65. J. L. Chermant and F. Osterstock, "Fracture Toughness and Fracture of WC-Co Composites," ***Journal of Materials Science,*** Vol. 11, 1976, p. 1939.

66. L. Lindau, in "Proceedings of 4th International Conference on Fracture," University of Waterloo Press, Canada, 1977, p. 21.

67. J. R. Pickens and J. Gurland, "The Fracture Toughness of WC-Co Alloys in SENB Specimens Precracked by Electrodischarge Machining," ***Materials Science and Engineering,*** Vol. 33, 1978, p. 135.

68. M. Nakamura and J. Gurland, "The Fracture Toughness of WC-Co Two Phase Alloys - A Preliminary Model," ***Metallurgical Transactions,*** Vol. 11A, 1980, p. 141.

69. E. A. Almond, "Deformation Characteristics and Mechanical Properties of Hardmetals," ***Science of Hard Materials***, Plenum Press, New York, 1983, p. 517.

70. M. F. Yan, "Sintering of Ceramics and Metals," ***Advances in Powder Technology***, American Society for Metals, 1982, p. 99.

71. C. T. Liu and C. L. White, "Design of Ductile Polycrystalline Ni_3Al Alloys," ***High-Temperature Ordered Intermetallic Alloys***, C. C. Koch, C. T. Liu, and N. S. Stoloff, Ed., Materials Research Society, Pittsburgh, PA, 1985, p. 365.

72. R. V. Sara, E. Rudy, and J. R. Hoffman, "Binary Alloy Phase Diagrams," ***ASM Handbook***, Vol. 3, ASM International, 1992, p. 115.

73. J. L. Murray, "Binary Alloy Phase Diagrams," ***ASM Handbook***, Vol. 3, ASM International, 1992, p. 114.

74. P. Nash, M. F. Singleton, and J. L. Murray, "Binary Alloy Phase Diagrams," ***ASM Handbook***, Vol. 3, ASM International, 1992, p. 49.

75. N. S. Stoloff, "Ordered Alloys for High Temperature Applications," ***High-Temperature Ordered Intermetallic Alloys***, C. C. Koch, C. T. Liu, and N. S. Stoloff, Ed., Materials Research Society, Pittsburgh, PA, 1985, p. 3.

76. U. R. Kattner and B. P. Burton, "Binary Alloy Phase Diagrams," ***ASM Handbook***, Vol. 3, ASM International, 1992, p. 44.

77. "Flexural Strength of High Performance Ceramics at Ambient Temperature," ***Military Standard 1942 (MR)***, Department of the Army, Washington, D. C., 1983.

78. P. E. Price and S. P. Kohler, "Cold Isostatic Pressing of Metal Powders," ***Metals Handbook***, Vol. 7, American Society for Metals, 1984, p. 444.

79. H. Holleck, "The Constitution as the Basis for Recent and Future Developments of Wear Resistant Materials," ***Specialty Steels and Hard Materials***, Pergamon Press, Oxford, 1983, p. 383.

80. T. Miyoshi, N. Sagawa, and T. Sassa, "A Study on Evaluation of K_{IC} for Structural Ceramics," ***J. Jpn. Soc. Mech. Eng.***, Vol. 51, No. 471, 1985, p. 2489 (in Japanese).

81. K. Tanaka, "Elastic/Plastic Indentation Hardness and Indentation Fracture Toughness: The Inclusion Core Model," ***Journal of Materials Science***, Vol. 22, 1987, p. 1501.

82. C. G. McKamey, "Iron Aluminides," ***Physical Metallurgy and Processing of Intermetallic Compounds***, Chapman & Hall, New York, 1996, p. 351.

83. J. D. Rigney and J.J. Lewandowski, "Effects of Reinforcement Size and Distribution on Fracture Toughness of Composite Nickel Aluminide Intermetallics," ***Materials Science and Engineering***, Vol. 158A, 1992, p. 31.

84. J. H. Schneibel and M. G. Jenkins, "Slow Crack Growth at Room Temperature in FeAl," ***Scripta Metallurgica et Materialia***, Vol. 28, 1993, p. 389.

85. G. Frommeyer, "Metallic Composite Materials," ***Physical Metallurgy***, North-Holland Physics Publishing, Amsterdam, 1983, p. 1861.

86. A. M. Human and H. E. Exner, "The Corrosion of Two-Phase Cemented Carbides," Fifth International Conference on the Science of Hard Materials, Maui, Hawaii, February, 1995.

87. "Standard Test Method for Apparent Porosity in Cemented Carbides," ASTM Standard B276-91, ***ASTM Book of Standards***, 1991.

88. W. D. Kingery, H. K. Bowen, and D. R. Uhlmann, ***Introduction to Ceramics***, John Wiley & Sons, Inc., New York, 1976.

89. E. M. Schulson, "Brittle Fracture and Toughening," ***Physical Metallurgy and Processing of Intermetallic Compounds***, Chapman & Hall, New York, 1996, p. 56.

APPENDIX

Table 2.1. Historical development of cemented carbides used as cutting tools (23, 24).

Year(s)	WC-based cemented carbides	Year(s)	WC-free cemented carbides
1922-25	WC + Co		
1927	Graphite-free WC + Co		
1928-29	WC + stellite binders	1929-31	TiC + Mo_2C + Ni, Cr, Mo
1931	WC + TiC + Co	1930-31	TaC + Ni, Co
1931	WC + TaC(VC, NbC) + Co	1931	TiC + TaC + Co
1932	WC + TiC + (Ta, Nb)C + Co	1931	TiC + Cr, Mo, W, Ni, Co
1938	WC + Cr_3C_2 + Co	1938	TiC + VC + Ni, Fe
		1944	TiC + NbC + Ni, Co
		1948-50	TiC + (Mo_2C, TaC) + Ni, Co, Cr
		1949	TiC + VC + NbC + Mo_2C + Ni
1951	WC + Ni	1952-81	TiC + heat-treatable binder
1956	WC + TiC + (Ta, Nb)C + Cr_3C_2 + Co		
1959	WC + TiC + HfC + Co		
1965	Hot isostatic compaction (HIP)	1965-70	TiC + Mo_2C + Ni, Mo
1967-70	Submicron WC + Co		
1967-70	WC + Fe, Ni, Co		
1968-69	WC + TiC + (Ta, Nb)C + HfC + Co	1968-70	(Ti, Mo)C + Ni, Mo, Cr
1969-80	Coated carbide tools		
1975	Cast carbide		
1976-81	Coated carbide tools on tailored substrates	1976	(W, Mo)C + Co

Table 2.2. Selected properties of tungsten carbide (WC) (5, 23, 26-28, 79).

Property	Value	Sources
Crystal Structure	Hexagonal	5, 23, 28
Standard Free Energy of Formation	-40 ± 2 kJ/mol	26
Theoretical Density	15.63 g/cm^3	5
Melting Temperature	2800°C (5050°F)	5, 23, 28
Young's Modulus	696 GPa (101×10^6 psi)	5, 23, 26, 28
Hardness (low value)	1800 kg/mm^2	27
(high value)	2200 kg/mm^2	5, 23, 26, 28
Transverse Rupture Strength	600 MPa	26
Fracture Toughness, K_{IC}	7.5 MPa$\sqrt{m}$	79
Thermal Conductivity	120 W/m K	26
Coefficient of Thermal Expansion	5.2 µm/m K	5, 23, 28

Table 2.3. Selected properties of titanium carbide (TiC) (5, 23, 26, 28, 79).

Property	Value	Sources
Crystal Structure	Face-centered cubic (FCC)	23
Standard Free Energy of Formation	-183 ± 2 kJ/mol	26
Theoretical Density	4.94 g/cm^3	5, 23, 28
Melting Temperature	3100°C (5600°F)	5, 23, 28
Young's Modulus	451 GPa (65.4 x 10^6 psi)	5, 23, 28
Hardness	3000 kg/mm^2	5, 23, 26, 28
Transverse Rupture Strength	400 MPa	26
Fracture Toughness, K_{IC}	3.8 MPa$\sqrt{m}$	79
Thermal Conductivity	21 W/m K	26
Coefficient of Thermal Expansion	7.7 µm/m K	5, 23, 26, 28

Table 2.4. Selected properties of nickel aluminide (Ni_3Al) (31).

Property	Value
Crystal Structure	$L1_2$ (ordered FCC)
Critical Ordering Temperature	1390°C (2535°F)
Melting Temperature	1390°C (2535°F)
Density	7.50 g/cm^3
Young's Modulus	179 GPa (25.9 x 10^6 psi)

Table 2.5. Selected properties of iron aluminide (FeAl) (31).

Property	Value
Crystal Structure	B2 (ordered BCC)
Critical Ordering Temperature	1250°C (2280°F)
Melting Temperature	1250°C (2280°F)
Density	5.56 g/cm^3
Young's Modulus	261 GPa (37.8 x 10^6 psi)

Table 2.6. Summary of fracture toughness equations used for radial crack systems (49-52, 80, 81).

Equation	Author(s)	Reference
$K_{Ic} = 0.0752\ (P/c^{3/2})$	Evans, Charles	50
$K_{Ic} = 0.0175\ (E/H)^{1/2}\ (P/c^{3/2})$	Lawn, Evans, Marshall	51
$K_{Ic} = 0.0160\ (E/H)^{1/2}\ (P/c^{3/2})$	Anstis, Chantikul, Lawn, Marshall	49
$K_{Ic} = 0.0309\ (E/H)^{2/5}\ (P/c^{3/2})$	Niihara, Morena, Hasselman	52
$K_{Ic} = 0.0180\ (E/H)^{1/2}\ (P/c^{3/2})$	Miyoshi, Sagawa, Sassa	80
$K_{Ic} = 0.0725\ (P/c^{3/2})$	Tanaka	81

Table 3.1. Nominal compositions of Ni_3Al alloys.

Alloy	Element: Weight %; [Atomic %]				
	Al	B	Cr	Zr	Ni
IC-15	12.7 [24.0]	0.05 [0.24]	-	-	87.3 [75.8]
IC-50	11.3 [21.7]	0.02 [0.10]	-	0.6 [0.3]	88.1 [77.9]
IC-218	8.5 [16.7]	0.02 [0.10]	7.8 [7.9]	0.8 [0.46]	82.9 [74.8]

Table 3.2. Average particle size and chemical analysis of tested WC powders.

WC powder type	Average particle size, μm	Total carbon content, weight %	Free carbon (graphite) content, weight %	Oxygen content, weight %
Fine	0.8	6.14	0.04	0.25
Medium	2.3	6.15	0.05	0.04
Coarse	5 - 8	6.12	0.03	0.01

Table 3.3. Summary of compositions tested.

Sample Name	Carbide Type	Carbide Size, μm	Ni_3Al Binder Type	Binder Content,	
				weight %	volume %
IBC 43	WC	2.3	IC-50	20	34
IBC 44	WC	0.8	IC-50	20	34
IBC 45	WC	5-8	IC-50	20	34
IBC 56	WC	2.3	IC-50	50	68
IBC 57	WC	2.3	IC-50	67	81
IBC 58	WC	2.3	IC-50	90	95
CS 1	WC	2.3	IC-50	20	34
CS 2	WC	2.3	IC-50	10	19
CS 3	WC	2.3	IC-50	30	47
CS 4	WC	0.8	IC-50	20	34
CS 5	WC	2.3	IC-15	20	34
CS 6	WC	2.3	IC-218	20	34
CS 7	TiC	1-3	IC-50	44	34
CS 8	TiC w/ Al_2O_3	1-3	IC-50	47	34
CS 9	WC	2.3	Fe-40 at.% Al	20	39

Table 4.1. Green density and percent theoretical density for green specimens.

Sample ID	Volume, cm^3	Mass, grams	Green density, g/cm^3	Theoretical density, g/cm^3	Percent theoretical density, %
IBC 43-1	3.1	24.6	7.9	12.8	61.6
IBC 43-2	3.1	24.7	8.0	12.8	62.1
IBC 43-3	3.1	24.7	7.9	12.8	61.6
IBC 44-1	3.3	23.8	7.2	12.8	56.2
IBC 44-2	3.3	23.8	7.2	12.8	55.7
IBC 44-3	3.4	24.0	7.1	12.8	55.0
IBC 45-2	2.7	24.9	9.4	12.8	73.0
IBC 45-3	2.6	24.9	9.5	12.8	73.6
IBC 45-4	2.6	25.0	9.5	12.8	74.3
IBC 56-1	3.5	23.8	6.8	10.1	67.2
IBC 56-2	3.5	24.1	6.8	10.1	66.9
IBC 56-3	3.6	24.1	6.7	10.1	65.6
IBC 57-1	3.9	24.6	6.4	9.1	70.4
IBC 57-2	4.0	24.8	6.2	9.1	68.0
IBC 57-4	4.0	24.7	6.2	9.1	68.0
IBC 58-2	4.4	24.4	5.5	7.9	69.6
IBC 58-4	4.5	24.6	5.5	7.9	69.2
CS 1-1	3.5	24.6	7.0	12.8	54.7
CS 1-2	3.5	24.6	7.0	12.8	54.3
CS 1-4	3.5	24.7	7.1	12.8	55.5
CS 2-1	3.3	24.6	7.5	14.1	52.9
CS 2-2	3.3	24.8	7.6	14.1	54.1
CS 2-4	3.2	24.5	7.6	14.1	54.0
CS 3-1	3.5	24.6	7.0	11.8	59.5
CS 3-2	3.6	24.8	7.0	11.8	59.1
CS 3-3	3.6	24.6	6.8	11.8	57.3
CS 4-1	3.4	23.7	6.9	12.8	53.8
CS 4-2	3.4	23.9	7.0	12.8	54.4
CS 4-3	3.4	24.0	7.0	12.8	54.4
CS 5-2	3.7	24.8	6.6	12.8	51.7
CS 5-4	3.8	24.9	6.5	12.8	50.9
CS 6-1	3.2	24.0	7.6	12.8	59.2
CS 6-2	3.2	24.2	7.7	12.8	59.6
CS 6-3	3.2	24.2	7.6	12.8	59.1
CS 7-1	6.8	24.9	3.7	5.8	63.0
CS 7-2	6.4	25.0	3.9	5.8	67.1
CS 7-3	6.4	25.0	3.9	5.8	67.2
CS 8-1	6.2	24.5	4.0	5.4	72.6
CS 8-2	6.2	24.7	4.0	5.4	73.1
CS 8-3	6.2	24.8	4.0	5.4	73.2
CS 9-1	3.6	23.8	6.7	11.8	56.5
CS 9-2	3.6	24.0	6.7	11.8	56.4
CS 9-3	3.6	24.1	6.7	11.8	56.4

Note: IBC 45-1, 57-3, 58-1, 58-3, and CS 1-3, 2-3, 5-1, and 5-3 were damaged.

Table 4.2. Archimedes density and percent theoretical density for IBC composites.

Post-Sintered Densities					Post-Hot Isostatic Compacted Densities*			
Sample and Sintering Temperature	Bulk Density, g/cm³	Theoretical Density, g/cm³	Percent Theoretical Density, %	Percent Open Porosity, %	Bulk Density, g/cm³	Theoretical Density, g/cm³	Percent Theoretical Density, %	Percent Open Porosity, %
1500°C								
IBC 43-1	10.6	12.8	82.8	24.5	10.6	12.8	82.5	22.6
IBC 44-1	11.0	12.8	85.7	0.5	11.4	12.8	88.9	0.3
IBC 45-2	11.1	12.8	86.7	9.9	11.8	12.8	91.5	8.2
IBC 56-1	10.3	10.1	101.6	0	-	-	-	-
IBC 57-1	9.5	9.1	105.4	0.1	-	-	-	-
IBC 58-2	7.9	7.9	99.3	0.7	-	-	-	-
CS 1-1	11.6	12.8	90.7	6.4	11.9	12.8	92.5	5.1
CS 2-1	10.9	14.1	77.3	22.3	11.1	14.1	78.4	19.4
CS 3-1	11.0	11.8	93.2	0.6	11.8	11.8	99.9	0
CS 4-1	8.8	12.8	68.7	18.9	9.8	12.8	76.7	19.4
CS 5-2	7.7	12.8	60.2	23.7	8.7	12.8	67.7	25.8
CS 6-1	10.1	12.8	78.6	15.1	11.1	12.8	86.3	13.2
CS 7-1	4.6	5.8	79.9	10.2	4.8	5.8	82.9	10.1
CS 8-1	4.3	5.4	78.7	19.4	4.4	5.4	80.4	13.4
CS 9-1	10.5	11.8	88.6	1.3	11.7	11.8	98.5	0
1550°C								
IBC 43-2	10.2	12.8	79.7	23.3	10.4	12.8	81.0	20.5
IBC 44-2	11.5	12.8	89.5	0.3	11.7	12.8	91.1	0
IBC 45-3	11.3	12.8	88.0	2.9	12.1	12.8	93.8	0.8
IBC 56-2	10.1	10.1	100.1	0	-	-	-	-
CS 1-2	12.3	12.8	95.6	0.2	12.3	12.8	95.6	0.2
CS 2-2	11.6	14.1	82.4	16.4	11.6	14.1	82.4	16.4
CS 3-2	11.7	11.8	99.4	0	11.7	11.8	99.4	0
CS 4-2	10.1	12.8	78.5	18.6	10.1	12.8	78.5	18.6
CS 5-3	9.4	12.8	73.0	21.6	9.4	12.8	73.0	21.6
CS 6-2	11.4	12.8	88.7	12.3	11.4	12.8	88.7	12.3
CS 7-2	5.3	5.8	91.1	2.4	5.3	5.8	91.1	2.4
CS 9-2	11.8	11.8	99.8	0	11.8	11.8	99.8	0
1600°C								
IBC 43-3	10.5	12.8	82.0	7.8	11.2	12.8	86.8	10.5
IBC 44-3	11.2	12.8	87.6	0.3	11.5	12.8	89.3	0.4
IBC 45-4	11.1	12.8	86.3	5.8	11.4	12.8	88.9	11.3
CS 1-3	12.4	12.8	96.7	0.1	12.4	12.8	96.7	0.1
CS 2-4	11.5	14.1	81.7	16.6	11.5	14.1	81.7	15.7
CS 4-3	10.3	12.8	80.3	15.7	10.3	12.8	80.6	15.2
CS 5-4	11.3	12.8	88.0	3.5	11.3	12.8	88.0	3.1
CS 6-3	11.8	12.8	91.9	4.9	11.8	12.8	92.2	5.8
CS 7-3	5.4	5.8	93.8	1.5	5.5	5.8	94.3	1.0
CS 8-2	4.8	5.4	88.3	11.1	4.8	5.4	88.3	9.4

* Hot isostatic compaction conducted at 1495°C.

Table 4.3. Vickers hardness results for IBC composites.

Sample and Sintering Temperature	Vickers Hardness, kg/mm^2	Standard Deviation, kg/mm^2	Vickers Hardness, GPa	Standard Deviation, GPa
1500°C				
IBC 43-1	503	24	4.9	0.2
IBC 44-1	1253	98	12.3	1.0
IBC 45-2	745	56	7.3	0.6
CS 1-1	924	66	9.1	0.6
CS 2-1	744	31	7.3	0.3
CS 3-1	865	30	8.5	0.3
CS 4-1	1305	58	12.8	0.6
CS 5-2	677	43	6.6	0.4
CS 6-1	1034	82	10.1	0.8
CS 7-1	1171	75	11.5	0.7
CS 8-1	359	22	3.5	0.2
CS 9-1	926	15	9.1	0.1
1550°C				
IBC 43-2	425	80	4.2	0.8
IBC 44-2	1112	116	10.9	1.1
IBC 45-3	719	17	7.0	0.2
CS 2-2	879	25	8.6	0.2
CS 3-2	942	36	9.2	0.4
CS 4-2	1423	70	14.0	0.7
CS 5-3	781	54	7.7	0.5
CS 6-2	1090	33	10.7	0.3
CS 7-2	1195	59	11.7	0.6
CS 9-2	1002	16	9.8	0.2

Table 6.1. Average percent theoretical density of flexure bars machined from disks.

Sample	Average Percent Open Porosity, %	Average Percent Theoretical Density, %	Final Average Percent Theoretical Density, %	Standard Deviation, %
CS 1-A	0.11	89.9	93.6	3.74
CS 1-B	0.04	97.3		
CS 3-B	0.07	96.4	96.9	0.52
CS 3-C	0.01	97.4		
CS 7-A	0.05	98.0	98.0	0.02
CS 7-B	0.22	98.0		
CS 9-A	0.09	98.9	98.9	0.07
CS 9-B	0.02	99.0		

Table 6.2. Vickers hardness results for selected IBC composites.

Sample	Indent Load, kg	Vickers Hardness, kg/mm^2	Standard Deviation, kg/mm^2	Vickers Hardness, GPa	Standard Deviation, GPa
CS-1	30	850	24	8.3	0.24
	50	815	3	8.0	0.03
CS-3	30	805	20	7.9	0.20
	50	755	2	7.4	0.02
CS-7	30	1035	51	10.1	0.50
	50	985	32	9.7	0.31
CS-9	30	887	5	8.7	0.05
	50	890	9	8.7	0.09

Table 6.3. Average room-temperature and high-temperature flexural strength for selected IBC composites.

Sample	Average Room-Temperature Flexural Strength, MPa	Standard Deviation, MPa	Average 800°C Flexural Strength, MPa	Standard Deviation, MPa
CS-1	1142	187	857*	0*
CS-3	1199	144	1133	151
CS-7	688	34	541	122
CS-9	1791	69	585**	26**

* Only one bar of CS-1 was tested.

** Results are invalid for CS-9.

Table 6.4. Fracture toughness results calculated from indentation fracture methods.

Sample, Indent Number	K_{IC}, MPa√m Authors [Reference]										Average K_{IC}, MPa√m	Standard Deviation, MPa√m
	Evans, Charles [50]	Lawn, Evans, Marshall [51]	Anstis, Chantikul, Lawn, Marshall [49]	Niihara, Morena, Hasselman [52]	Miyoshi, Sagawa, Sassa [80]	Tanaka [81]	Niihara [52]	Blendell [53]	Evans [54]	Lankford [55]		
CS-1												
1	14.2	24.3	22.2	28.8	25.0	13.6	13.3	12.8	12.6	31.5		
2	13.5	23.2	21.2	27.5	23.9	13.0	11.6	12.6	12.4	29.9		
3	14.4	24.8	22.6	29.3	25.5	13.9	14.3	12.9	12.7	32.3	19.7	6.9
4	14.3	24.6	22.5	29.1	25.3	13.8	13.9	12.9	12.7	32.0		
5	13.8	23.7	21.7	28.1	24.4	13.3	12.3	12.7	12.5	30.7		
CS-3												
1	14.5	24.0	22.0	28.7	24.7	14.0	17.0	12.0	11.8	31.4		
2	14.4	23.8	21.8	28.4	24.5	13.9	16.3	12.0	11.8	31.2		
3	15.2	25.1	22.9	29.9	25.8	14.6	23.0	12.2	11.9	32.8	20.4	6.8
4	14.4	23.9	21.8	28.5	24.5	13.9	16.6	12.0	11.8	31.3		
5	15.0	24.7	22.6	29.5	25.5	14.4	21.3	12.2	11.9	32.5		
CS-7												
1	11.2	15.2	13.9	18.8	15.6	10.8	6.4	10.4	10.4	19.4		
2	11.3	15.2	13.9	18.9	15.7	10.9	7.0	11.0	10.9	21.4		
3	10.8	14.6	13.4	18.2	15.1	10.4	6.5	10.6	10.5	19.7	13.2	3.9
4	10.7	14.5	13.3	18.0	14.9	10.3	6.4	10.5	10.5	19.5		
5	10.9	14.8	13.5	18.4	15.2	10.5	6.5	10.6	10.6	19.9		
CS-9												
1	17.4	29.8	27.3	35.3	30.7	16.7	36.5	14.3	14.0	39.1		
2	17.2	29.5	27.0	34.9	30.3	16.5	29.8	14.2	13.9	38.6		
3	17.2	29.5	27.0	34.9	30.4	16.6	28.1	14.2	13.9	38.3	24.9	8.4
4	16.9	29.0	26.5	34.3	29.8	16.3	22.1	14.0	13.8	37.1		
5	17.0	29.2	26.7	34.5	30.0	16.4	23.7	14.1	13.8	37.5		

Table 6.5. Fracture toughness results calculated from indentation strength method.

Sample, bar designation	Indent Load, kg	Flexural Strength, MPa	Vickers Hardness, GPa	Young's Modulus, GPa	K_{IC}, MPa√m	Average K_{IC}, MPa√m	Standard Deviation, MPa√m
CS-1							
1B	30	1226	8.3	436	26.3	26.3	0.0
CS-3							
All bars fractured at points other than the indent.							
CS-7							
2A	30	625	10.1	328	14.9		
2B	30	513	10.1	328	12.9	15.2	2.1
3B	50	668	9.7	328	17.9		
CS-9							
1A	50	1359	8.7	474	32.4		
3A	30	1485	8.7	474	30.5	33.0	2.3
1B	50	1567	8.7	474	36.0		

Table 6.6. Average corrosion penetration rates for continous immersion tests.

Acid, Sample Tested	Area exposed, cm^2	Mass lost, g	Average CPR*, mils/yr	Average CPR*, µm/day
10% HNO_3				
CS 1-B	1.20	0.2667	565	39
CS 3-C	1.75	0.3946	604	42
CS 7-B	1.22	0.3490	1615	112
CS 9-A	1.17	0.0130	29	2.01
10% HCL				
CS 1-B	1.24	0.0032	7	0.46
CS 3-C	1.05	0.0035	9	0.62
CS 7-B	1.12	0.0030	15	1.05
CS 9-B	0.81	0.5890	1894	132
10% H_2SO_4				
CS 1-B	1.40	0.0020	4	0.25
CS 3-C	1.35	0.0076	15	1.05
CS 7-B	1.26	0.0044	20	1.37
CS 9-B	1.17	1.0782	2400	167

* Corrosion penetration rate

Table 6.7. Average corrosion penetration rates for discontinuous immersion tests.

Acid, Sample Tested	Area exposed, cm^2	Mass lost, g	Average CPR*, mils/yr	Average CPR*, µm/day
10% HNO_3				
CS 1-A	1.50	0.4393	744	52
CS 3-B	1.35	0.7707	1528	106
CS 7-A	1.19	0.2588	1228	85
CS 9-B	1.13	0.0035	8	0.56
10% HCL				
CS 1-A	1.20	0.0018	4	0.27
CS 3-B	1.32	0.0055	11	0.78
CS 7-A	1.08	0.0004	2	0.15
CS 9-B	1.17	2.1765	4844	337
10% H_2SO_4				
CS 1-A	1.55	0.0043	7	0.49
CS 3-B	1.13	0.0002	0.474	0.03
CS 7-A	0.84	0.0034	23	1.59
CS 9-B	1.50	1.5237	2645	184

* Corrosion penetration rate

Table 6.8. Results of microstructural parameter measurements.

Sample	Volume Fraction of Carbide Phase (V_C)	Carbide Grain Size, μm (d)	Contiguity of Carbide Phase (C_C)	Mean Free Path of Binder Phase, μm (λ)
CS-1	0.60	4.7	0.39	5.1
CS-3	0.49	2.2	0.31	3.3
CS-7	0.61	3.1	0.41	3.4
CS-9	0.59	2.0	0.36	2.2

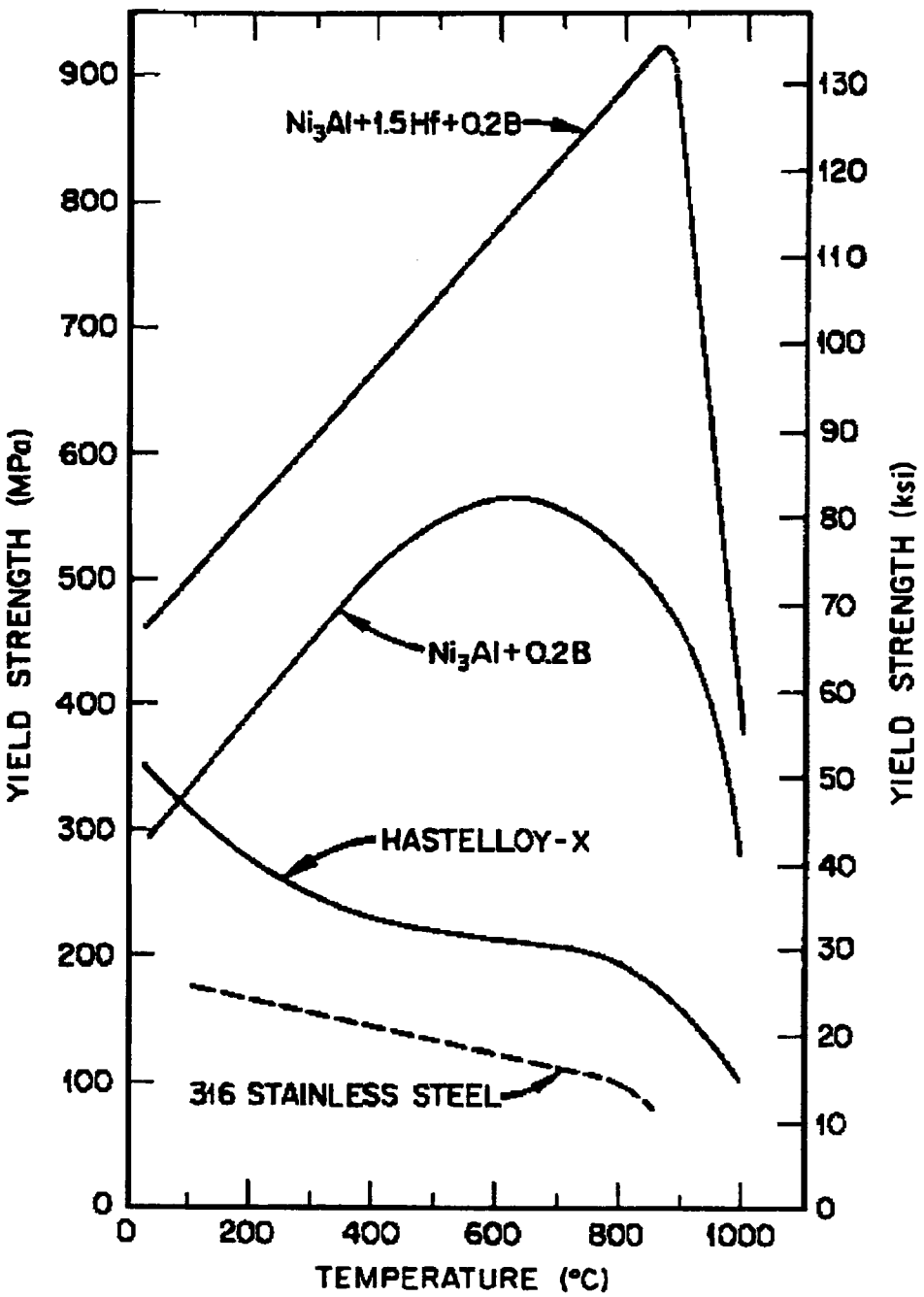
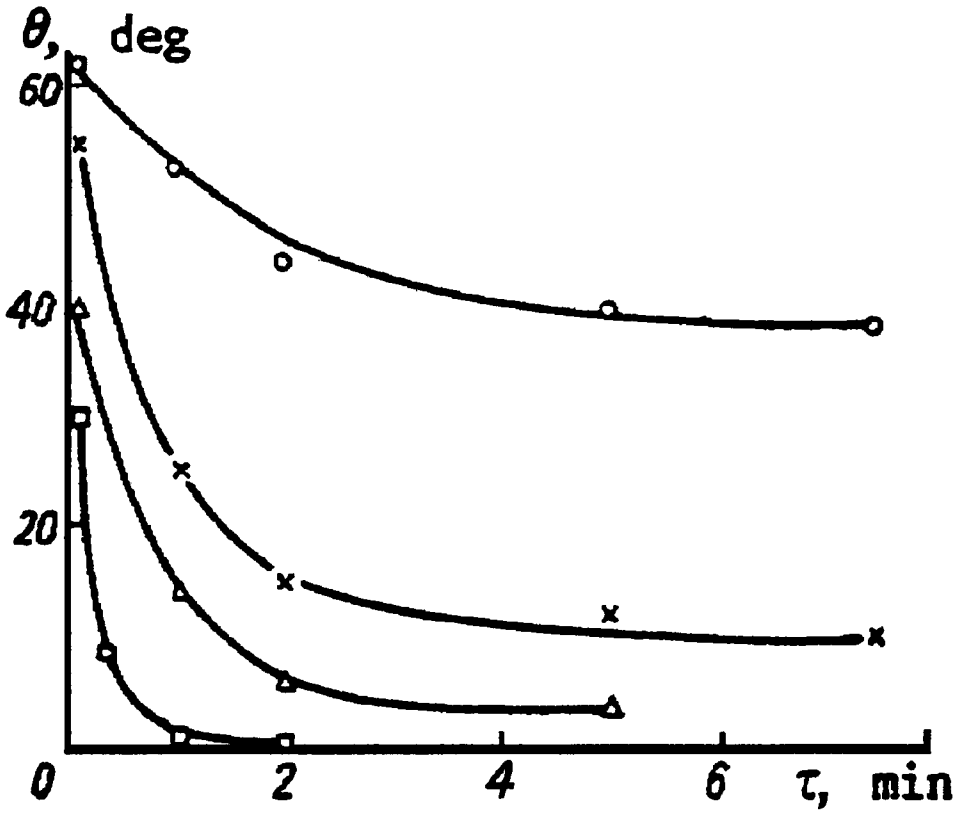


Figure 1.1. Strength of advanced aluminides as a function of temperature (71).



o: TiC
×: (Ti, W)C, 50:50
Δ: (Ti, W)C, 30:70
□: WC

Figure 2.1. Wetting of various carbides by Ni_3Al in a vacuum of 1.33×10^{-2} Pa at 1400°C (4).

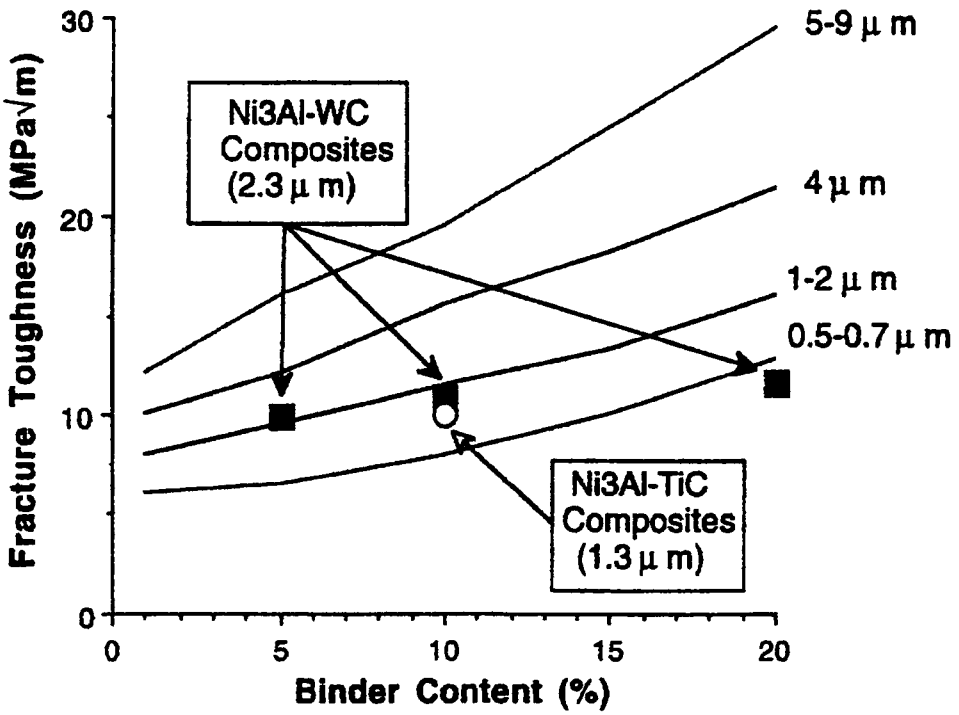


Figure 2.2. Fracture toughness as a function of binder content for WC-Ni_3Al and TiC-Ni_3Al compared to previous work (solid lines) on WC-Co. Particle sizes of carbides with Ni_3Al binder are shown in boxes, and particle sizes of WC with Co binder are shown next to each line (19).

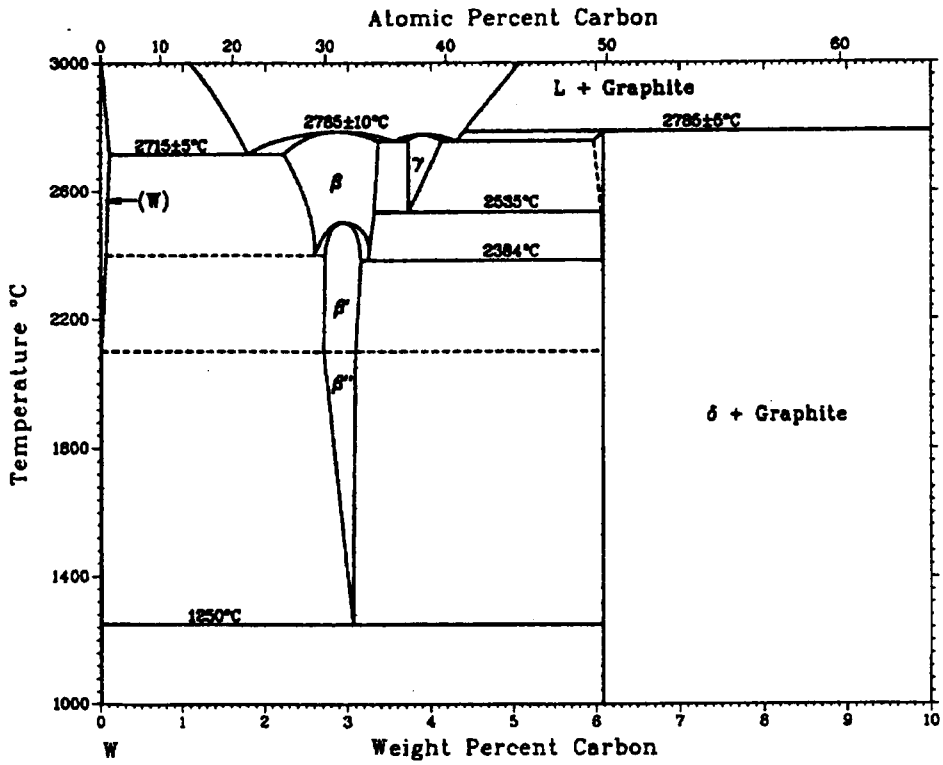


Figure 2.3. W-C phase diagram (72).

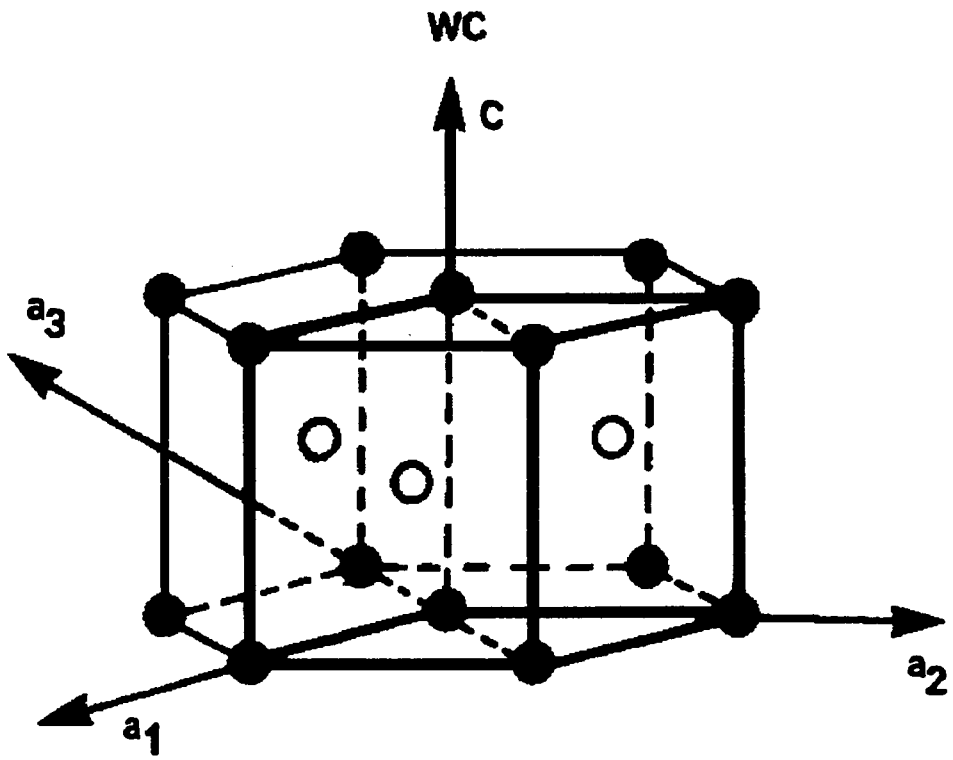


Figure 2.4. Unit cell of WC (24). Black circles represent tungsten, and white circles represent carbon.

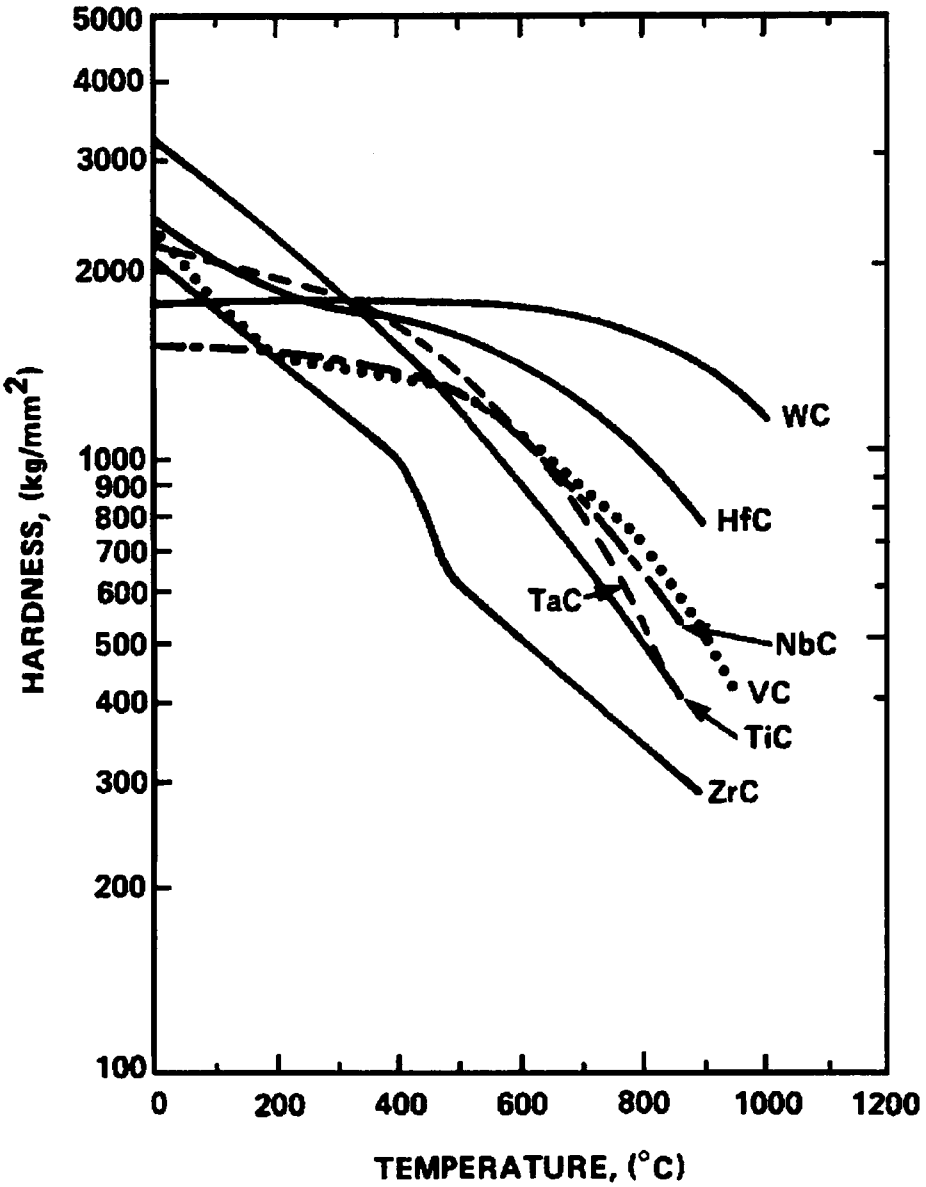
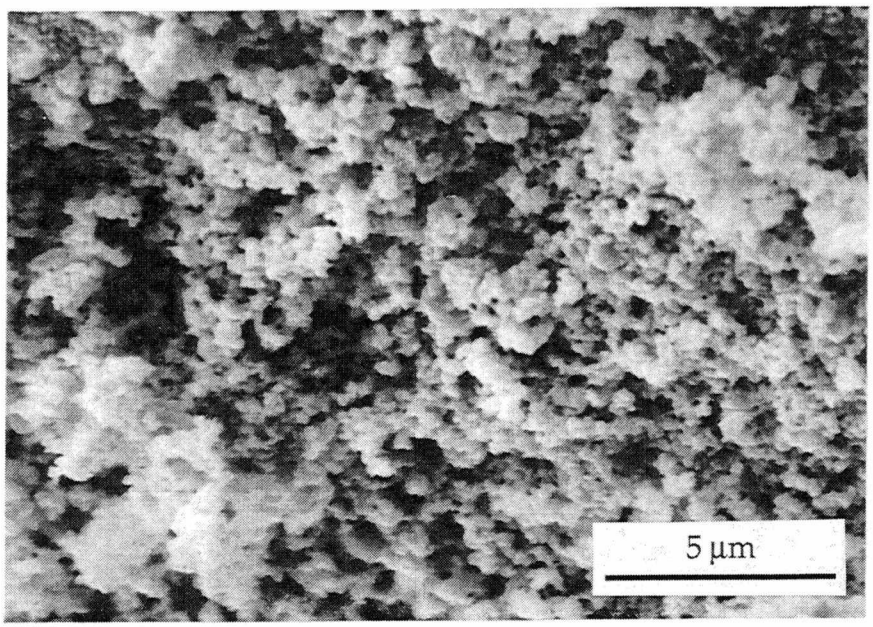
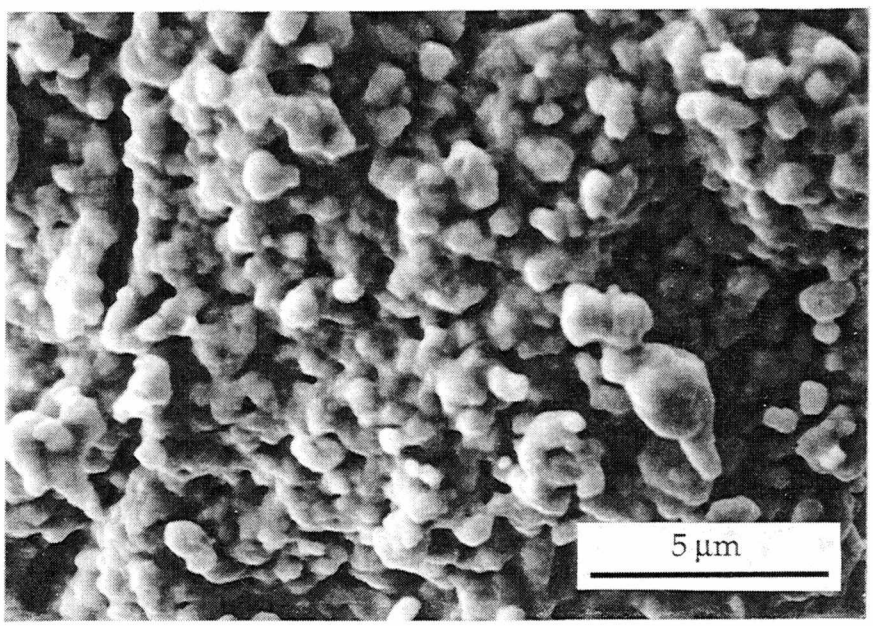


Figure 2.5. Effect of temperature on the hardness of some transition metal carbides (24).



(a) 0.8 μm



(b) 2.3 μm

Figure 2.6. Scanning electron micrographs of 0.8 μm and 2.3 μm WC powders.

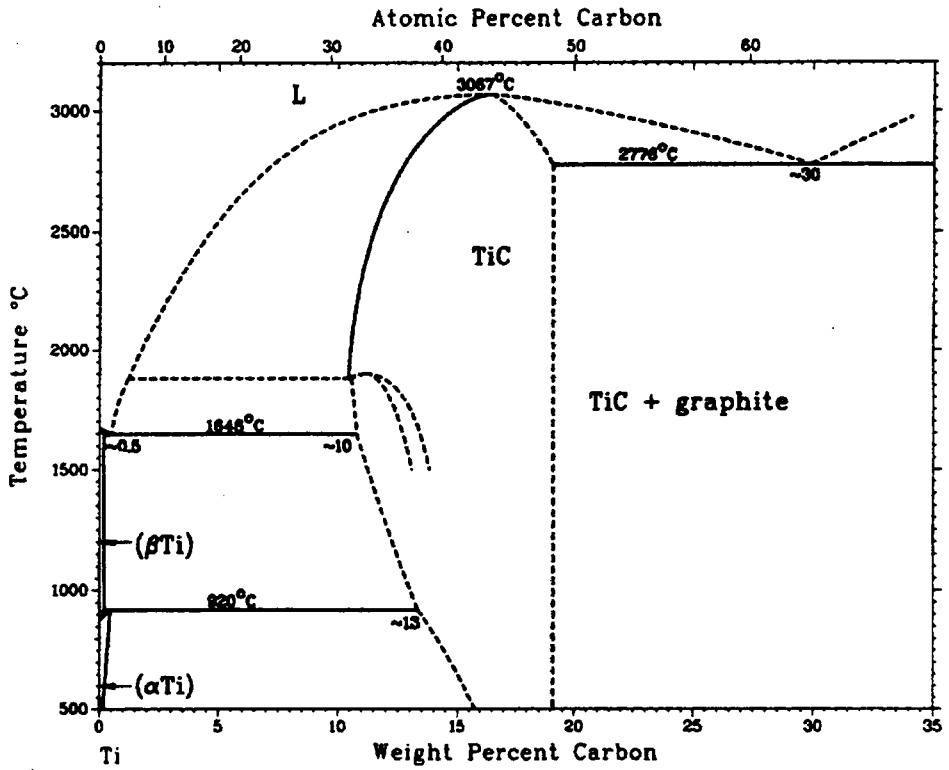


Figure 2.7. Ti-C phase diagram (73).

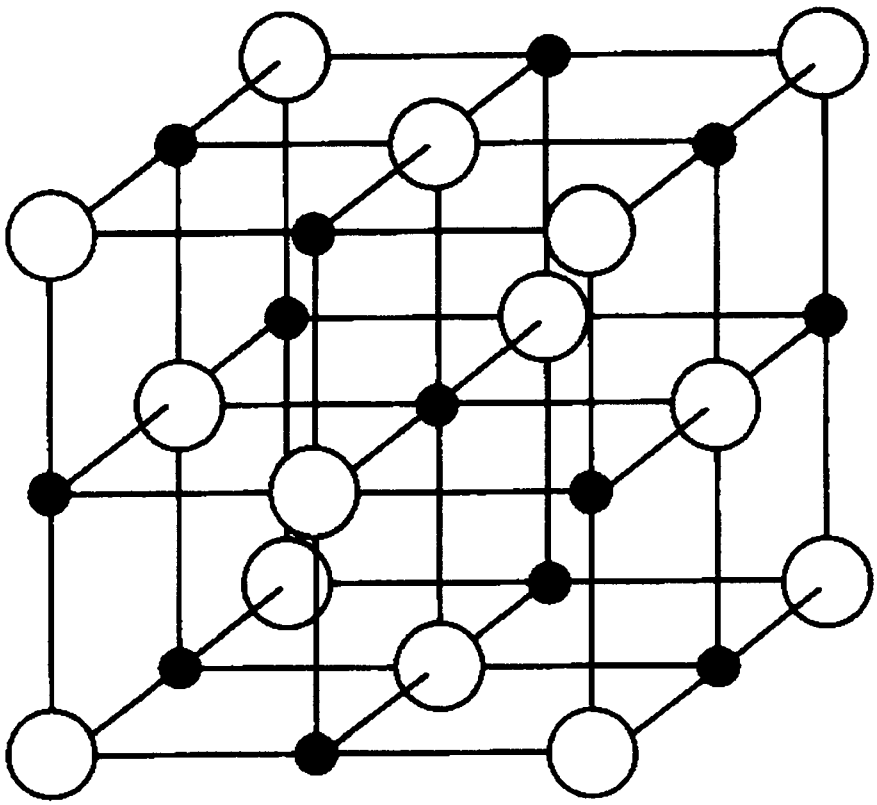


Figure 2.8. Unit cell of TiC (33). White circles represent titanium, and black circles represent carbon.

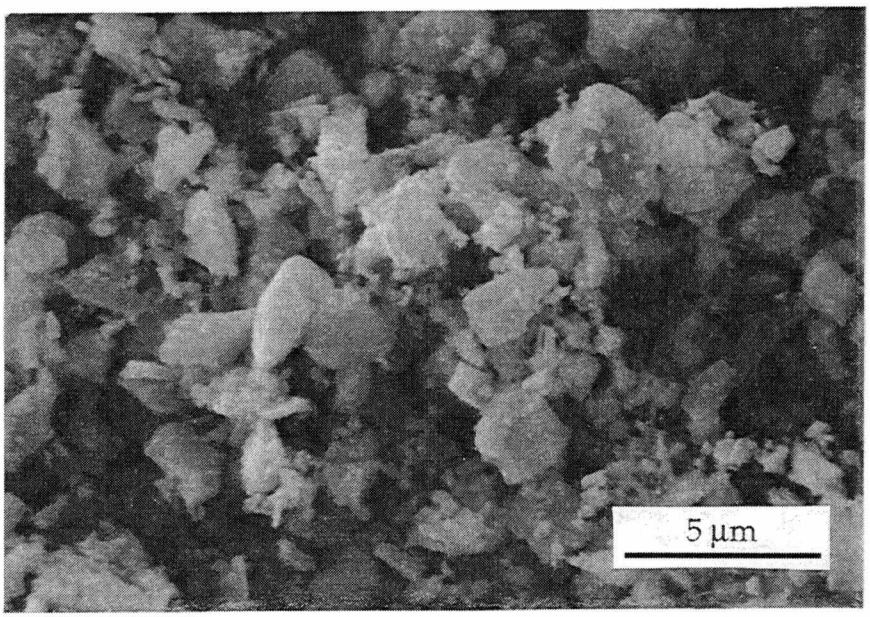


Figure 2.9. Scanning electron micrograph of 1-3 µm TiC powder.

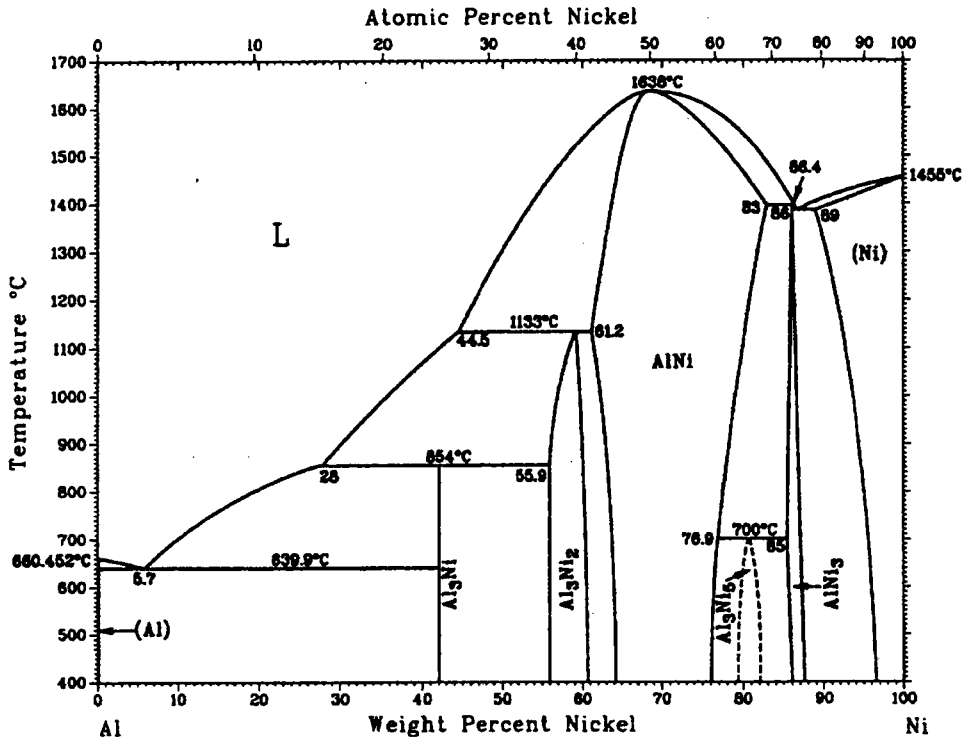


Figure 2.10. Ni-Al phase diagram (74).

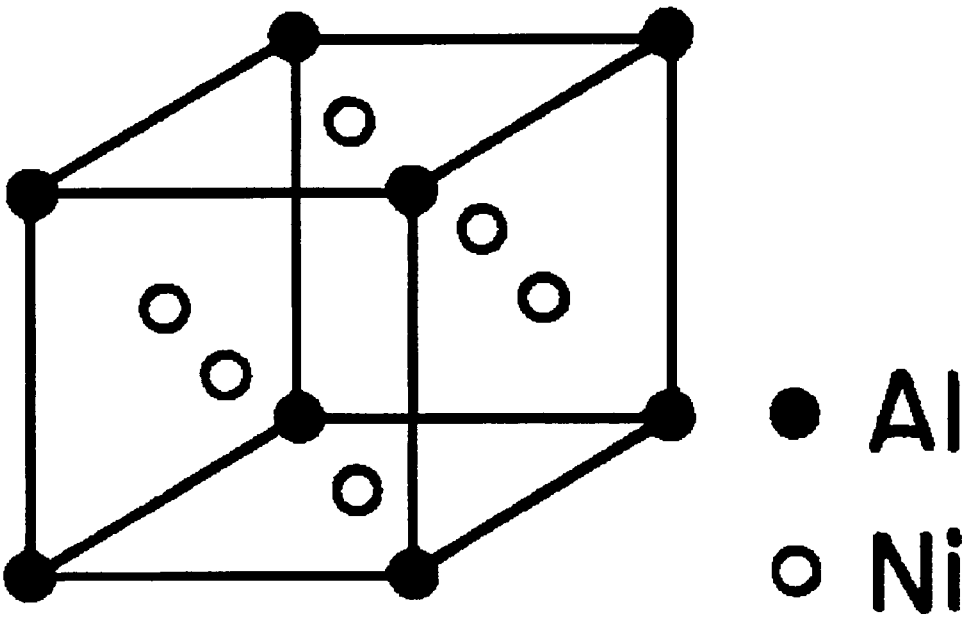


Figure 2.11. Unit cell of Ni_3Al (31).

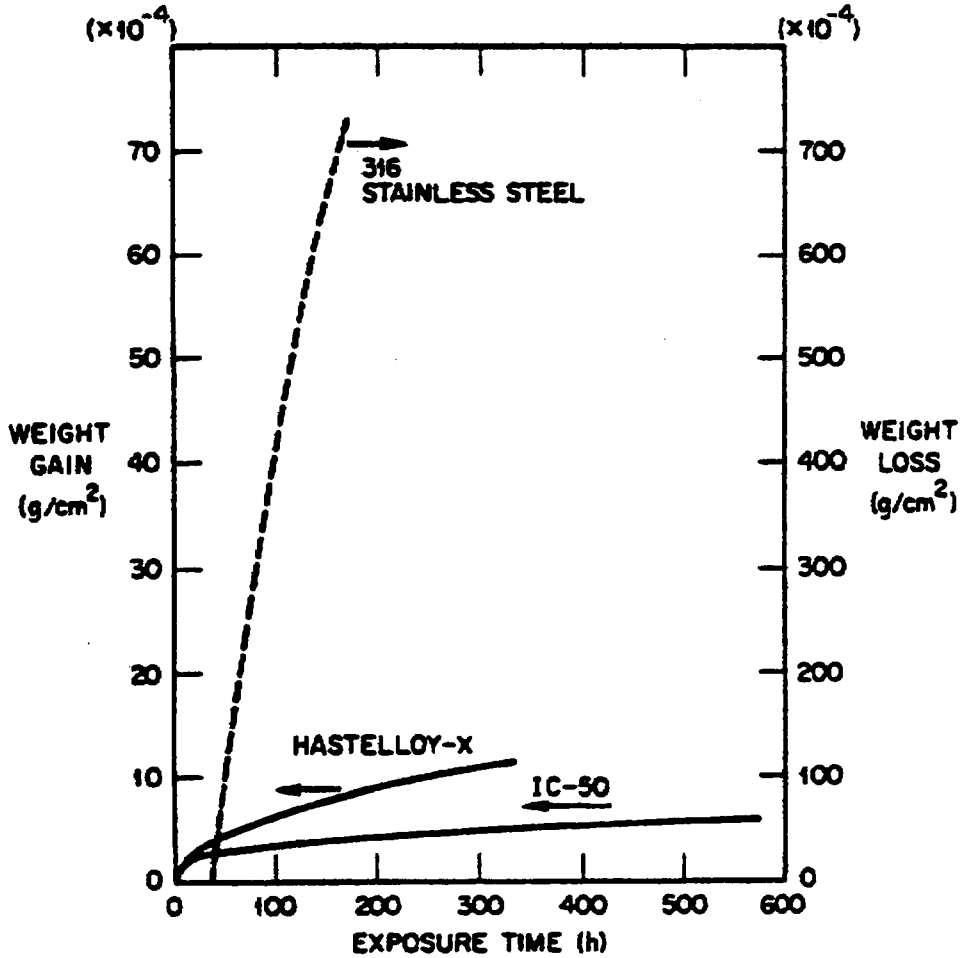


Figure 2.12. Oxidation of Ni_3Al (IC-50) compared to other alloys (75).

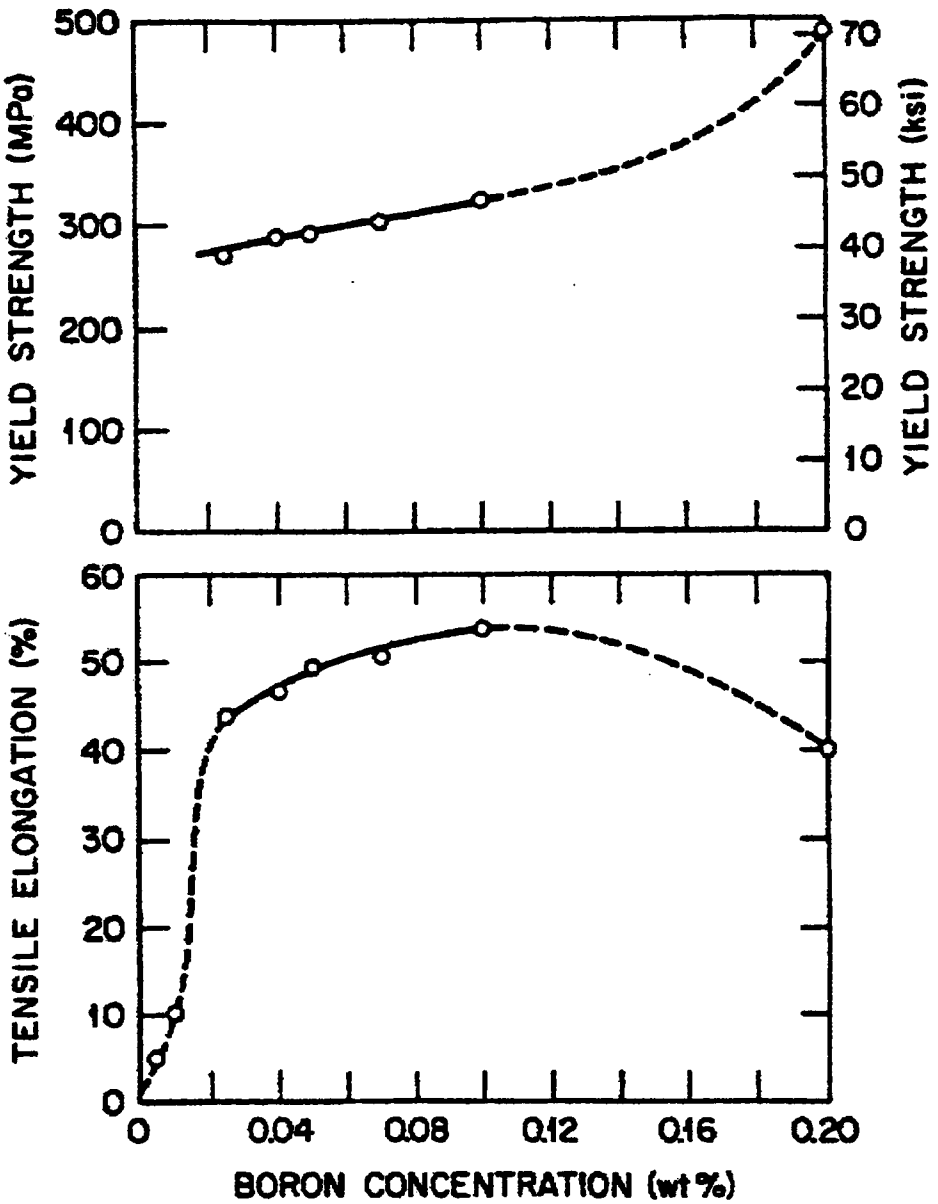
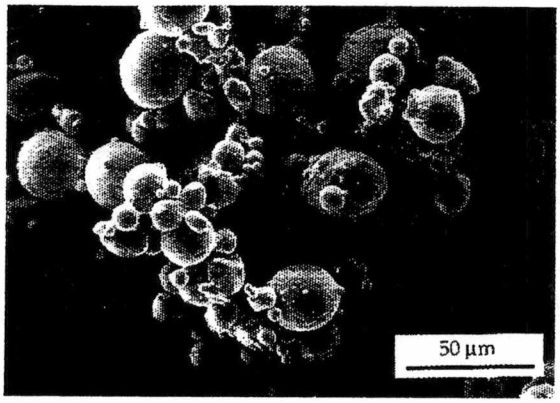
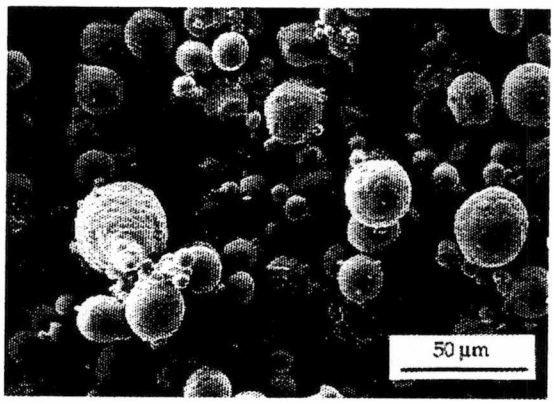


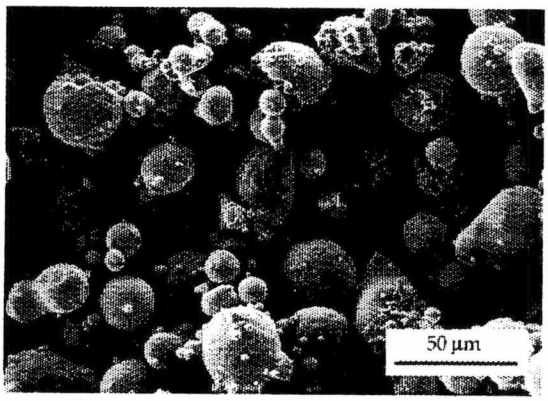
Figure 2.13. Effect of boron additions on tensile elongation and yield strength in Ni_3Al containing 24 at.% Al (71).



(a) IC-15



(b) IC-50



(c) IC-218

Figure 2.14. Scanning electron micrographs of IC-15, IC-50, and IC-218 Ni_3Al alloy powders.

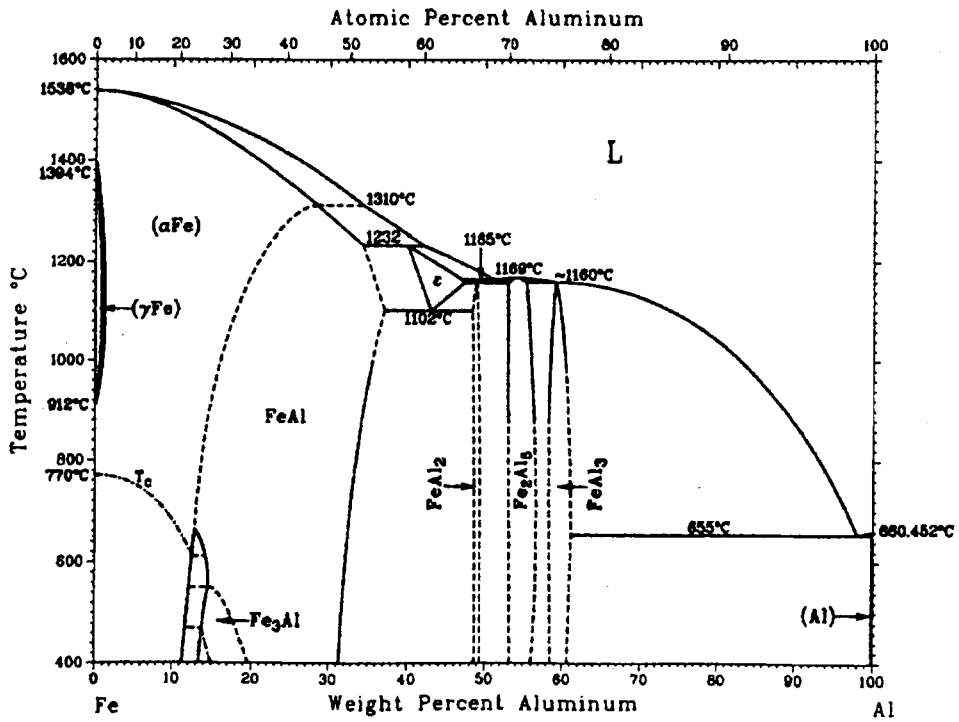


Figure 2.15. Fe-Al phase diagram (76).

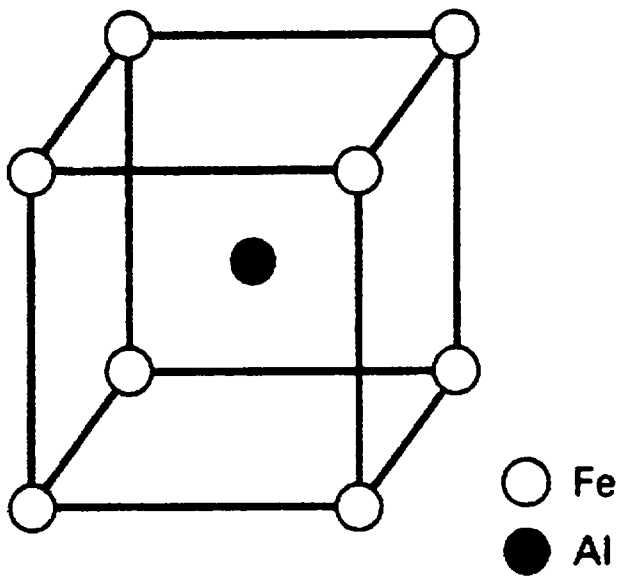


Figure 2.16. Unit cell of FeAl (31).

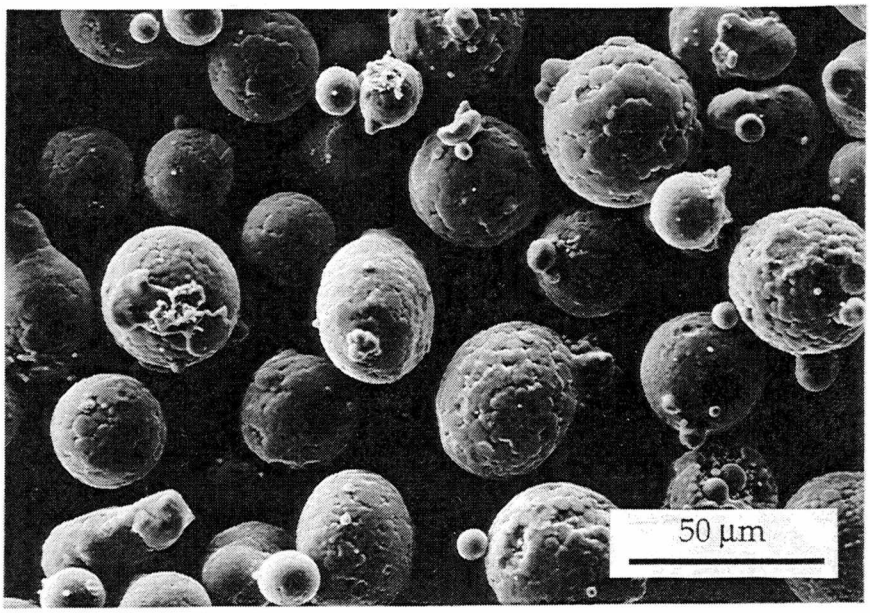
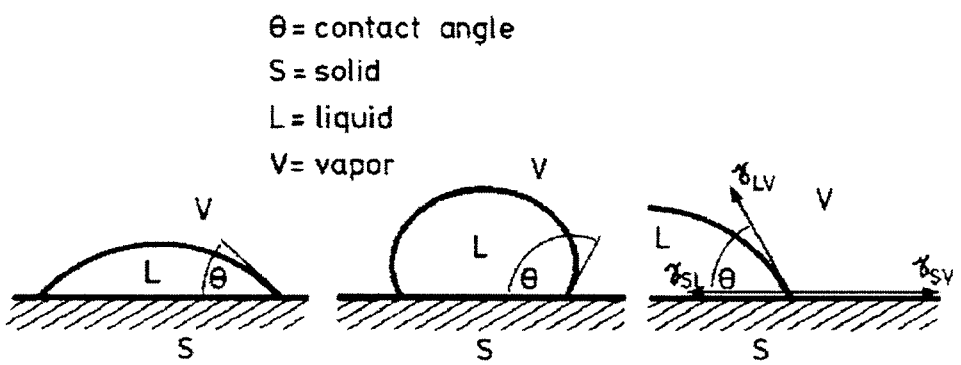


Figure 2.17. Scanning electron micrograph of FeAl powder.



(a) good wetting (b) poor wetting (c) energy balance

Figure 2.18. Schematic diagram illustrating surface energy equilibrium in wetting (c) and contact angles which produce good wetting (a) and poor wetting (b) (35).

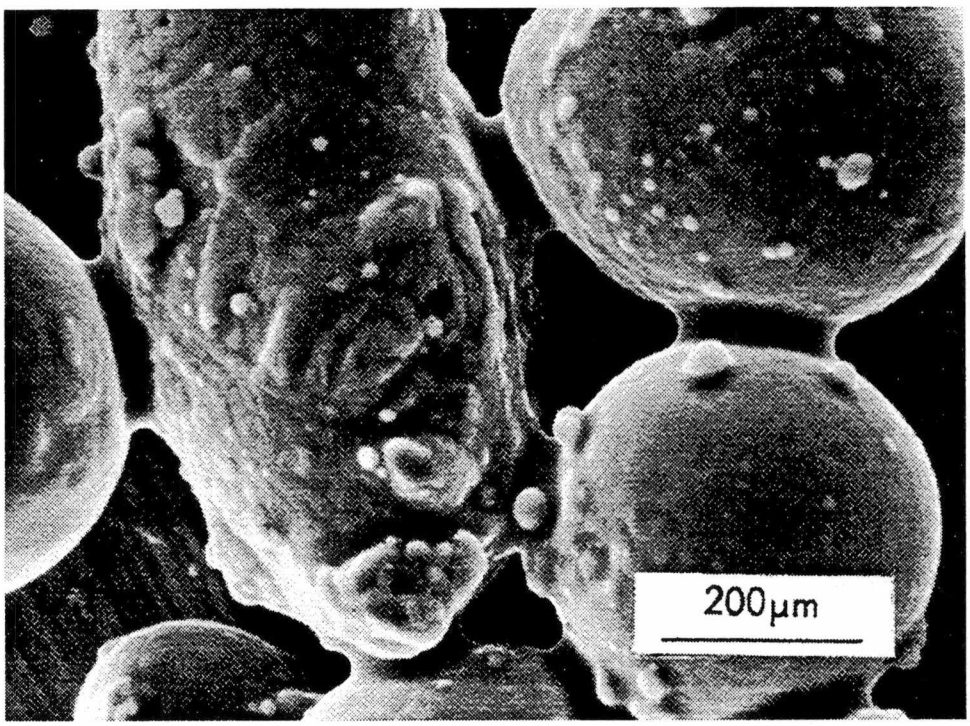


Figure 2.19. Bridging of particulate solids associated with a wetting liquid during the initial stage of liquid phase sintering (35).

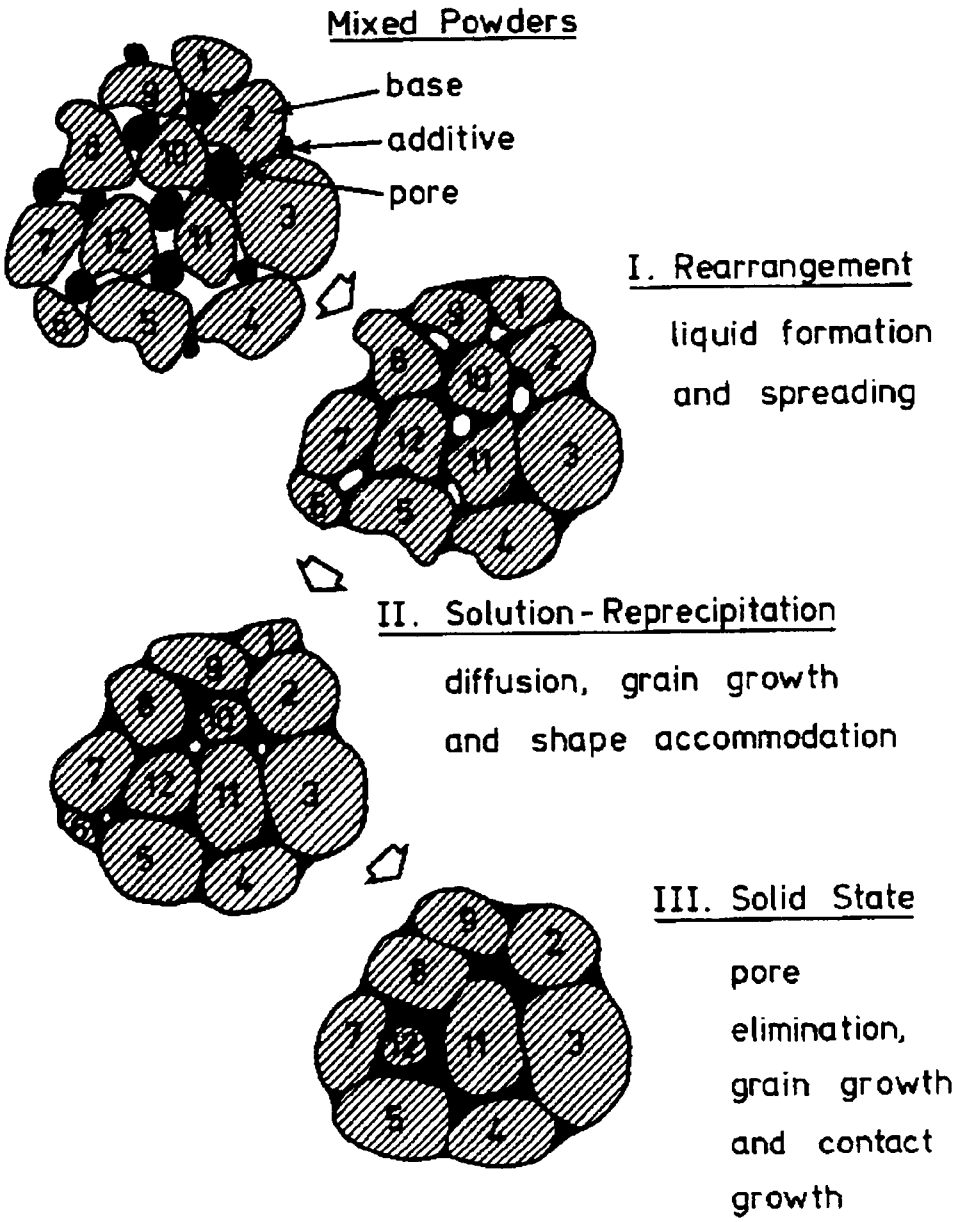


Figure 2.20. Schematic diagram illustrating the three overlapping stages of liquid phase sintering (35).

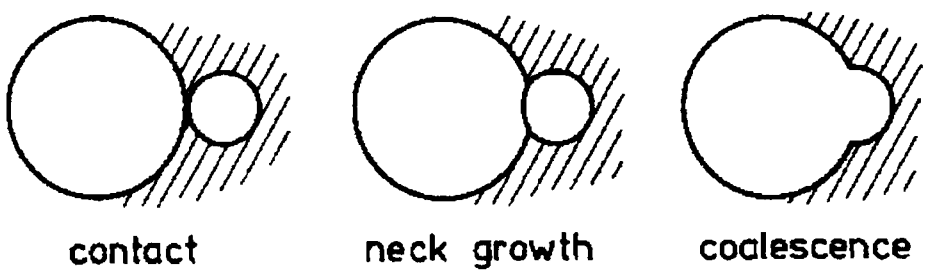


Figure 2.21. Mechanism of grain growth during liquid phase sintering (35).

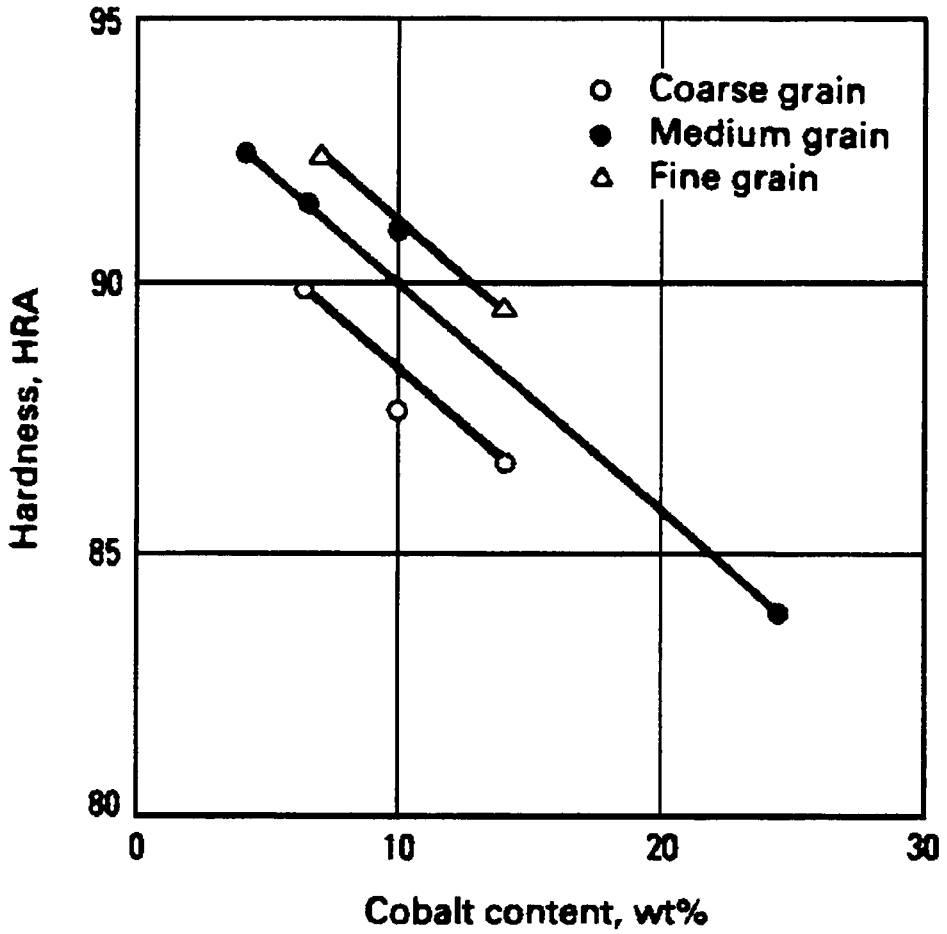
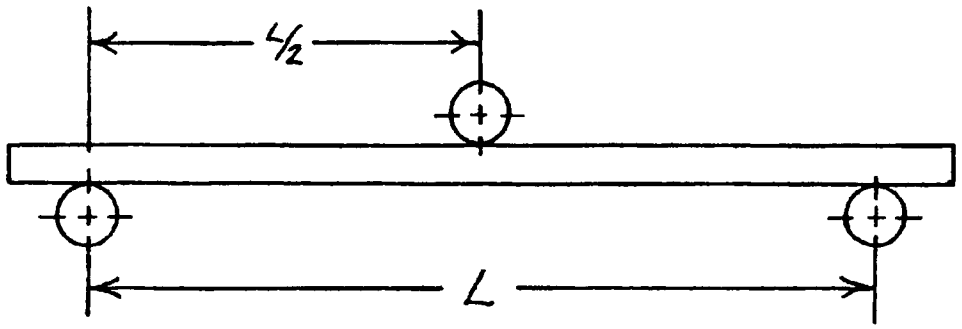
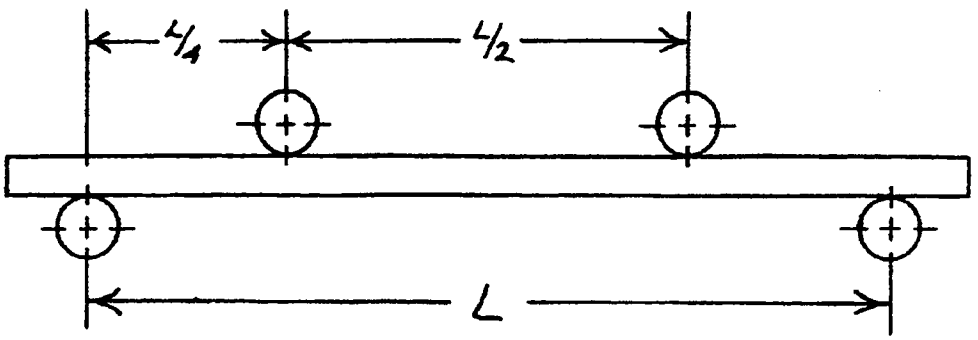


Figure 2.22. Hardness as a function of cobalt content and carbide grain size in WC-Co (1).

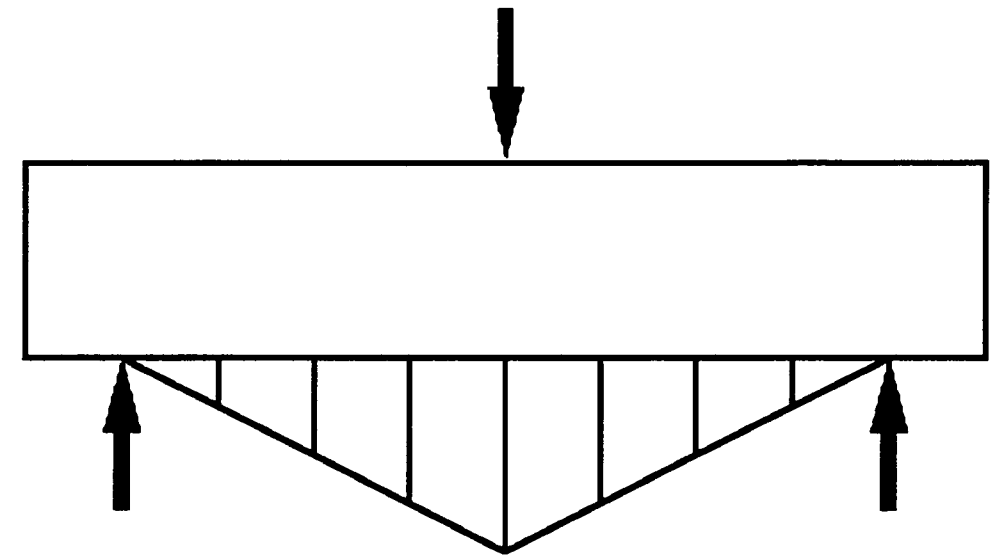


(a) 3-point loading

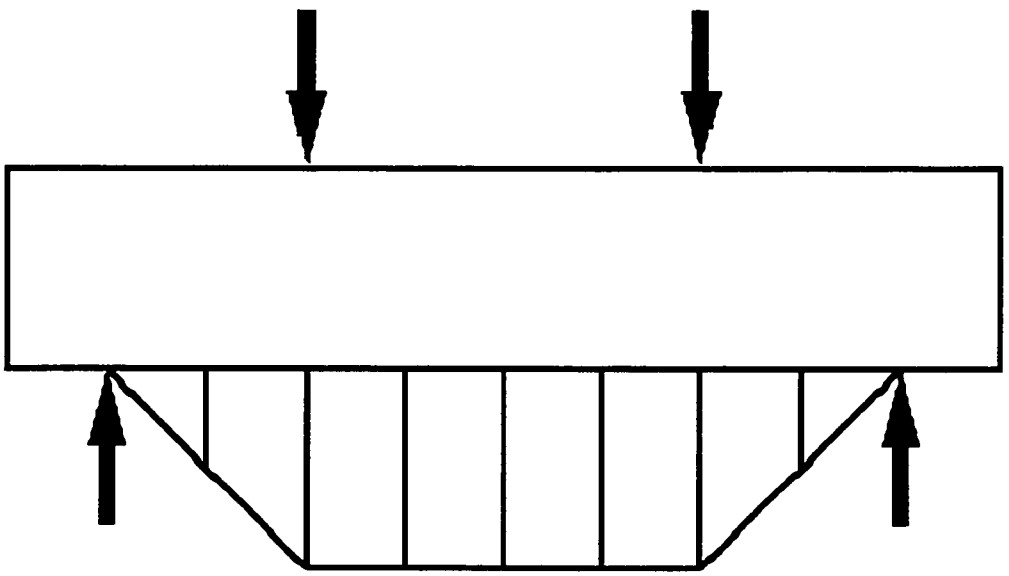


(b) 4-point loading

Figure 2.23. Schematic diagram illustrating the difference between 3- and 4-point loading (77).



(a) 3-point loading



(b) 4-point loading

Figure 2.24. Tensile stress distribution in 3- and 4-point bending bars (41).

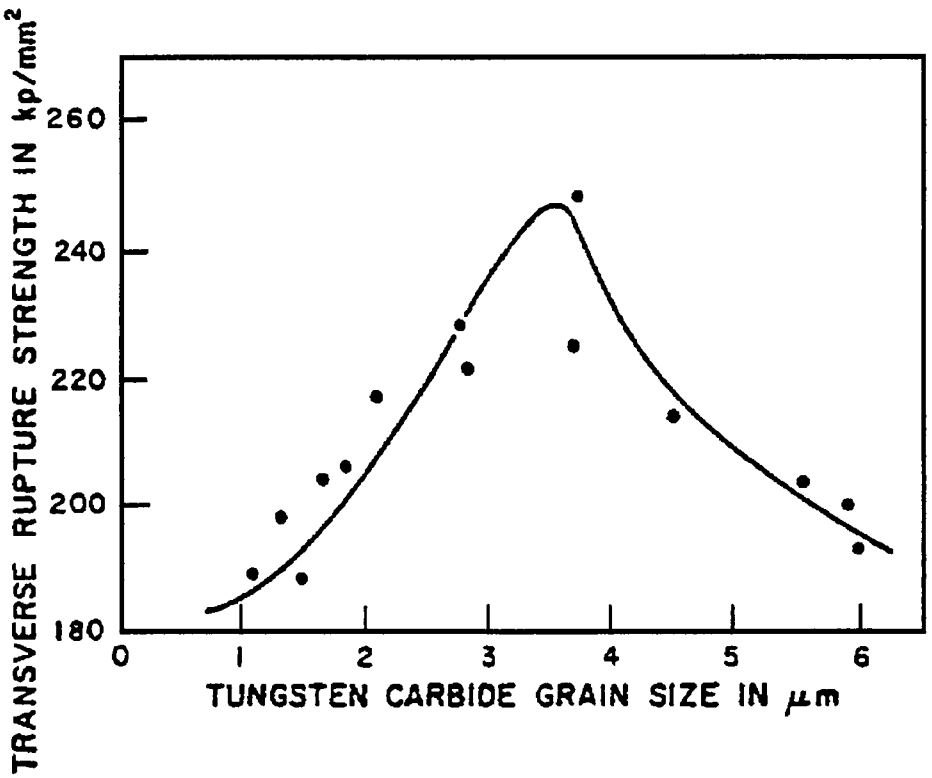
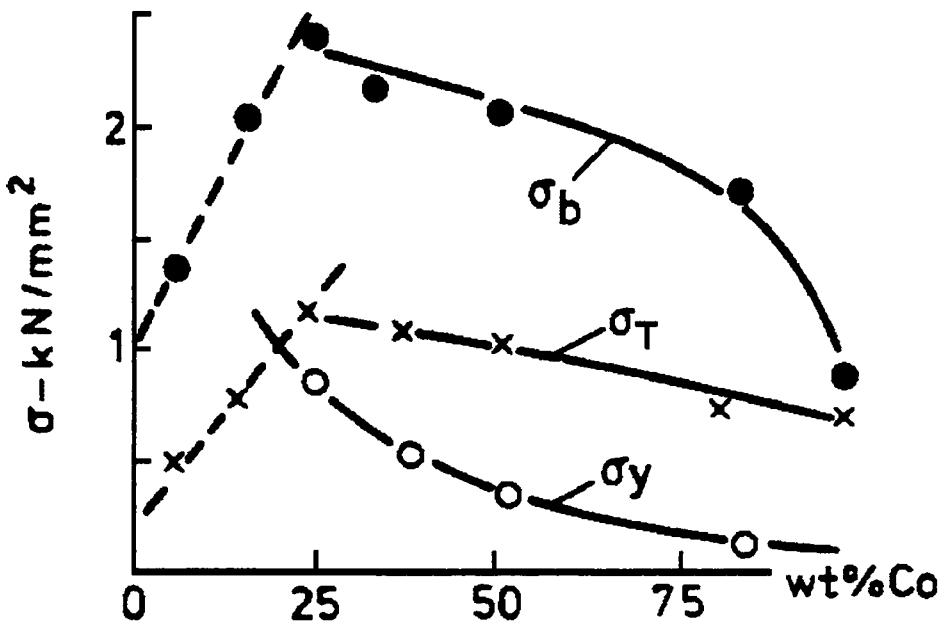


Figure 2.25. Transverse rupture strength as a function of WC grain size in WC-Co (24).



σ_b: flexural strength
σ_T: tensile strength
σ_y: yield strength

Figure 2.26. Strength as a function of cobalt content in WC-Co (69).

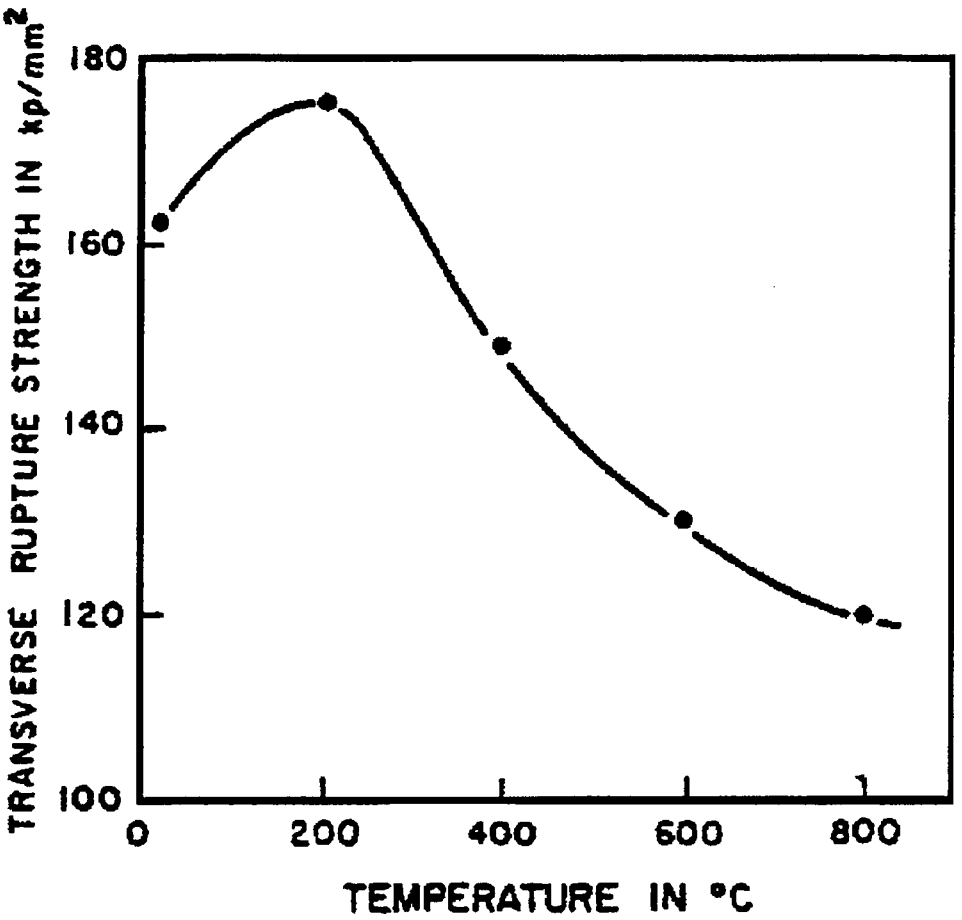


Figure 2.27. Transverse rupture strength as a function of temperature in a WC-Co alloy (44).

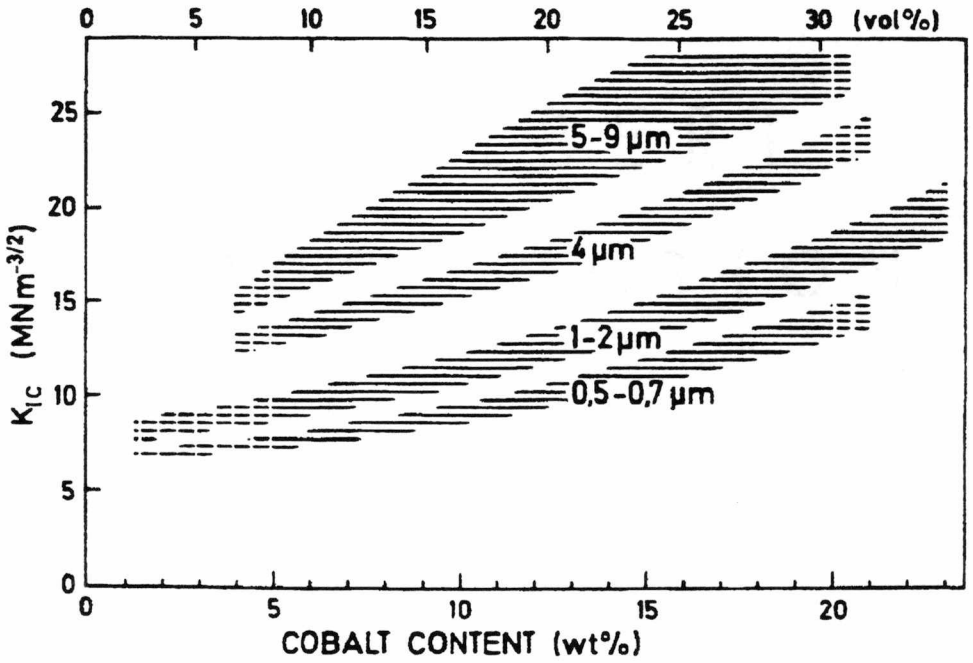
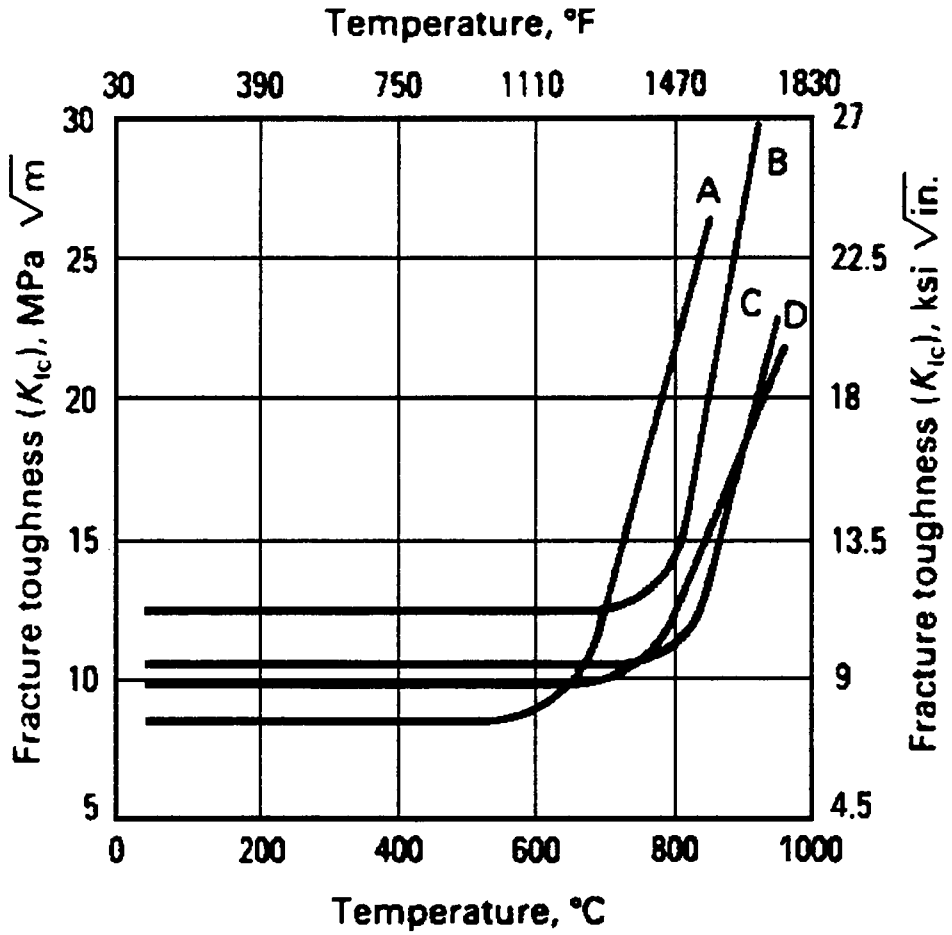
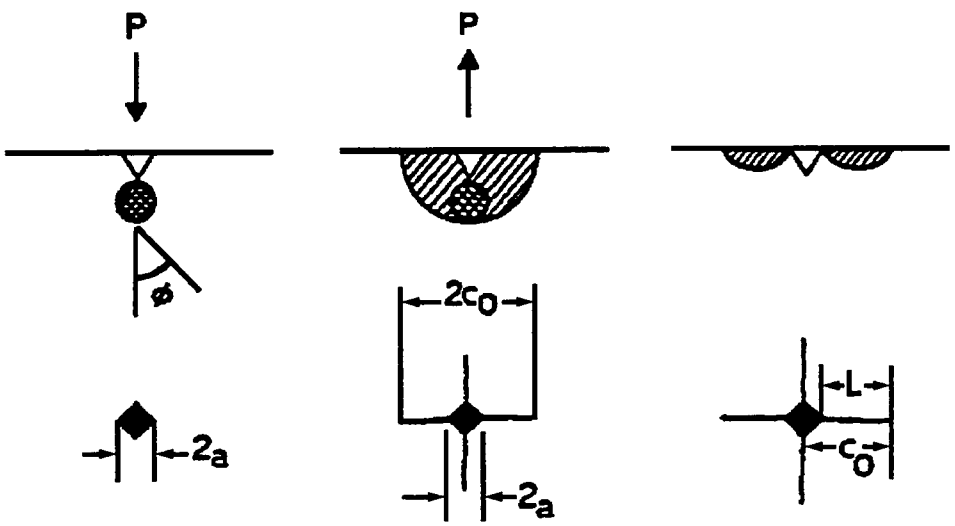


Figure 2.28. Fracture toughness as a function of cobalt content and carbide grain size in WC-Co (13).



A: 86WC-2TaC-12Co
B: 85WC-9(Ti, Ta, Nb)C-6Co
C: 80WC-12(Ti, Ta, Nb)C-8Co
D: 96WC-4Co

Figure 2.29. Fracture toughness as a function of temperature for several WC-Co alloys (1). Compositions listed are in wt.%.



(a) median (b) radial (c) Palmqvist

Figure 2.30. Schematic diagram illustrating types of crack systems formed around an indent (46).

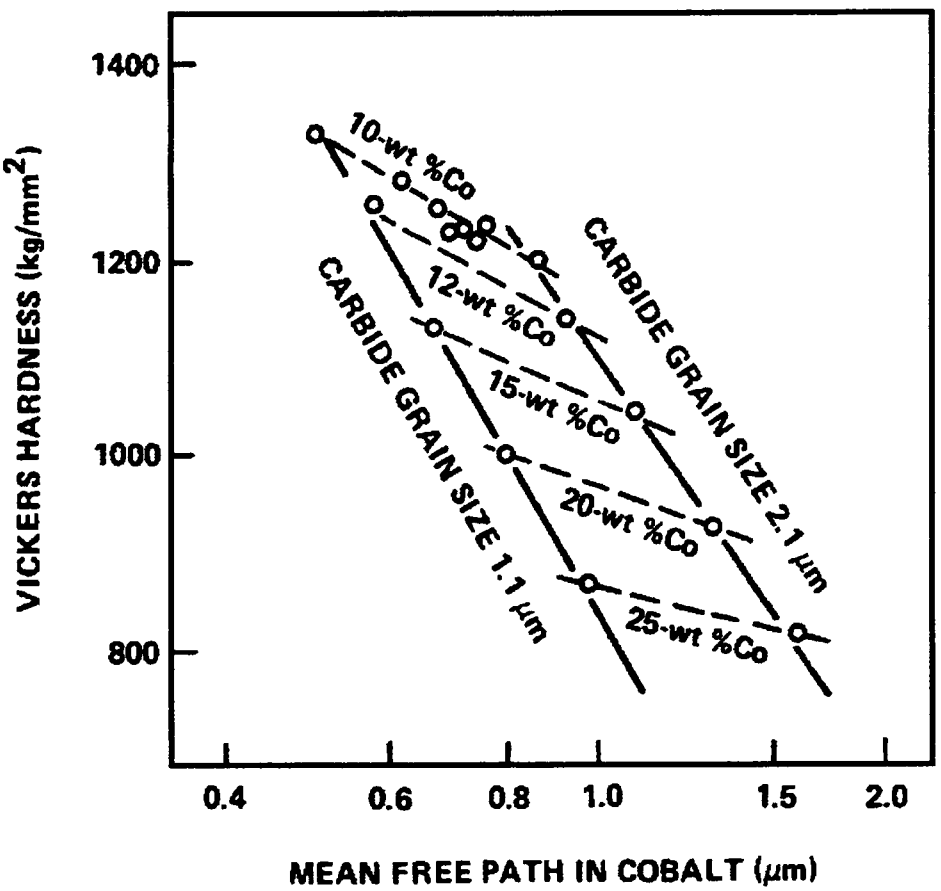


Figure 2.31. Hardness as a function of cobalt mean free path, cobalt content, and carbide grain size in WC-Co (24).

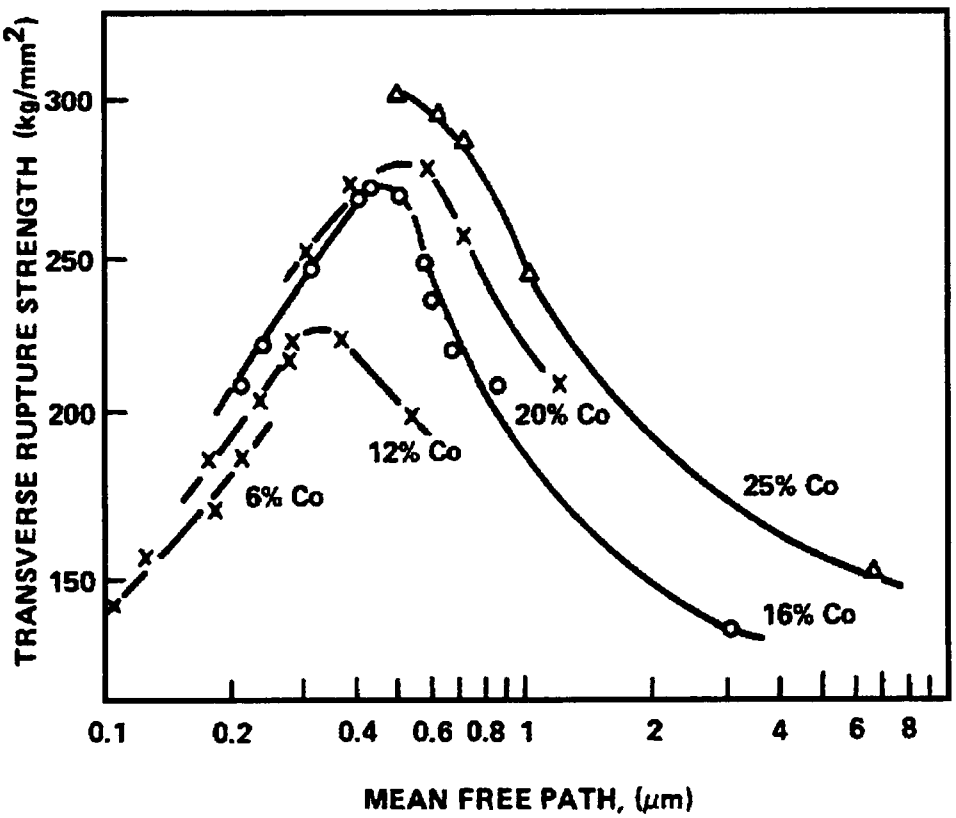


Figure 2.32. Transverse rupture strength as a function of cobalt mean free path and cobalt content in WC-Co (24).

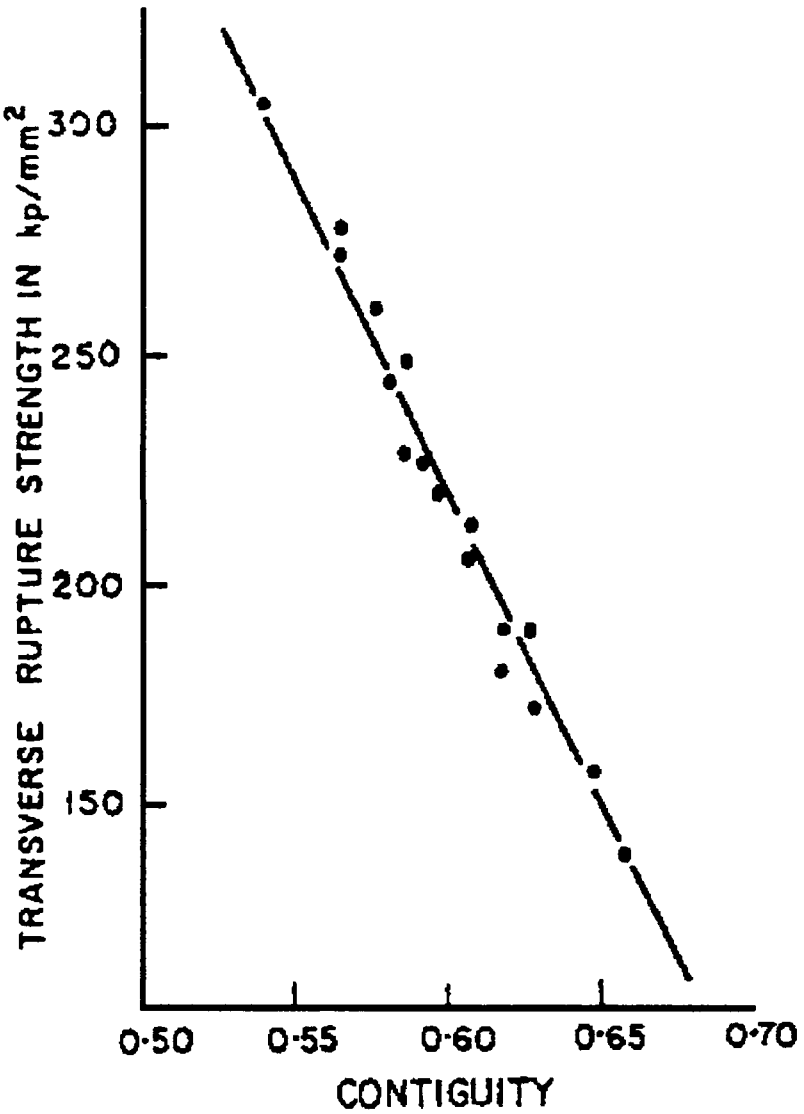


Figure 2.33. Transverse rupture strength as a function of contiguity in WC-Co (44).

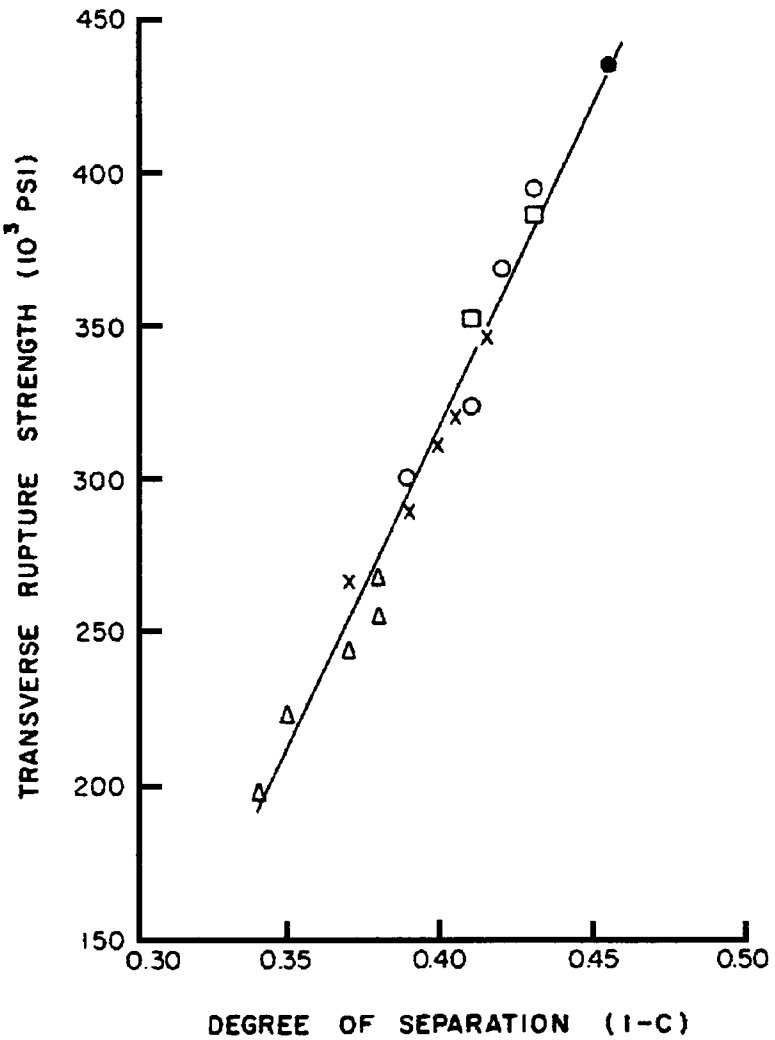
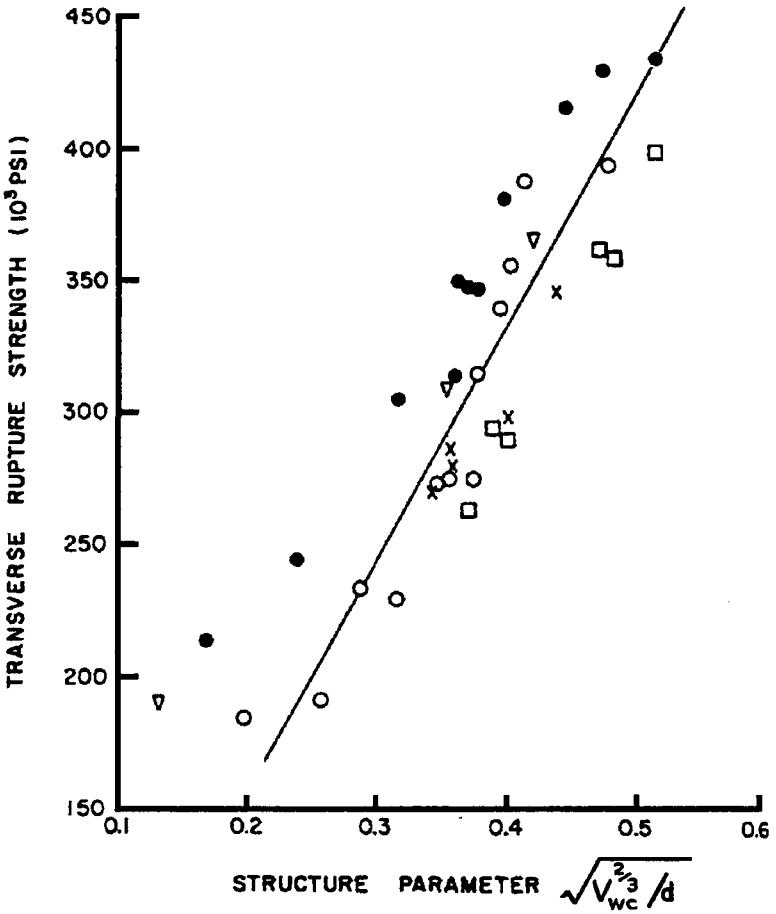


Figure 2.34. Transverse rupture strength as a function of degree of separation in WC-Co (64). Compositions are listed in wt.%.



∇ : 50% WC
• : 63% WC
□: 69% WC
o : 75% WC
x : 81% WC

Figure 2.35. Transverse rupture strength as a function of structure parameter in WC-Co (64). Compositions are listed in wt.%.

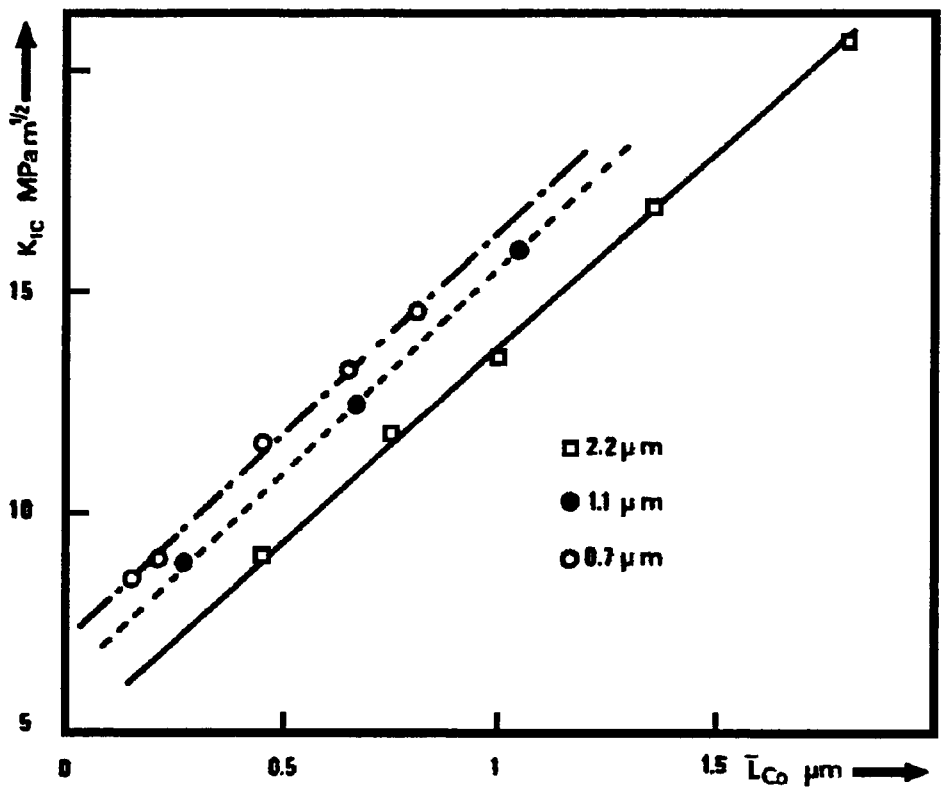


Figure 2.36. Fracture toughness as a function of cobalt mean free path and carbide grain size in WC-Co (65).

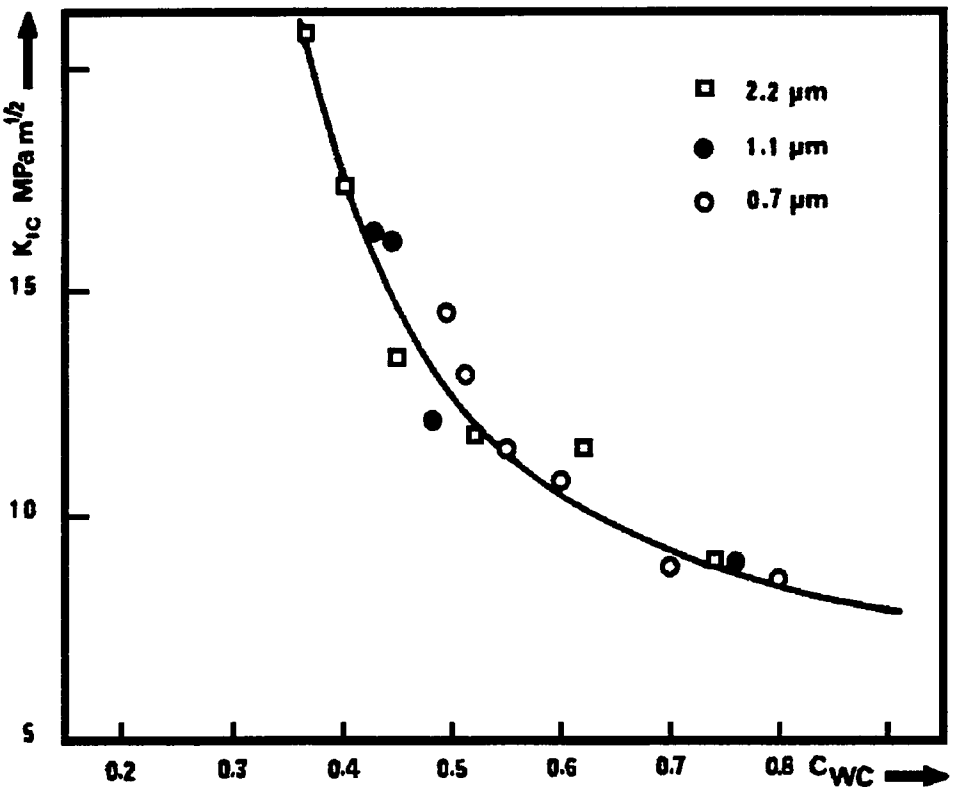


Figure 2.37. Fracture toughness as a function of contiguity and carbide grain size in WC-Co (65).

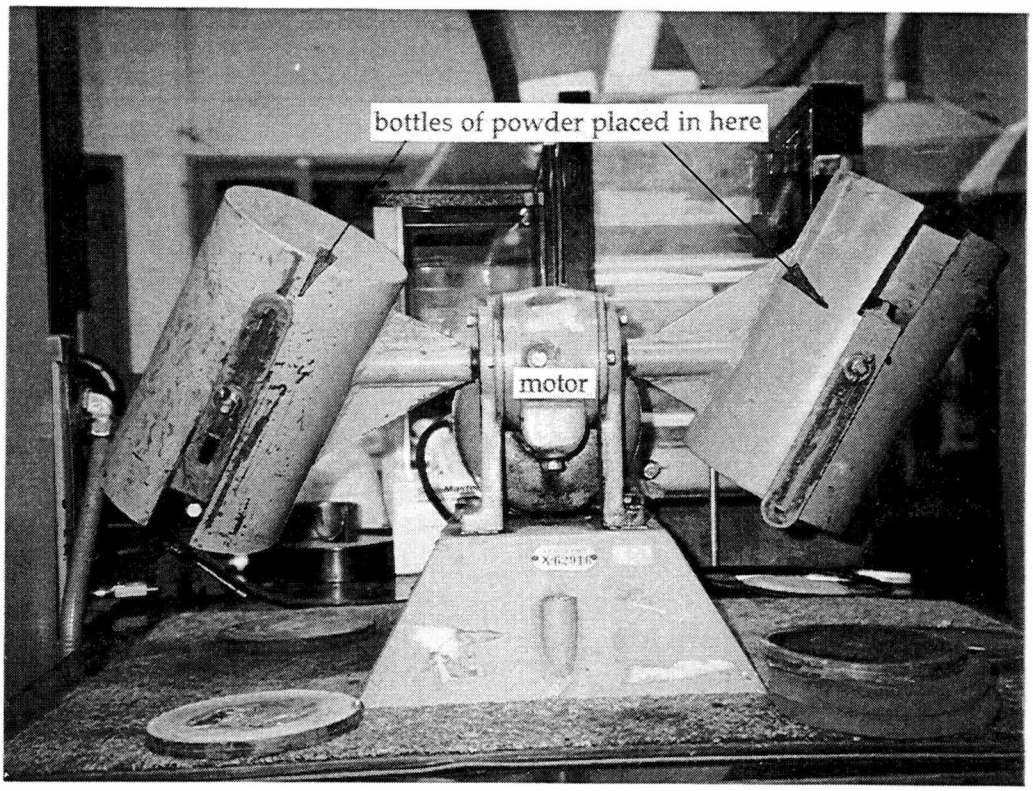


Figure 3.1. Oblique blenders used during wet-blending.

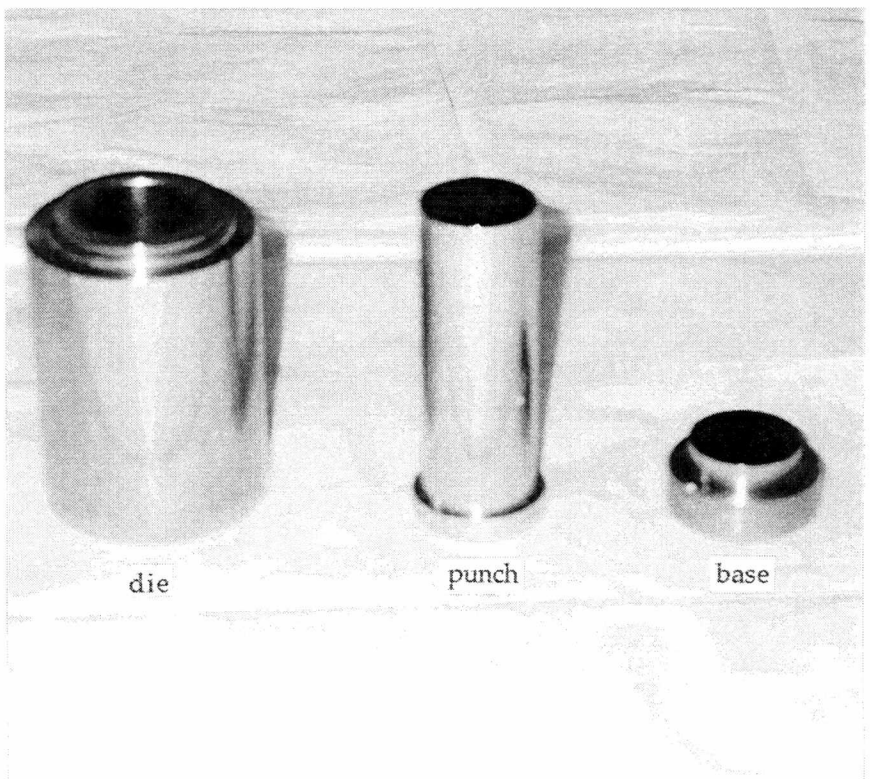


Figure 3.2. Die, punch, and base used during axial compaction of powders.

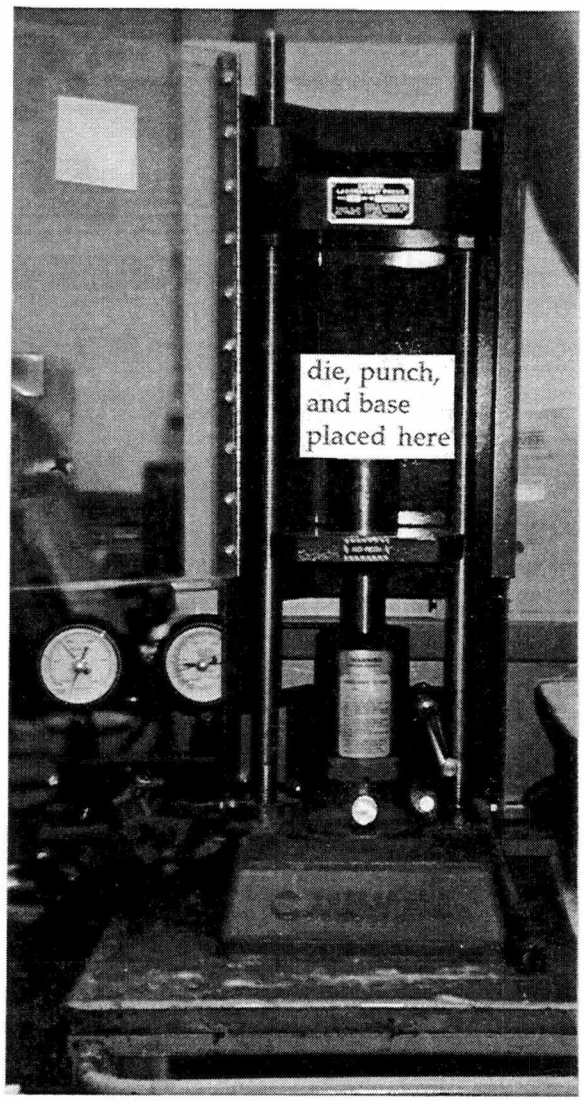


Figure 3.3. Hydraulic press used during axial compaction of powders.

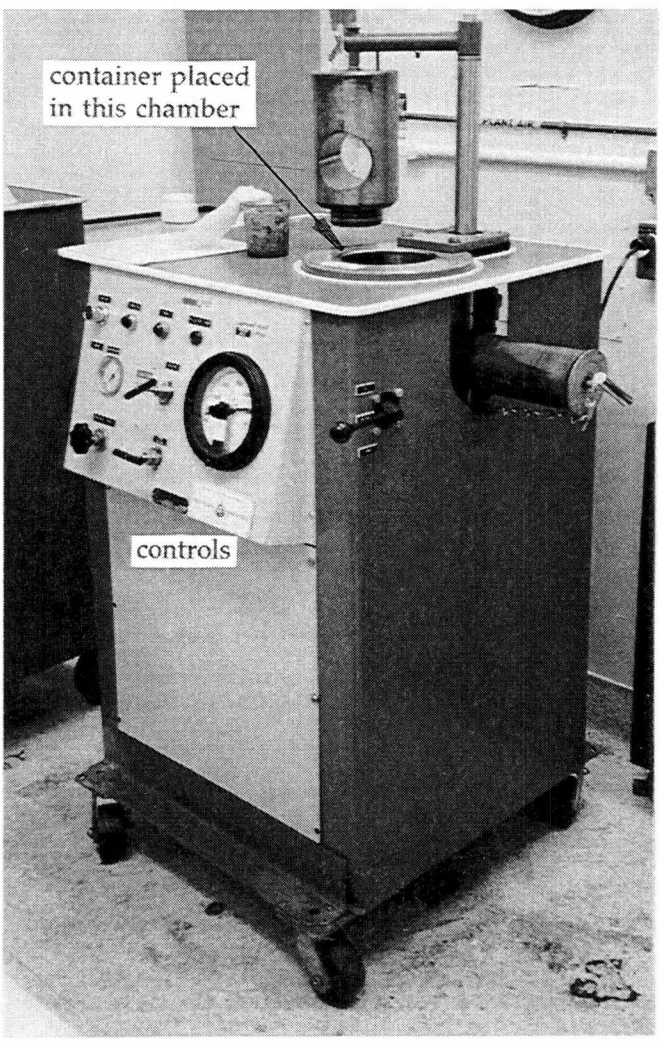


Figure 3.4. Pressure vessel used during cold isostatic compaction of powders.

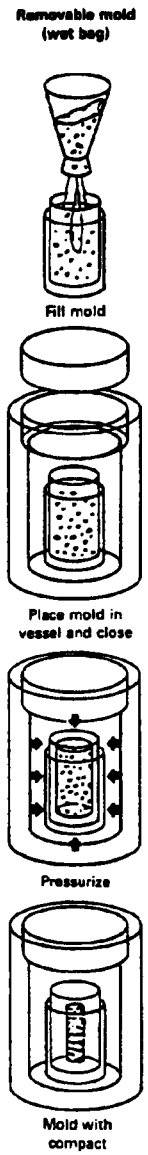


Figure 3.5. Schematic diagram illustrating steps involved in wetbag isostatic compaction of powders (78).

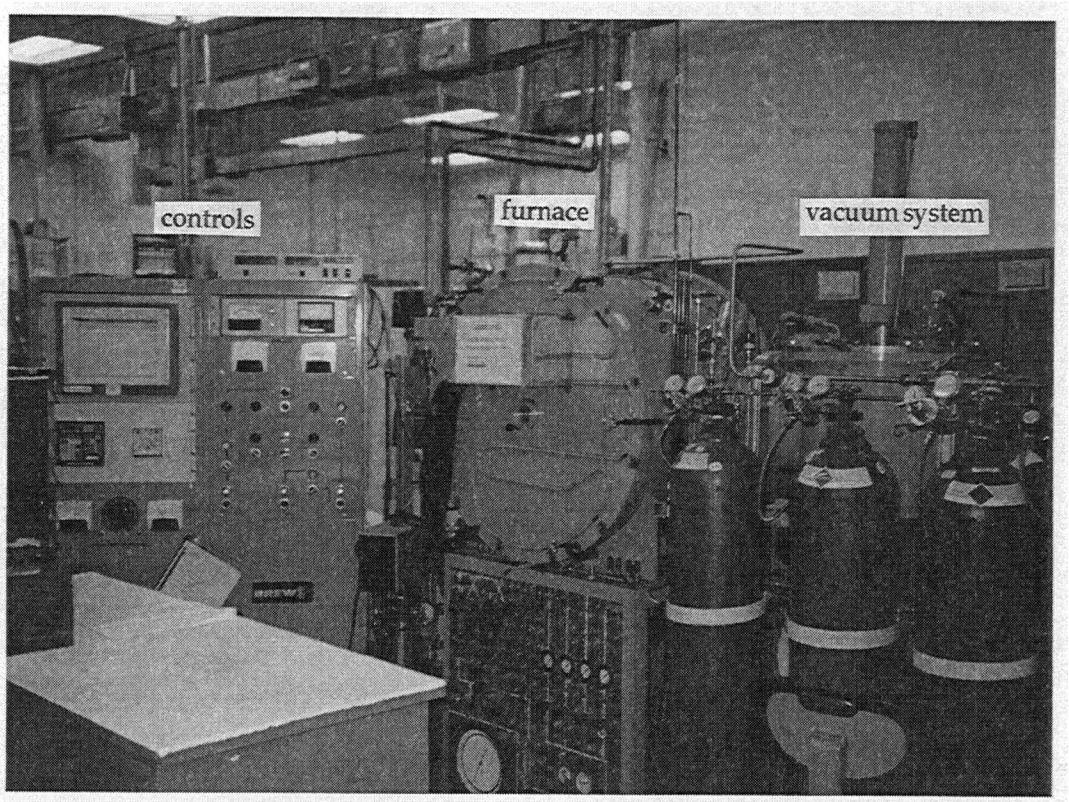


Figure 3.6. Batch-type vacuum furnace used for sintering of IBC composites.

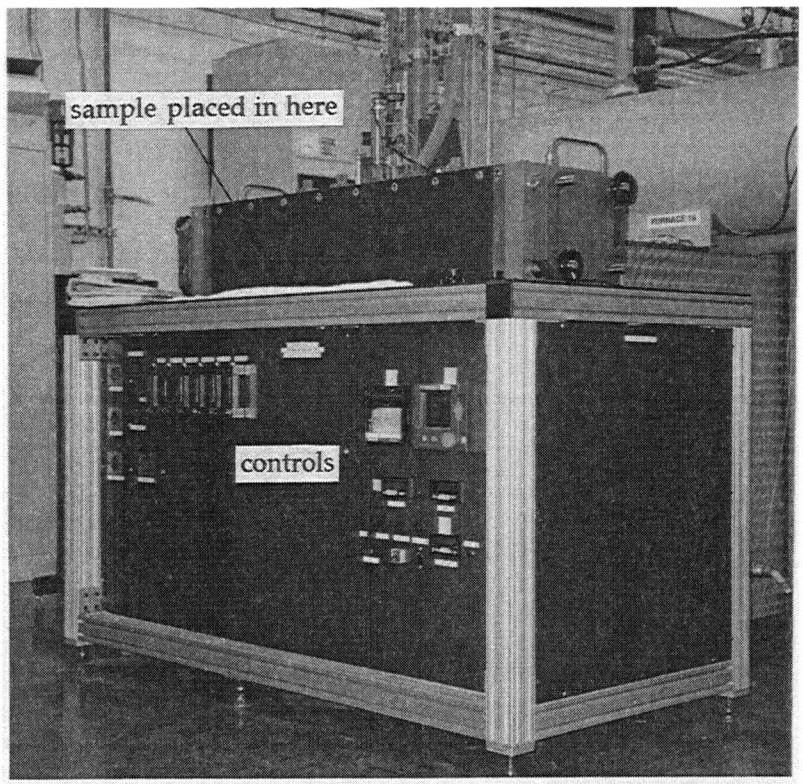


Figure 3.7. Vacuum furnace used for hot isostatic compaction of IBC composites.

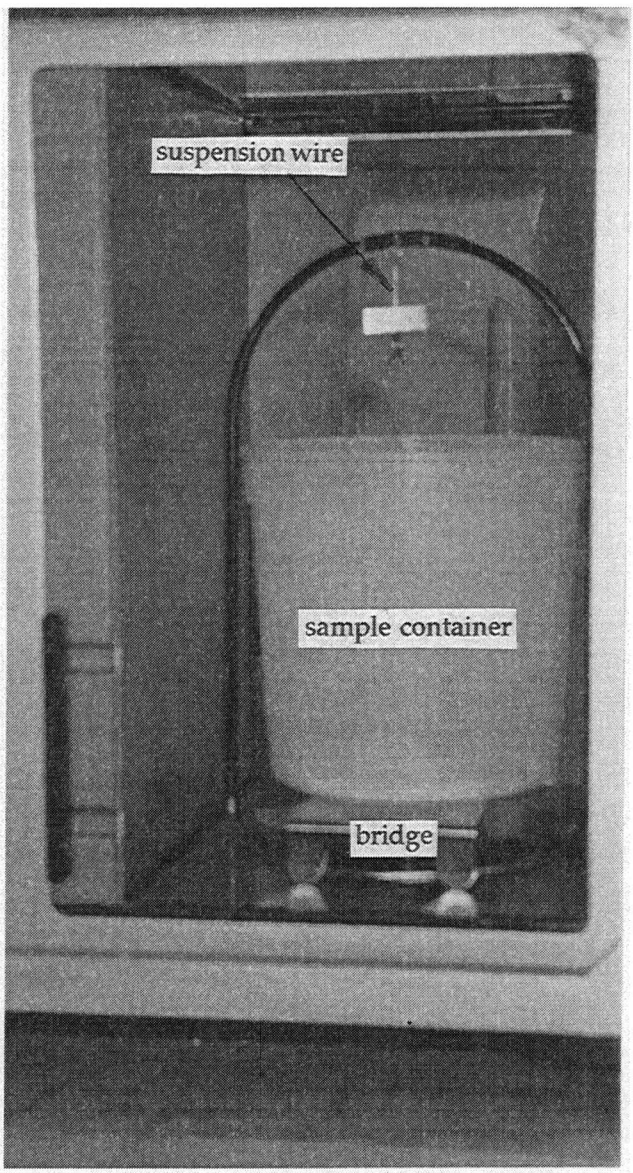


Figure 3.8. Apparatus used for measuring Archimedes density of IBC composites.

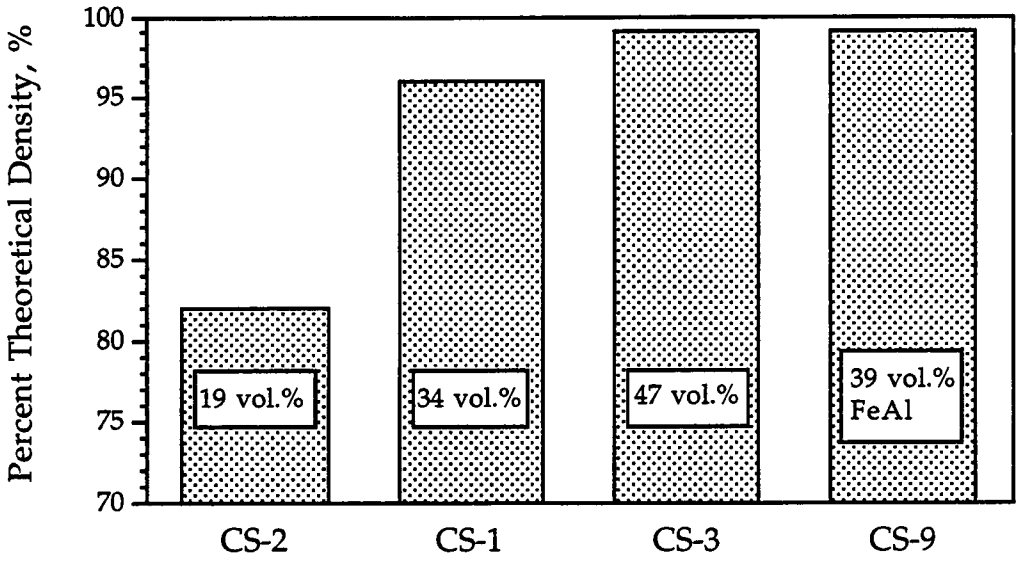


Figure 4.1. Effect of binder content on percent theoretical density at a sintering temperature of 1550°C. The CS-1, -2, and -3 composites contain Ni_3Al. Each of the composites contains WC having an average particle size of 2.3 μm.

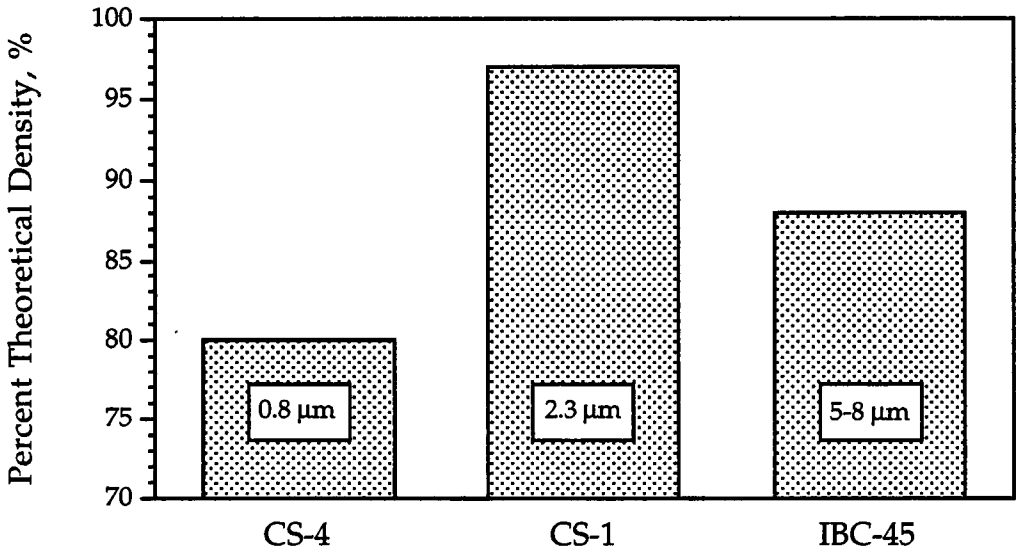


Figure 4.2. Effect of carbide size on percent theoretical density at a sintering temperature of 1600°C. Each of the composites contains WC and 34 vol.% of the IC-50 Ni_3Al binder.

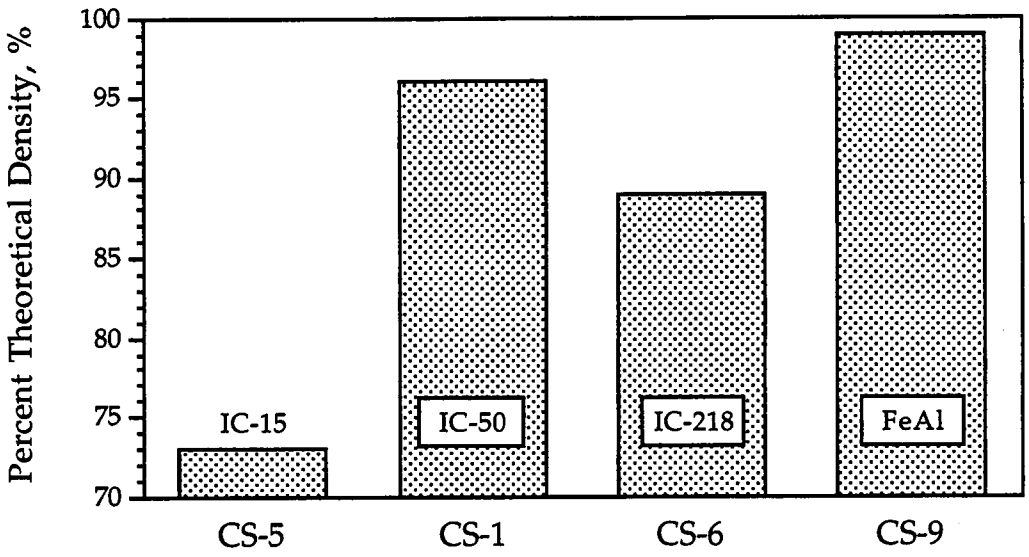


Figure 4.3. Effect of binder type on percent theoretical density at a sintering temperature of 1550°C. Each composite contains WC having an average particle size of 2.3 μm. The binder content for CS-1, -5, and -6 is 34 vol.% and 39 vol.% for CS-9.

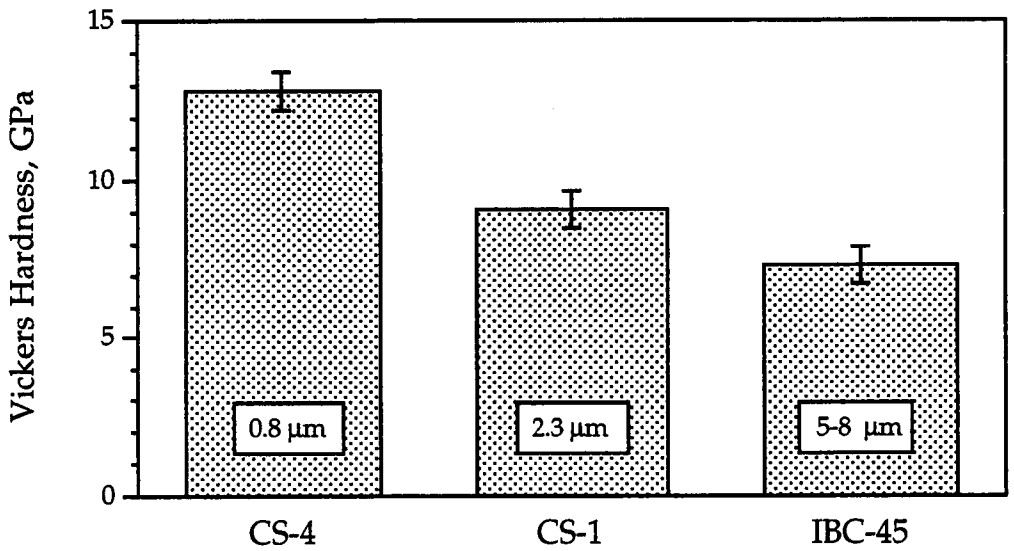


Figure 4.4. Effect of carbide size on Vickers hardness at a sintering temperature of 1500°C. Each of the composites contains WC and 34 vol.% of the IC-50 Ni_3Al binder.

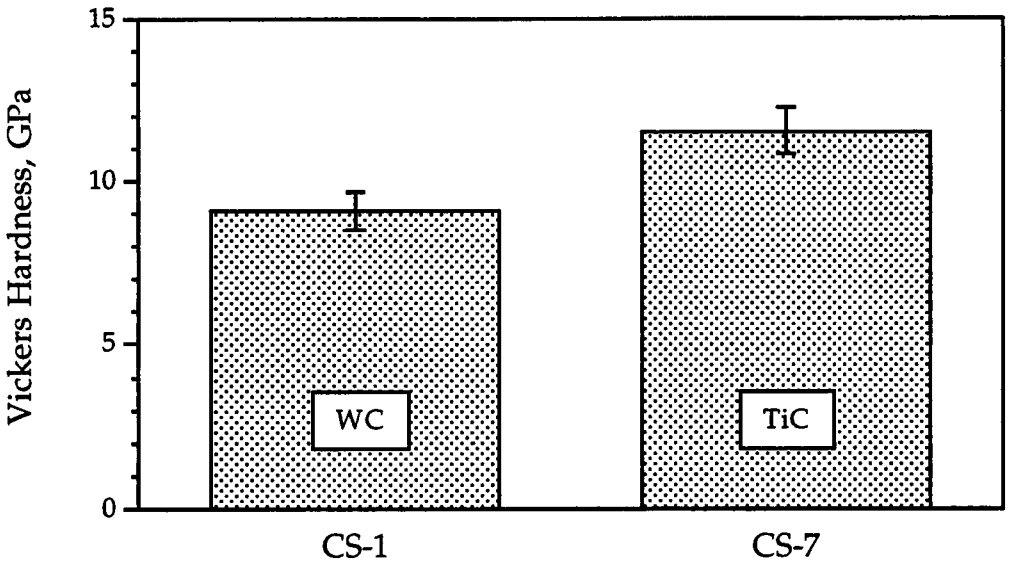


Figure 4.5. Effect of carbide type on Vickers hardness at a sintering temperature of 1500°C. Both composites contain 34 vol.% of the IC-50 Ni_3Al binder and have similar carbide particle sizes.

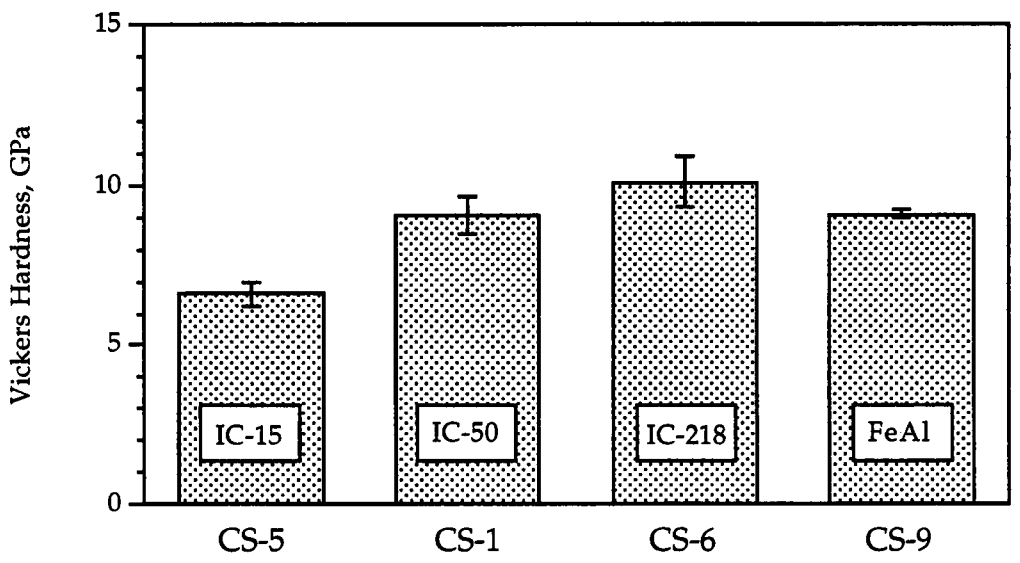


Figure 4.6. Effect of binder type on Vickers hardness at a sintering temperature of 1500°C. Each composite contains WC having an average particle size of 2.3 μm. The binder content for CS-1, -5, and -6 is 34 vol.% and 39 vol.% for CS-9.

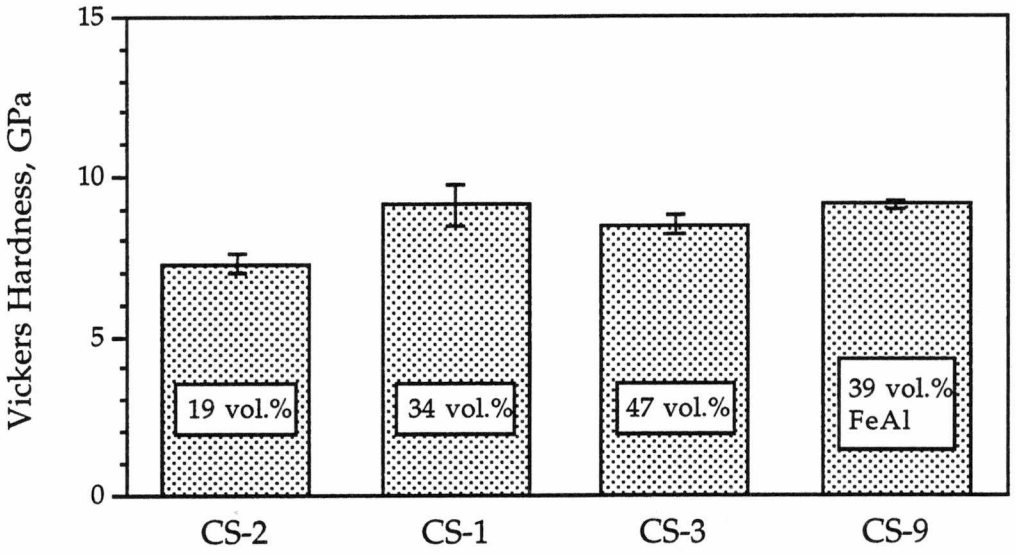


Figure 4.7. Effect of binder content on Vickers hardness at a sintering temperature of 1550°C. The CS-1, -2, and -3 composites contain Ni_3Al. Each of the composites contains WC having an average particle size of 2.3 μm.

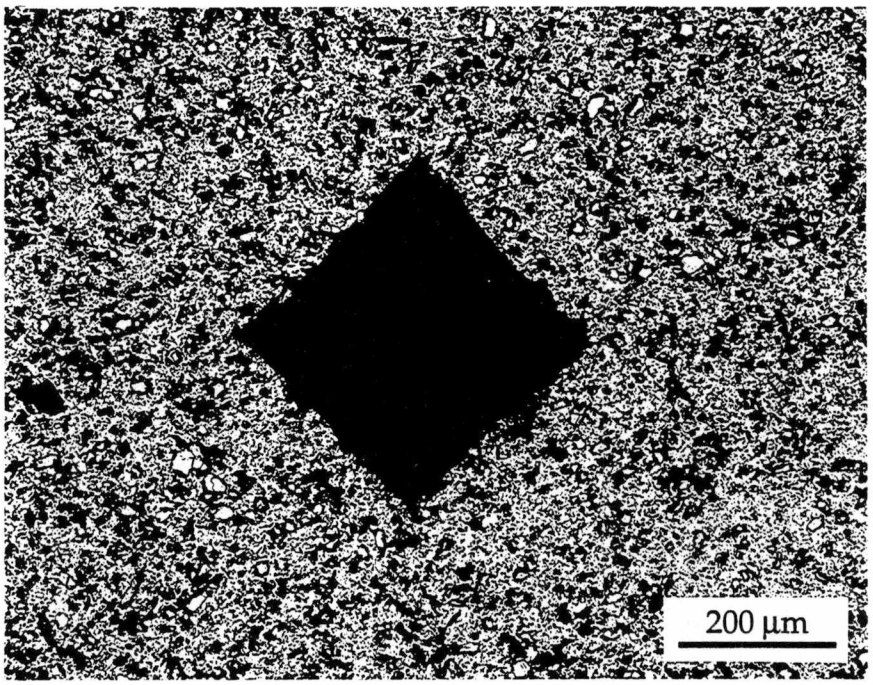


Figure 4.8. Polished surface of CS 5-3. Black spots indicate large amount of porosity. CS 5-3 attained only 73% theoretical density.

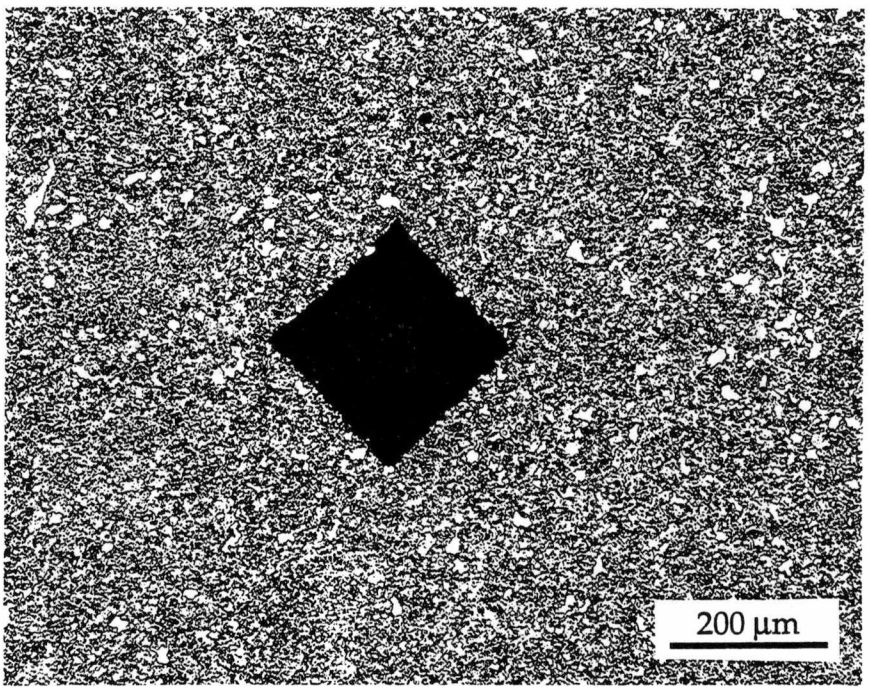


Figure 4.9. Polished surface of CS 3-1. Absence of black spots indicate no porosity is present. CS 3-1 attained 99.9% theoretical density.

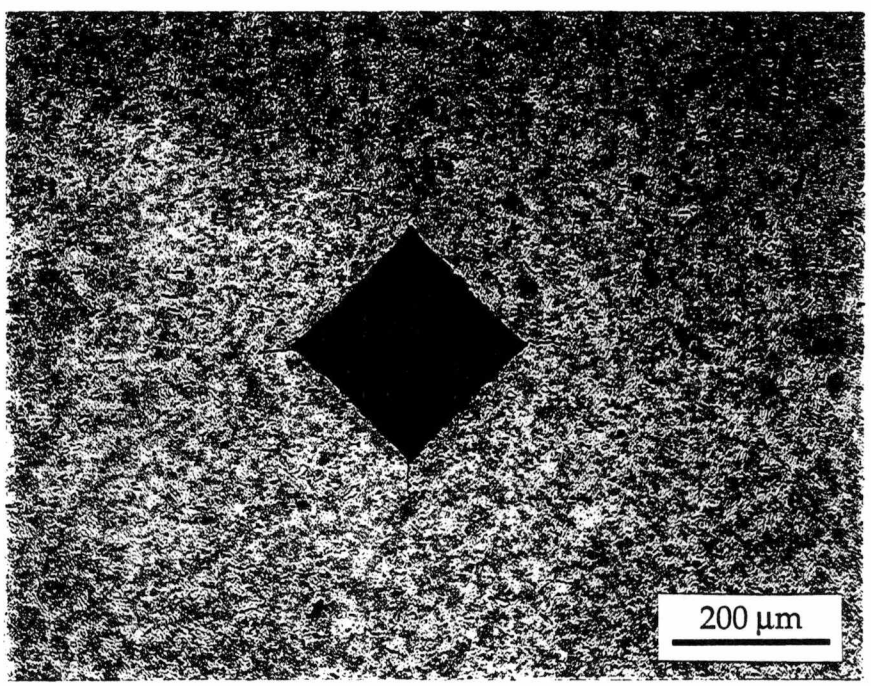


Figure 4.10. Polished surface of CS 9-1. Small amount of black spots are present indicating little porosity. CS 9-1 attained 98.5% theoretical density.

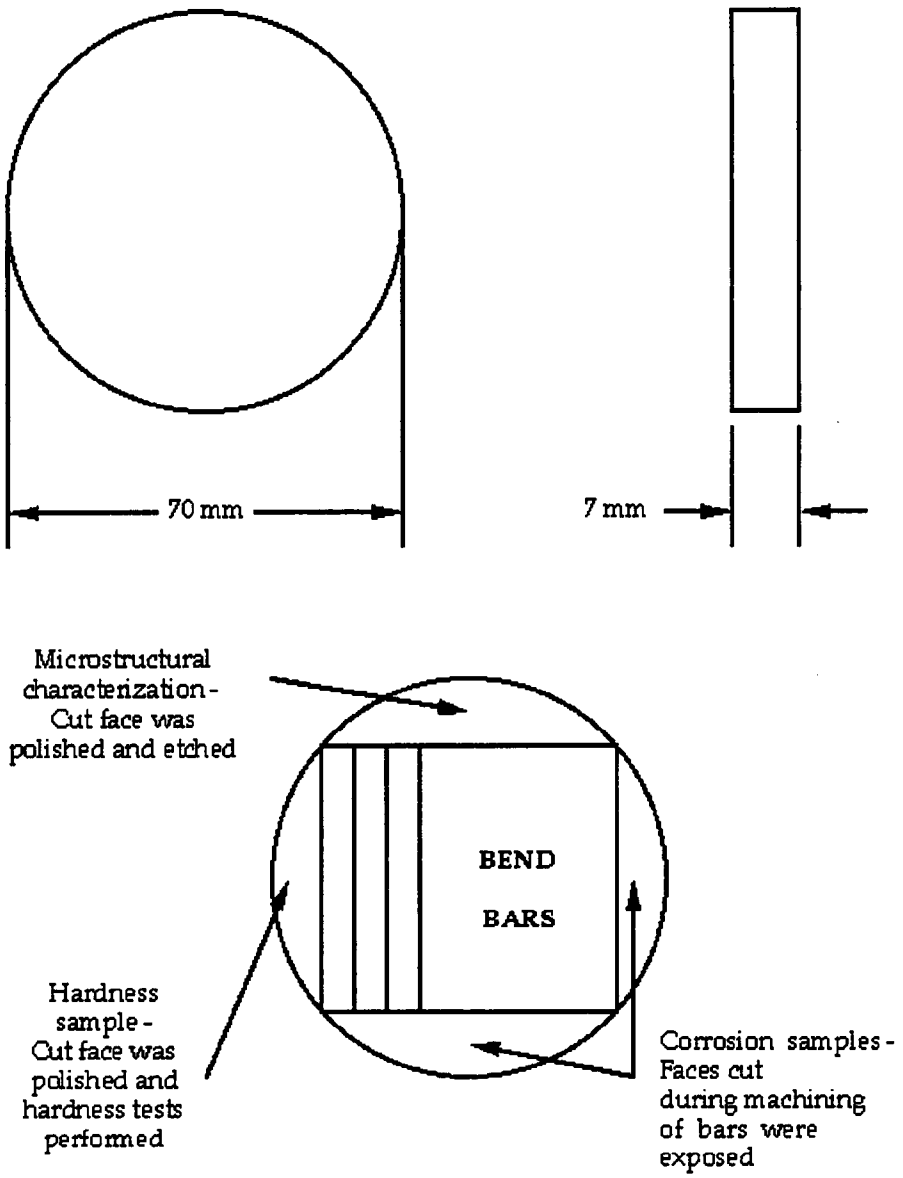


Figure 5.1. Schematic diagram illustrating the tests performed on each disk portion.

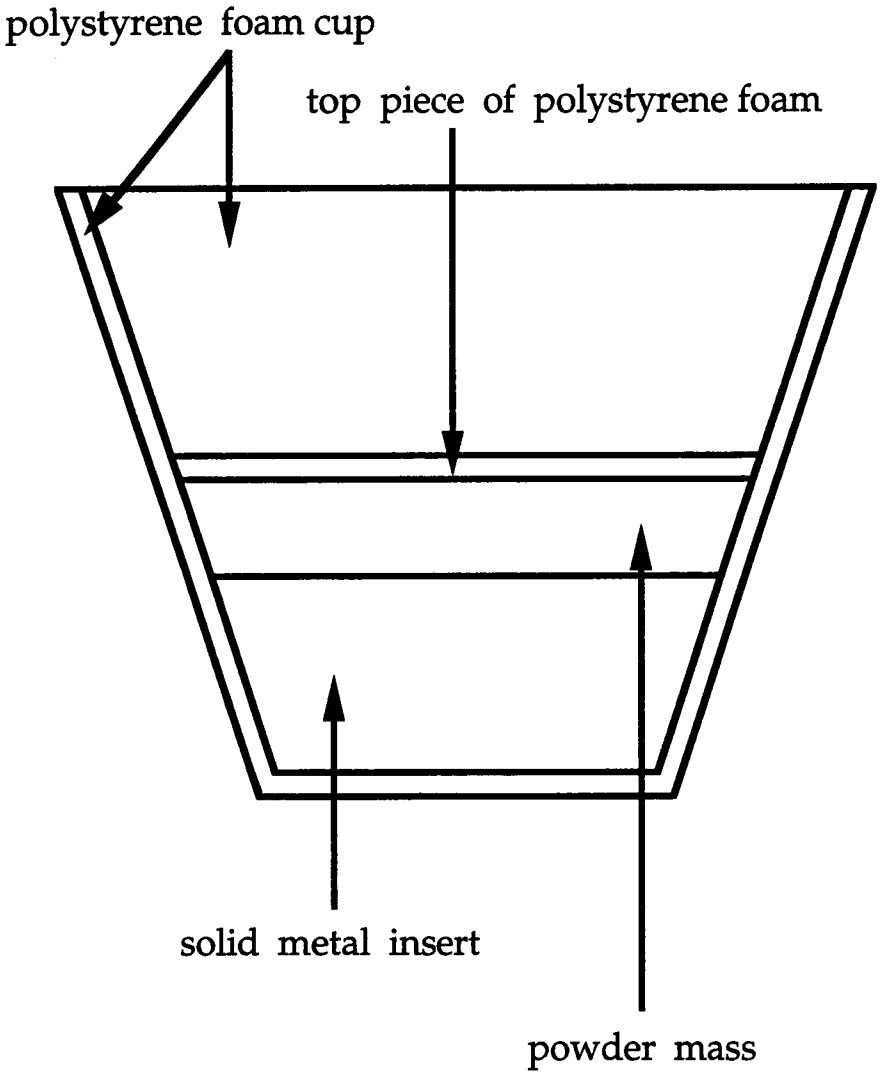


Figure 5.2. Schematic diagram illustrating the polystyrene foam container and metal filler insert used in the cold isostatic compaction of selected IBC composites.

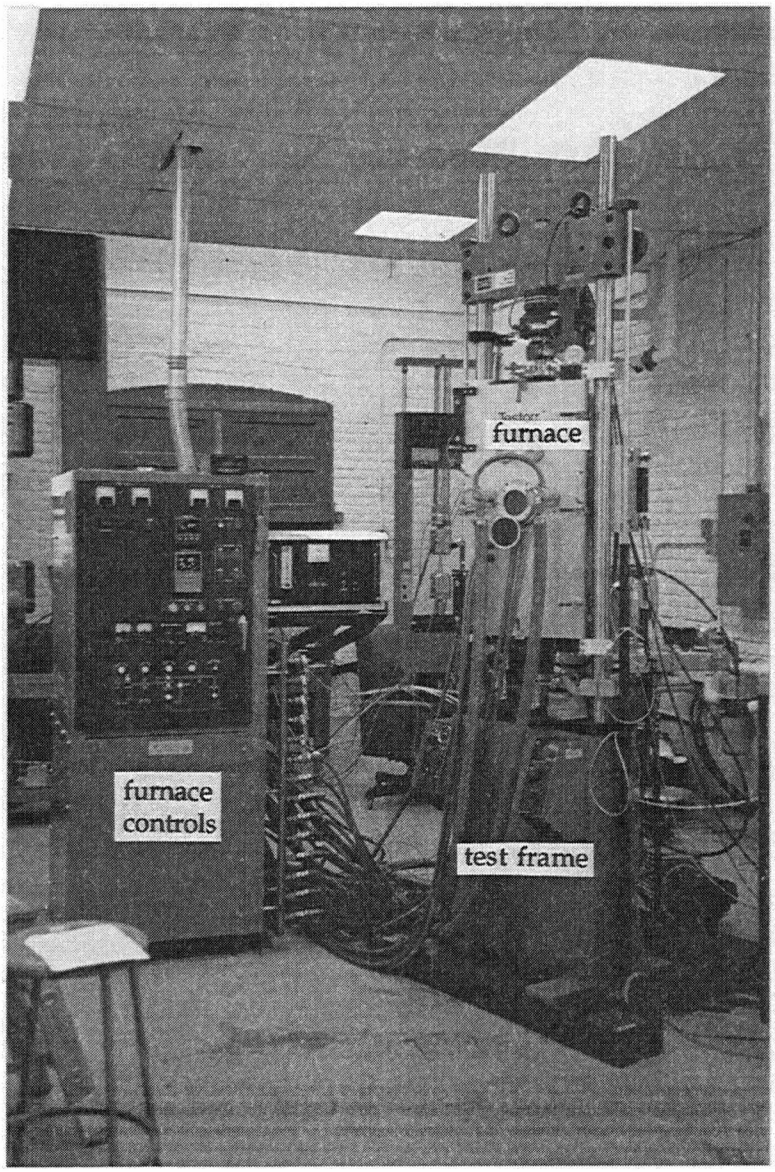


Figure 5.3. MTS electro-hydraulic testing frame and Centorr vacuum furnace used in the room- and high-temperature flexure testing.

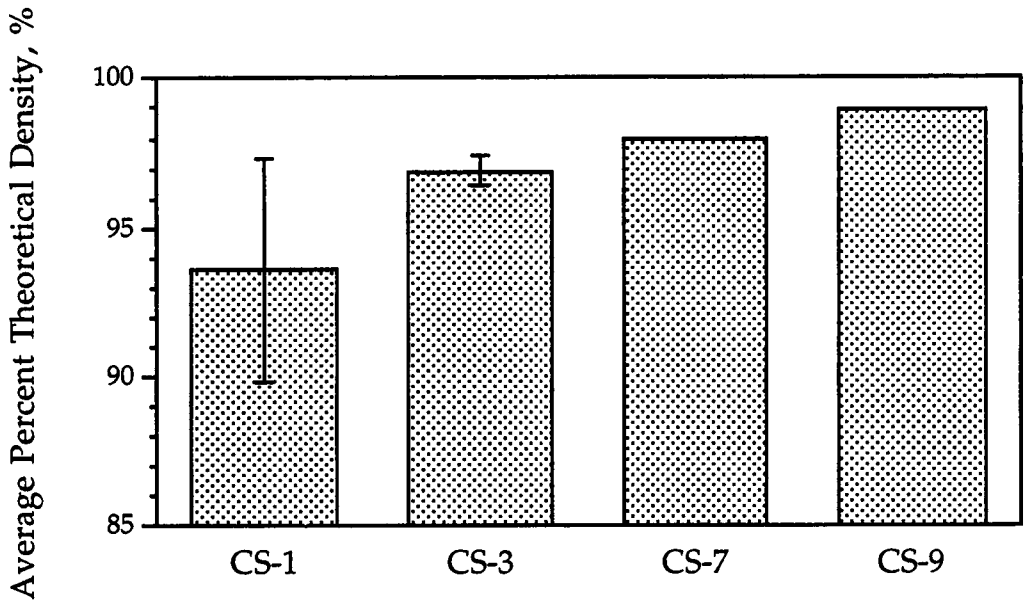


Figure 6.1. Final average percent theoretical densities as a function of composition.

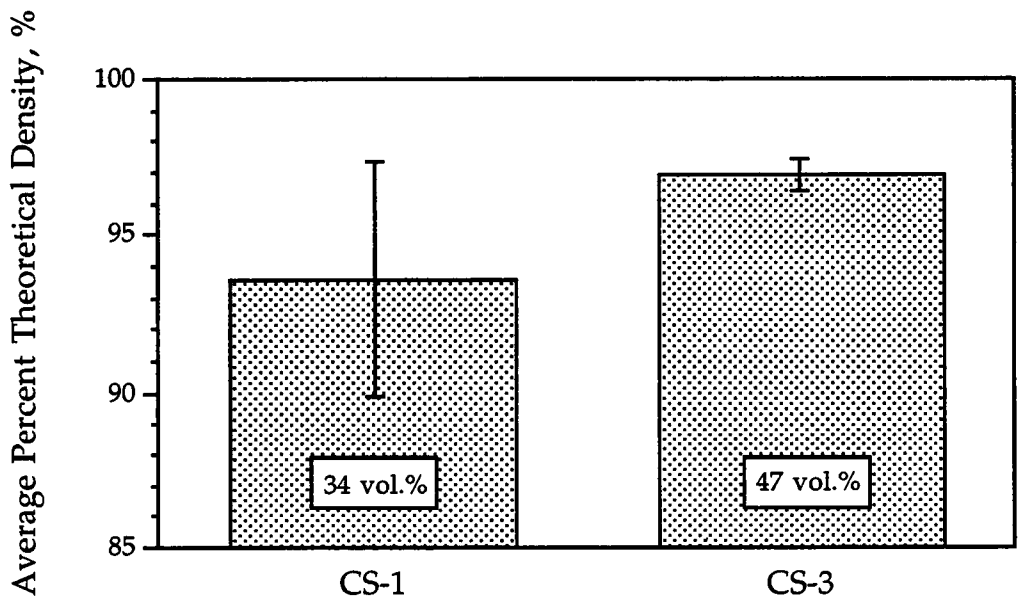


Figure 6.2. Effect of binder content on final average percent theoretical densities for selected IBC composites. Both composites contain WC having an average particle size of 2.3 μm.

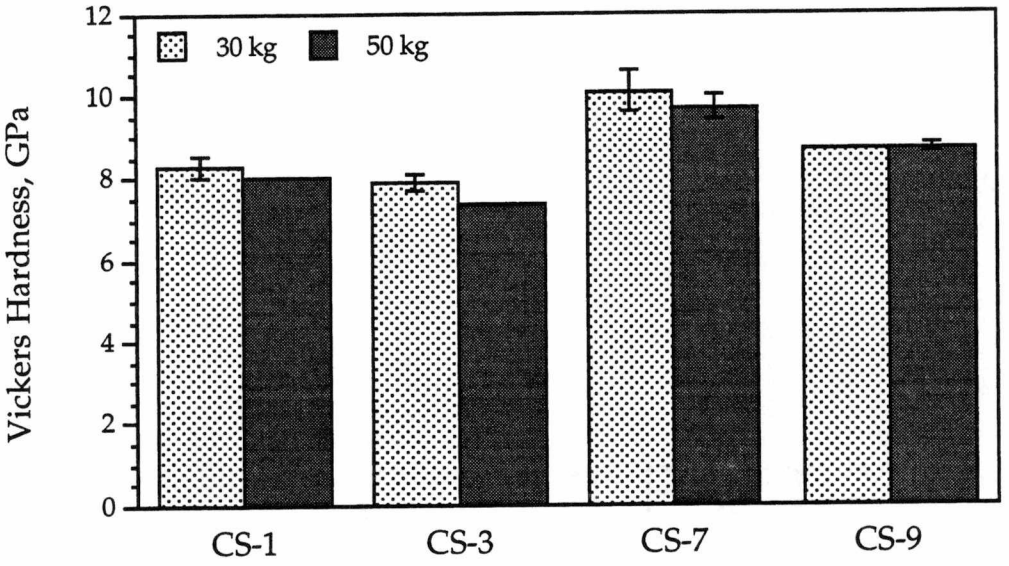


Figure 6.3. Vickers hardness as a function of composition and indent load.

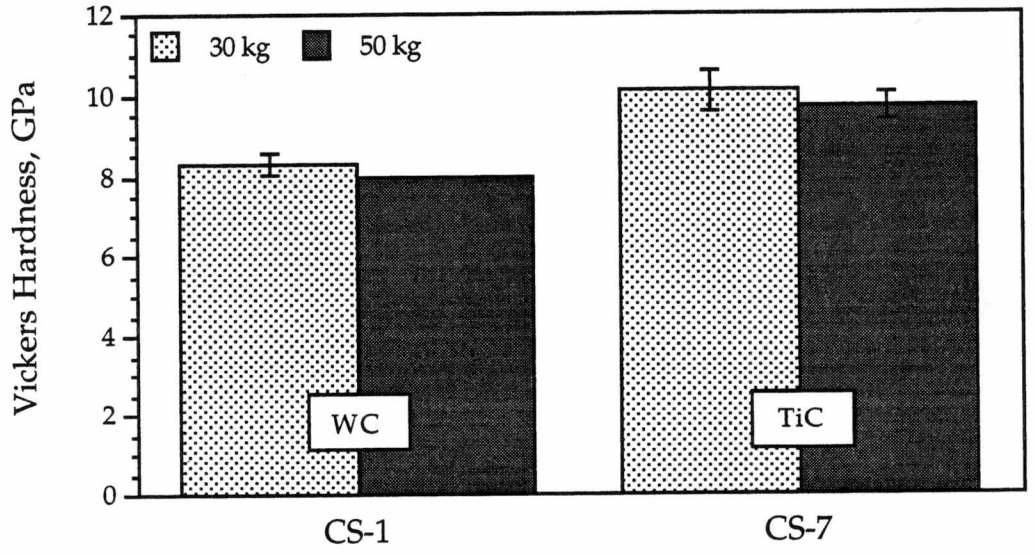


Figure 6.4. Effect of carbide type and indent load on Vickers hardness for selected IBC composites. Both composites contain 34 vol.% of the IC-50 Ni_3Al binder and have similar carbide particle sizes.

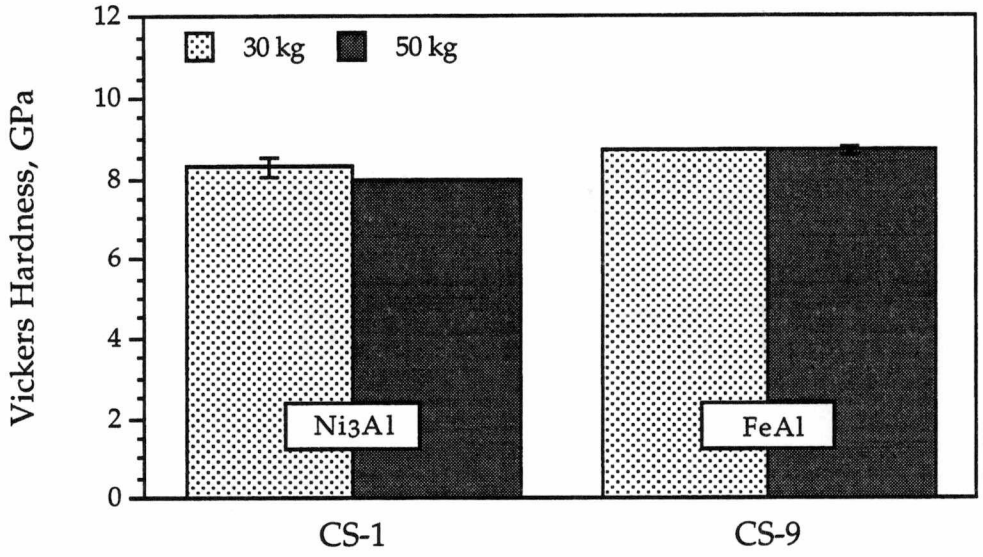


Figure 6.5. Effect of binder type and indent load on Vickers hardness for selected IBC composites. Both composites contain WC with an average particle size of 2.3 μm. The binder content for CS-1 is 34 vol.% and 39 vol.% for CS-9.

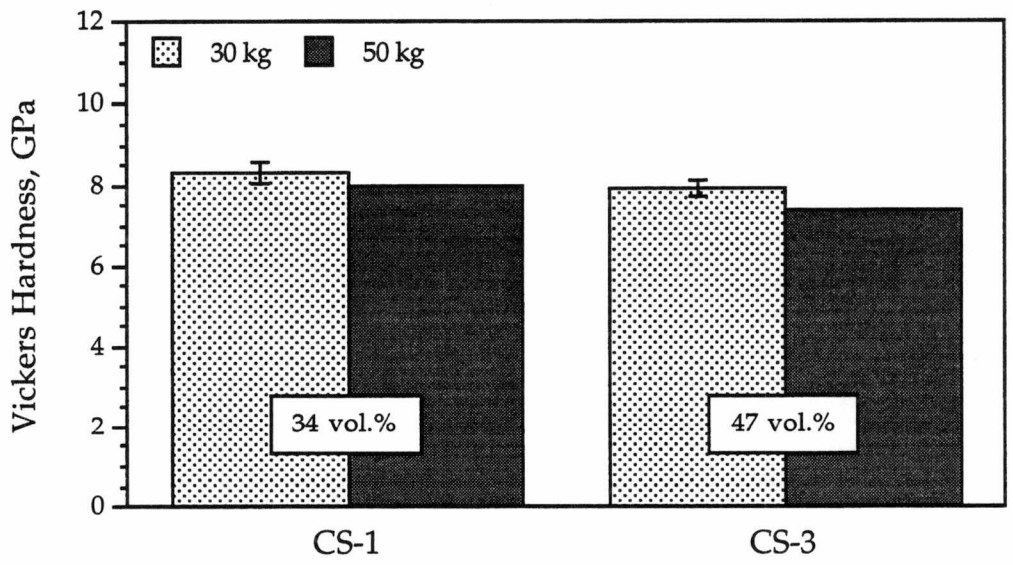


Figure 6.6. Effect of binder content and indent load on Vickers hardness for selected IBC composites. Both composites contain WC having an average particle size of 2.3 μm and the same IC-50 Ni_3Al binder.

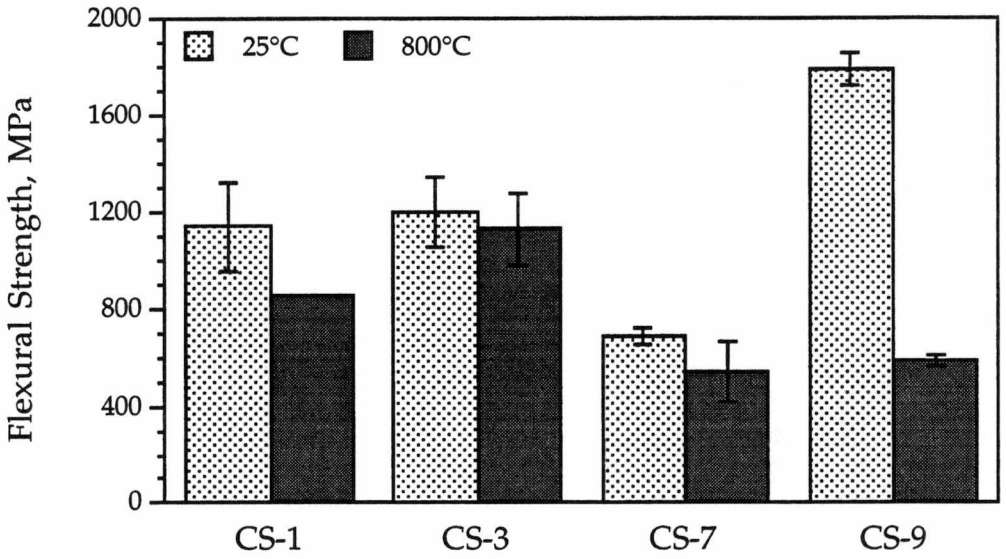


Figure 6.7. Flexural strength as a function of composition and temperature. Note that high-temperature strength values for CS-9 are invalid. Also note that only one high-temperature strength value was obtained for CS-1.

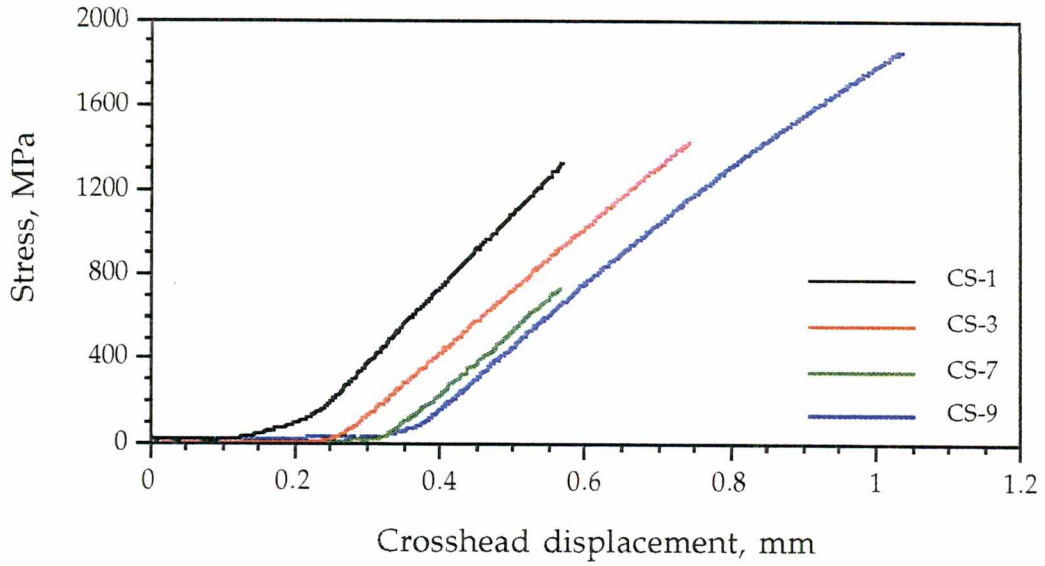


Figure 6.8. Typical stress versus crosshead displacement curves obtained at room temperature.

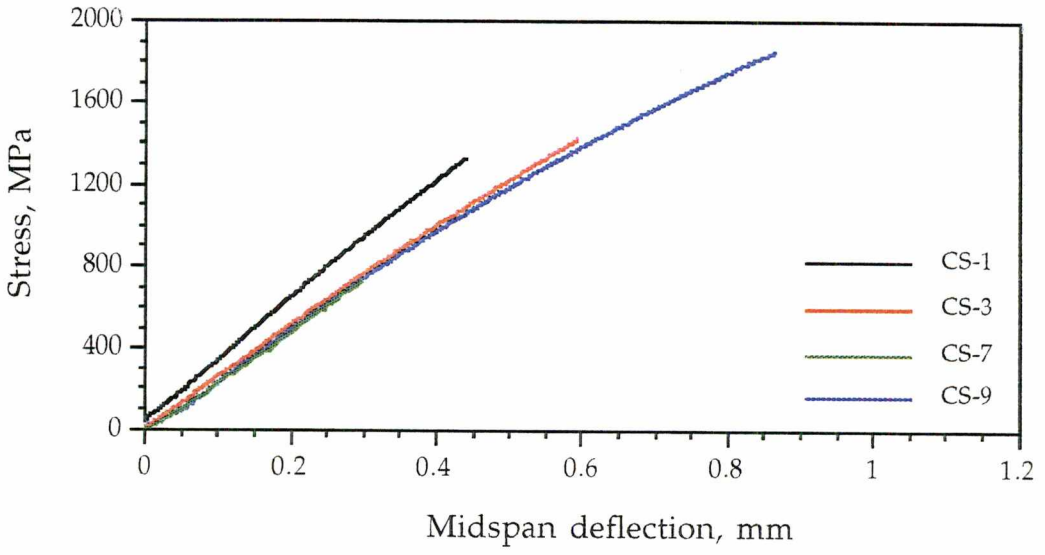


Figure 6.9. Typical stress versus midspan deflection curves obtained at room temperature.

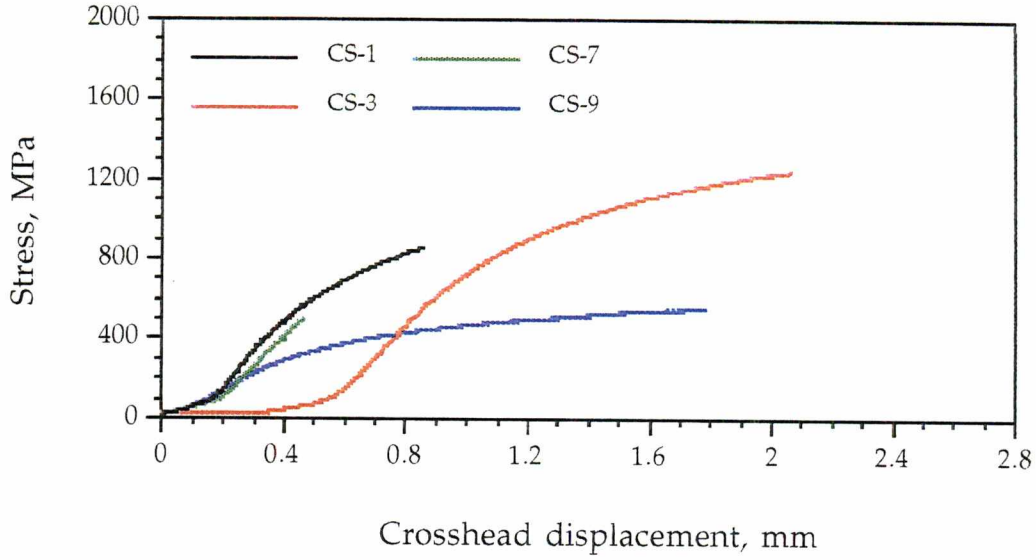


Figure 6.10. Typical stress versus crosshead displacement curves obtained at 800°C.

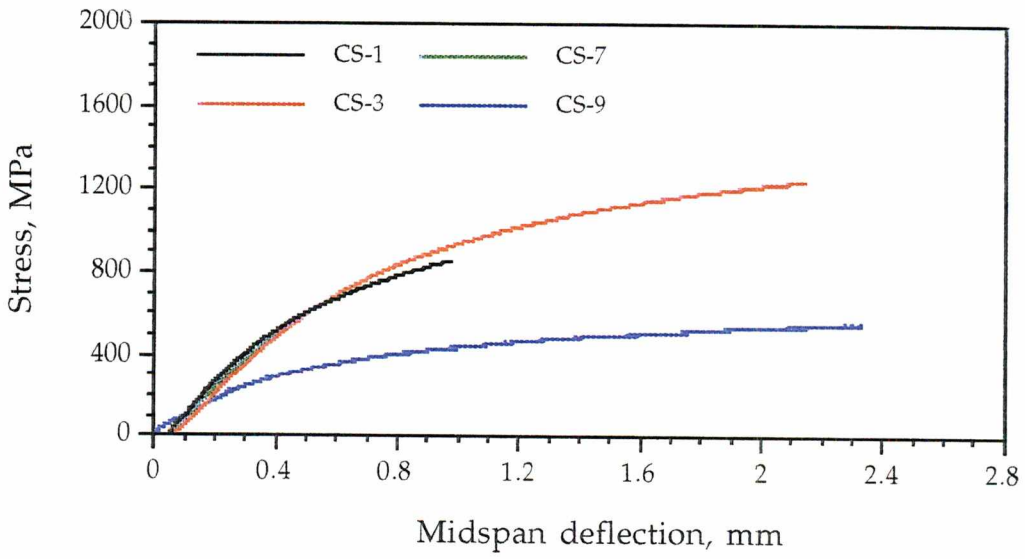


Figure 6.11. Typical stress versus midspan deflection curves obtained at 800°C.

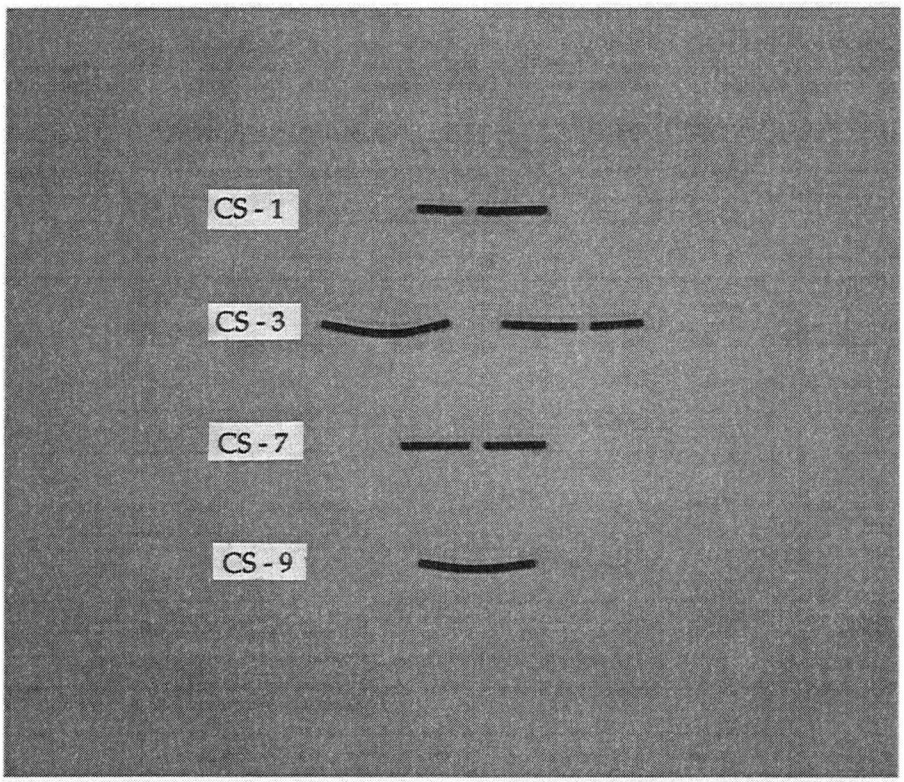


Figure 6.12. Plastic deformation of flexure bars at 800°C.

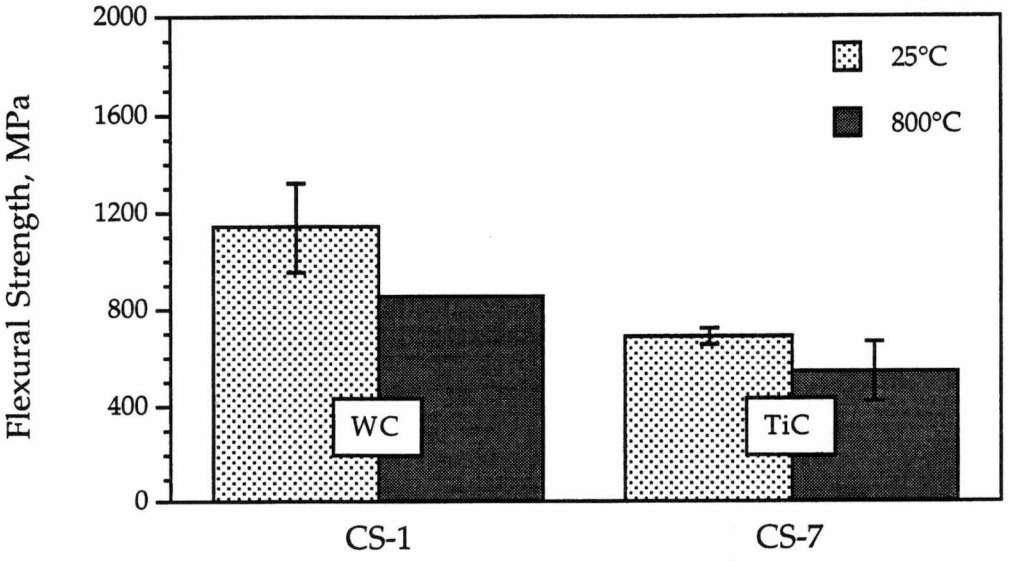


Figure 6.13. Effect of carbide type and temperature on flexural strength for selected IBC composites. Both composites contain 34 vol.% of the IC-50 Ni_3Al and have similar carbide particle sizes.

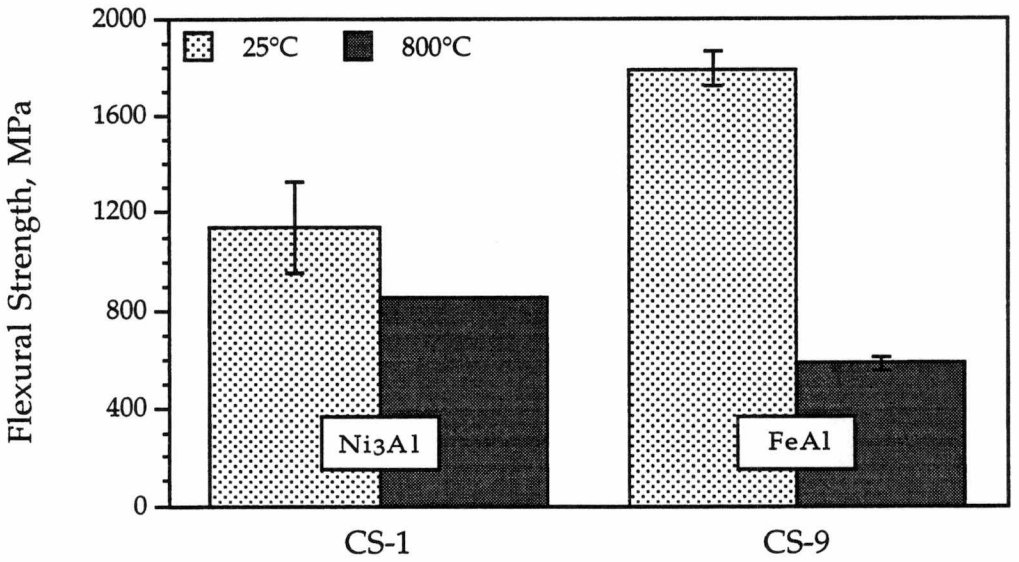


Figure 6.14. Effect of binder type and temperature on flexural strength for selected IBC composites. Both composites contain WC having an average particle size of 2.3 μm. The binder content for CS-1 is 34 vol.% and 39 vol.% for CS-9. Note that the high-temperature strength values for CS-9 are invalid.

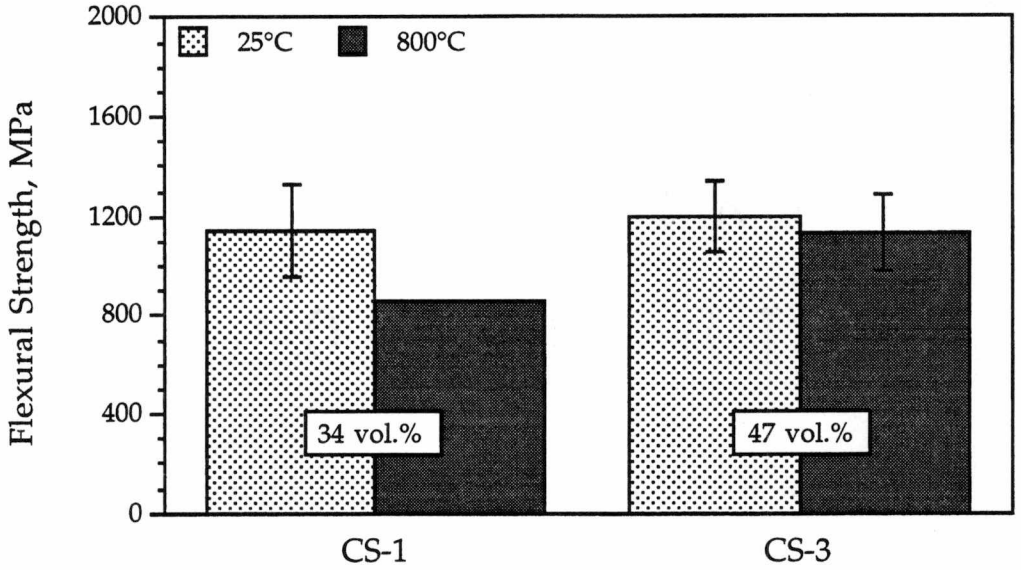


Figure 6.15. Effect of binder content and temperature on flexural strength for selected IBC composites. Both composites contain WC having an average particle size of 2.3 μm and the same IC-50 Ni_3Al binder.

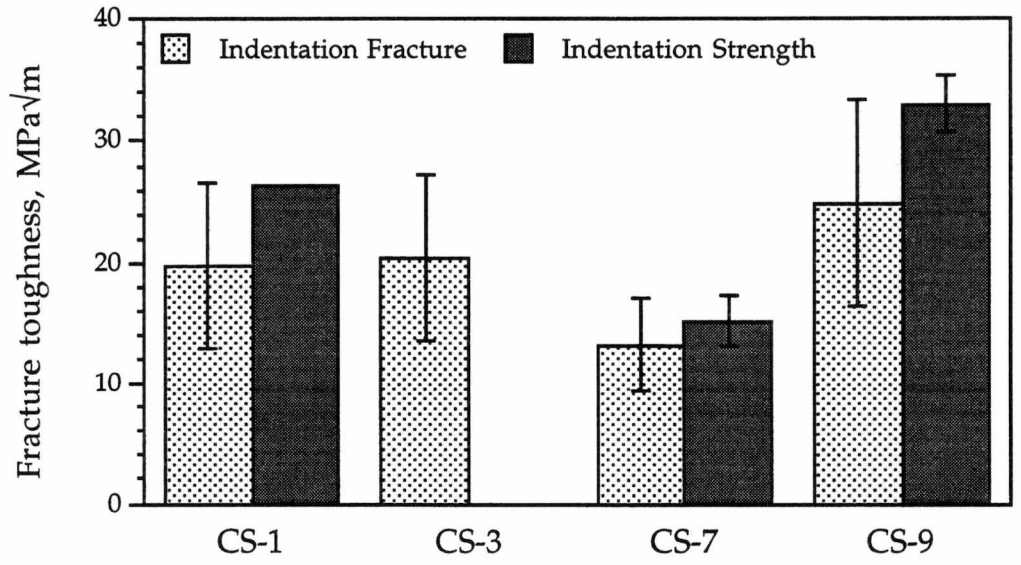


Figure 6.16. Fracture toughness as a function of composition and method. Note that only one K_{IC} value was obtained for CS-1 and no K_{IC} values were obtained for CS-3 using the indentation strength method.

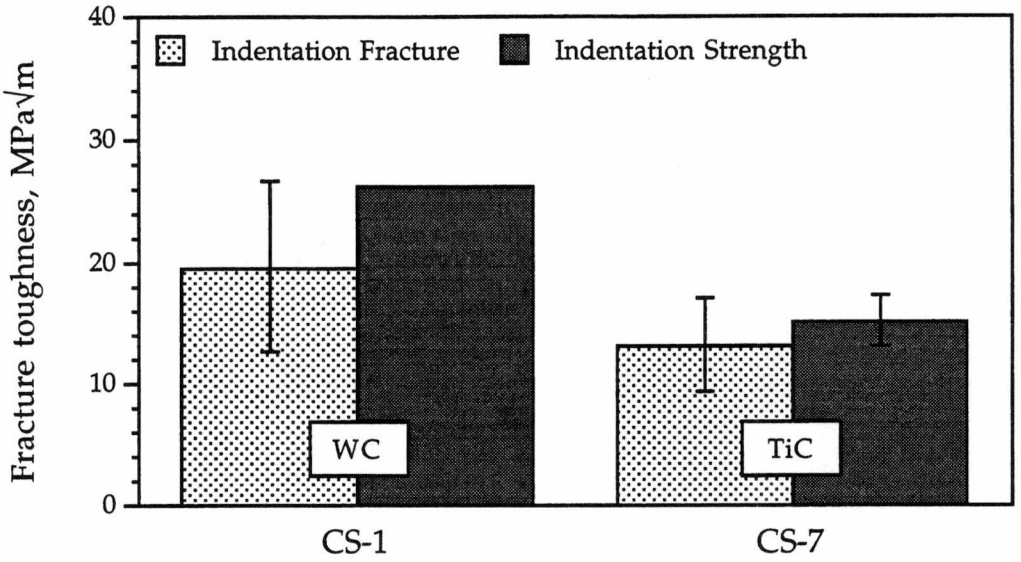


Figure 6.17. Effect of carbide type and method on fracture toughness for selected IBC composites. Both composites contain 34 vol.% of the IC-50 Ni_3Al binder and have similar carbide particle sizes. Note that only one K_{IC} value was obtained for CS-1 using the indentation strength method.

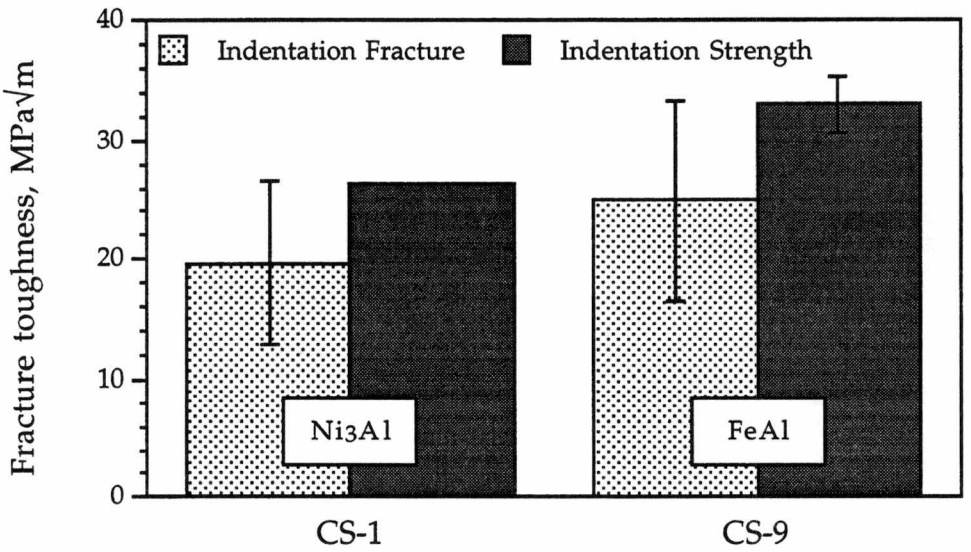


Figure 6.18. Effect of binder type and method on fracture toughness for selected IBC composites. Both composites contain WC having an average particle size of 2.3 μm. The binder content for CS-1 is 34 vol.% and 39 vol.% for CS-9. Note that only one K_{IC} value was obtained for CS-1 using the indentation strength method.

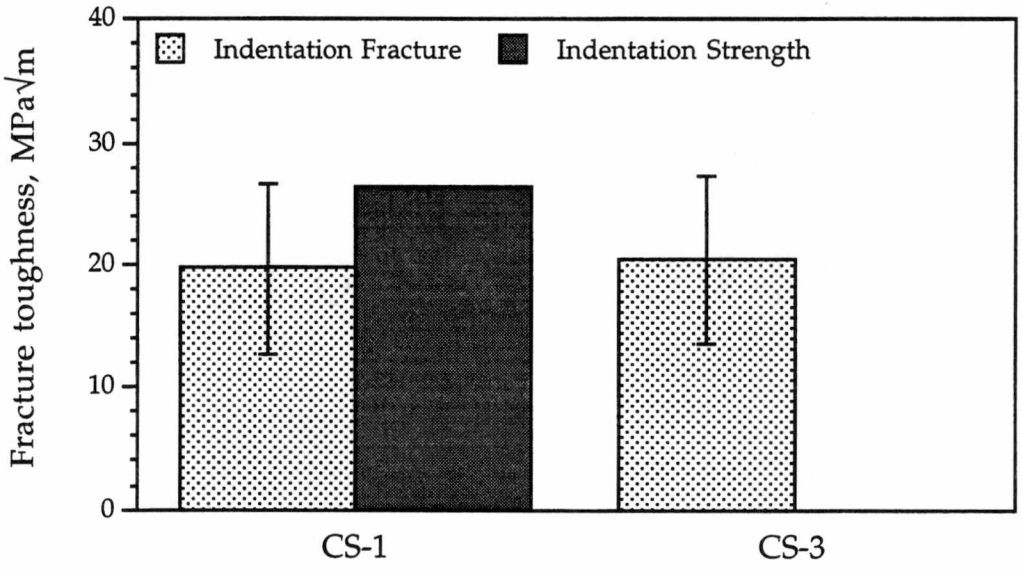


Figure 6.19. Effect of binder content and method on fracture toughness for selected IBC composites. Both composites contain WC having an average particle size of 2.3 μm and the same IC-50 Ni_3Al binder. Note that only one K_{IC} value was obtained for CS-1 and no K_{IC} values were obtained for CS-3 using the indentation strength method.

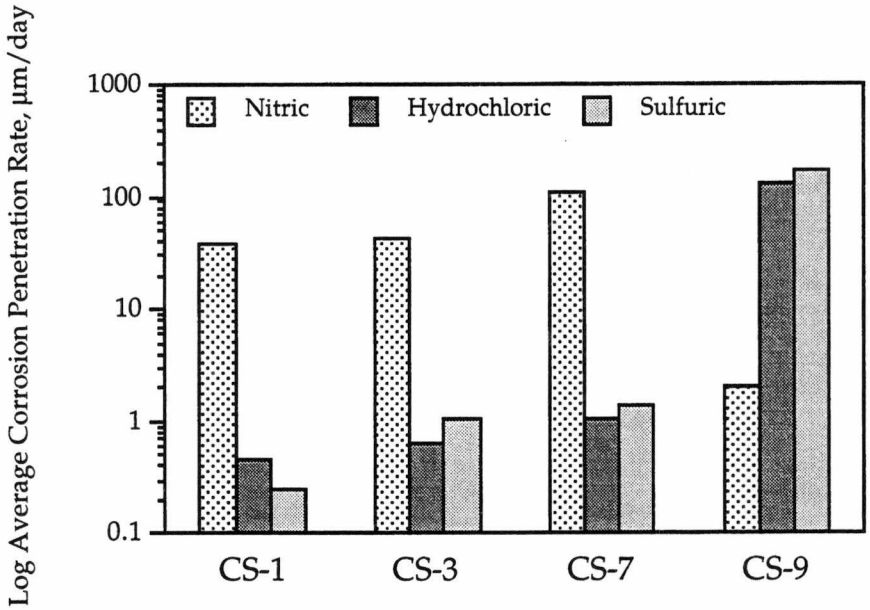


Figure 6.20. Average corrosion penetration rate as a function of composition and immersion acid for continuous tests. Tests were conducted for 96 hours at room-temperature.

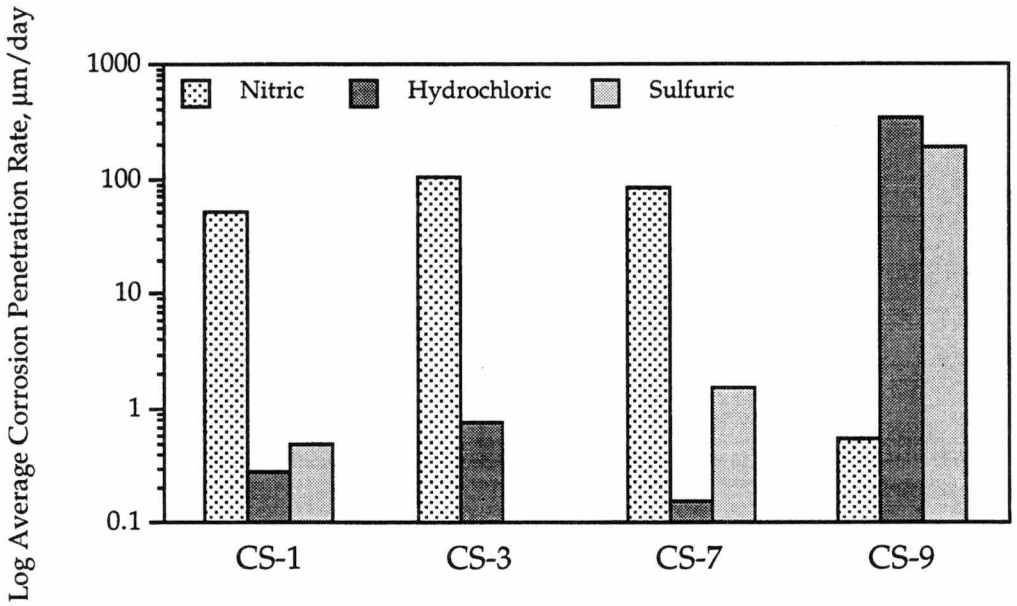


Figure 6.21. Average corrosion penetration rate as a function of composition and immersion acid for discontinuous tests. Tests were conducted for 96 hours at room-temperature. Note that the average CPR for CS-3 in sulfuric acid was less than 0.1 µm/day.

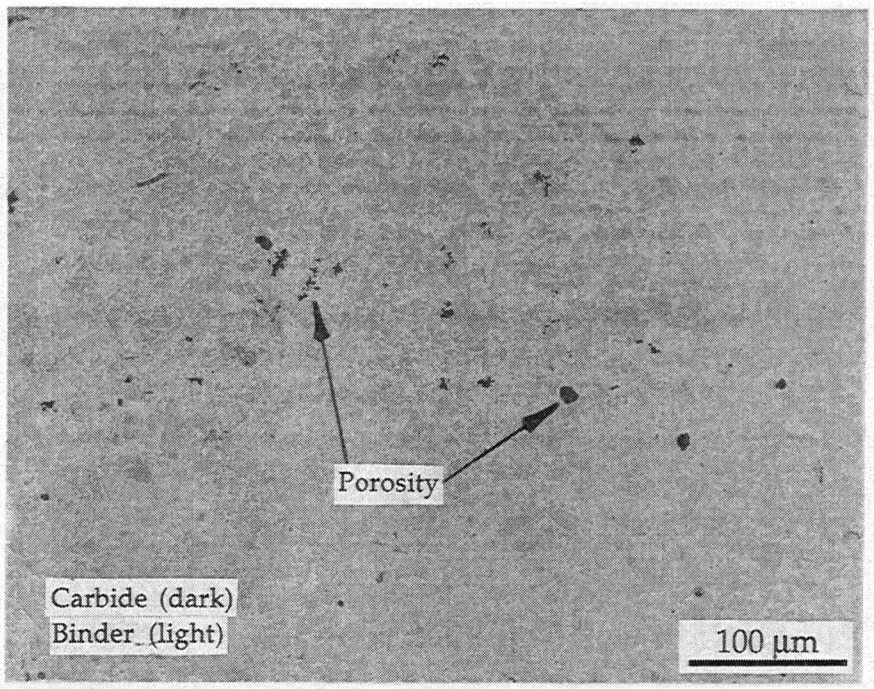


Figure 6.22. CS-1 composite showing Type A06 porosity and region of interconnected porosity.

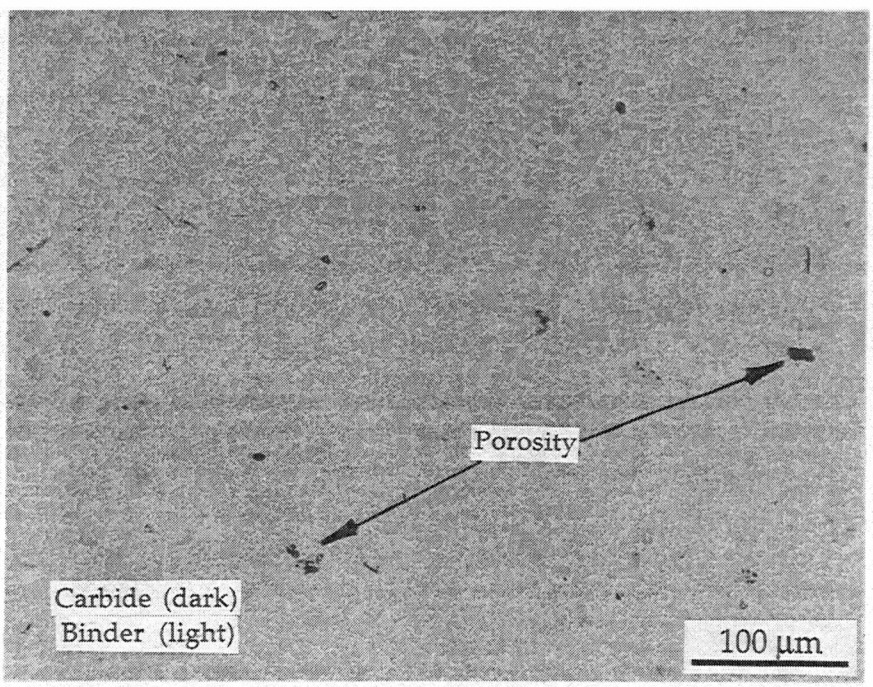


Figure 6.23. CS-1 composite showing Type A04 porosity.

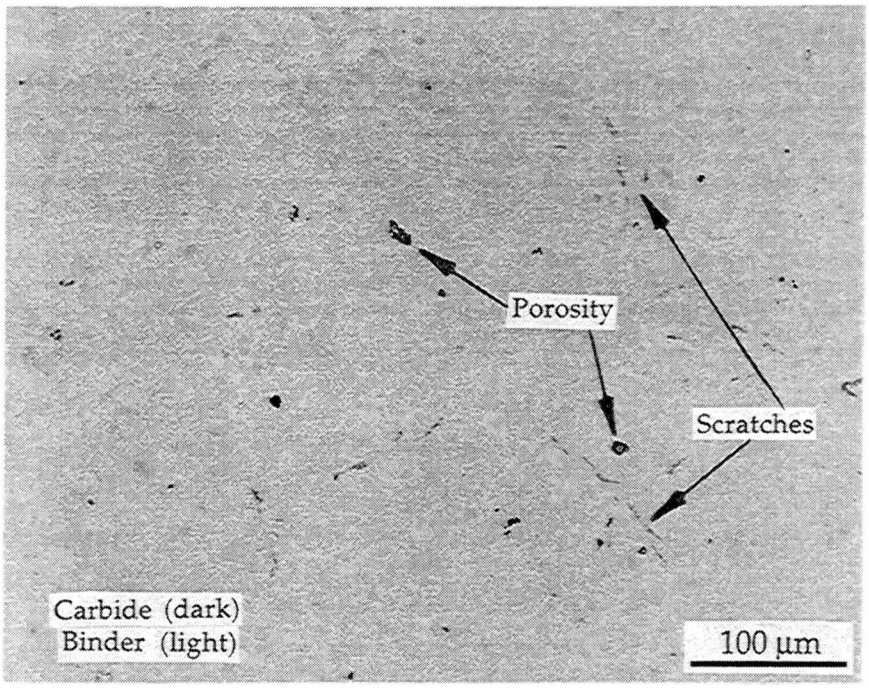


Figure 6.24. CS-3 composite showing Type A04 porosity.

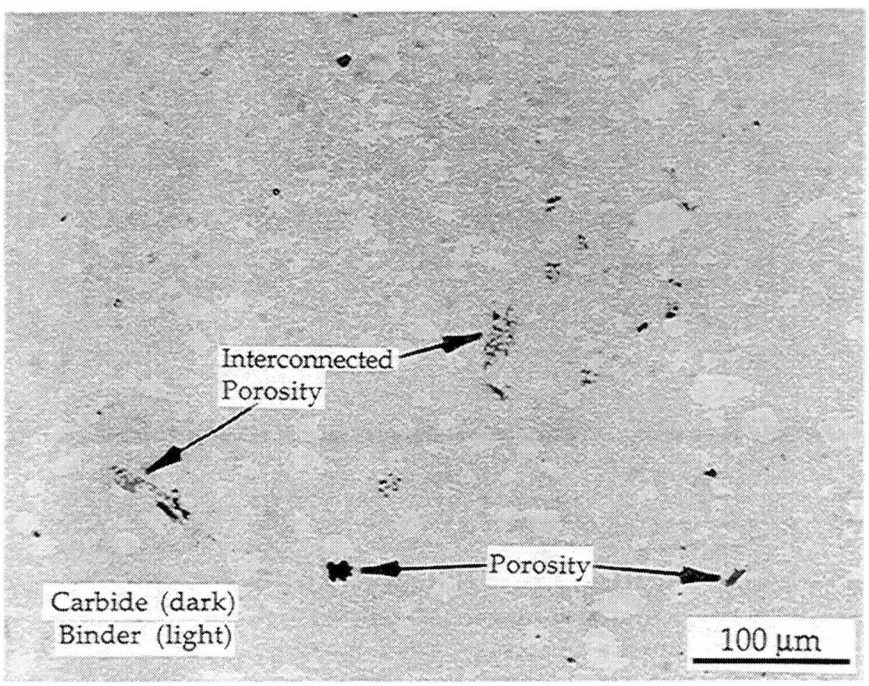


Figure 6.25. CS-7 composite showing Type A04 porosity and large regions of interconnected porosity.

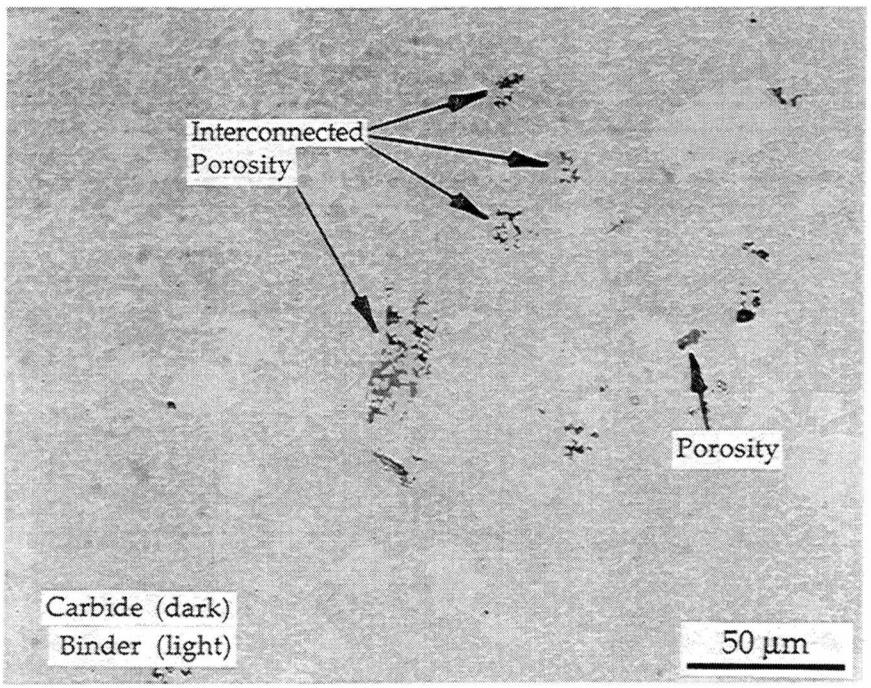


Figure 6.26. CS-7 composite showing large regions of interconnected porosity.

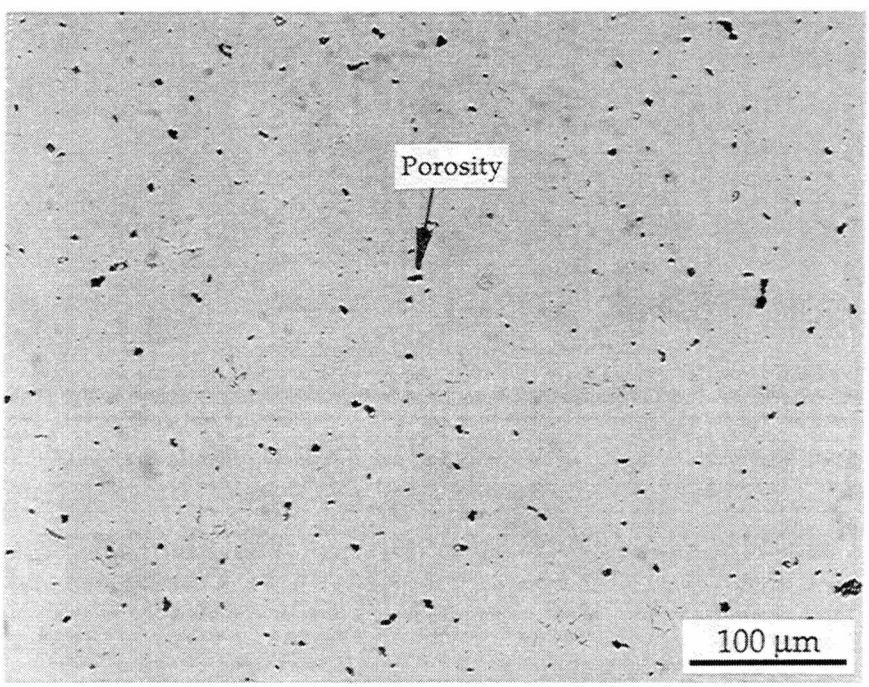


Figure 6.27. CS-9 composite showing Type A08 porosity.

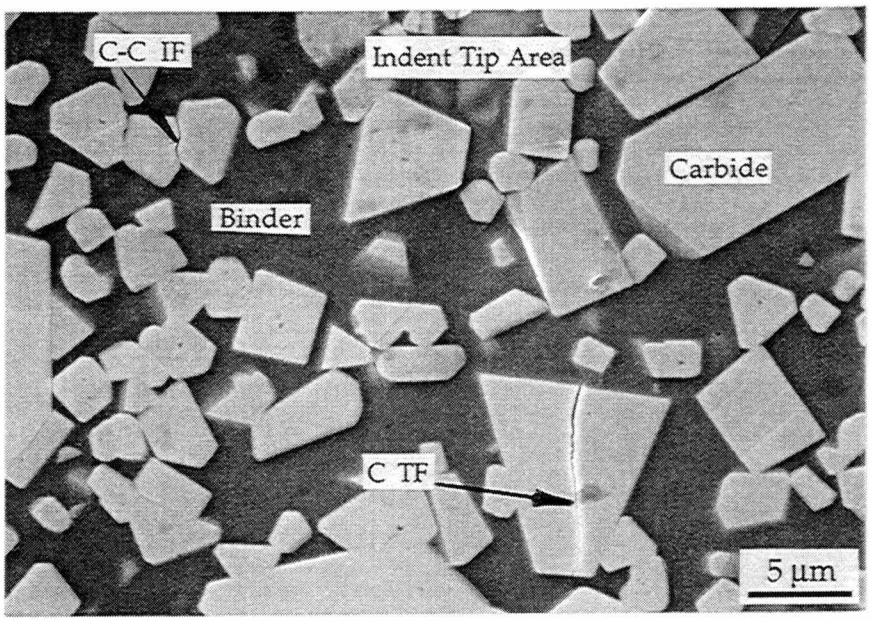


Figure 6.28. First indent area of CS-1 showing only two cracks.

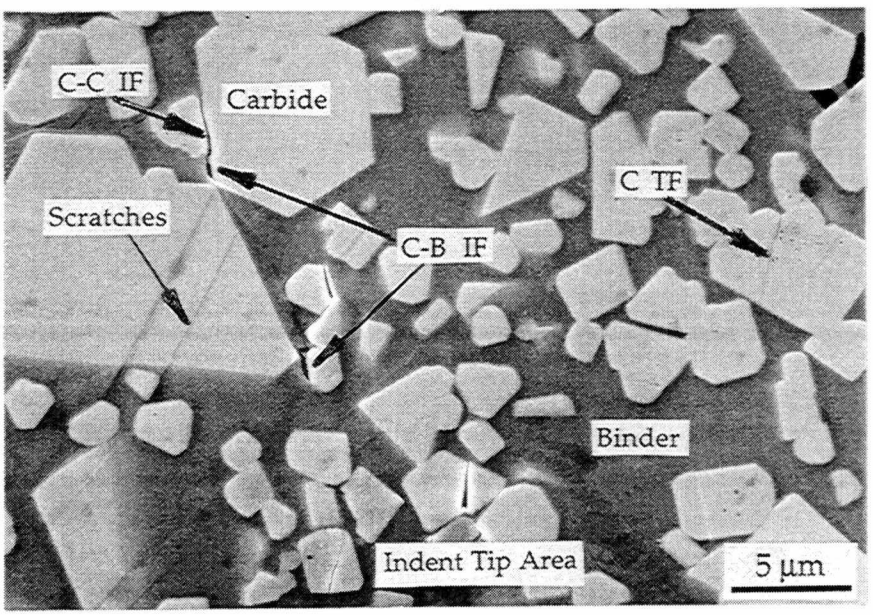


Figure 6.29. Second indent area of CS-1 showing only five cracks.

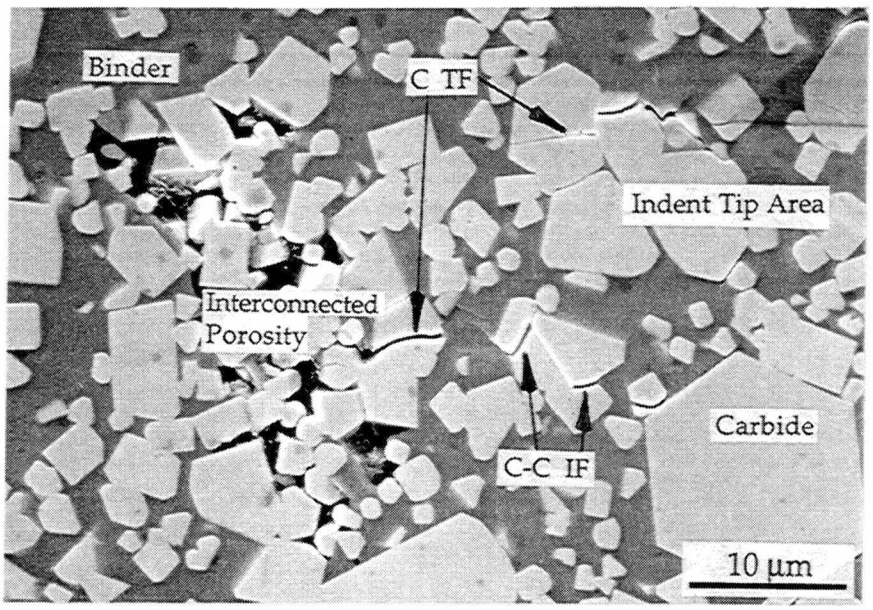


Figure 6.30. Third indent area of CS-1 showing only a few cracks and a region of interconnected porosity.

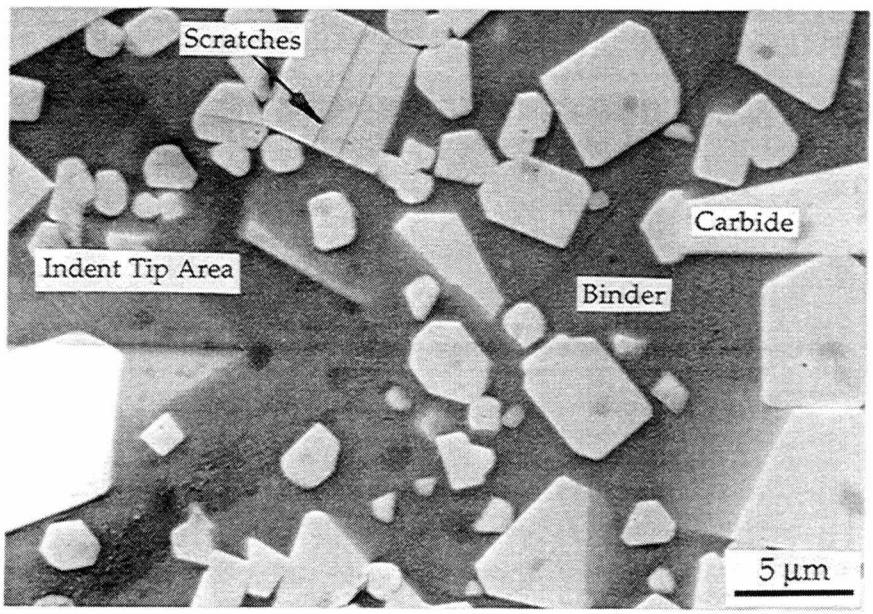


Figure 6.31. Fourth indent area of CS-1 showing no cracks.

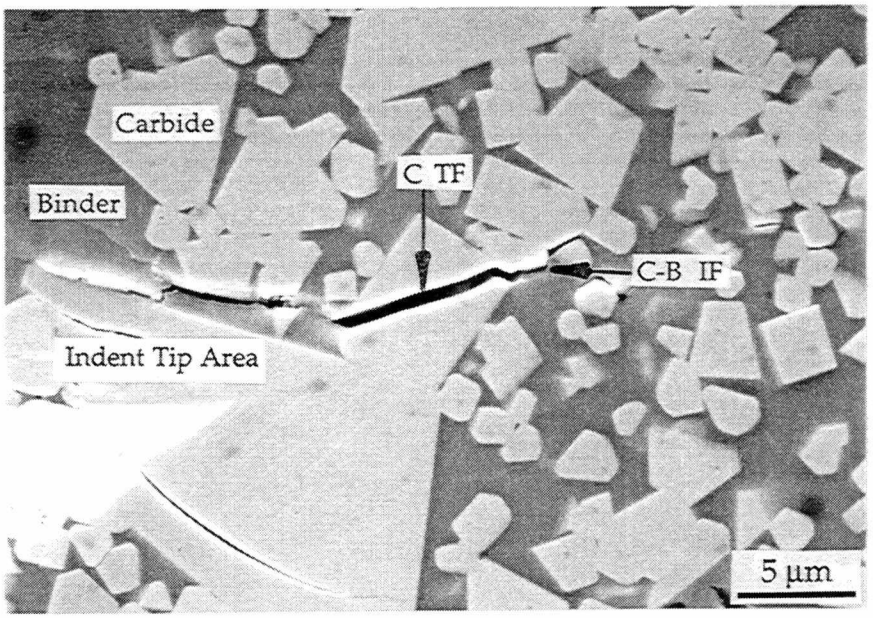


Figure 6.32. First indent area of CS-3 showing a short crack.

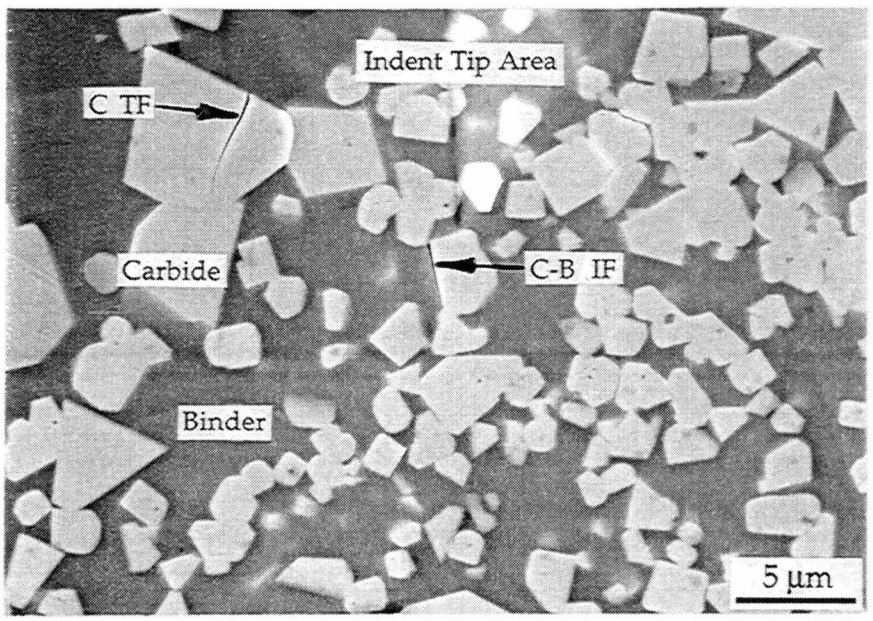


Figure 6.33. Second indent area of CS-3 showing only two cracks.

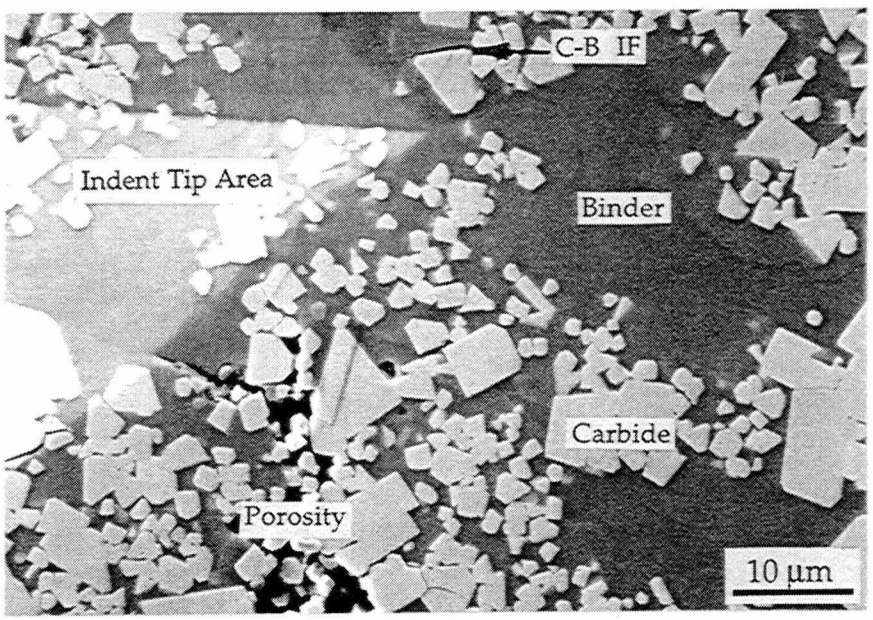


Figure 6.34. Third indent area of CS-3 showing one crack and a region of interconnected porosity.

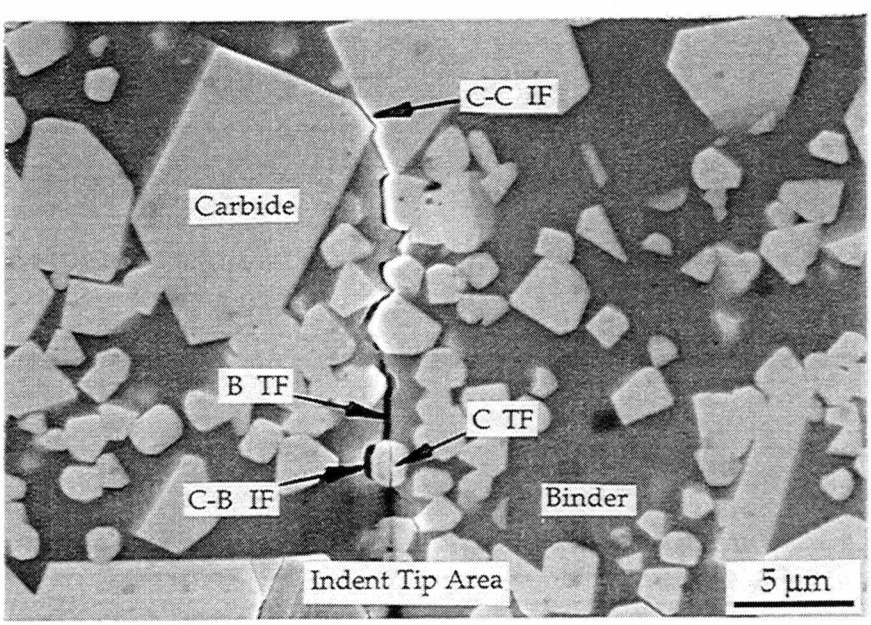


Figure 6.35. Fourth indent area of CS-3 showing all four types of cracking.

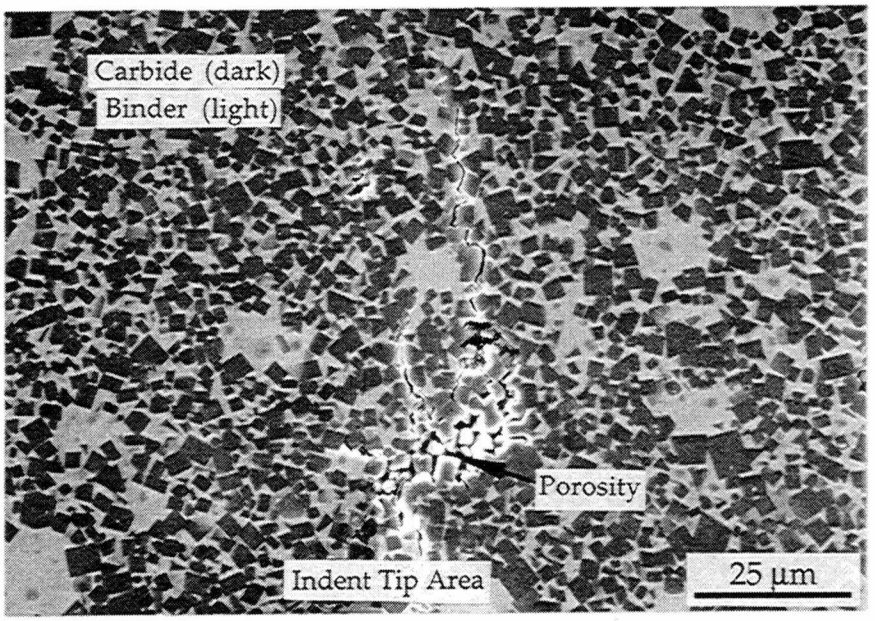


Figure 6.36. First indent area of CS-7 showing long crack extension.

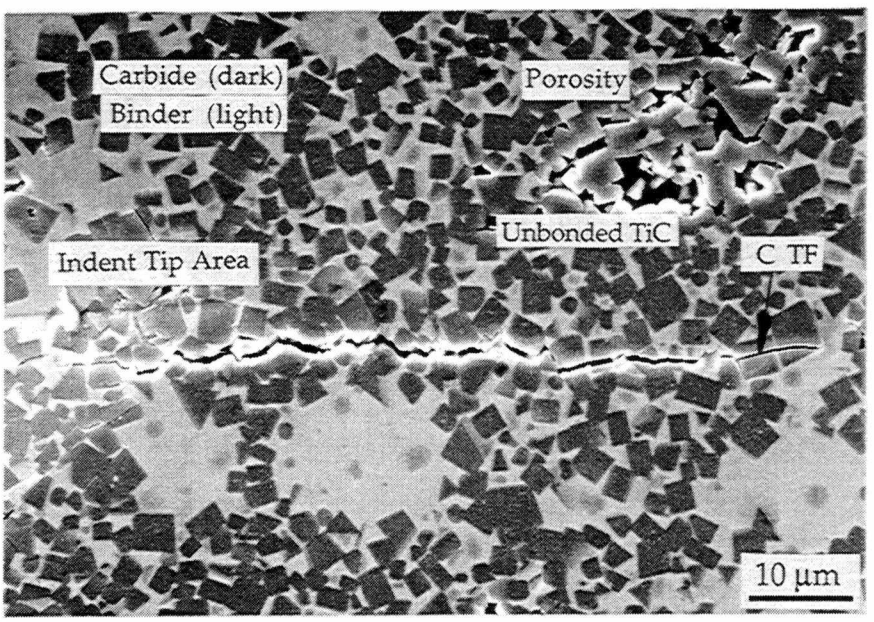


Figure 6.37. Second indent area of CS-7 showing interconnected porosity, unbonded TiC, and Ni_3Al pools.

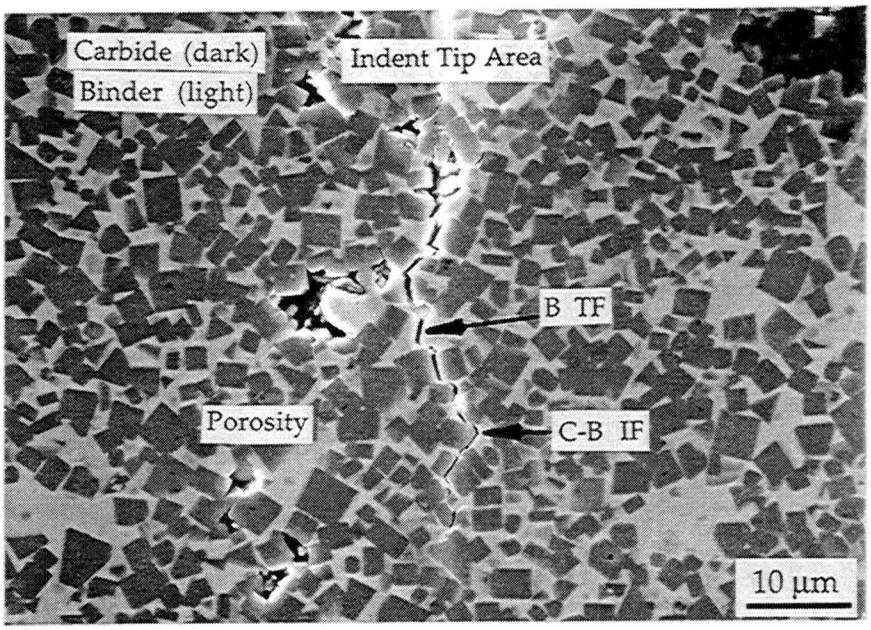


Figure 6.38. Third indent area of CS-7 showing several regions of porosity.

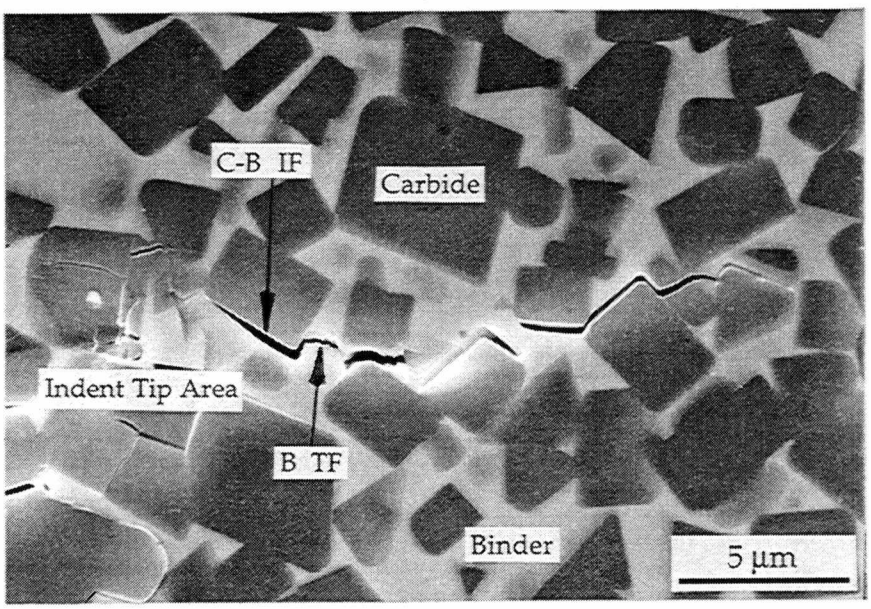


Figure 6.39. Fourth indent area of CS-7 showing the path of a crack.

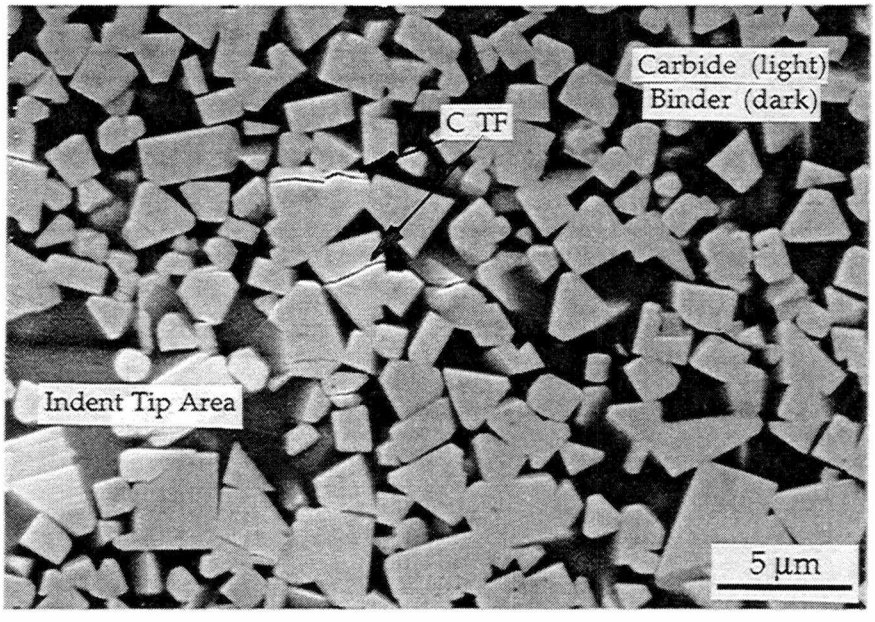


Figure 6.40. First indent area of CS-9 showing only two cracks through carbide grains.

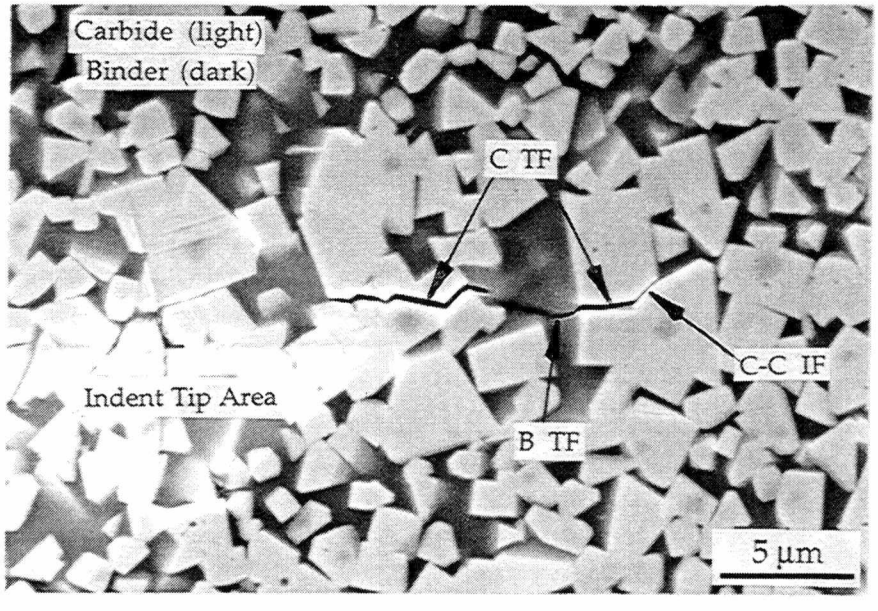


Figure 6.41. Second indent area of CS-9 showing only one crack.

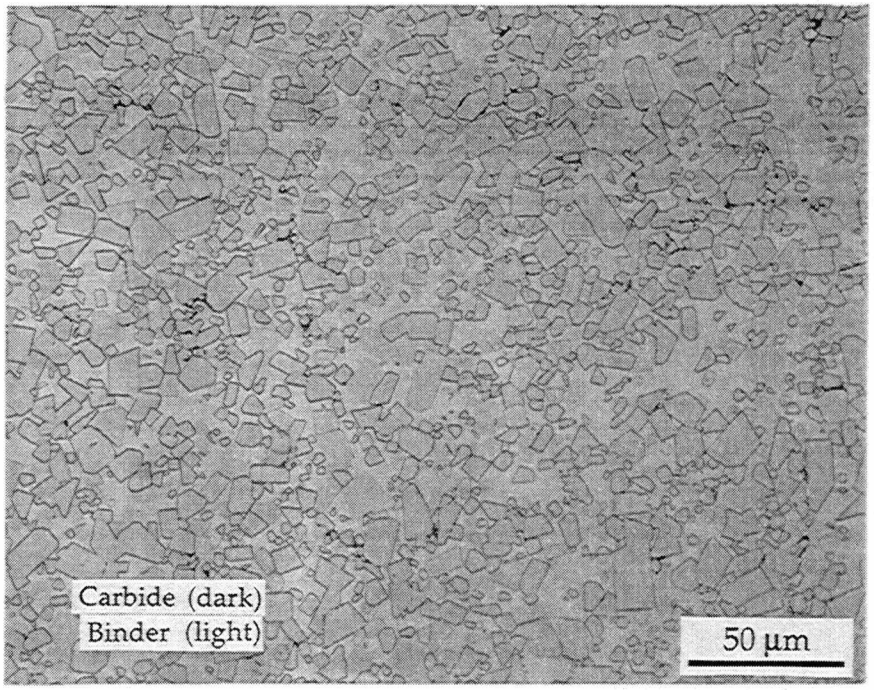


Figure 6.42. Etched microstructure of CS-1.

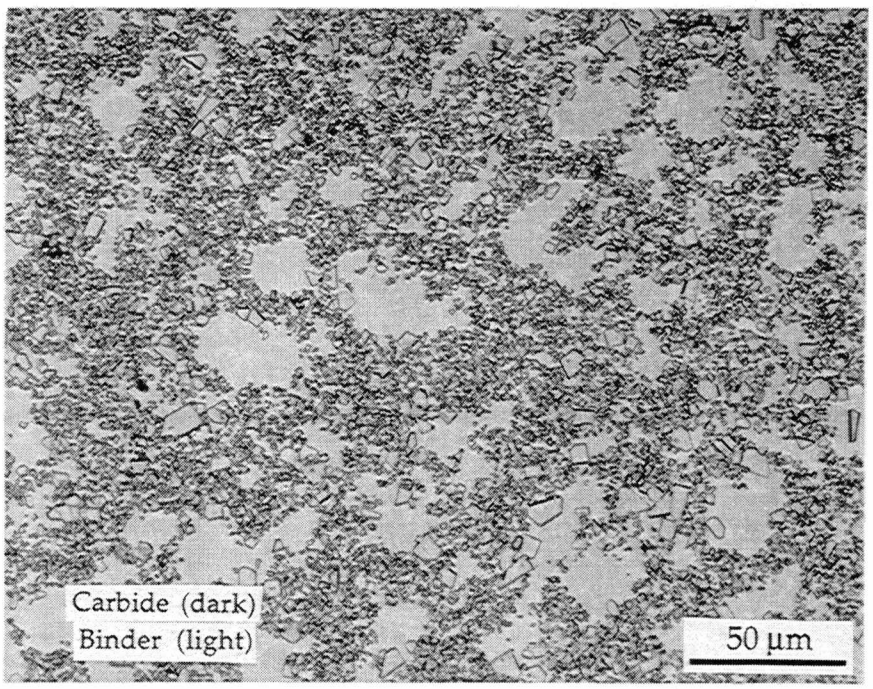


Figure 6.43. Etched microstructure of CS-3.

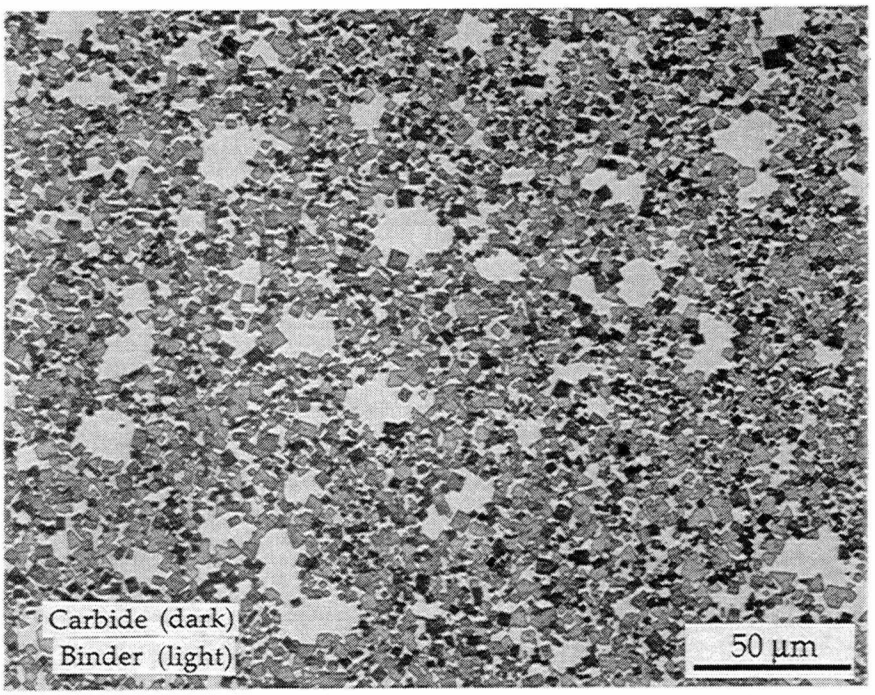


Figure 6.44. Etched microstructure of CS-7.

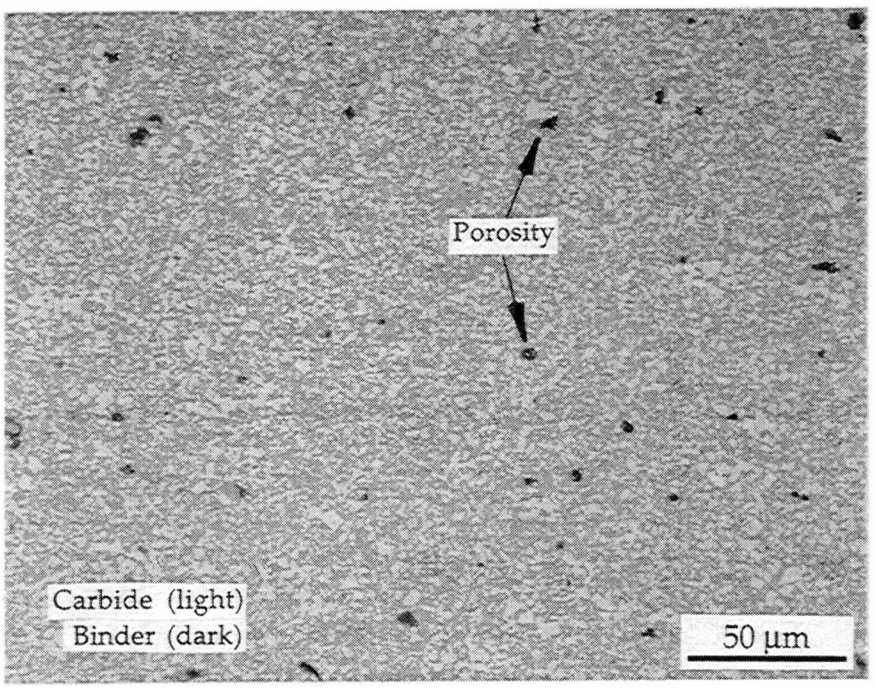


Figure 6.45. Etched microstructure of CS-9.

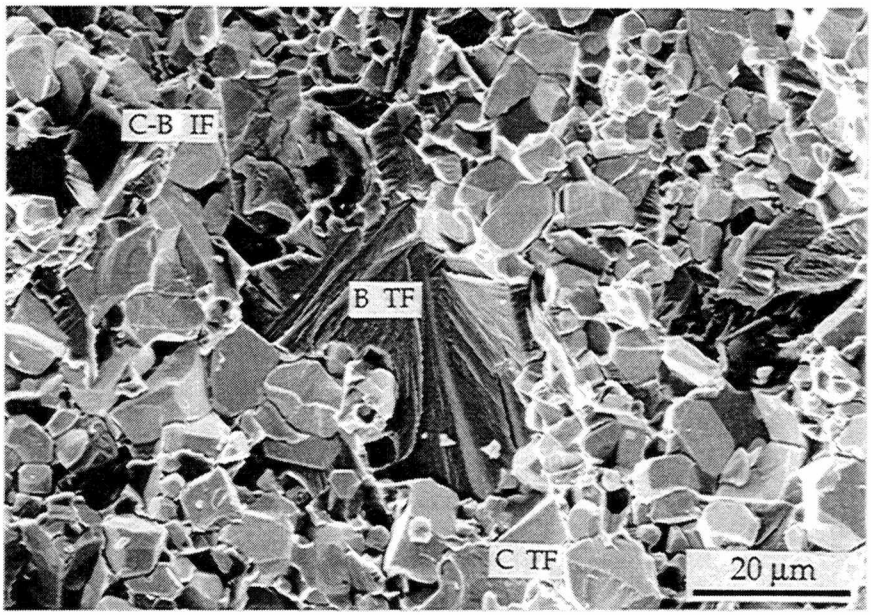


Figure 6.46. Fracture surface of CS-1 showing three different fracture types.

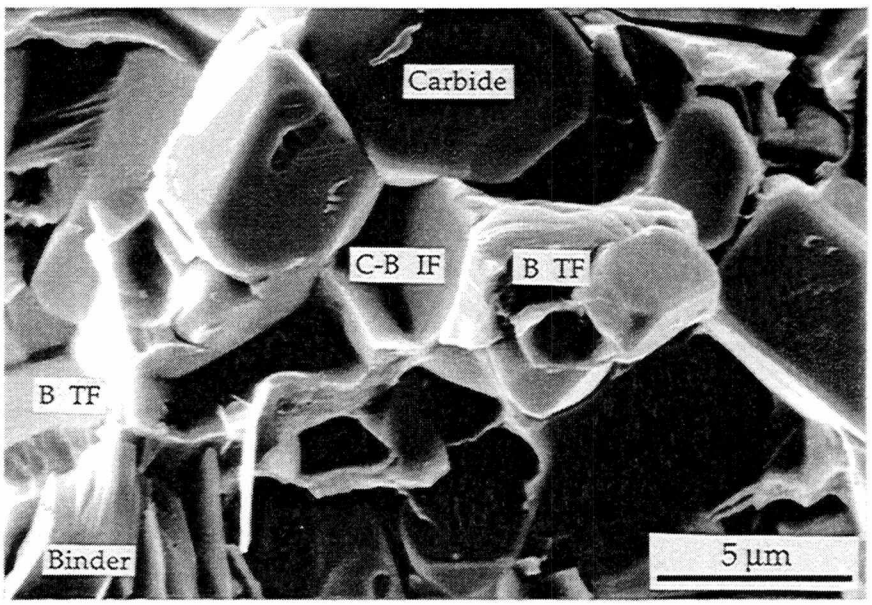


Figure 6.47. Fracture surface of CS-1 showing carbide-binder debonding and transgranular fracture of the binder.

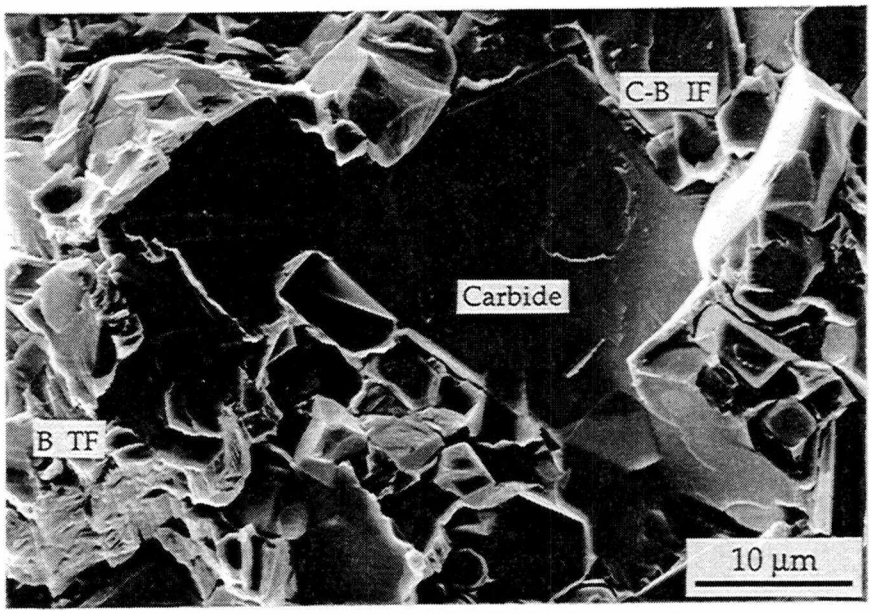


Figure 6.48. Secondary image of fracture surface of CS-1.

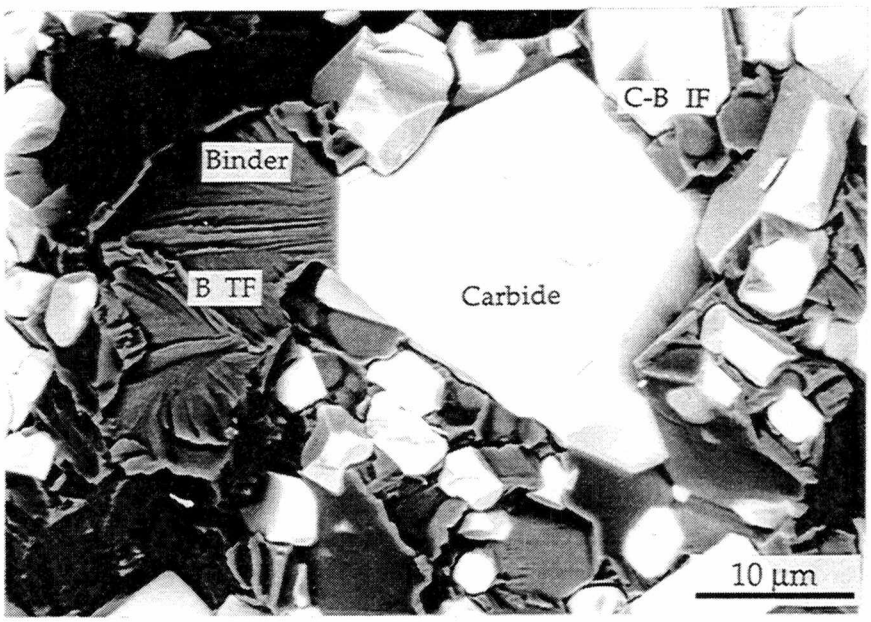


Figure 6.49. Backscattered image of fracture surface of CS-1.

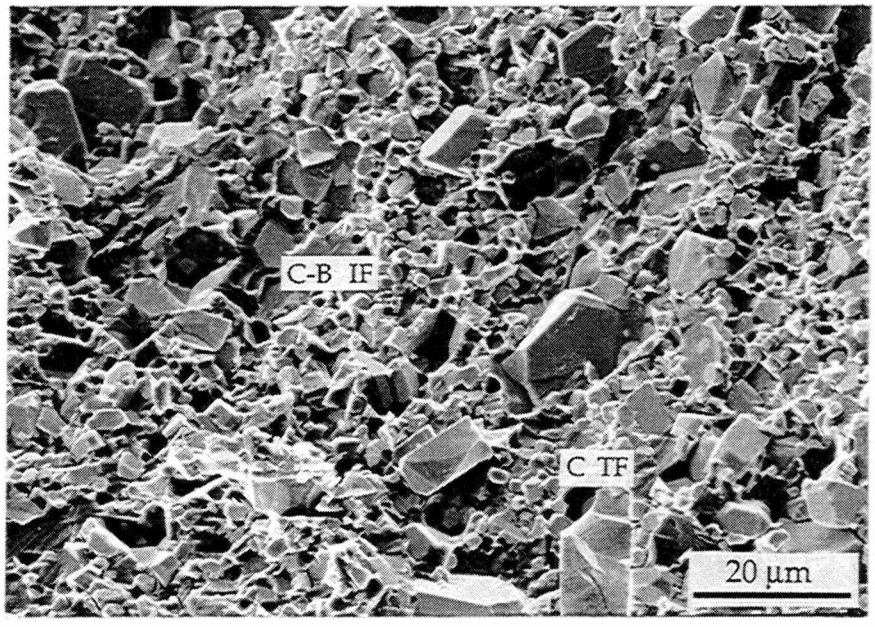


Figure 6.50. Fracture surface of CS-3 showing two types of fracture.

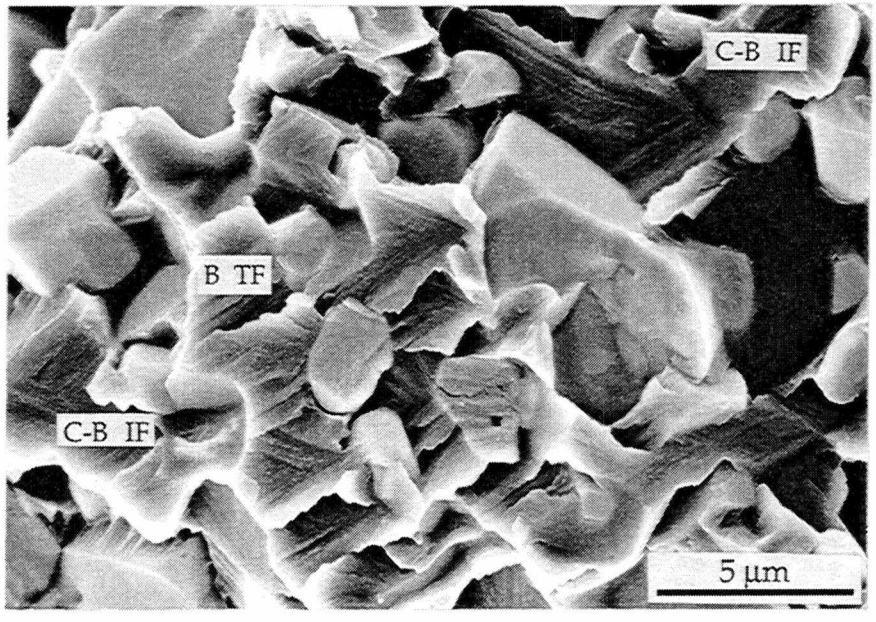


Figure 6.51. Fracture surface of CS-3 showing transgranular fracture of the binder and carbide-binder interfacial debonding.

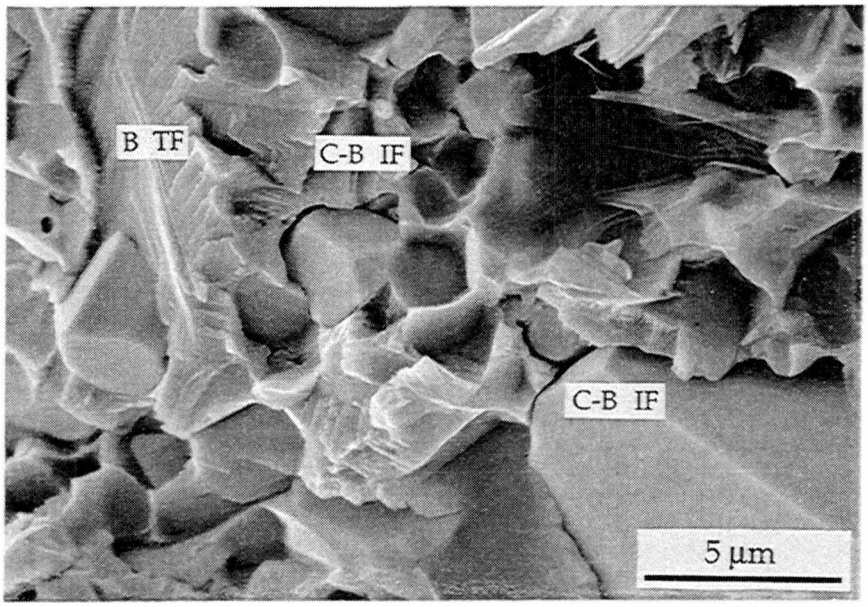


Figure 6.52. Second fracture surface of CS-3 showing binder transgranular fracture and carbide-binder interfacial debonding.

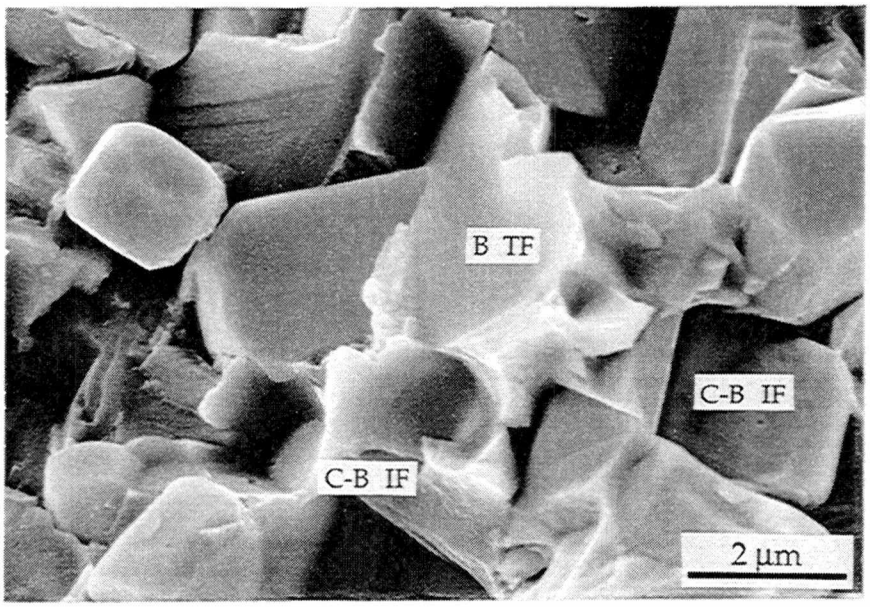


Figure 6.53. Third fracture surface of CS-3 showing binder transgranular fracture and carbide-binder interfacial debonding.

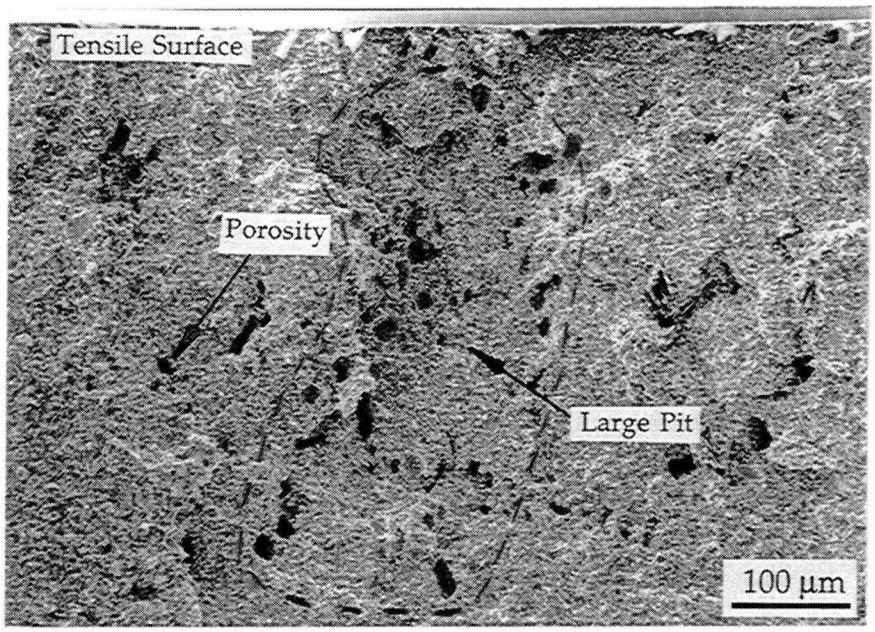


Figure 6.54. Fracture surface of CS-7 showing large pit and porosity.

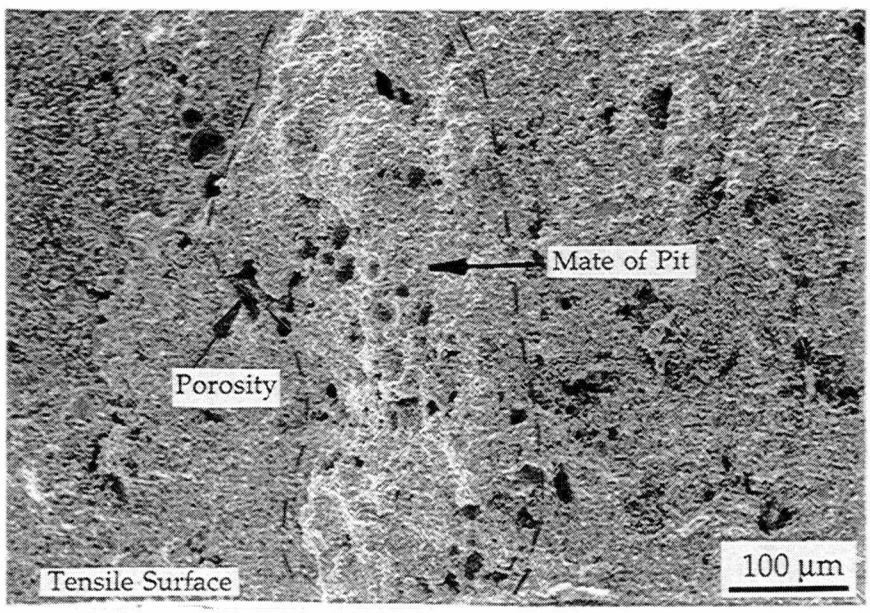


Figure 6.55. Fracture surface of CS-7 showing mate of pit and porosity.

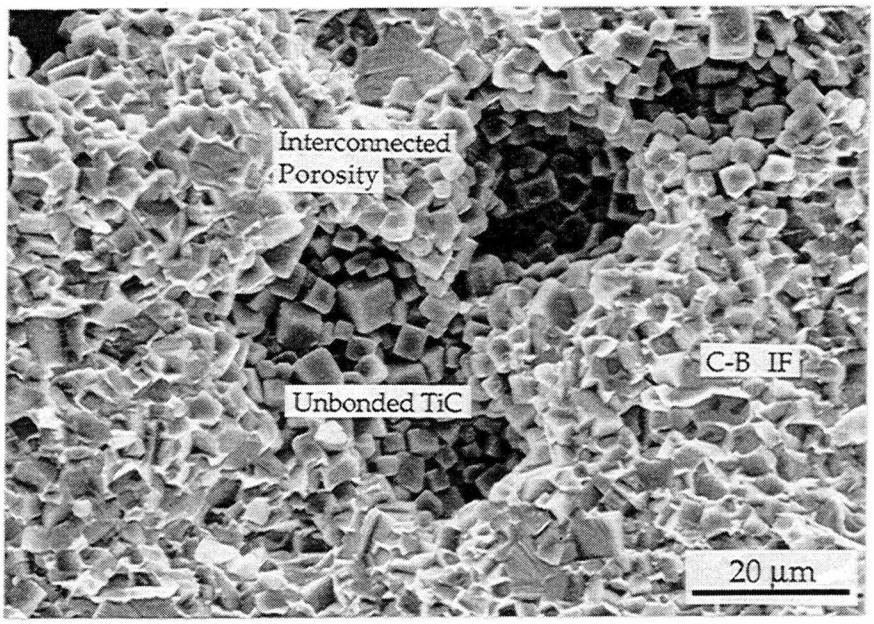


Figure 6.56. Fracture surface of CS-7 showing large areas of unbonded TiC.

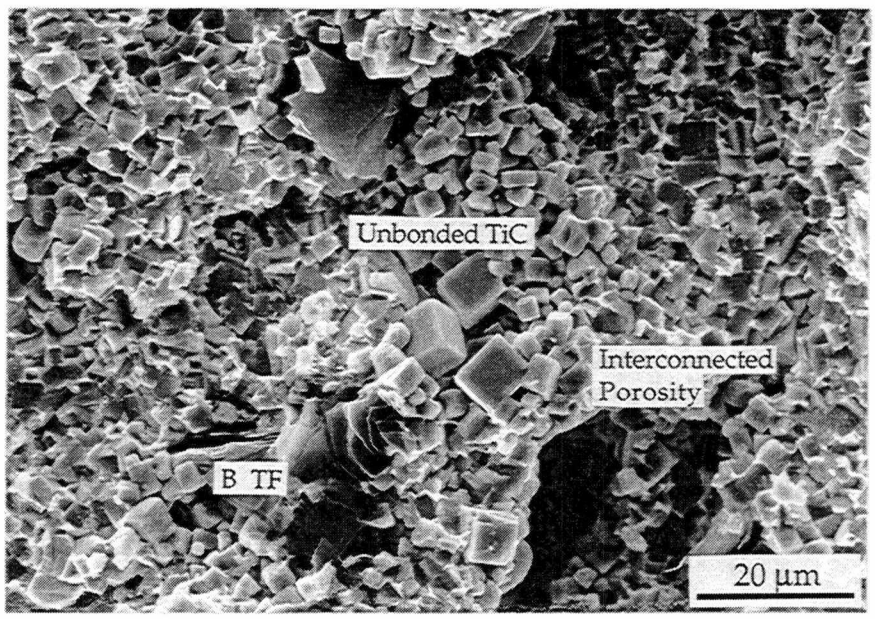


Figure 6.57. Fracture surface of CS-7 showing large pores, unbonded TiC, and binder transgranular fracture.

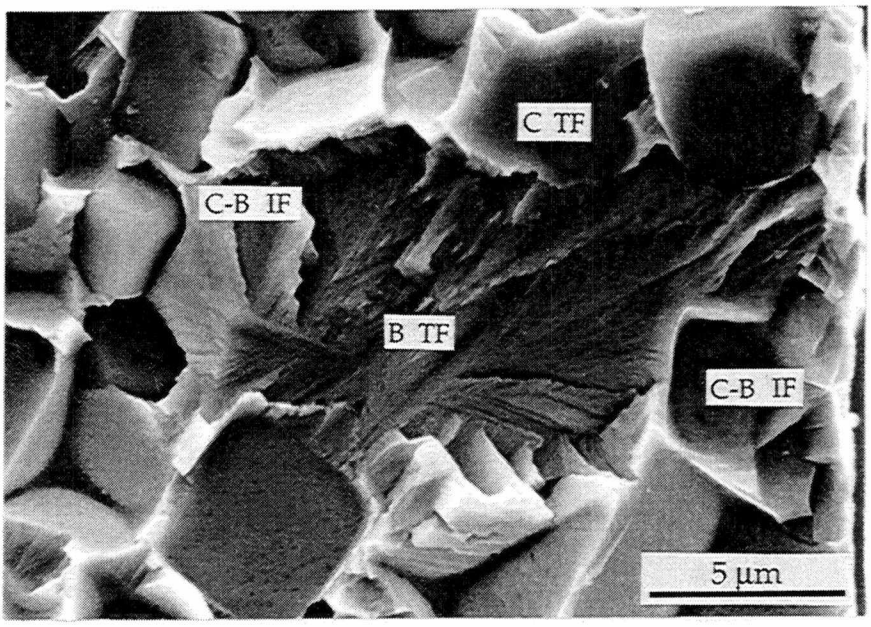


Figure 6.58. Fracture surface of CS-7 showing both types of transgranular fracture and carbide-binder debonding.

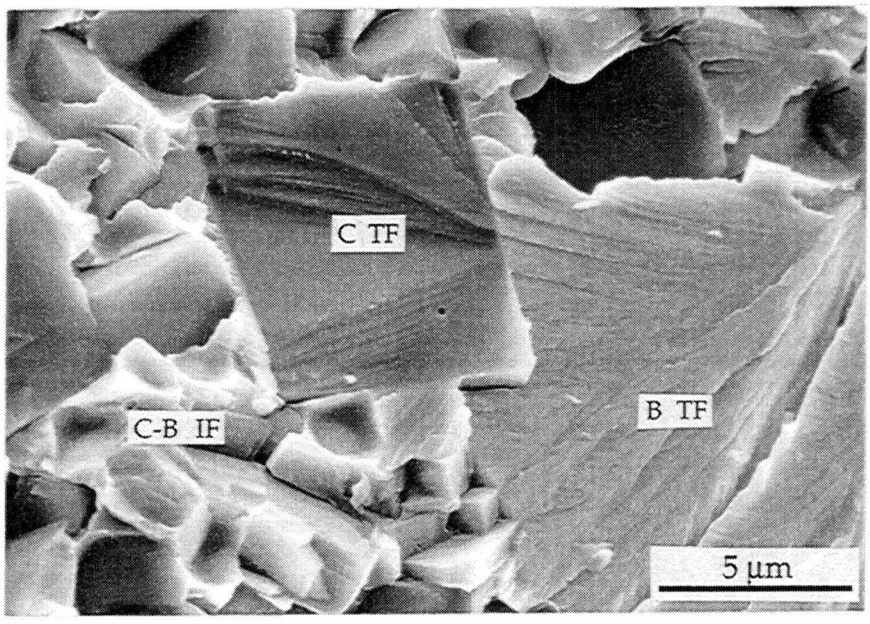


Figure 6.59. Second fracture surface of CS-7 showing both types of transgranular fracture and carbide-binder debonding.

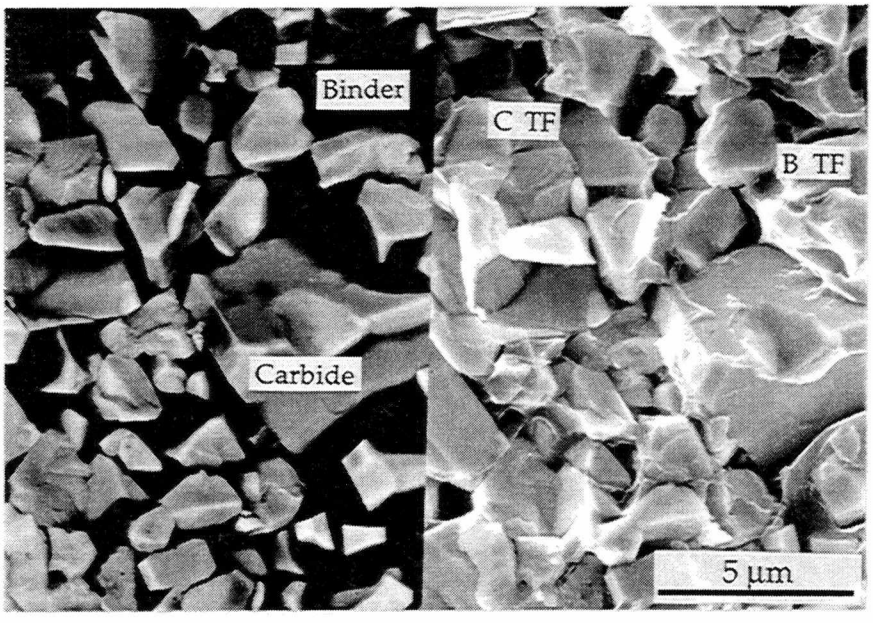


Figure 6.60. Backscattered (L) and secondary (R) images of fracture surface of CS-9 showing transgranular fracture.

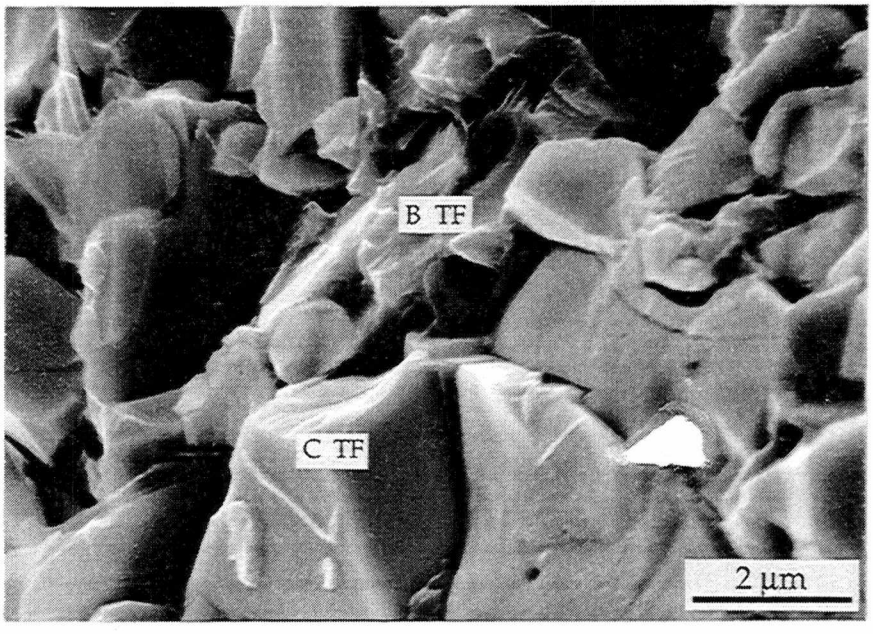


Figure 6.61. Fracture surface of CS-9 showing transgranular fracture.

VITA

The author, Chuck Brandon Thomas, was born in Kingsport, Tennessee on May 31, 1972. He attended Sullivan Central High School in Blountville, graduating in June, 1990. The author enrolled in the College of Engineering at the University of Tennessee at Knoxville in August, 1990, and he was financially supported by the Racheff Metallurgy Scholarship and the Phillip W. Moffitt Endowment. After completing his third year of studies, the author received the Hoechst-Celanese Corporation Outstanding Junior Award. He earned the Bachelor of Science degree in Materials Science and Engineering and graduated *magna cum laude* in August, 1994. The author also began work leading to the Master of Science degree in August, 1994. He was supported financially as a graduate research assistant by the U. S. Department of Energy and Martin Marietta Energy Systems, Inc. The Master of Science degree in Metallurgical Engineering was awarded in August, 1996. His primary thesis advisor was Professor Peter K. Liaw.

The author married the former Deborah Michelle Gibson of Knoxville in June, 1994.

The author is a member of Tau Beta Pi, The American Society for Materials International (ASM International), and The Minerals, Metals, and Materials Society (TMS).